

THERMAL ENERGY STORAGE WITH SENSIBLE HEAT IN AN AIR-ALUMINA  
PACKED BED USING AXIAL FLOW, AXIAL FLOW WITH LAYERS AND  
RADIAL FLOW

By  
Mohammad Mahdie Saleh Al-Azawii

A dissertation submitted in partial fulfillment  
of the requirements for the degree

of

Doctor of Philosophy

In

Mechanical Engineering

MONTANA STATE UNIVERSITY  
Bozeman, Montana

July 2020

©COPYRIGHT

by

Mohammad Mahdie Saleh Al-Azawii

2020

All Rights Reserved

DEDICATION

This dissertation is gratefully dedicated to my loving Father, Mother, Siblings, Wife and Children, for their inspiration; and to those who have supported and encouraged me throughout my education life.

## ACKNOWLEDGMENTS

I'm grateful to my supervisor, Dr. Ryan Anderson for his constant guidance, help and support throughout my PhD study here at Montana State University. I have enjoyed working on this project and appreciated the useful knowledge that I have gained from you especially in scientific and academic research. I'm also thankful to the other members of my committee, Drs. Sarah Codd, Pablo Bueno, and Erick Johnson who have continuously supported me throughout the course of my PhD program. I'd also like to acknowledge and thank the undergraduate students who worked with me in the lab: Megan Danczyk, Carter Theade, Andrew Akerstrom, Duncan Jacobsen, and Celestia Hammond. Special thanks also to the staff of the Mechanical and Industrial Engineering Department, Machining lab, Office of International Programs, and INTERLINK International Institutes at Montana State University for their big support and help.

I'm grateful to my parents and siblings for their great support from grade school to grad school; I wouldn't have made it this far without you. I'm thankful to my wife, Ghusn, you've always been there to advise me, helped me focus on my study, and made my life in Bozeman a wonderful experience; and to my beautiful children, Basma, Ali, and Yousef who have made me always smiling. Thanks also to my colleagues and friends who have supported and helped me throughout my study.

The author acknowledges Montana State University for financial support. The author acknowledges the Higher Committee for Educational Development in Iraq for supporting his scholarship through the Iraqi government funding and the University of Misan for supporting his scholarship.



## TABLE OF CONTENTS

1. INTRODUCTION AND BACKGROUND.....	1
1.1 Introduction .....	1
1.2 Energy Storage Technologies.....	4
1.2.1 Thermal Energy Storage.....	6
1.2.2 Sensible and Latent Heat Storage .....	8
1.2.3 Single-Tank Versus Two Tanks Storage.....	13
1.2.4 Packed Bed Systems.....	14
1.3 Modeling Approaches .....	18
1.4 Operating Conditions .....	23
1.5 Packed Bed Energy Losses.....	31
1.5.1 Pressure Drop Losses .....	31
1.5.2 Thermal Losses .....	32
1.5.3 Axial Thermal Dispersion Losses .....	36
1.6 First and Second Laws of Thermodynamics, Energy and Exergy .....	38
1.7 Energetic and Exergetic Efficiencies .....	40
1.8 Preface.....	46
References.....	49
2. EXPERIMENTAL STUDY ON CYCLIC BEHAVIOR OF THERMAL ENERGY STORAGE IN AN AIR-ALUMINA PACKED BED.....	63
Contribution of Authors and Co-Authors .....	63
Manuscript Information Page.....	64
Abstract.....	65
2.1 Introduction .....	66
2.2 Experimental Methods, Numerical Model, and Thermal Exergy Analysis .....	71
2.2.1 Storage Vessel.....	71
2.2.2 Experimental Conditions .....	74
2.2.3 Modeling Approach.....	76
2.2.4 Exergy Analysis .....	78
2.3 Experimental Results and Conditions.....	80
2.3.1 Model Results and Experimental Repeatability.....	80
2.3.2 Full Charge and Discharge .....	82
2.3.3 Partial Charge-Discharge Cycles .....	86
2.3.4 Hold Time Between Charge-Discharge Cycles .....	92
2.4 Conclusions .....	94
Acknowledgements.....	96
References.....	96

## TABLE OF CONTENTS — CONTINUED

3. EXPERIMENTAL STUDY OF LAYERED THERMAL ENERGY STORAGE IN AN AIR-ALUMINA PACKED BED USING AXIAL PIPE INJECTIONS .....	103
Contribution of Authors and Co-Authors .....	103
Manuscript Information Page.....	104
Abstract.....	105
3.1 Introduction .....	106
3.2 Experimental Methods, and Thermal Exergy Analysis .....	113
3.2.1 Storage Vessel, Axial pipe Injection, and Temperature Measurements.....	114
3.2.2 Experimental Conditions and Design.....	116
3.2.3 Modeling Approach to Determine Thermal Dispersion Losses: Adiabatic Vs. Non-Adiabatic.....	118
3.2.4 Exergy Analysis .....	121
3.3 Results and Discussion.....	123
3.3.1 Full Charge and Discharge: Effects of Flow Rates and Number of Layers.....	125
3.3.2 Recovery Temperature for One, Two, and Three Layers.....	134
3.3.3 Quantification of Thermal Dispersion and Heat Losses to the Environment .....	136
3.4 Conclusions .....	142
Acknowledgements.....	143
Appendix 3.A .....	143
References.....	145
4. EXPERIMENTAL STUDY OF THERMAL BEHAVIOR DURING CHARGING IN THERMAL ENERGY STORAGE GAS PACKED BED USING RADIAL PIPE .....	152
Contribution of Authors and Co-Authors .....	152
Manuscript Information Page.....	153
Abstract.....	154
4.1 Introduction .....	155
4.2 Experimental Setup, Energy and Charging Efficiency Analysis .....	161
4.2.1 Storage Packed Bed with Radial Pipe Injection.....	161
4.2.2 Experimental Conditions and Design.....	164
4.2.3 Energy Analysis .....	167
4.3 Results and Discussion.....	169
4.3.1 Effect of Variable Hole Size in the Radial Pipe; Hole Diameter and Numbered of Zones with Fixed Diameter .....	170
4.3.2 Effect of Plates on Temperature Uniformity in the Bed.....	173

## TABLE OF CONTENTS — CONTINUED

4.3.3: Comparison of Axial and Radial Flow Charging: Outlet Temperature, Wall Losses, Energy Stored and Charging Efficiency.....	177
4.4 Conclusion.....	182
Acknowledgements.....	183
Appendix 4.A .....	184
References .....	185
 5. CONCLUSIONS AND RECOMMENDATIONS.....	 191
5.1 Conclusions .....	191
5.2 Recommendations.....	196
References .....	206
 CUMULATIVE REFERENCES CITED .....	 207
 APPENDICES.....	 221
APPENDIX A: Pieces of Apparatus and Equipment Used in the Lab; and Screenshots of LabView Code and Data Analysis .....	222
Table A.1 Storage Packed Bed Apparatus. Internal Insulation, and Internal Thermocouples.....	223
Table A.2 Packed Bed Associated Equipment.....	230
Table A.3 Screenshots of LabView Code and DAQ System Connections/Channels.....	236
Table A.4 Screenshots of Data Analysis .....	241
APPENDIX B: Experimental Protocols.....	245
B.1 Normal Configuration Packed Bed Setup Protocol .....	246
B.1.1 Charging and Discharging Test Protocol .....	249
B.2 Layers Configuration Packed Bed Setup Protocol.....	250
B.2.1 Charging and Discharging Test Protocol .....	252
B.3 Radial Configuration Packed Bed Setup Protocol.....	254
B.3.1 Charging and Discharging Test Protocol .....	257
B.4 Removing the Beads from the Storage Vessel for Normal, Layers and Radial Configurations Protocol .....	258
APPENDIX C: Specific Heat Capacity Variation.....	260
APPENDIX D: LabView, Data Analysis, Temperature Controller and Calibration of Flow and Temperature .....	263
D.1 LabView Code Protocol.....	264

TABLE OF CONTENTS — CONTINUED

D.2 Data Analysis Protocol.....	265
D.3 Temperature Controller and Heater Protocol.....	268
D.4 Calibration Protocol.....	269
D.4.1 Normal Configuration Calibration Protocol.....	270
D.4.2 Layers Configuration Calibration Protocol.....	270
D.4.3 Radial Configuration Calibration Protocol.....	271
D.5 Flowmeter Calibration and Calculations of Flowrate Protocol.....	272
D.6 Air Purity and Muffler.....	272
APPENDIX E: Part Numbers and Manufacturer for the Equipment Used in the Lab.....	273

## LIST OF TABLES

Table	Page
1. The thermophysical properties of some solid materials.....	29
2. Materials used as insulation in TES systems.....	35
3. Time for Charging and Discharging Processes.....	75
4. Time for Partial Charge-Discharge Cycles .....	75
5. The Thermophysical properties and conditions Used.....	78
6. Percentage Exergy for Full Charge-Discharge Cycle.....	86
7. Percentage Exergy for Hold on Time.....	93
8. Dimensions of TES Packed Bed.....	115
9. Time for Charging and Discharging Processes.....	117
10. The Thermophysical properties Used in Model.....	119
11. Percentage of flow split used in the model.....	120
12. Percentage Exergy for Best and Worst Cases.....	125
13. Percentage Exergy and Dispersive Losses with Layers .....	139
14. Specifications of Radial Tubes .....	166
15. The Thermophysical Properties of Air and Alumina.....	169
16. Specifications of Solid Plate.....	174
17. Energy and Percentage Charging Efficiency for Axial and Radial Flows ....	180
A1. Charging and Discharging Schemes with Percentage Exergy.....	144
A2. Percentage Charging Efficiency for All Designs.....	185
B1. Distances Between Heater and Vessel inlet.....	249

## LIST OF TABLES CONTINUED

Table	Page
C1. Percentage Exergy with Heat Capacity Variations .....	261
C2. Percentage Exergy at Constant and Time dependent Storage Temperature .....	262
D1. MATLAB Code for Exergy Efficiency .....	267
D2. Calibration Results for Three Layers .....	271
D3. Air Flow Calibration.....	272
E1. List of Part Numbers Used in the Lab .....	274

## LIST OF FIGURES

Figure	Page
1. Packed Bed Configurations .....	3
2. Thermal Energy Storage Forms .....	5
3. Linear Concentrator Power Plant with TES Tanks .....	7
4. CSP Plant Cost .....	8
5. Formation of Thermal Front .....	14
6. Schematic of Horizontal TES Tank Showing Charge/Discharge Processes .....	15
7. Storage Vessel Domains and Radial Direction of Heat Losses .....	33
8. Thermal Energy Storage Publications .....	46
9. Schematic of Experimental Setup (Axial Configuration) .....	72
10. Model and Experimental Results .....	82
11. Temperature Profiles During Charging .....	83
12. Temperature Profiles During Discharging .....	85
13. Temperature Profiles with Cycles During Charging .....	88
14. Temperature Profiles with Cycles During Discharging .....	89
15. Recovery Temperature for Multiple Repeated Cycles .....	90
16. Exergy Efficiency, Stanton Number and Thermal Dispersion with Cycles .....	92
17. Temperature Profiles During Discharging (Holding on) .....	94
18. Schematic of Experimental Setup (Axial Pipe Injection Configuration) .....	114
19. Temperature Profiles During Charging with Two Layers .....	127
20. Temperature Profiles During Discharging with Two Layers .....	130

## LIST OF FIGURES CONTINUED

Figure	Page
21. Temperature Profiles During Charging/discharging with Two Layers.....	132
22. Temperature Profiles During Charging/Discharging with Three Layers.....	133
23. Recovery Temperature for Two and Three layers .....	135
24. Model and Experimental Recovery Temperature for 1, 2, and 3 Layers .....	138
25. Schematic of Radial Tube and Solid Plates.....	161
26. Schematic of Experimental Setup (Radial Flow Configuration).....	162
27. Temperature Profiles During Radial Charging (Designs A and E) .....	172
28. Average Temperature with Standard Deviation (Even Flow) .....	173
29. Temperature Profiles with Zero and One Plate .....	175
30. Temperature Profiles with Zero, One and Two plates .....	176
31. Temperature Profiles with Standard Deviation (Two plates).....	176
32. Outlet and Surface Wall Temperatures .....	178
33. Temperature Profiles with Axial and Radial flow Charging.....	179
34. Radial Tube Failure.....	203
A1. Temperature Profiles During Radial Charging (Designs B, C, D and F).....	184
B1. Sinusoidal Temperature Function Between Heater and Vessel Inlet.....	248
B2. Custom Flange for Pipe Injection.....	252
B3. Cover Flange for Radial Flow.....	257
B4. Pipe Connections for Normal Discharging with Radial Charging.....	258



LIST OF FIGURES CONTINUED

Figure	Page
C1. Storage Temperature at Four Flow Rates .....	262
D1. Heater and Associated Equipment .....	268
D2. Temperature Controller Front Window.....	269
D3. Muffle Used to Reduce Noise.....	272

## ABSTRACT

Thermal behavior in a packed bed thermal energy storage (TES) system is studied experimentally. TES systems are a promising solution to integrate renewable energy sources such as solar energy. The performance of such systems can be affected by different variables such as storage material size/type, pressure, temperature, heat transfer fluid (HTF), storage type (sensible/latent heat), and flow rate. Although these variables have been studied in literature, the resulting thermal dispersion and heat losses to the environment have been considered in few studies. This thesis studies the thermal behavior of an air-alumina TES packed bed focusing on dispersion and heat losses to quantify the thermal performance. Reducing their effects can improve the thermocline and thus thermal efficiency. The research efforts in this work quantify these effects and provide two new methods to reduce thermal dispersion and increase exergetic efficiency. Three configurations were considered in the present study. In the first configuration, a traditional packed bed is used focusing on performance for multiple partial cycles. This configuration quantified the thermal performance and served as a basis to compare the results from the other configurations. Dispersion effects were found to accumulate before a steady state was achieved during cycling. In the second and third configurations, novel pipe injection techniques were used to charge/discharge the bed. First, the normal bed is divided into layers via inserting pipes along the bed's axial length, focusing on a full charge-discharge cycle. Results show that exergy efficiency increases with flow rate and number of layers. The thermocline improved and dispersion losses decreased with number of layers. Second, a perforated pipe to facilitate radial flow was inserted at the center of the bed along the axial length to heat the bed. Radial charging shows higher charging efficiency compared to normal axial charging. Pipe injection is a novel method and a promising technique that improves the thermal performance of a lab scale storage bed, especially the layering method. Radial injection warrants more investigation to quantify its performance in thermal cycles.

## CHAPTER ONE

INTRODUCTION AND BACKGROUND1.1 Introduction

The global demand on energy usage is increasing with a steadily growing population. Fossil fuel sources such as coal, oil and natural gas have been used for decades to produce the daily necessary energy. The usage of fossil energy is increasing in order to match the demand, and fossil fuels represent a driver for the world's economy. However, the heavy usage of fossil energy worldwide has led to climate change or global warming, which has different effects such as temperature rise, wildfires, drought, floods, rising sea level and severe storms[1]. According to the U.S. Department of Energy (DOE), the global warming effects threaten US energy infrastructure, and thus the United States' growth, national security, energy security and quality of life. Therefore, the DOE supports research to develop renewable energy systems and reduce the harmful effects of fossil energy [2].

Although the renewable energy sources such as solar energy, wind energy, and ocean currents are considered as clean energy sources, they suffer from inherently low energy density and discontinuous availability. The intermittent nature of such sources could be reduced via using energy storage systems [3]. Renewable energy sources such as solar energy can be stored in the form of heat during the daytime. Then, the stored energy can be used when there is a shortage of solar energy or an increase in demand. This thesis investigates thermal energy storage in an air-alumina packed bed focusing on quantification of the thermal behavior via studying and analyzing the temperature

distribution (thermal front), dispersion losses, heat losses, exergetic efficiency and charging efficiency. This is achieved experimentally via first studying the full charge-discharge cycle and multiple partial charge-discharge cycles. Then, new techniques are used to charge-discharge the bed and control the thermal front, which are axial segmentation and radial pipe injections. These novel schemes inject and recover heated gas via an internal piping network within the packed bed. A schematic of the three configurations that have been studied are shown in Figure 1. Figure 1 a-c shows the packed bed that was designed, installed, and commissioned at Montana State University. The storage container in Figure 1a is 120 cm in length (100 cm for the bed domain and 20 cm for the free space at the inlet and outlet of the bed), fabricated and hydro-tested by the vendor, Power Service, Inc. The internal insulation (Promat Inc., custom design) is 120 cm in length. A rigid calcium silicate insulation sheet with  $\frac{1}{2}$  inch thickness was covered the cover flanges inside, providing a continuous internal insulation domain. The introductory section covers work that has been done on storage systems including energy storage technologies, storage packed bed systems, experimental and numerical approaches, operating conditions, packed bed losses, first and second law of thermodynamics, and exergetic and energetic efficiencies.

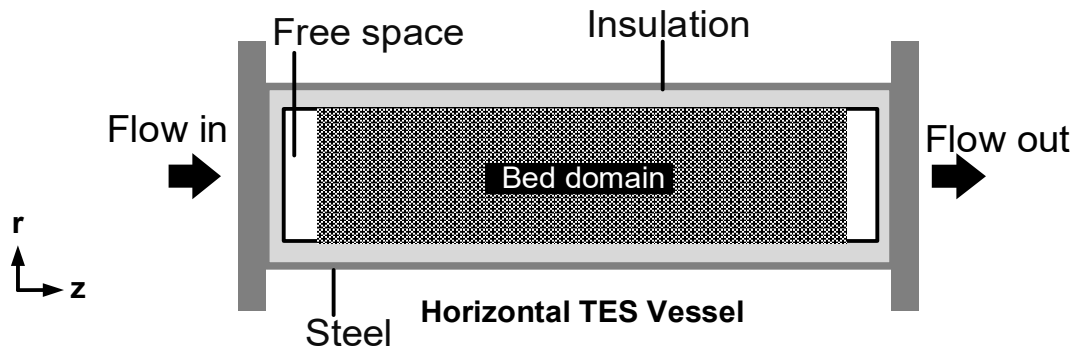
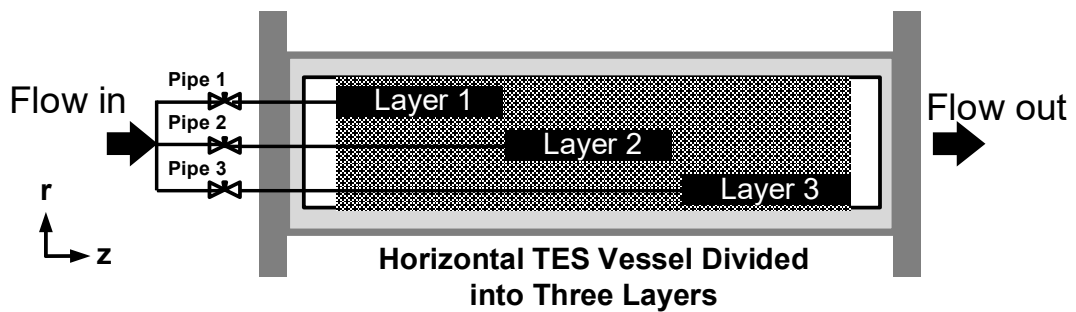
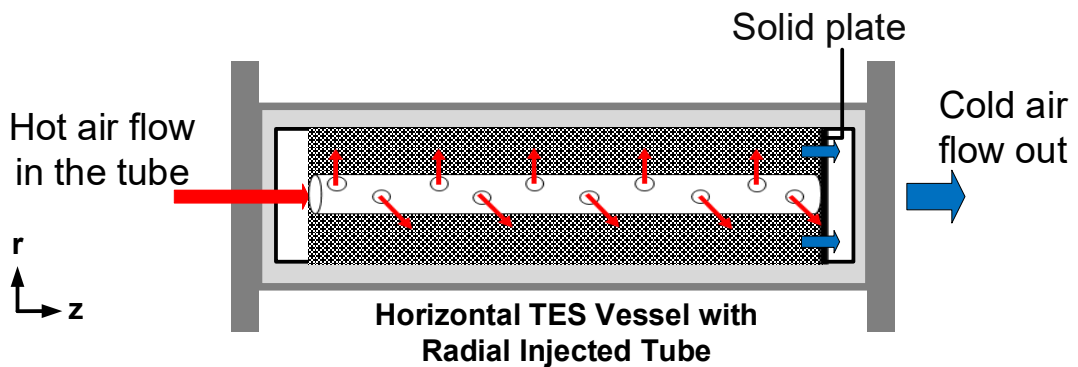
(a) Normal Configuration:(b) Layering Configuration:(c) Radial Configuration:

Figure 1: The three configurations that have been used in the present study, showing the storage vessel only (not to scale). (a) The normal axial flow configuration, (b) The layering axial flow configuration with three injected pipes to divide the bed domain into three layers, and (c) Radial flow configuration, showing the radial injected tube and solid plate at the outlet. Not: schematics with more details can be seen in chapter 1, 2, and 3 for each configuration, explaining the experimental setup of the packed bed and all other required devices.

## 1.2 Energy Storage Technologies

Energy storage is the technology of storing energy in different forms for a later usage at peak times or when demand increases. Energy can be stored in five major methods: chemical energy storage, mechanical energy storage, biological storage, magnetic storage, and heat storage or thermal energy storage (TES) [4]. In chemical energy storage, battery energy storage (electrochemical energy) systems have been used and considered as a promising technology [5, 6]. The City University of New York (CUNY) Energy Institute developed a low-cost zinc anode rechargeable battery that can be used for grid-scale energy storage [5, 6]. The battery energy storage market is expected to grow from \$1.98 billion US dollar in 2018 to \$8.54 billion US dollar by 2023 [5, 6]. In mechanical energy storage, energy can be stored in different forms such as pumped-hydro- storage (water storage reservoirs at two different elevations, which are used to produce electricity) or energy storage in pressurized gas (mechanical tanks to store gases such as hydrogen to power the fuel cells in automobiles) [7, 8]. In biological storage, energy is stored in a chemical form using biological processes, but limited knowledge is available on biological energy storage [4]. In magnetic storage, energy is stored in a magnetic field, and superconducting materials have been used in magnetic energy storage systems [4]. The storage efficiency expected from superconducting magnetic energy storage systems is 80-90% [4]. The fifth important method to store energy is thermal energy storage, which can be achieved via changing the internal energy of materials thermally (sensible and latent heat storage) due to a change in the temperature, or via using reversible endothermic chemical reactions, where the energy

can be recovered via the reverse exothermic reaction [9]. TES methods can be classified as shown in Figure 2 [7] and will be the focus of the thesis. Specifically, the sensible heat storage method is considered in this work via a solid storage medium, which is explained next.

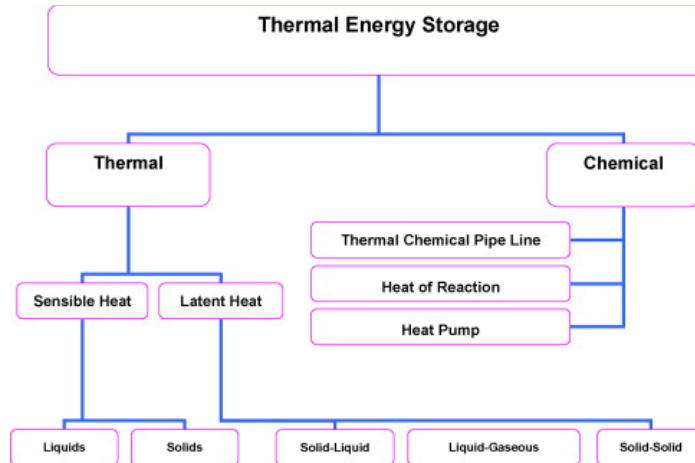


Figure 2. The methods to store energy in form of heat (TES) [7], Permission License Number: 4832121269556.

The performance of energy storage systems depends on several properties such as capacity, power, efficiency, storage period, charge-discharge time and cost of the system. These properties must be considered to optimize the energy storage systems [10]. An efficient and effective energy storage system will help to offset the variability of renewable energy sources and increase their overall efficiency, which helps to overcome the mismatch between the energy supply and demand. Therefore, energy storage systems are needed to integrate renewable energy sources in energy production and reduce the use of fossil sources.

### 1.2.1 Thermal Energy Storage

As mentioned above, energy can be stored thermally in different methods, which is known as TES. In sensible and latent heat storage, thermal energy storage systems store energy by heating/cooling the storage domain to a specified temperature. Then, the stored energy can be used later. Ultimately, the energy generation will be continuously available for any type of application such as heating and cooling [11], solar cooking [12, 13] and power generation in solar power plants [9, 14]. In power plants, concentrated solar power (CSP) plants generate electricity from solar power. Systems such as solar power towers and parabolic trough collectors concentrate solar energy by reflecting the sunlight to a receiver as shown in Figure 3 [15]. At the receiver, a heat transfer fluid such as air or molten-salt is heated to the desired temperature, and then the heated fluid can be used to generate electricity. Solar energy is a renewable energy source, abundant, sustainable, clean and globally stable [16], which could be a promising energy source. However, it varies during the day hours (higher output at noon) and the seasons of the year (higher output at summer time). An alternative source is needed to match the demand at peak times (e.g. evening, morning and winter). Therefore, proper thermal energy storage can extend the hours in a day the plant can work during the evening or bad weather conditions. Thermal energy storage tank(s) can be incorporated within the CSP plants as shown in Figure 3, which represents an important component to increase the effectiveness of the whole system.



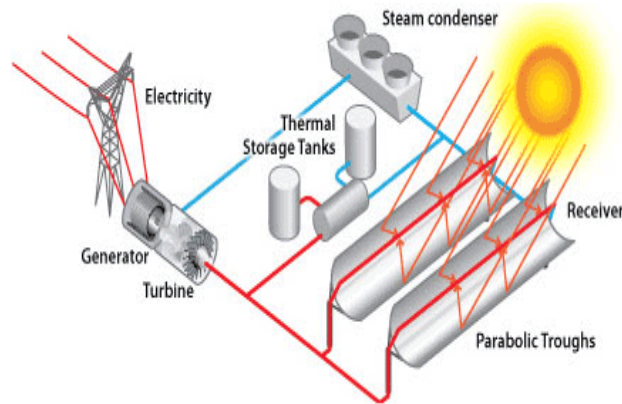


Figure 3. A linear concentrator power plant using parabolic trough collectors and two-tank thermal energy storage [15] .

The production of electricity from power plants using renewable energy sources such as solar energy increased globally in the last few years. For example, the net production from solar energy increased from 8,161 GWh in 2007 to 253,593 GWh in 2015 [17]. The DOE Solar Energy Technologies Office has reported the 2030 targets for concentrating solar power (CSP) to make it a competitive technology [18]. Figure 4 [18] shows the impact of including a thermal energy storage system on the cost in CSP. As can be seen, the levelized cost of electricity (LCOE, \$/kWh) decreased from \$0.21 in 2010 to \$0.098 in 2018, and the goal is to reduce the cost to \$0.05 in 2030. An efficient storage system will lead to a reduction in CSP cost. The National Renewable Energy Laboratory discussed the targets for CSP in their CSP 2030 report [19], where more information can be found.

## Concentrating Solar-Thermal Power Progress and Goal

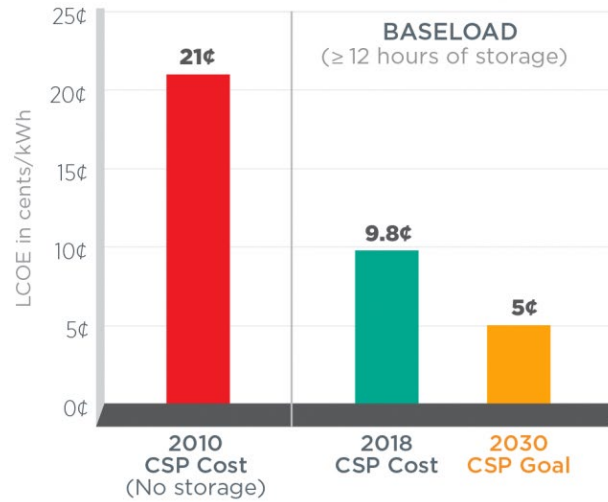


Figure 4. The concentrating solar power cost with and without energy storage [18]

### 1.2.2 Sensible and Latent Heat Storage

Sensible heat storage (SHS) is one of the most significant methods used to store thermal energy. Sensible energy is an internal energy component related to the kinetic energies of the atoms/molecules. At higher temperature, the molecules will have higher kinetic energy, and thus higher internal energy known as sensible energy [20, 21]. In sensible heat, energy can be stored in a material by raising its temperature. The amount of heat stored in the material represents the product of specific heat, amount of the storage material (mass) and the temperature difference

$$Q = \int_{T_1}^{T_2} mC_p(T)dT \quad (1.1)$$

where  $Q$  is the amount of heat (sensible heat) gained via heating the material,  $T_1$  and  $T_2$  are the initial and final temperature of the storage material,  $m$  is the material mass, and  $C_p$  is the specific heat capacity of the material [21, 22]. The specific heat capacity is a function

of temperature,  $C_p(T)$ . However, over a small range of temperature, the variation of  $C_p$  is typically small and can be neglected. Therefore, Eqn. 1.1 can be written as:

$$Q = mC_p(T_2 - T_1) \quad (1.2)$$

In Eqn. 1.2,  $m = \rho V$ , and thus Eqn. 1.2 can be rewritten as:

$$Q = \rho V C_p (T_2 - T_1) \quad (1.3)$$

where  $\rho$  is the density and  $V$  is the volume of the storage material.

The storage medium should have several characteristics to be used as storage material. In addition, the best storage materials should be chosen based on the type of application such as low or high temperature applications (e.g. house heating/cooling and electricity power production) [23, 24]. These characteristics are:

- 1- High specific heat capacity or volumetric heat capacity: The high specific heat capacity ensures a large amount of heat energy can be stored in a relatively small volume, decreasing the capital cost.
- 2- Long-term stability under thermal cycling: The storage medium should exhibit long-term stability under multiple thermal cycles, low degradation of the material, and high thermal performance. For instance, at high temperature, concrete develops cracks after multiple repeated cycles.
- 3- Compatibility with its containment: High thermal performance requires good compatibility of the storage medium with its containment. For example, using water as storage medium at high temperature requires high cost insulation and pressure withstanding containment due to high vapor pressure of water.

- 4- Low cost and availability: The cost of the storage medium is a significant factor, and the selection of storage materials depends on their thermophysical properties, availability and cost. For instance, rocks are cheap and easily available compare to metals, which reduces the capital and operational costs.
- 5- High density: High density will reduce the storage volume of the storage system, increasing the energy stored and reducing the capital cost.
- 6- High thermal conductivity. The thermal conductivity increases the rate of heat absorbed or released during charging/discharging processes. A high rate of conduction within the particles is needed to avoid temperature gradients within the solid particles. For example, the thermal conductivity of aluminum oxide is 32.6 W/m.K at 25°C while the thermal conductivity for brick is 0.69 W/m.K at 29°C, which makes aluminum oxide a good candidate to be selected as storage material. However, aluminum oxide is expensive compared to brick.
- 7- Materials should be non-corrosive, non-toxic, and non-flammable: It is very important to use materials that are non-corrosive to increase the life of storage equipment, non-toxic and non-flammable (or explosive) for the people involved and environment.

SHS has considered liquid and solid storage media. Liquid storage media include water, oils, molten salts and liquid metals [23, 24]. Solid storage media include aluminum, aluminum oxide (alumina), copper, cast iron, steel, rocks, magnesia, sand, sandstone, clay, brick, wood, stone granite, stone limestone, and concrete [23-25]. The selection of SHS materials for low and high temperature ranges and a review of different storage materials

with several applications have been reported [23, 24, 26, 27]. There are advantages and disadvantages associated with these materials. For example, water is a strong candidate to store the energy in the form of SHS due to its high specific heat capacity ( $4182 \text{ J kg}^{-1} \text{ K}^{-1}$ ), but its temperature range is limited (  $5\text{-}95^\circ\text{C}$ ) [8]. At temperature above  $100^\circ\text{C}$ , water will be a vapor and the storage vessel should be able to withstand the vapor pressure and thus the storage vessel cost will increase with temperature [28]. Solid materials like rocks, aluminum oxide, etc. are widely used to store energy in applications that involved low and high temperature ranges although the heat storage densities of these solid materials are less than water's storage density [28]. Solid materials absorb and release energy without change in their phase (liquid/solid phase). The energy absorbed/released occurs in a storage vessel (usually known as storage packed bed). The physical properties of some solid materials used in sensible heat storage are provided in section 1.5. Storage materials with good properties and cheaper prices are the best candidates to be used in SHS. Wyman et al. [28] reviewed the collector and energy storage technologies for intermediate temperature storage applications. Regarding the solid storage materials for SHS, four materials were reported ( $\text{SiO}_2$ , Rock,  $\text{Al}_2\text{O}_3$ ,  $\text{MgO}$ ,  $\text{Fe}$ ) in the study [28]. The storage capacity per unit volume ( $\text{GJ/m}^3$ ) as a function of temperature showed high storage capacity for  $\text{Fe}$ , then  $\text{MgO}$ ,  $\text{Al}_2\text{O}_3$ , Rock, and  $\text{SiO}_2$  respectively. However, the storage medium cost in dollars per unit energy stored ( $\text{\$/MJ}$ ) as a function of temperature was reported too; the rock was the cheaper material, then  $\text{SiO}_3$ ,  $\text{MgO}$ ,  $\text{Al}_2\text{O}_3$ , and  $\text{Fe}$  respectively.

Latent heat storage is another significant method to store thermal energy in the form of heat by undergoing phase change (solid-solid, solid-liquid, and vice versa) such

as organic paraffin compounds and inorganic metallic materials as can be seen in Figure 2 [7]. Storing the energy using latent heat has been used in literature, focusing on the thermocline in single-tank storage [29-31]. Phase change materials have high energy density and can store and release heat at a constant temperature [32]. In contrast, sensible heat has an inherent disadvantage, which is the drop of outflow temperature toward the end of a discharge period. Due to a fixed temperature for phase change, latent heat storage suffers from relatively low efficiency for large temperature ranges. However, using both showed an increase in the efficiency of the packed bed system [32]. Currently, a combination of sensible and latent heat storage media has been investigated to improve the TES performance by stabilizing the exit temperature during the discharge cycles [32-34]. Focus on the multi-layer solid phase change materials (MLSPCMs) concept has increased in the last few years. In CSP plants, the combination of latent heat storage (LHS) and sensible heat storage (SHS) is proposed as the effective alternative concept for TES as discussed by Galione et al. [29, 35, 36]. They studied the MLSPCMs packed bed system using molten-salt as HTF, quartzite rock and sand as solid sensible heat medium, and KOH with different melting temperatures as PCMs. Their study showed an increase in the efficiency of the system and improvement of the thermocline in the bed because of a thermal buffering effect provided by PCMs at the inlet and outlet of the storage tank. Furthermore, Zanganeh et al [32, 33] studied MLSPCMs using air as HTF, rocks as solid materials for sensible heat, and different materials ( $\text{AlSi}_{12}$ , NaF, LiF and NaBr) as PCMs for latent heat storage showing that a small amount of PCM (1.33% of total volume) is

sufficient to help in stabilizing the air outlet temperature during the recovery cycle.

Reviews of PCMs are given in [7, 24, 37-41].

### 1.2.3 Single-Tank Versus Two-Tanks Storage

Conventional concentrated solar thermal power plants use two-tank storage systems. One tank is used for hot fluid and the second tank is used for cold fluid [42]. Two-tank systems are used to store the energy in either active or passive systems [9, 14]. The active system is then divided into direct and indirect systems. In the direct system, the storage medium is the same HTF, where the hot and cold fluids are stored in two-tanks. In the indirect system, there are two fluids, one to store the heat and the second fluid to serve as HTF [43]. The indirect method is considered expensive compared to the direct method [44]. The passive storage system is a two medium system: solid medium to store energy and fluid medium to heat up and cool down the solid medium during storage/recovery processes [45].

Pacheco et al. [46] introduced the concept of single-tank storage, known as thermocline, where the hot and cold HTF is contained in the same storage tank. Pacheco et al. compared the single-tank thermocline to two-tank storage and found that the thermocline system is about 66% of the cost of a two-tank storage system for parabolic trough power plants. In addition, according to the U. S. Department of Energy, the two-tank storage system is expensive, and the single-tank thermocline system reduces the cost as was demonstrated at the Solar One power tower [44]. The thermal performance of single-tank storage is directly related to the stratification (thermocline) in the packed bed system. Stratification means having two zones in the bed domain (hot zone and cold zone),

which is separated with temperature gradients forming a thermocline as shown in Figure 5a-b. Figure 5b assumes an ideal storage case in terms of thermocline, where the right side of the bed is at low temperature and the left side of the bed is at high temperature without mixing between the zones. A bed domain with perfect thermocline will lead to high thermal performance and thus high exergy efficiency [47].

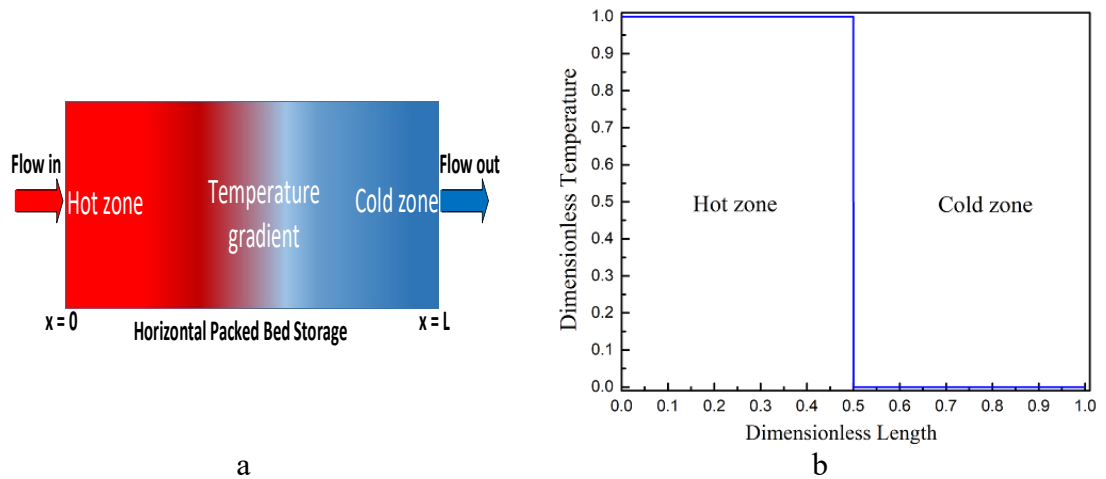


Figure 5. (a) The formation of a thermal front in a storage bed during the charging process and (b) the temperature distribution with the axial position ( $x = 0 - L$ ) showing the sharp temperature profile.

#### 1.2.4 Packed Bed Systems

A packed bed is a volume of porous media formed by filling a container/vessel with packing materials to provide a large surface area of contact between heat transfer fluid and packing materials. In TES systems, the packed bed is considered the best structure to be used as storage [48]. Packed bed devices are widely used in several applications such as CSP plants. The packing materials (storage materials) represent the first phase, which is used to store energy via gaining heat due to the contact with the second phase, hot HTF such as air, water, or molten-salt. The stored energy in the form of heat can be extracted from the material by radiation, convection or conduction [8].



In concentrated solar power plants, packed bed systems play a significant role to increase the efficiency of the power plants via increasing the number of hours the plant can work. As explained earlier, the storage tank(s) are placed between the receiver and the generator, Figure 3. To utilize the energy, two processes are required as shown in Figure 6, charging and discharging processes. During the charging process, hot HTF such as air, argon, molten-salt or supercritical CO<sub>2</sub> [49] passes through the storage tank from left to right, depositing the heat in the storage media and then leaving as cooler gas. Then, during the discharging process, a cold HTF passes through the storage tank from right to left to recover the stored energy and leaves as heated fluid. The recovered hot fluid can be used based on the type of application, such as to generate electricity.

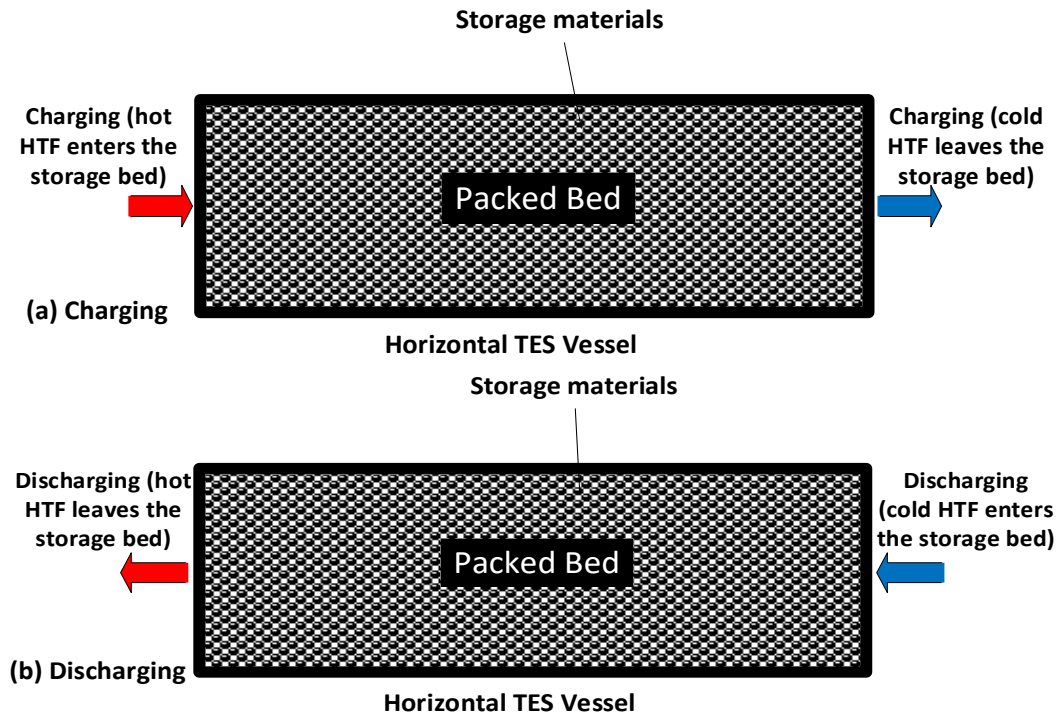


Figure 6: Schematic of a horizontal packed bed storage showing the charging/discharging processes with solid materials inside the tank. The red and blue arrows represent the hot and cold HTF flowing through the storage bed during the two processes. Note: the direction of charge/discharge processes is arbitrary, it could be in the opposite direction of a and b.

In most concentrated power plants and literature, the storage tank used is vertical. However, horizontal storage tanks have been analyzed [50], proposed and studied in the present thesis [51, 52]. The packed bed design, shape, size and dimensions play a significant role in its performance as a storage device [53]. For instance, in the design of a cylindrical packed bed, the surface to volume ratio is very important to consider because heat losses to the environment increases with increasing surface to volume ratio, which will affect the thermal behavior and the thermal efficiency. Surface to volume ratio could be reduced via increasing the diameter of the cylindrical vessel. High aspect ratio (height to diameter ratio) reduces thermal exergy losses but increases the pressure drop [54]. Decreasing the aspect ratio by decreasing the height of the tank leads to a reduction in pressure drop [53].

The thermocline's performance in the single-packed bed storage is affected via several parameters. These parameters have been covered in literature, which include heat transfer fluid, flow rate, storage material size and type, void fraction, thermal storage shape, and storage type (sensible, latent, or a combination of them). Meier et al. [55] found that low porosity, low velocity, small particle size, high particles density, and large heat capacity of storage materials leads to improved temperature stratification. Solid particles with large diameters and high thermal conductivity improve the stratification at high mass flow rate [55]. Storage tank structure also affects the thermocline thickness. For instance, the packed bed structure showed the thinnest thermocline region compared to rod-bundle structure, parallel-plate structure, and channel-embedded structure, and this led to increases

in the recovery efficiency and recovery time [48]. A single-storage packed bed is used in the present study, aiming to further improve its performance.

In TES packed bed systems, heat transfer between HTF and solid materials is one of the important requirements to store-release the energy during charging-discharging as mentioned in section 1.2.2. Heat transfer between the fluid and solid materials occurs by convection, which is controlled by a coefficient of heat transfer. The heat transfer coefficient is calculated from the heat flow rate intensity (heat flux) and temperature difference (thermodynamic driving force of heat flow) as showing in Eqn. 1.4 [21].

$$q = h\Delta T \quad (1.4)$$

where:  $q$  is the heat flux in  $\text{W}/\text{m}^2$ ,  $h$  is heat transfer coefficient in  $\text{W}/\text{m}^2\cdot\text{K}$  and  $\Delta T$  is the temperature difference in K.

In TES systems, the heat transfer coefficient is affected by different parameters such as porosity, particle Reynolds number [56], and mass flow rate [57]. Several correlations are used to calculate convective heat transfer coefficient between fluid and solid particles such as between air and alumina beads [58, 59], air and rock beads [60], molten salt and quartzite rocks [61] and thermal oil and rock [62]. These correlations typically depend on Reynolds number (Re), Prandtl number (Pr), and the system geometry.

### 1.3 Modeling Approaches

Heat transfer from fluid to solid or solid to fluid in TES packed bed systems are studied and analyzed using three approaches, analytical, numerical and experimental. In modeling efforts, four models that have been used in literature are reported [63]: the single phase model, Schumann's model, the continuous solid phase models, and models with thermal gradient inside the particles. These models can be classified into two groups: single phase and two phase models. The two phases in the packed bed are fluid and solid phases. The general governing energy equations in a porous medium are shown below, which represents the first law of thermodynamics in porous a medium [64]:

The fluid phase:

$$\rho_f C_{p,f} \frac{\partial T_f}{\partial t} + \rho_f C_{p,f} V \cdot \nabla T_f = \nabla \cdot (k_f \nabla T_f) + q_f''' \quad (1.5)$$

The solid phase:

$$\rho_s C_{p,s} \frac{\partial T_s}{\partial t} = \nabla \cdot (k_s \nabla T_s) + q_s''' \quad (1.6)$$

where: subscripts  $f$  and  $s$  are the fluid and solid domains, respectively and  $q_f'''$  ( $\text{W}/\text{m}^3$ ) is the source term in the fluid domain. Note: the source term such as viscous dissipation, heat generation, chemical energy, and electrical energy are neglected in the fluid phase as will be seen next, and  $q_s'''$  ( $\text{W}/\text{m}^3$ ) is the source term in solid domain, which will represent the heat losses through the insulation and steel in the present study.

Eqns. 1.5 and 1.6 are the microscopic form of energy equation in the fluid and solid domains. These equations can be simplified by volumetric averaging over a volume

element of the medium, which leads to the macroscopic form of energy equations, Eqns. 1.7 and 1.8 for heat transfer in the porous medium [64-66] .

The fluid phase:

$$\varepsilon \rho_f C_{p,f} \frac{\partial T_f}{\partial t} + \rho_f C_{p,f} V \cdot \nabla T_f = \varepsilon \nabla \cdot (k_f \nabla T_f) + (\varepsilon) q_f''' + h(T_s - T_f) \quad (1.7)$$

The solid phase:

$$(1 - \varepsilon) \rho_s C_{p,s} \frac{\partial T_s}{\partial t} = (1 - \varepsilon) \nabla \cdot (k_s \nabla T_s) + (1 - \varepsilon) q_s''' + h(T_f - T_s) \quad (1.8)$$

where  $h$  is the heat transfer coefficient per unit volume ( $\text{W}/\text{m}^3 \cdot \text{K}$ ), which controls heat transfer between the fluid and solid phases.

Adaptations of Eqns. 1.7 and 1.8 are used to solve and analyze heat transfer in the fluid and solid phases in a fixed packed bed storage system, where three different models are reported [63]. In 1929, Schumann [67] introduced his model, which is a one dimensional, two phase (solid and fluid) and transient model. This model predicts the axial and transient fluid/solid temperature distribution. Schumann's model assumes no heat conduction in the radial direction, no heat conduction in the fluid and no heat conduction between the storage materials (solid particles). The resulting equations have been solved analytically. Later, researchers solved the same problem but included the effects of the solid particles' conductivity [68], radial variation [69], and heat transfer coefficient that controls convective heat transfer between fluid and solid [70, 71] . Handley and Heggs [72] solved numerically (Crank-Nicholson method) a modified version of Schumann's model assuming there is thermal conduction in the solid materials and resistance to heat transfer within the solid phase. Sanderson and Cunningham [73] used Schumann's model to show the impact of particle diameter on axial dispersion and

pressure drop. In addition, Schumann's model was adapted to study the thermal performance of a packed bed system with latent heat thermal energy storage [74, 75].

The second model is the continuous solid phase model, where the solid medium (solid particles) are treated as a solid continuum, and two energy equations are written to represent solid and fluid phases. As can be seen in Eqns. 1.7 and 1.8 above, the energy balance of the fluid-solid phases include the enthalpy changes, the heat exchanged by conduction (axially for 1-D and axially and radially for 2-D), the convection heat transfer between fluid and solid, and the heat losses from the storage vessel wall. The continuous solid phase model is similar to the Schumann's model. However, Schumann's model assumes no heat conduction in radial direction, no conduction in the fluid phase, and no conduction in the solid phase. Cascetta et al. [58] used a two-phase, one dimensional modified Schumann model to study the thermocline in an alumina packed bed with different heat transfer fluids, where the thermal conduction in the fluid phase is considered in the analysis, and the volumetric convective heat transfer between the solid particle and fluid is defined in terms of convective heat transfer coefficient. The model predicted both the solid and fluid temperature distribution along the height of the storage tank. Anderson et al. [59] used a two-equation model, which included heat losses, heat transfer coefficient and thermophysical properties as a function of temperature to analyze a packed bed with air-alumina phases. The model determined the transient axial temperature in the fluid and solid phases and neglected the radial temperature gradient.

The third model is the model with thermal gradient in the solid phase (concentric dispersion model), which assumes a temperature gradient within the particles and no heat

transfer between the particles. This model is used to solve the thermal behavior inside the particle. Ismail and Henríquez [76] developed the concentric dispersion model by dividing a storage tank of spherical capsules filled with PCMs into a number of axial layers, where a conductive 1-D phase change model was used to analyze the solidification process inside the spherical capsule along with convection boundary conditions on the capsules surface.

The second group is the single phase model (one equation model), where the fluid and solid are assumed in local thermal equilibrium ( $T_f = T_s = T$ ) [66]. The general governing equations for the single phase model can be derived from the two phase models equations, Eqns. 1.5 and 1.6 [66]. Averaging over an element volume of solid and fluid mediums, the final single phase model equation with equivalent properties denoted by subscript  $eq$  used to solve for the transient temperature distribution in the radial and axial (  $r$ - and  $z$ -) direction of the storage packed bed domain in the present study is:

$$(\rho C_p)_{eq} \frac{\partial T}{\partial t} + (\rho C_p)_f V \cdot \nabla T_f = \nabla \cdot (k_{eq} \nabla T) + Q_{loss} \quad (1.9)$$

where:

$$(\rho C_p)_{eq} = \epsilon \rho_f C_{p,f} + (1 - \epsilon) \rho_s C_{p,s} \quad (1.10)$$

$$k_{eq} = \epsilon k_f + (1 - \epsilon) k_s \quad (1.11)$$

$Q_{loss}$  (W/m<sup>3</sup>) represents heat losses via conduction through the solid domains and natural convection from the vessel walls. For the solid domains (insulation and steel), Eqn. 1.12 is used [77].

$$(\rho C_p)_i \frac{\partial T}{\partial t} = \nabla \cdot (k_i \nabla T) \quad (1.12)$$

where the subscript  $i$  denotes either the insulation or the steel vessel.

Eqn. 1.9 above analyzes heat transfer in a packed bed system using the continuum approach. The properties with subscript  $eq$  represent the equivalent/effective thermal conductivity and heat capacity of heat transfer mechanisms (conduction, convection and radiation), where the radiations impacts are usually ignored [63]. Different correlations have been derived experimentally and theoretically to calculate the effective thermal conductivity [78-80]. The single phase model has been proposed and analyzed in several studies. Anderson et al. [59] reported that the difference between the fluid and solid temperatures are very small in an air-alumina packed bed system with two phase models. Later, Anderson et al. [77] showed that the single equation model approach is appropriate for an air-alumina storage system, where the single phase model results matched the experimental results well. Therefore, this approach is considered appropriate for the air-alumina system and is used in the present study [51, 52]. Bindra et al. [47] developed a numerical model, where single equation model and two-equation model are considered, the model included heat losses, thermal gradient inside the particles, and axial heat transfer in the fluid and phase change materials. Vortmeyer and Schaefer [81] derived the single phase equation from the two phase equations for an adiabatic packed bed without assuming thermal equilibrium between the fluid and solid phases, by assuming the second derivative of fluid and solid temperature are the same. In addition, the two groups of models are used in analyzing the thermal performance of packed bed energy storage using latent heat storage. A review by de Gracia and Cabeza [38] provided a comprehensive understanding of different numerical models that have been used to analyze latent heat storage inside packed beds.



Beasley and Clark [69] summarized several thermal energy storage models in one and two dimensions. In addition, a review on packed bed solar energy storage systems has been reported via Singh et al. [25] summarizing the experimental and analytical studies on TES systems for different governing parameters such as storage materials, heat transfer fluids, heat transfer coefficients correlations, flow phenomenon, and pressure drop. These parameters are discussed in subsequent sections of this introduction.

#### 1.4 Operating Conditions

The operating conditions have a significant impact on thermal behavior during charging and discharging processes. These parameters are the packed bed (design, shape and orientation), inlet temperature, pressure, heat transfer fluid, flow rate, and type and size of storage materials. The operating conditions have dramatic influences on charging-discharging times, enhancement of heat transfer between fluid and solid media, amount of energy stored and recovered, thermal front formation, heat losses by conduction/convection, pressure drop, axial thermal dispersion, thermocline thickness, storage efficiency, recovery efficiency, exergetic efficiency, and cycle efficiency. These parameters have been studied analytically, numerically and experimentally. As mentioned in section 1.2.3, the single-tank storage is considered the best compared to two-tank storage. Therefore, this section covers the experimental and numerical studies on single-tank storage focusing on different operating conditions.

Three different shapes of packed bed storage have been proposed and studied: rectangular, truncated conical, and cylindrical shapes [53]. Sanderson and Cunningham

[82] studied experimentally a vertical flow packed bed, where a storage tank of rectangular cross-section was used with five different packing arrangements. The rectangular packed bed is used to prevent flow from channeling through the voids at the tank wall, which usually occurs in cylindrical storage beds.

However, the rectangular cross-section increases the pressure drop due to the corner effects [53]. The conical vessel was proposed and analyzed numerically and experimentally by Zanganeh et al [83] to study and compare the thermocline in a truncated conical shape to a cylindrical shape of the same volume experimentally. The proposed truncated cone storage tank immersed in the ground and tested. The authors reported three advantages for using this shape: exploiting the effect of lateral earth pressure at higher load bearing; reducing the normal force on the bed wall during thermal expansion of storage materials (rocks) via guiding them upward; and providing a large storage volume at the top of bed, where the temperature is high and thus the surface-to-volume ratio is small and wall thermal losses are small too. It was reported that energy stored in truncated conical storage is higher and the wall heat losses are reduced due to the larger volume to surface ratio. However, the heat losses from the conical storage's cover is high due to the large diameter at the top of storage tank. The cylindrical storage tank is most recommended in research and real applications in terms of mechanical problems, no corner effects, availability, and less surface area for a specific area of cross section [53]. Beasley and Clark [69] analyzed the transient response in a cylindrical packed bed where the inlet fluid temperature was arbitrary time-varying during charging/discharging processes experimentally and numerically. The temperature was

measured axially and radially in the storage tank. The radial velocity variations and wall thermal losses are considered in the analysis. Anderson et al. [59] studied a sensible heat storage system in a cylindrical bed experimentally. The authors used internal insulation designed as cylindrical blocks with a continuous “pipe in pipe” system to avoid any gas leak. Using internal insulation avoids heating the tank walls (usually steel metal) directly with the HTF. It could also reduce the radial temperature variation and wall losses as was suggested [84].

The orientation of the storage tank has been studied too. Typically, the storage tank is oriented vertically or horizontally. The vertical layout is the most used in research and real life applications, where the tank is hot at the top and cold at the bottom [44, 46, 59, 61] to create a thermocline. The vertical layout provides advantages for thermal stratification. The horizontal layout can provide mechanical stability and may be a more reasonable option for storage and accessibility in industry [85]. In addition, it was proved experimentally that the thermocline and thus efficiency can be improved in the horizontal packed bed [52], where the packed bed domain is divided into several layers and each layer was charged/discharged separately. Several studies that investigated and analyzed the design of the packed bed are tabulated in [53] for more information.

Inlet temperature is the second important parameter in the analysis of the packed bed systems. The selection of inlet temperature (low or high) depends on the type of application. Low temperature power cycles such as Organic Rankine and Kalina cycles have been reported as well [86] for temperature ranges from 61.5–482.2°C. Hettiarachchi et al. [87] presented a cost effective design optimization method for binary Organic

Rankine Cycle (ORC) using low-temperature geothermal heat source (70-90 °C). In concentrated solar power (CSP) plants, high temperature cycles play an important role in the development of solar energy production and utilization. An air-rock thermal energy storage system at high temperature, 650°C, was analyzed for CSP applications, where a 6.5 MWh<sub>th</sub> pilot-scale thermal storage unit was fabricated and tested [83]. Meier et al. [55] studied an air-rock bed at a high temperature, 700°C, where a mathematical model was developed to analyze the transient thermal behavior and was validated with a small experimental storage tank. High-temperature TES rock packed bed was analyzed for air-based CSP plants [57] at an inlet temperature of 800 K, focusing on charging/discharging characteristics, cyclic operation, overall thermal efficiency and capacity ratio. Heller et al. [88] studied a solar operated Brayton gas turbine system using air at high temperature, 1000 °C for CSP. Tijani and Spoelstra [89] studied the design, development and test of a thermoacoustic-Stirling engine using air as working fluid at high temperature. At 620°C, the engine performance was 41% of the Carnot performance, producing 300 W of acoustic power. Johnson et al. [49] studied supercritical carbon dioxide as HTF in a TES packed bed numerically, where suitable operating conditions for supercritical Brayton cycle were used. The inlet temperature during storage was 750°C and 500°C during recovery. The recovery cutoff temperature was 700°C, which is the minimum temperature required for the turbine inlet.

Direct steam generation using parabolic trough collectors, Fresnel collectors and solar power receivers was also studied/analyzed. In commercial solar thermal electricity plants, thermal energy storage systems have been used in two ways: The steam accumulator

for direct steam generation plants and the two-tank storage of molten-salts for parabolic trough or tower technology [90]. Laing et al. [91] studied thermal energy storage system using a combination of latent and sensible heat for direct steam generation with storage capacity of approximately 1MW. The storage system was constructed for testing at the conventional power plant of Endesa in Carboneras (Spain) with temperature up to 400°C. A review of commercial thermal energy storage in CSP plants using steam vs. molten salts has been reported [90].

Based on the type of application and the appropriate inlet temperature, a heat transfer fluid can be chosen. Different types of HTFs have been studied such as liquids like water, molten-salt, thermal oil, and palm oil, supercritical fluids such as supercritical carbon dioxide, or gases like air and argon. Each type of HTF has advantages and disadvantages when used in TES packed bed systems such as cost, technical and operational problems, flammability, freezing temperature, corrosiveness, availability, limitation on temperature range, degradation or chemical instability, volumetric heat capacity, thermal conductivity, toxicity, and safety concerns [32, 83]. For example, the freezing temperature for molten salt is 120-220°C and thus the costs of maintenance and operation is high [58]. Air has a low volumetric heat capacity and thermal conductivity. On the other hand, air is free, has no limitation on temperature range, does not suffer degradation and is not a toxic gas [32]. Gases like air have no chemical issues and can operate at high temperature ranges and thus increases the energetic storage capacity [92]. Air has been studied numerically and experimentally [59, 77, 84, 93] and has been considered as a suitable HTF candidate. In general, liquids have advantageous physical

properties, which leads to good heat transfer between liquid/solid systems and thus improves thermal performance. However, liquids cannot operate at high temperature (water maximum temperature is 100°C and solar salt is 600°C) and are expensive in some cases. Cascetta et al. [58] investigated numerically the transient behavior of an alumina packed bed storage for multiple repeated cycles using three heat transfer fluids (air, oil, and molten salt). It was found that oil and molten salt show good performance for multiple cycles compared to air. However, air showed similar performance to the other fluids during repeated cycles by modifying the temperature limits (modifying the inlet and outlet temperature during charging/discharging processes). Erregueragui et al. [94] numerically analyzed a quartzite packed bed storage system to test the performance of Palm oil as heat transfer fluid. The performance of Palm oil compared with two different synthetic oils found that the amount of energy stored using Palm oil is 16% higher than that of the other synthetic oils at the same fluid temperature. Thus, Palm oil could be used successfully as HTF below 300°C. Physical properties for different heat transfer fluids are reported in [53, 92].

The last parameter of operating conditions is the storage material (type, size, and shape). Table 1 shows the physical properties of some solid materials used in sensible heat storage. Typically, the packing materials are selected based on several factors mentioned in section 1.2.2 such as type of application, cost, etc. As can be seen in Table 1, alumina, steel and copper have good thermal properties. However, they are expensive.

Table 1: The thermophysical properties of some solid materials [8, 25].

Solid materials	Density (kg/m <sup>3</sup> )	Specific heat (J/ kg K)	Thermal conductivity (W/ m K)	Volumetric heat capacity (10 <sup>6</sup> J/m K)
Aluminum	2707	896	204 at 20 °C	2.4255
Aluminum oxide	3990	772.9	32.6 at 25 °C	3.0838
Brick	1698	840	0.69 at 29 °C	1.4263
Concrete	2240	1130	0.9-1.3	2.5310
Copper	8954	383	385 at 20 °C	3.4294
Rocks	2560	879	-	2.2503
Steel	7840	465	-	3.6456
Stone limestone	2500	900	1.26-1.33	2.0800

The storage materials have been investigated by several studies. Aly and El-Sharkawy [95] studied numerically the effect of three different storage materials (aluminum, steel and rock ) on thermal performance. They found that the energy stored in the steel bed was higher than that of rock and aluminum bed. Also, aluminum showed higher performance than rock in the first 6 hours of charging. Mawire et al. [96] studied experimentally and numerically the thermal behavior of a storage tank TES using three different solid materials: fused silica glass, alumina, and stainless steel. Alumina showed the highest exergy to energy ratio during the charging process and the fastest rate of energy storage. The size of packing materials has a significant influence on pressure drop and intraparticle temperature gradients. Smaller solid materials increase the heat exchange contact area between HTF and solid materials, improve the heat transfer and stratification, improve the flow uniformity, reduce the Biot number of solid particles, and reduce flow channeling in the storage bed, but increase pressure losses [53, 92]. Larger solid particles will lead to high Biot number ( $Bi$ ) and thus temperature gradients within the particles must be considered. The Biot number is a dimensionless quantity, which represent the ratio of

thermal resistances, conduction to convection (thermal resistance inside the solid particle to thermal resistance at the surface of the particle) as shown in Eqn. 1.13.

$$Bi = \frac{hL_c}{k} \quad (1.13)$$

where:  $h$  is a convective heat transfer coefficient ( $W/(m^2 \cdot K)$ ),  $k$  is the thermal conductivity of the material ( $W/(m \cdot K)$ ), and  $L_c$  is a characteristic length (m) of the geometry considered (for spheres,  $L_c =$  sphere diameter). The Biot number must be less than 0.1 ( $Bi < 0.1$ ) in order to neglect the intra-particle temperature gradient [59]. Therefore, the size and thermal conductivity of solid particles should be considered if solid materials with big sizes are selected as storage materials. For example, aluminum oxide has high thermal conductivity at low temperature and low thermal conductivity at high temperature (33 W/m.K at 20°C and 6.7 W/m.K at 1200°C) [59]. Anderson et al. [59] reported that for aluminum oxide with  $d_p = 6$  mm, the  $Bi$  number = 0.17 at 1200 °C and high flow rate (20 SCFM), which means there is a potential for temperature gradient within the particles. In the present study, the size of the beads used is 6 mm and the maximum temperature used is 150°C, where the thermal conductivity is 24.5 W/m.K. The Biot number was checked and it was less than 0.1 all work in this thesis.

The shape of solid particles affects the void fraction of the packed bed and thus the thermal behavior. Warkhade et al. [97] studied experimentally the effects of small sized, different shaped concrete storage materials in a sensible TES system. The three shapes of solid particles are sphere, cube and cylinder with void fractions of 0.48, 0.32 and 0.27 respectively. It was found that high void fraction leads to low energy storage. Typically, for spheroidal solid materials with single size, the void fraction is in the range of (0.3 –



0.4) [53]. It was reported experimentally that decreasing of void fraction will lead to an increase in stratification and thus improve the efficiency [98]. In [98], five different shapes of large storage elements of concrete were used leading to five different values of void fraction. However, this will create a flow resistance as the number of flow channels will be reduced and thus the pressure drop will increase. Therefore, a balance between different parameters should be considered.

### 1.5 Packed Bed Energy Losses

Pressure drop, thermal losses to the environment, and axial thermal dispersion are the major losses in packed bed thermal energy storage. Thermal losses reduce the energy stored/recovered, and thus reduce the system efficiency. A high pressure drop is a parasitic energy loss via increased pump/compressor power.

#### 1.5.1 Pressure Drop Losses

The pressure difference between the inlet and outlet allows the flow of HTF through the packed bed. However, high pressure drop leads to a decrease in the bed efficiency. Several parameters affect the pressure drop such as bed height or length, particle size, porosity, density of HTF, and HTF velocity and viscosity [53, 99]. The Ergun equation can be used to calculate the pressure drop, which relates the flow and pressure drop to Reynolds number and friction factor [99] as shown in Eqn. 1.14. Eqn. 1.14 is known as the Ergun equation, which is the sum of a viscous term (Kozeny-Carman equation) and inertia term (Burke-Plummer equation ) [92].

$$\Delta P = \frac{150\mu L(1-\varepsilon)^2}{D_p^2 \varepsilon^3} v_{sup} + \frac{1.75L\rho(1-\varepsilon)}{D_p \varepsilon^3} v_{sup}^2 \quad (14)$$

where:  $\Delta P$  is the pressure drop across the bed,  $L$  is the length of the bed,  $D_p$  is the diameter of the solid beads,  $\mu$  is the dynamic viscosity of the fluid,  $\rho$  is the density of the fluid,  $\varepsilon$  is the void fraction (porosity) of the bed, and  $v_{sup}$  is the superficial velocity, which is the velocity of fluid through an empty tube at the same mass flow rate. Pressure drop decreases with high porosity, low velocity and large particle size as was reported [55, 100, 101]. Several studies on pressure drop evaluation were tabulated by Gautam and Saini [53]. In the present study, the pressure drop based on the Ergun equations is very small. Therefore, the pressure drop impact is neglected in the current experimental work, though it must be considered for large scale systems.

#### 1.5.2 Thermal Losses to the Environment

Heat losses occurs by two methods: conduction through the bed solid domains (e.g. wall and insulation) and natural convection from vessel wall to the ambient. A schematic of thermal losses through the walls can be seen in Figure 7. Heat losses are an inherent effect and cannot be avoided but can be reduced, for example, by using thick insulation or a very low thermal conductivity insulation [59]. Decreasing the surface to volume ratio [53] via designing large-diameter storage tanks can help in the reduction of thermal losses. In addition, the top and bottom of the storage tank should be insulated due to the high temperature difference with the ambient [46, 101, 102], which leads to an increase in heat losses. In addition, the flanges at top and bottom can act as large thermal sinks, leading to high thermal losses.

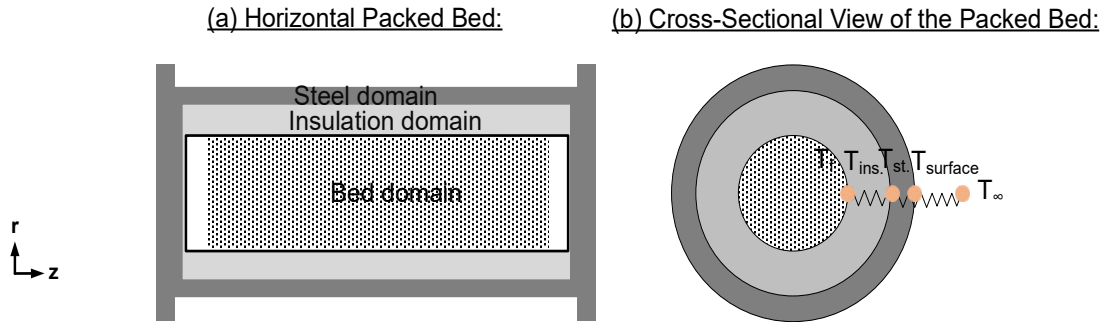


Figure 7: (a) The storage packed bed showing the bed, insulation and steel domains. (b) Radial direction of heat losses by conduction through the solids (insulation and steel) and by convection from the surface to the ambient.

Anderson et al. [59] studied the effect of heat losses via analyzing the exterior wall Stanton number ( $St_w$ ), a dimensionless number that represents the heat transfer coefficient of the exterior storage wall ( the ratio of heat transferred through exterior wall to thermal capacity of solids). It was found that the thermal performance decreases with increases of Stanton wall number. The study suggested using a shorter vessel, increasing fluid flow velocity, increasing the volumetric heat capacity of the solid particles, or lowering the overall radial losses in the system (lower insulation conductivity, thicker insulation, or reduced free convection loss) to reduce the wall losses. The wall Stanton number is analyzed in chapter two. Meier et al. [55] included the heat losses through the insulated walls in their model due to the small bed scale that was used, where the surface-to-volume ratio was high. Their analysis showed the temperature degradation caused by wall heat losses and the experimental wall heat loss measurements matched the model results. Zanganeh et al. [32] studied a combined sensible and latent TES system at high temperature, where thermal losses from the walls were considered. Three layers of insulation (Table 2) were used to minimize the thermal losses through the walls. The first

55% of the tank length was insulated with a thicker layer (three layers) to account for the temperature stratification. The results showed the thermal losses remained below 3.5% of the total input energy due to the large thermal inertia of the insulation. Cascetta et al. [93, 103, 104] studied air-alumina TES packed bed system numerically and experimentally, where radial temperature distribution was analyzed. Their results showed that the steel wall cannot be neglected during storage/recovery periods and approximately 30–40% of the radial distance can be affected, leading to a temperature degradation from the centerline of the bed to the wall (from high constant temperature to low wall temperature. This radial temperature reduction reduces the energy stored/recovered and thus affects thermal efficiency. In another study, Cascetta et al. [84] assumed an adiabatic boundary condition for outer insulated walls and constant heat transfer coefficient condition to the environment from non-insulated parts of a packed bed storage tank. Their results showed a temperature reduction in the radial direction close to the wall during charging/discharging processes. Also, the charging efficiency is below 1 (95%) because of thermal losses through the wall and thermal energy stored in the vessel itself (wall and flanges). They suggested using an internal insulation could reduce the wall losses and improve the thermal efficiency. An internal insulation is used [51, 52] to mitigate the radial temperature difference and avoid heating the storage vessel walls. The model results showed a negligible temperature gradient in the radial direction of the packing material when sufficient insulation is used.

Typical insulation materials are materials that have low thermal conductivity to reduce the thermal losses through the walls. These materials should be inexpensive to reduce the capital cost of the storage system. Typically, external insulation is used in most

of the studies to insulate the storage tank. A few studies that used internal insulation were reported [51, 52, 59, 77]. Internal insulation can be the best option to reduce heat losses. However, there are some disadvantages related to using internal insulation such as technical issues (insertion inside the bed, where only solid rigid insulations can be used and high potential for leaking, which could be difficult to fix using a sealant), cost (it might be more expensive than external insulation due to special custom design), and reducing the storage domain by narrowing the bed diameter. In addition, thermal losses can occur through the storage cover in case of cylindrical storages with flanges cover [51, 52], or other storage covers like conical cover [83], which is a big mass. Therefore, the cover flanges should be insulated from inside. In [51, 52], the cover flanges were insulated from inside with a rigid calcium silicate insulation sheet (McMaster Carr, 9353K31) of ½ inch in thickness, providing a continuous internal insulation to minimize the thermal losses through the vessel walls and the inlet/outlet flanges. The thermal conductivity for calcium silicate insulation is about 0.05-0.07 W/m. K in the temperature range of 250-450 K. Table 2 presents some insulation types reported in literature with their properties.

Table 2: Some reported materials that have been used as insulation in TES systems.

Insulation type	Thickness (mm)	Thermal conductivity (W/m. K)	Internal or external	Inlet temperature used (°C)	Reference
Mineral wool	100	0.04	external	300	Cascetta et al. [84, 93, 103, 104]
Felt	40/60/50	0.046 -0.078	external	575	Zanganeh et al. [32]
Microtherm	20/0/0	0.026- 0.038			
Rockwool	100/100/0	0.038			
Glass wool	50	0.04	external	65	Warkhade at al. [97]
Foamglas	400	0.045	internal	650	Zanganeh et al. [83]
Cylindrical blocks	92.837	-	internal	120	Anderson et al. [59]
Microtherm	1.27	0.025	internal	150	Al-azawii et al. [51, 52]

### 1.5.3 Axial Thermal Dispersion Losses

The third significant contributor to bed losses is axial thermal dispersion. Dispersion can be defined as the spreading of heat or mass [105]. Dispersion occurs due to molecular thermal diffusion and mechanical dispersion in heat and fluid flow in a fluid saturated porous medium [66, 105]. Mechanical dispersion in porous media is a result of hydrodynamic mixing of fluid elements passing through porous domain channels [66]. There are four major reasons that allow mixing in a porous medium: obstructions, where fluid elements of the same velocity vary in distance from each other due to the tortuous nature of the domain, local pore accessibility, eddies in turbulent flow, and recirculation due to reduced pressure in local regions [66]. In addition, dispersion can occur due to molecular thermal diffusion and convection as was reported by Gunn [106]. These losses contribute to the reduction of thermal performance. As was shown in Figure 5b, in the single-tank storage system, the ideal case of the temperature front propagating through the bed is a square wave. This wave would proceed along the length of the bed forming only two zones, hot zone with  $T_{hot}$  and cold zone with  $T_{cold}$ . Dispersion losses contribute to the spreading of the temperature front along the length of bed domain, and as a result this thermocline reduces the system efficiency [52]. Axial thermal dispersion is affected by different factors such as HTF, particle size/type, temperature and flow rate, which have been studied.

Cascetta et al. [58, 93] studied the influence of different operating conditions on thermocline behavior for multiple repeated cycles, where the dispersion effect was analyzed. In [58], a numerical investigation on air-alumina packed bed temperature

distribution and thermocline formation was carried out. It was found that dispersion reduces the energy stored and leads to thermocline degradation for multiple repeated cycles. In addition, the authors suggested modifying the temperature limits as a solution to overcome the dispersion effects that occur during charging /discharging cycles. In [93], the influence of operating conditions (mass flow rate and temperature) and physical properties (aspect ratio, length to diameter ratio) on the thermal performance and thermocline formation were investigated experimentally focusing on the thermal dispersion phenomenon. The study showed a reduction in the bed performance due to the dispersion effect. The energy stored was improved and the dispersion was reduced via increasing the temperature threshold limit (higher value of the dimensionless temperature). Saez and McCoy [107] analyzed numerically the thermal performance of air-rock bed, where the axial thermal dispersion was included in the model by adding the thermal axial dispersion coefficient,  $k_z = 0.7k + \epsilon\rho c_p vR$  to the governing equations.

Anderson et al. [59] reported that axial thermal dispersion increases with particle size and flow rate, which increases the exergetic loss. In the present study, the impact of axial thermal dispersion on exergy efficiency is presented [51, 52] providing an estimation of the relative contribution of dispersion losses. The segmentation/layering technique presented in [52] represents a novel method to reduce the dispersion losses and increase the efficiency.

### 1.6 First and Second Laws of Thermodynamics, Energy and Exergy

Thermodynamics can be defined as the science of energy, which is related to heat and power or mechanical work as stated by early observations [108]. Modern thermodynamics includes all forms of energy and their relation to macroscopic parameters such as pressure, volume and temperature. It also includes energy transformation to different forms such as heat and mechanical, electrical, chemical, magnetic, and electrostatic [8, 108]. Physically, energy is the ability to make change or do work, and it is a conservative quantity (energy cannot be created or destroyed; it can only change forms) [108], which is the first law of thermodynamics. This means that energy is a thermodynamic property. There are several forms of energy such as thermal, mechanical, kinetic, potential, electric, chemical and nuclear. The sum of all forms of energy in a system represent the total energy in the system.

Typically, thermodynamics deals with the change of the total energy. In thermodynamics analyses, the total energy of the system can be represented/classified via two groups, macroscopic and microscopic forms of energy [20]. The macroscopic forms of energy are potential and kinetic energies, where the entire system possesses the energy with respect to an outside fixed reference such as position and velocity references. The other forms of energy are those related to the molecular/atomic level of the system, known as microscopic energies. Internal energy represents the sum of all microscopic energy forms such as sensible energy, latent energy, chemical energy and nuclear energy [20], and it has the symbol  $U$  or  $\Delta U$  to represent the change in internal energy. These forms of energy can be either contained or stored into the system. Sensible energy is



usually known as sensible heat but in thermodynamics, it is known as thermal energy [20]. Sensible energy is an important form of internal energy to store the energy in the form of heat based on a temperature rise.

The first law of thermodynamics deals with the quantity or amount of energy. In real life applications, the quality of energy is important in addition to the quantity. The second law of thermodynamics emphasizes the quality concept. The second law has been used to analyze and optimize different engineering devices. The quality concept is well defined by studying and analyzing the exergy. Exergy (availability) or work potential of energy is the maximum work that can be extracted from a system at high temperature and its surrounding at low temperature before reaching thermal equilibrium [108, 109]. Therefore, for any energy source, the amount of useful work that can be extracted from the source is more important than the amount of energy the source has. Exergy is not a conservative quantity and can be destroyed unless a reversible process occurs between the system and the surrounding. Exergy converges to zero and is completely destroyed when the system temperature equals the ambient temperature (when an irreversible process occurs). Maximum exergy can be achieved when the process is completely reversible, which is an ideal case. In packed bed systems, maximum exergy can be achieved when the storage tank has a sharp temperature profile forming a thermocline as was shown in section 1.2.3 (Figure 5a-b), thus leading to high thermal performance [47]. Therefore, exergy represent a useful tool to analyze and quantify the performance of TES systems.

### 1.7 Energetic and Exergetic Efficiencies

The ultimate goal of any device is to obtain higher performance. This performance can be represented by determining the efficiency based on the power input and power output. In TES systems, the thermal efficiency is analyzed based on the first law and second law of thermodynamics. The thermal efficiency is simply the ratio of energy or exergy output from the system to the total energy or exergy input to the system as in Eqn. 1.15 [108]:

$$\text{Thermal efficiency} = \frac{\text{Energy or exergy output}}{\text{Energy or exergy input}} \quad (1.15)$$

The maximum efficiency that can be achieved is 100%, which means the energy supplied to the system equals the energy received from the system (ideal case). In TES systems, energy losses such as heat losses to the ambient and thermal axial dispersion losses reduce the energy/exergy stored/recovered during charging/discharging processes and thus reduce thermal efficiency.

As explained earlier, energy is a measure of quantity only and is conserved for all processes based on the 1<sup>st</sup> law. It does not depend on the properties of environment, but it depends on the properties of a matter or energy flow. However, an energy balance does not provide information about the degradation of energy during a process and does not quantify the quality of products or wastes exiting from a system [108, 110]. Chapter four of the present study focuses on thermal behavior during the charging process only. Therefore, the energy concept (1st law analysis) is used to calculate the energy stored in the packed bed and thus determine the charging efficiency. The thermal charging

efficiency is the ratio of stored energy to the supplied energy from the source as can be seen in Eqn. 1.16:

$$\zeta_{charging} = \frac{\text{Energy stored}}{\text{Energy supplied}} \quad (1.16)$$

The energy stored in the storage materials can be calculated from the 1<sup>st</sup> law of thermodynamics (steady-flow thermal energy equation) [21]:

$$Q_{bed} = \int_{T_0}^{T_{bed}} m C_p(T) dT = m \int_{T_0}^{T_{bed}} C_{p_{alumina}}(T) dT \quad (1.17)$$

where  $Q_{bed}$  is the energy gained via heating the storage materials in the storage tank,  $T_0$  and  $T_{bed}$  are the initial and bed temperature (local storage temperature),  $m$  is the mass of the alumina beads, and  $C_{p_{alumina}}$  is the heat capacity of the alumina beads. The heat capacity of the alumina beads as a function of temperature was used.

The energy supplied is calculated from mass flow rate, specific heat capacity and inlet temperature of HTF for the entire storage time, which can be written mathematically in Eqn. 1.18:

$$Q_{supplied} = \dot{m} C_p \int_{t_s} \Delta T dt = \dot{m} C_{p_{air}} \int_0^{t_s} (T_{hot} - T_0) dt \quad (1.18)$$

where  $\dot{m}$  is the mass flow rate, which is constant during the charging process, and  $C_{p_{air}}$  is the specific heat capacity of the fluid (considered constant in the range of temperature used here),  $T_{hot}$  is the set inlet temperature (e.g.  $T_{hot} = 75^\circ\text{C}$  in Chapter 4),  $T_0$  is the ambient temperature, and  $t_s$  is the storage time.

The ratio of the energy stored Eqn. 1.17 to the energy supplied Eqn. 1.18 is the charging efficiency:

$$\zeta_{charging} = \frac{Q_{bed}}{Q_{supplied}} = \frac{m \int_{T_0}^{T_{bed}} C_{p_{alumina}}(T) dT}{\dot{m} C_{p_{air}}(T_{hot} - T_0) t_s} \quad (1.19)$$

Exergy is measure of both the quantity and quality, and it can be used to overcome the limitations of the 1<sup>st</sup> law of thermodynamics. In TES packed bed systems, exergy represents the best unit to quantify the performance of a packed bed storage tank. Therefore, it is used to analyze the thermal behavior as will be seen in chapters two and three. To determine the thermal exergetic efficiency, the net useful work in the storage and recovery processes should be defined. The exergy of any system is referenced relative to the ambient conditions surrounding the system. Therefore, the exergy value depends on the state of system and the state of the environment (surrounding). The exergy is zero when the system and its surrounding are in equilibrium [108, 110]. If a closed system undergoes a reversible process between a specific state and its surrounding, the useful work produced during this reversible process is the exergy of the system. The total useful work produced when the system undergoes a reversible process from a specific state to the ambient state is [108]:

$$W_{total\ useful} = U - U_0 + P_0(V - V_0) - T_0(S - S_0) \quad (1.20)$$

where:  $W_{total\ useful}$  is the total useful work that can be extracted from the system and its surrounding as both undergo a reversible process, which represents the exergy of the system.  $U$ ,  $V$  and  $S$  are internal energy, volume and entropy, respectively. The properties with no subscript refer to the given state and with the subscript 0 refers to reference state. It is also known as the physical component of exergy of the closed system.

A closed system may have kinetic and potential energies, and the total energy for any closed system is the summation of its internal, kinetic and potential energies. Kinetic

and potential energies are forms of mechanical energy, which can be converted to work [108]. Therefore, the exergy for a closed system with mass  $m$  (nonflow exergy) is the summation of its total useful work, potential exergy and kinetic exergy [108]. Some references takes into account the chemical component of the nonflow exergy of the system [109, 110].

$$\mathcal{E}_{nonflow} = W_{total\ useful} + m \frac{v^2}{2} + mgz \quad (1.21)$$

By substituting Eqn. 20 in Eqn. 21, the nonflow exergy is:

$$\mathcal{E}_{nonflow} = U - U_0 + P_0(\mathbb{V} - \mathbb{V}_0) - T_0(S - S_0) + m \frac{v^2}{2} + mgz \quad (1.22)$$

where:  $\mathcal{E}_{nonflow}$  is the exergy of the closed system. The terms  $\frac{v^2}{2}$  and  $gz$  are the kinetic and potential components of exergy of the closed system and are usually neglected in TES systems.

The exergy for an open system is usually called the exergy of flow. The exergy of a matter under flow is the sum of nonflow exergy and the exergy related to the flow energy, which is the energy needed to have flow in a system like a pipe or duct [108].

The exergy related to the flow energy is the subtraction of flow work ( $P\mathbb{V}$ ) and the work done against the atmosphere ( $P_0\mathbb{V}$ ), which can be written as:

$$X_{flow} = (P - P_0)(\mathbb{V}) \quad (1.23)$$

The exergy of flowing fluid is the sum of Eqns. 1.22 and 1.23, which can be written as [108-110]:

$$\mathcal{E}_{flow} = U - U_0 + P_0(\mathbb{V} - \mathbb{V}_0) - T_0(S - S_0) + m \frac{v^2}{2} + mgz + (P - P_0)(\mathbb{V}) \quad (1.24)$$

By simplifying Eqn. 1.24, the total exergy associated with a stream of matter is:

$$\Xi_{flow} = (U + PV) - (U_0 + P_0V_0) - T_0(S - S_0) + m\frac{v^2}{2} + mgz \quad (1.25)$$

Enthalpy is defined as

$$H = (U + PV) \quad (1.26)$$

For a fluid stream with negligible kinetic and potential energies as in thermal energy storage systems, the kinetic and potential energy terms are usually neglected. Therefore Eqn. 1.25 becomes:

$$\Psi = (H - H_0) - T_0(S - S_0) = m(h - h_0) - mT_0(s - s_0) \quad (1.27)$$

Eqn. 1.27 represents the physical component of the exergy transfer associated with a stream of matter [109].

For an ideal gas (air in the present study), the change in enthalpy is

$$\Delta H = mCp\Delta T = mCp(T - T_0) \quad (1.28)$$

and the change in entropy is

$$\Delta S = mCp\ln\left(\frac{T}{T_0}\right) + mR\ln\left(\frac{P}{P_0}\right) \quad (1.29)$$

The pressure change is very small in the packed bed used in the study. Thus, Eqn. 1.27 will be simplified to [109]:

$$\Psi = mCp(T - T_0) - mCpT_0\ln\left(\frac{T}{T_0}\right) \quad (1.30)$$

Finally, to calculate the thermal exergetic efficiency for the packed bed system, the net exergy during the storage and recovery processes must be determined. The net exergy during the storage and recovery streams for a particular charging/discharging time is:

$$\Psi = \left[ \dot{m}Cp(T_{s(r)} - T_0) - \dot{m}CpT_0\ln\left(\frac{T_{s(r)}}{T_0}\right) \right] t_{s(r)} \quad (1.31)$$

where:  $\dot{m}$  is the mass flow rate and  $C_p$  is specific heat (considered constant in the range of temperature used in the present study, 20- 150°C). The change of specific heat is shown in Appendix C.  $T_0$  is the room or reference temperature (20.5 – 22°C in the lab),  $T_{s(r)}$  is the system temperature (the charge or discharge temperature) measured during storage/recovery processes, and  $t_{s(r)}$  is the charge/discharge time. The subscripts  $s$  and  $r$  refer to storage and recovery processes, respectively.

Eqn. 1.31 can be written in the form of exergy recovery and exergy storage as:

$$\Psi_{recovery} = \int_{t_r} \left[ \{\dot{m}C_p(T_r - T_0)\} - \left\{ \dot{m}T_0C_p \ln\left(\frac{T_r}{T_0}\right) \right\} \right] dt \quad (1.32)$$

The storage temperature is constant during the entire charging period and thus the storage exergy can be written as:

$$\Psi_{storage} = \left[ \{\dot{m}C_p(T_s - T_0)\} - \left\{ \dot{m}T_0C_p \ln\left(\frac{T_s}{T_0}\right) \right\} \right] t_s \quad (1.33)$$

The equation used to calculate the thermal exergetic efficiency has been adopted from [59] with the assumption that  $C_p$  is constant. The final equation, Eqn. 1.34 used in the present study to calculate the thermal exergetic efficiency is the ratio of the net exergy in recovery, Eqn. 1.32 to the net exergy in storage, Eqn. 1.33). The flow mass flow rate and specific heat are constant during storage/recovery processes and thus are dropped out:

$$\xi = \frac{\Psi_{recovery}}{\Psi_{storage}} = \frac{\int_{t_p} \left[ \{(T_r - T_0)\} - \left\{ T_0 \ln\left(\frac{T_r}{T_0}\right) \right\} \right] dt}{\left[ \{(T_s - T_0)\} - \left\{ T_0 \ln\left(\frac{T_s}{T_0}\right) \right\} \right] t_p} \quad (1.34)$$

### 1.8 Preface

As explained earlier, thermal energy storage using packed bed systems is a promising solution to utilize renewable energy sources such as solar. Figure 8 shows the number of journal articles from 2000 to 2020 from the keyword search “Packed Bed Thermal Energy Storage” in the Ei Compendex database, highlighting the importance of this topic as many researchers are focusing on this study in the last few years.

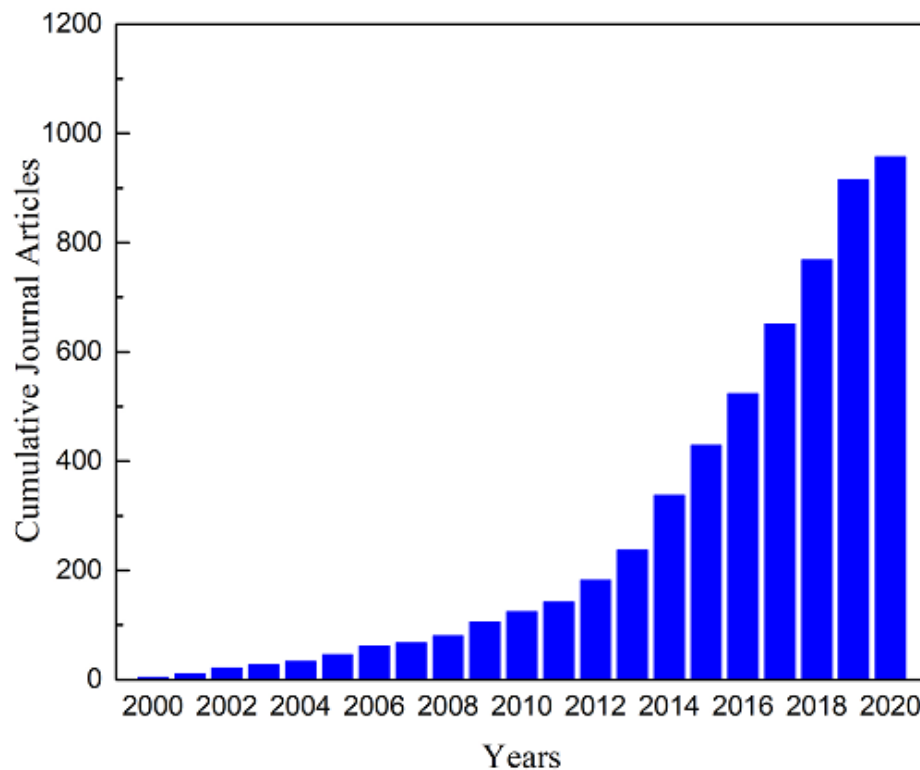


Figure 8. Cumulative number of journal articles from the keyword search “packed bed thermal energy storage” in the Compendex database accessed 06-29-2020.

The present thesis investigates the thermal performance of lab scale TES packed bed systems. Two major contributors (heat loss and axial thermal dispersion) to the degradation of thermal performance were investigated and analyzed. Results are quantified



by exergetic efficiency for normal and layered axial flow configurations. A first law charging efficiency is presented for the radial flow configuration. Chapter two focuses on studying the cyclic behavior of multiple repeated charge-discharge cycles. While the cyclic behavior had been studied in literature based on a first law analysis, in this thesis the second law analysis (exergy) is used to quantify the thermal cyclic behavior, where partial charge/discharge cycles were analyzed for the first time. The impact of thermal losses and dispersion losses were quantified as well. The quantified results represent a significant baseline for chapter three and four. Chapter three introduces a new, novel method for TES systems not tested experimentally before in the literature. The significant achievement of this chapter is providing 17 different charging/discharging schemes, which apply the proposed method (pipe injection) and quantify exergetic efficiency. The results show that segmenting the bed domain into several layers reduces the axial thermal dispersion losses, and as a result improves the thermocline and exergy efficiency. In addition, the results show that the orientation of the storage tank does not matter, and a narrow thermocline can be achieved in a single-tank with a horizontal layout. The results are considered a strong proof of concept for real life applications. Chapter four introduce another flow configuration to charge the bed, charging the bed domain radially instead of axially. The concept of radial flow in TES systems had been proposed and analyzed in literature. However, the method used in this study is new and different, where a perforated tube is inserted at the center of the bed domain, providing a radial flow distribution through the bed. The radial flow concept is introduced by designing and testing six different tubes experimentally. Designing a radial tube can provide uniform radial flow along the length

of the bed domain. The radial tubes were designed via changing the hole sizes to obtain even flow. The results of the most even flow show that energy stored and the charging efficiency of the radial flow configuration is higher than that of axial flow from the first law analysis. Chapters two and three are republications of work that has already been published in peer reviewed journals[51, 52]. Chapter 4 is a republication of work that is currently accepted pending revisions in a peer reviewed journal. Chapter five provides the final summary of the study and recommendations for future work. Appendix A includes images and screenshots of the storage apparatus, all equipment used to run the experiments, LabView code and data analysis. Appendix B details the experimental setup for the three configurations that have been tested (normal, layers and radial configuration). This includes the design/installation of axial and radial injected pipes the procedures to run the experiments, and how to operate data collection in chapters 2, 3 and 4. Appendix C shows the exergy calculations assuming a variation in  $Cp$ , specific heat, as a function of temperature, and exergy calculations assuming a change in storage temperature (integration of  $T_s(t)$  vs. constant  $T_s$ ). Appendix D explains the LabView interface and the code used to collect the experimental data; data analysis protocol to analyze the collected data based on charging/discharging processes; the procedure to run/control the heater; the calibration protocol to control the inlet temperature for the three configurations; how to control the mass flowrates for pipe injections with several layers; flowmeter calibration; and compressed air source and purity of the used air. Appendix E includes the part numbers for the entire equipment used in the lab.

## References

1. Panteli, M. and P. Mancarella, *Influence of extreme weather and climate change on the resilience of power systems: Impacts and possible mitigation strategies*. Electric Power Systems Research, 2015. **127**: p. 259-270.
2. *United States: MAP: How Climate Change Threatens America's Energy Infrastructure in Every Region*. 2015 [cited 2019 July 8]; Available from: <https://www.energy.gov/articles/map-how-climate-change-threatens-america-s-energy-infrastructure-every-region>.
3. Li, P., *Energy storage is the core of renewable technologies*. IEEE Nanotechnology Magazine, 2008. **2**(4): p. 13-18.
4. Dinçer, I.b., *Thermal energy storage : systems and applications*. 2nd ed.. ed, ed. M. Rosen. 2011: Chichester, England : Wiley.
5. *The battery energy storage system market is expected to grow from USD 1.98 billion in 2018 to reach USD 8.54 billion by 2023, at a CAGR of 33.9% between 2018 and 2023*. 2018 [cited 2019 30 May]; Available from: [http://link.galegroup.com/apps/doc/A533445555/AONE?u=mtlib\\_1\\_1123&sid=AONE&xid=e7923f07](http://link.galegroup.com/apps/doc/A533445555/AONE?u=mtlib_1_1123&sid=AONE&xid=e7923f07).
6. *Taking battery technology from the lab to the big city*. 2013 [cited 2019 12 June]; Available from: <https://www.energy.gov/articles/taking-battery-technology-lab-big-city>.

7. Sharma, A., et al., *Review on thermal energy storage with phase change materials and applications*. Renewable and Sustainable Energy Reviews, 2009. **13**(2): p. 318-345.
8. Huggins, R.A., *Energy Storage*. 2010, Boston, MA: Boston, MA: Springer US.
9. Gil, A., et al., *State of the art on high temperature thermal energy storage for power generation. Part 1—Concepts, materials and modellization*. Renewable and Sustainable Energy Reviews, 2010. **14**(1): p. 31-55.
10. IRENA, *Thermal Energy Storage: Technology Brief E17*. January 2013, International Renewable Energy Agency: Abu Dhabi.
11. Chen, H., et al., *Progress in electrical energy storage system: A critical review*. 2009. p. 291-312.
12. Muthusivagami, R.M., R. Velraj, and R. Sethumadhavan, *Solar cookers with and without thermal storage—A review*. Renewable and Sustainable Energy Reviews, 2010. **14**(2): p. 691-701.
13. Indora, S. and T.C. Kandpal, *Institutional cooking with solar energy: A review*. Renewable and Sustainable Energy Reviews, 2018. **84**: p. 131-154.
14. Medrano, M., et al., *State of the art on high-temperature thermal energy storage for power generation. Part 2—Case studies*. Renewable and Sustainable Energy Reviews, 2010. **14**(1): p. 56-72.
15. *Linear concentrator system basics for concentrating solar power*. 2013 [cited 2019 13 June]; Available from:

<https://energy.gov/eere/energybasics/articles/linear-concentrator-system-basics-concentrating-solar-power>.

16. Perez, R. and M. Perez, *A fundamental look at energy reserves for the planet*. Vol. 50. 2009.
17. IRENA, *Renewable Energy Statistics 2017*. 2017, International Renewable Energy Agency: Abu Dhabi.
18. *Goals of the Solar Energy Technologies Office*. [cited 2020 March, 20]; Available from: <https://www.energy.gov/eere/solar/goals-solar-energy-technologies-office>.
19. Murphy, C., et al., *The Potential Role of Concentrating Solar Power within the Context of DOE's 2030 Solar Cost Targets*. 2019, National Renewable Energy Lab.(NREL), Golden, CO (United States).
20. Cengel, Y.A., J.M. Cimbala, and R.H. Turner, *Fundamentals of thermal-fluid sciences*. 2012.
21. Incropera, F.P., *Fundamentals of heat and mass transfer*. 6th ed. / Frank P. Incropera ... [et al.].. ed. 2007, Hoboken, NJ: Hoboken, NJ : John Wiley.
22. Lane, G.A. and N. Shamsundar, *Solar heat storage: Latent heat materials, Vol. I: Background and scientific principles*. 1983, American Society of Mechanical Engineers.
23. Hasnain, S.M., *Review on sustainable thermal energy storage technologies, Part I: heat storage materials and techniques*. *Energy Conversion and Management*, 1998. **39**(11): p. 1127-1138.

24. Alva, G., et al., *Thermal energy storage materials and systems for solar energy applications*. Renewable and Sustainable Energy Reviews, 2017. **68**: p. 693-706.
25. Singh, H., R.P. Saini, and J.S. Saini, *A review on packed bed solar energy storage systems*. Renewable and Sustainable Energy Reviews, 2010. **14**(3): p. 1059-1069.
26. Fernandez, A.I., et al., *Selection of materials with potential in sensible thermal energy storage*. Solar Energy Materials and Solar Cells, 2010. **94**(10): p. 1723-1729.
27. Khare, S., et al., *Selection of materials for high temperature sensible energy storage*. Solar Energy Materials and Solar Cells, 2013. **115**: p. 114-122.
28. Wyman, C., J. Castle, and F. Kreith, *A review of collector and energy storage technology for intermediate temperature applications*. Solar Energy, 1980. **24**(6): p. 517-540.
29. Galione, P., et al., *A new thermocline-PCM thermal storage concept for CSP plants. Numerical analysis and perspectives*. Energy Procedia, 2014. **49**: p. 790-799.
30. Nithyanandam, K., R. Pitchumani, and A. Mathur, *Analysis of a latent thermocline storage system with encapsulated phase change materials for concentrating solar power*. Applied Energy, 2014. **113**: p. 1446.
31. Ramana, A., et al., *Experimental investigation of the LHS system and comparison of the stratification performance with the SHS system using CFD simulation*. Solar energy, 2014. **103**: p. 378-389.

32. Zanganeh, G., et al., *Experimental and numerical investigation of combined sensible–latent heat for thermal energy storage at 575 °C and above*. Solar Energy, 2015. **114**: p. 77-90.
33. Zanganeh, G., et al., *Stabilization of the outflow temperature of a packed-bed thermal energy storage by combining rocks with phase change materials*. Applied Thermal Engineering, 2014. **70**(1): p. 316-320.
34. Okello, D., et al., *An experimental investigation on the combined use of phase change material and rock particles for high temperature (~350 °C) heat storage*. Energy Conversion and Management, 2014. **79**: p. 1-8.
35. Galione, P., et al., *Multi-layered solid-PCM thermocline thermal storage concept for CSP plants. Numerical analysis and perspectives*. Applied energy, 2015. **142**: p. 337-351.
36. Galione, P., et al., *Multi-layered solid-PCM thermocline thermal storage for CSP. Numerical evaluation of its application in a 50 MWe plant*. Solar Energy, 2015. **119**: p. 134-150.
37. Farid, M.M., et al., *A review on phase change energy storage: materials and applications*. Energy Conversion and Management, 2004. **45**(9): p. 1597-1615.
38. de Gracia, A. and L.F. Cabeza, *Numerical simulation of a PCM packed bed system: a review*. Renewable and Sustainable Energy Reviews, 2017. **69**: p. 1055-1063.

39. Lin, Y., G. Alva, and G. Fang, *Review on thermal performances and applications of thermal energy storage systems with inorganic phase change materials*. Energy, 2018. **165**: p. 685-708.
40. Wei, G., et al., *Selection principles and thermophysical properties of high temperature phase change materials for thermal energy storage: A review*. Renewable and Sustainable Energy Reviews, 2018. **81**: p. 1771-1786.
41. Elias, C.N. and V.N. Stathopoulos, *A comprehensive review of recent advances in materials aspects of phase change materials in thermal energy storage*. Energy Procedia, 2019. **161**: p. 385-394.
42. Herrmann, U., B. Kelly, and H. Price, *Two-tank molten salt storage for parabolic trough solar power plants*. Energy, 2004. **29**(5): p. 883-893.
43. Kelly, B., *Thermal storage commercial plant design study for a 2-tank indirect molten salt system final report, May 13, 2002 - December 31, 2004*, D. Kearney, et al., Editors. 2006, Golden, Colo. : National Renewable Energy Laboratory: Golden, Colo.
44. *Concentrating solar power thermal storage system basics*. 2013 [cited 2018 July 31]; Available from: <https://energy.gov/eere/energybasics/articles/concentrating-solar-power-thermal-storage-system-basics>.
45. Tamme, R., et al. *Innovative thermal energy storage technology for parabolic trough concentrating solar power plants*. in *Proceedings EuroSun*. 2002.



46. Pacheco, J.E., S.K. Showalter, and W.J. Kolb, *Development of a molten-salt thermocline thermal storage system for parabolic trough plants*. Journal of solar energy engineering, 2002. **124**(2): p. 153-159.
47. Bindra, H., et al., *Thermal analysis and exergy evaluation of packed bed thermal storage systems*. Applied Thermal Engineering, 2013. **52**(2): p. 255-263.
48. Wu, M., et al., *The impact of concrete structure on the thermal performance of the dual-media thermocline thermal storage tank using concrete as the solid medium*. Applied Energy, 2014. **113**: p. 1363-1371.
49. Johnson, E., et al., *Thermal energy storage with supercritical carbon dioxide in a packed bed: Modeling charge-discharge cycles*. The Journal of Supercritical Fluids, 2018. **137**: p. 57-65.
50. Prenzel, M., et al., *Thermo-fluid dynamic model for horizontal packed bed thermal energy storages*. Energy Procedia, 2017. **135**: p. 51-61.
51. Al-Azawii, M.M.S., et al., *Experimental study on the cyclic behavior of thermal energy storage in an air-alumina packed bed*. Journal of Energy Storage, 2018. **18C**: p. 239-249.
52. Al-Azawii, M.M.S., et al., *Experimental study of layered thermal energy storage in an air-alumina packed bed using axial pipe injections*. Applied Energy, 2019. **249**: p. 409-422.
53. Gautam, A. and R. Saini, *A review on technical, applications and economic aspect of packed bed solar thermal energy storage system*. Journal of Energy Storage, 2020. **27**: p. 101046.

54. Cárdenas, B., et al., *Effect of design parameters on the exergy efficiency of a utility-scale packed bed*. Journal of Energy Storage, 2018. **18**: p. 267-284.
55. Meier, A., C. Winkler, and D. Willemin, *Experiment for modeling high-temperature rock bed storage*. Solar Energy Materials, 1991. **24**(1-4): p. 255-264.
56. Wu, C. and G. Hwang, *Flow and heat transfer characteristics inside packed and fluidized beds*. Journal of heat transfer, 1998. **120**(3): p. 667-673.
57. Hänchen, M., S. Brückner, and A. Steinfeld, *High-temperature thermal storage using a packed bed of rocks – Heat transfer analysis and experimental validation*. Applied Thermal Engineering, 2011. **31**(10): p. 1798-1806.
58. Cascetta, M., et al., *Numerical investigation of a packed bed thermal energy storage system with different heat transfer fluids*. Energy Procedia, 2014. **45**: p. 598-607.
59. Anderson, R., et al., *Experimental results and modeling of energy storage and recovery in a packed bed of alumina particles*. Applied Energy, 2014. **119**: p. 521-529.
60. Coutier, J.P. and E. Farber, *Two applications of a numerical approach of heat transfer process within rock beds*. Solar Energy, 1982. **29**(6): p. 451-462.
61. Yang, Z. and S.V. Garimella, *Thermal analysis of solar thermal energy storage in a molten-salt thermocline*. Solar Energy, 2010. **84**(6): p. 974-985.
62. Bruch, A., J.F. Fourmigue, and R. Couturier, *Experimental and numerical investigation of a pilot-scale thermal oil packed bed thermal storage system for CSP power plant*. Solar Energy, 2014. **105**: p. 116-125.

63. Ismail, K.A.R. and R. Stuginsky Jr, *A parametric study on possible fixed bed models for pcm and sensible heat storage*. Applied Thermal Engineering, 1999. **19**(7): p. 757-788.
64. Bejan, A., *Convection heat transfer*. 4th ed.. ed. 2013: Hoboken, New Jersey : Wiley.
65. Hsu, C. and P. Cheng, *Closure schemes of the macroscopic energy equation for convective heat transfer in porous media*. International communications in heat and mass transfer, 1988. **15**(5): p. 689-703.
66. Nield, D.A. and A. Bejan, *Convection in porous media*. Vol. 3. 2013: New York: Springer.
67. Schumann, T.E., *Heat transfer: a liquid flowing through a porous prism*. Journal of the Franklin Institute, 1929. **208**(3): p. 405-416.
68. Amundson, N.R., *Solid-fluid interactions in fixed and moving beds fixed beds with small particles*. Industrial & Engineering Chemistry, 1956. **48**(1): p. 26-35.
69. Beasley, D.E. and J.A. Clark, *Transient response of a packed bed for thermal energy storage*. International Journal of Heat and Mass Transfer, 1984. **27**(9): p. 1659-1669.
70. Furnas, C., *Heat transfer from a gas stream to bed of broken solids*. Industrial & Engineering Chemistry, 1930. **22**(1): p. 26-31.
71. Löf, G. and R. Hawley, *Unsteady-state heat transfer between air and loose solids*. Industrial & Engineering Chemistry, 1948. **40**(6): p. 1061-1070.

72. Handley, D. and P. Heggs, *The effect of thermal conductivity of the packing material on transient heat transfer in a fixed bed*. International Journal of Heat and Mass Transfer, 1969. **12**(5): p. 549-570.
73. Sanderson, T. and G. Cunningham, *Performance and efficient design of packed bed thermal storage systems. Part 1*. Applied energy, 1995. **50**(2): p. 119-132.
74. Regin, A.F., S. Solanki, and J. Saini, *An analysis of a packed bed latent heat thermal energy storage system using PCM capsules: Numerical investigation*. Renewable energy, 2009. **34**(7): p. 1765-1773.
75. Felix, R., S. Solanki, and J. Saini. *Thermal performance analysis of phase change material capsules*. in *ISES 2005 Solar world congress*. 2005.
76. Ismail, K. and J. Henriquez, *Numerical and experimental study of spherical capsules packed bed latent heat storage system*. Applied Thermal Engineering, 2002. **22**(15): p. 1705-1716.
77. Anderson, R., et al., *Packed bed thermal energy storage: A simplified experimentally validated model*. Journal of Energy Storage, 2015. **4**: p. 14-23.
78. Wakao, N. and S. Kagei, *Heat and mass transfer in packed beds*. Vol. 1. 1982: Taylor & Francis.
79. Vortmeyer, D. and R.J. Schaefer, *Equivalence of one- and two-phase models for heat transfer processes in packed beds: one dimensional theory*. Chemical Engineering Science, 1974. **29**(2): p. 485-491.
80. Dixon, A.G. and D.L. Cresswell, *Theoretical prediction of effective heat transfer parameters in packed beds*. AIChE Journal, 1979. **25**(4): p. 663-676.

81. Vortmeyer, D. and R. Schaefer, *Equivalence of one-and two-phase models for heat transfer processes in packed beds: one dimensional theory*. Chemical Engineering Science, 1974. **29**(2): p. 485-491.
82. Sanderson, T.M. and G.T. Cunningham, *Packed bed thermal storage systems*. Applied Energy, 1995. **51**(1): p. 51-67.
83. Zanganeh, G., et al., *Packed-bed thermal storage for concentrated solar power – Pilot-scale demonstration and industrial-scale design*. Solar Energy, 2012. **86**(10): p. 3084-3098.
84. Cascetta, M., et al., *A comparison between CFD simulation and experimental investigation of a packed-bed thermal energy storage system*. Applied Thermal Engineering, 2016. **98**: p. 1263-1272.
85. Prenzel, M., et al., *Thermo-fluid dynamic model for horizontal packed bed thermal energy storages*, in *Energy Procedia*. 2017. p. 51-61.
86. Öhman, H. and P. Lundqvist, *Comparison and analysis of performance using Low Temperature Power Cycles*. Applied Thermal Engineering, 2013. **52**(1): p. 160-169.
87. Hettiarachchi, H.M., et al., *Optimum design criteria for an organic Rankine cycle using low-temperature geothermal heat sources*. Energy, 2007. **32**(9): p. 1698-1706.
88. Heller, P., et al., *Test and evaluation of a solar powered gas turbine system*. Solar Energy, 2006. **80**(10): p. 1225-1230.

89. Tijani, M. and S. Spoelstra, *A hot air driven thermoacoustic-Stirling engine*. Applied thermal engineering, 2013. **61**(2): p. 866-870.
90. González-Roubaud, E., D. Pérez-Osorio, and C. Prieto, *Review of commercial thermal energy storage in concentrated solar power plants: Steam vs. molten salts*. Renewable and sustainable energy reviews, 2017. **80**: p. 133-148.
91. Laing, D., et al., *Thermal energy storage for direct steam generation*. Solar Energy, 2011. **85**(4): p. 627-633.
92. Esence, T., et al., *A review on experience feedback and numerical modeling of packed-bed thermal energy storage systems*. Solar Energy, 2017. **153**: p. 628-654.
93. Cascetta, M., et al. *Experimental investigation of a packed bed thermal energy storage system*. in *Journal of Physics: Conference Series*. 2015. IOP Publishing.
94. Erregueragui, Z., et al., *Packed-bed thermal energy storage analysis: quartzite and palm-oil performance*. Energy Procedia, 2016. **99**: p. 370-379.
95. Aly, S. and A. El-Sharkawy, *Effect of storage medium on thermal properties of packed beds*. Heat Recovery Systems & CHP, 1990. **10 no.5/6**(1990): p. 509-517.
96. Mawire, A., et al., *Simulated performance of storage materials for pebble bed thermal energy storage (TES) systems*. Applied Energy, 2009. **86**(7): p. 1246-1252.
97. Warkhade, G.S., et al., *Experimental investigation of sensible thermal energy storage in small sized, different shaped concrete material packed bed*. World Journal of Engineering, 2016. **13**(5): p. 386-393.

98. Singh, H., R.P. Saini, and J.S. Saini, *Performance of a packed bed solar energy storage system having large sized elements with low void fraction*. Solar Energy, 2013. **87**(1): p. 22-34.
99. Yeboah, S. and J. Darkwa, *A critical review of thermal enhancement of packed beds for water vapour adsorption*. Renewable and Sustainable Energy Reviews, 2016. **58**: p. 1500-1520.
100. Kadoli, R. and T.A. Babu, *Performance studies on the desiccant packed bed with varying particle size distribution along the bed*. International journal of refrigeration, 2012. **35**(3): p. 663-675.
101. Kuravi, S., et al., *Investigation of a high-temperature packed-bed sensible heat thermal energy storage system with large-sized elements*. Journal of solar energy engineering, 2013. **135**(4).
102. Okello, D., O.J. Nydal, and E.J. Banda, *Experimental investigation of thermal de-stratification in rock bed TES systems for high temperature applications*. Energy conversion and management, 2014. **86**: p. 125-131.
103. Cascetta, M., et al., *A Study of a Packed-bed Thermal Energy Storage Device: Test Rig, Experimental and Numerical Results*. Energy Procedia, 2015. **81**: p. 987-994.
104. Cascetta, M., et al., *Experimental and Numerical Research Activity on a Packed Bed TES System*. Energies, 2016. **9**(9): p. 758.

105. Nakayama, A., F. Kuwahara, and Y. Kodama, *An equation for thermal dispersion flux transport and its mathematical modelling for heat and fluid flow in a porous medium*. Journal of Fluid Mechanics, 2006. **563**: p. 81-96.
106. Gunn, D., *Theory of axial and radial dispersion in packed beds*. Trans. Inst. Chem. Eng, 1969. **47**(10): p. T351-T359.
107. Saez, A.E. and B. McCoy, *Dynamic response of a packed bed thermal storage system—a model for solar air heating*. Solar Energy, 1982. **29**(3): p. 201-206.
108. Çengel, Y.A. and M.A. Boles, *Thermodynamics: An Engineering Approach*, -PDF. 2008: McGraw-Hill.
109. Bejan, A., *Thermal design and optimization*, ed. M.J. Moran and G. Tsatsaronis. 1996, New York: New York : John Wiley & Sons.
110. Dincer, I. and M.A. Rosen, *Exergy: energy, environment and sustainable development*. 2012: Newnes.



## CHAPTER TWO

EXPERIMENTAL STUDY ON CYCLIC BEHAVIOR OF THERMAL ENERGY  
STORAGE IN AN AIR-ALUMINA PACKED BEDContribution of Authors and Co-Authors

Manuscript in Chapter 2

Author: Mohammad M. S. Al-Azawii

Contributions: Installed the apparatus, collected the experimental data, performed the numerical model, performed the analyses, explained results, generated figures, and wrote the manuscript in preparation for editing and submission.

Co-Author: Carter Theade

Contributions: Collected experimental data, generated figures, and edited earlier and final manuscript.

Co-Author: Megan Danczyk

Contributions: Installed the apparatus, collected preliminary data, and edited the final manuscript.

Co-Author: Erick Johnson

Contributions: Assisted with Computational Fluid Dynamic (CFD) modeling, edited the manuscript.

Co-Author: Ryan Anderson

Contributions: Conceived the study and designed experiments, assisted in the preparation of the manuscript, provided important insight and details of the entire study and manuscript, discussed results and implications, and edited the earlier manuscript and final versions of the manuscript for submission.

Manuscript Information

Mohammad M.S. Al-Azawii, Carter Theade, Megan Danczyk, Erick Johnson, Ryan Anderson

Journal of Energy Storage

Status of Manuscript:

Prepared for submission to a peer-reviewed journal

Officially submitted to a peer-reviewed journal

Accepted by a peer-reviewed journal

Published in a peer-reviewed journal

Elsevier

Vol 18C, pages 239-249, August 2018

<https://doi.org/10.1016/j.est.2018.05.008>

EXPERIMENTAL STUDY ON CYCLIC BEHAVIOR OF THERMAL ENERGY  
STORAGE IN AN AIR-ALUMINA PACKED BED

Abstract

Thermal energy storage (TES) in a packed bed exemplifies important technology for concentrated solar thermal (CST) applications such as electricity production, desalination, enhanced oil recovery, fuel production and chemical processing. In this study, the cyclic charge-discharge behavior of packed bed TES was studied experimentally using alumina beads as packing material. Air was used as heat transfer fluid (HTF) with an inlet temperature of 150°C. This paper shows the effect of flow rates, partial charge-discharge cycling, and storage hold time on the exergetic efficiencies. The results indicate that the exergy efficiency increases from 35.7% to 55.4% with increasing flow rate from 0.0020 to 0.0061 m<sup>3</sup>/s. The exergy decays for multiple cycles before reaching a steady state. Over partial charge-discharge cycles at flow rates of 0.0020, 0.0034, 0.0048, and 0.0061 m<sup>3</sup>/s, the exergetic efficiency decays from 59.8% to 50.2%, 72.5% to 61.2%, 79.0% to 66.2%, and 83.1% to 69.2%, respectively. Heat losses and axial thermal dispersion are two important variables that affect the exergy efficiency, and the individual contributions were estimated via a model for the partial cycles. Heat losses were considered for three durations of holding: no hold, 30 min hold and 120 min hold. The exergy efficiency decays from 53.2% to 31.0% from no hold to 120 min hold due to the heat lost to the ambient.

Nomenclature

$\varepsilon$	porosity (-)
$\Xi$	exergy (W)
$\eta$	exergetic efficiency (-)
$\rho$	density (kg/m <sup>3</sup> )
$C_p$	specific heat capacity (J/kg K)
$L$	length of packed bed (m)
$k$	thermal conductivity (W/m K)
$\dot{m}$	mass flow rate (kg/s)
$m$	mass (kg)
$Q_{loss}$	energy losses to surrounding (W/m <sup>3</sup> )
$St_w$	Wall Stanton number (-)
$t$	time (s)
$T$	temperature (K)
$u_0$	mean velocity (m/s)
$U_{loss}$	Overall volumetric heat transfer coefficient for energy losses (W/m <sup>3</sup> K)
$V$	velocity (m/s)
$v$	propagation velocity (m/s)

Subscripts

$f$	fluid
$s$	solid
$h$	hot
$eq$	equivalent
$i$	solid domains (steel and insulation)
$0$	initial
$r$	recovery

2.1 Introduction

Energy demand continues to increase with a steadily growing global population. Many researchers are working to find new sources of energy as well as developing existing energy sources. Renewable energy sources such as solar, wind and ocean currents can be used to extract energy. Concentrated solar thermal (CST) is an emerging technology in several applications[1]. One application of this technology is concentrated

solar power (CSP) plants, where power plants can generate electricity from a high temperature heat transfer fluid. Low temperature power cycles have also been explored [2] at temperatures from 61.5 - 482.2°C. Low temperature power cycles, such as Organic Rankine or Kalina cycles, show promise in the future of solar energy production and utilization. An industrial plant that utilizes low temperature steam from the sun using solar-thermal collectors and generates energy at a lower price than that of natural gas has already been implemented by Sunvapor Inc. [3]. In addition, CST has many other applications. Its utilization in desalination could aid in global water demand, especially in places that border ocean with high sunlight density. In oil recovery, steam injection aids in lowering the viscosity of the oil reserve, which increases recovery. Fuel production and chemical processing applications are currently being researched and have promise in CO<sub>2</sub> capture and steam reforming of biomass or fossil fuels into hydrogen [1].

However, renewable energy sources have inherently low energy density and are not continuously available. The intermittent nature of renewable energy sources has led researchers to focus intensely on energy storage. These efforts have focused on improving energy storage technology as it represents a cornerstone of renewable energy sources [4]. Clean energy sources, such as solar energy, can be stored in the form of heat when there is a surplus of energy. This stored energy can then be used to continue operation when there is a shortage of solar flux. Thermal energy storage (TES) is a common energy storage practice, and sensible and latent heats are the most significant methods used to store energy in packed beds. A review on thermal energy storage

technologies with sensible and latent heats has been done [5]. In sensible heat storage, energy is stored in solid particles such as rocks or alumina. In latent heat storage, energy is stored when a phase change material (PCM) undergoes a change from solid to liquid. The choice of materials for energy storage is important, and the selection of materials for energy storage and a review on PCMs for different applications have been discussed [6-10]. Currently, a combination of sensible and latent heats has been investigated to stabilize the exit temperature during the discharge cycles [11-13]. Several experimental and numerical studies have been done investigating the thermal behavior of TES using sensible heat or latent heat with different types of HTF (air, molten salt and oil) [14-18].

To be a viable component in any application, the thermal efficiency of the TES must be high and is directly related to stratification in the storage tank. Stratification pertains to having a hot and a cold layer in the storage tank, which are separated with a temperature gradient (thermocline). In general, if the packed bed system has a sharp temperature profile or perfectly stratified zones (hot and cold zones with no mixing), the exergetic efficiency is higher [19]. The performance of TES systems can be affected by many different governing parameters. These parameters such as flow rate [20-27], particle size [26-29], thermal wall losses by convection [20], packing material [30], heat transfer fluid [25, 31, 32], and void fraction [24, 33] have been studied. These parameters have influences on the following: charging-discharging times, enhancement of heat transfer between fluid and solid media, amount of energy stored and recovered, thermal front temperature profile, heat losses, thermocline thickness, storage efficiency, and cycle efficiency. Similar to the present study, air and alumina packed beds have been

considered experimentally and numerically [20, 21, 34-36], where different parameters are considered such as mass flow rate, variable porosity in radial direction, the inlet-outlet temperature thresholds, and aspect ratio to show the thermal behavior and the stored/recovered energy for an individual charge/discharge cycle.

Singh et al. [37] reviewed analytical and experimental studies on packed bed solar energy systems finding extensive research, both analytical and experimental, has been conducted in these areas. However, the impact of such parameters on the exergetic efficiency for multiple partial charging-discharging cycles has not been investigated in detail. The behavior of the bed during charge-discharge cycles is also important, as the efficiency can vary during cycles and cycles can also impact thermal ratcheting [38, 39]. A study using a high temperature packed bed of rocks with air as HTF found overall efficiency exceeding 90% under optimal conditions as well as a steady state after twenty 6-h charge and discharge cycles [40]. The cycling behavior of a dual media thermocline with rock and sand as solid materials and thermal oil as the HTF was investigated experimentally [41]. The results showed that the charge and discharge energies reach a steady value after repeated cycling. Another study numerically and experimentally explored cyclic behavior using rocks with air as HTF, finding an increase in the first-law efficiency with cycle number until a constant efficiency was reached [42]. Their study charged a bed from  $\sim 17^{\circ}\text{C}$  to  $650^{\circ}\text{C}$  in the first cycle. In all cycles presented, the charge was always for 12h at  $650^{\circ}\text{C}$ , and discharging occurred with air entering at  $270^{\circ}\text{C}$  and continuing until the recovery outlet temperature was  $600^{\circ}\text{C}$ . This cycle definition led to their observed first-law results; however, the exergetic efficiency of these cycles was not

considered. Cyclic behavior for air-alumina systems were also considered [32, 43]. In [32], different heat transfer fluids (air, molten salt and oil) were used to numerically analyze the thermal behavior for multiple repeated cycles, showing reduced energy storage with increased cycle number. In [43], an experimental analysis showed similar results where a reduction in heat storage capacity after multiple cycles was noted.

These studies investigated energy storage with repeated cycles from a first law point of view, focusing on system efficiency. The present study investigates the thermal behavior with repeated cycles in a horizontal apparatus focusing on thermal exergy (second law analysis), showing the effect of axial thermal dispersion and heat losses for partial charging/discharging cycles. In the present paper, an experimental sensible heat storage system considered  $\alpha$ -alumina as storage material. Alumina has high thermal conductivity and high heat capacity, which makes it a desirable choice as a solid medium. While alumina is a relatively expensive packing material, its high thermal performance and stability may make it a suitable candidate for industrial applications. Air as HTF has been demonstrated for CSP plants by Heller et al. [44] and has been studied in other packed bed systems [15, 20, 21, 32, 40-43]. Air is free, non-toxic, and has no temperature limitation, making it a suitable option as HTF. This study focuses on the exergetic efficiency of a TES system with alumina as storage material and air as a HTF at 150°C experimentally. The experimental thermal exergy efficiency was determined for three cases: full charge-discharge cycles with four flow rates, multiple partial charge-discharge cycles, and three hold times at 0.0048 m<sup>3</sup>/s with full charge-discharge, which were analyzed as a function of heat loss. Estimates are provided for the relative contributions



of heat losses and thermal dispersion on the reduction in exergetic efficiency with partial cycles.

## 2.2 Experimental Methods, Numerical Model, and Thermal Exergy Analysis

This section details the properties of the experimental storage vessel, flow loop setup, and experimental conditions. The model is also introduced, which is utilized to verify the performance of the experimental setup at baseline conditions. Finally, the thermal exergy equations are presented for the charge-discharge cycles.

### 2.2.1 Storage Vessel

Figure 9 shows a schematic of the experimental setup. Air is provided from the compressed air line supplied from the building. Several valves are connected on the path of air to control its direction based on the charging or discharging cycles. Two filters removed water vapor (McMaster Carr 41745K21) and oil vapor particulates (McMaster Carr 8282K31). In charging, the clean dry air flows into the heater (Omega, AHPF-121) and then enters the horizontal packed bed to deposit heat into the storage materials. After leaving the packed bed, the air enters a heat exchanger (DudaDiesel, B3-12A-30ST) to cool the exiting air. During the discharge cycle, cold gas at room temperature (21.5°C) enters the packed bed in the opposite direction of charging and gains heat from the storage media. It then exits the storage vessel and is cooled by a heat exchanger (DudaDiesel, B3-12A-10ST) before being discharged to the room.

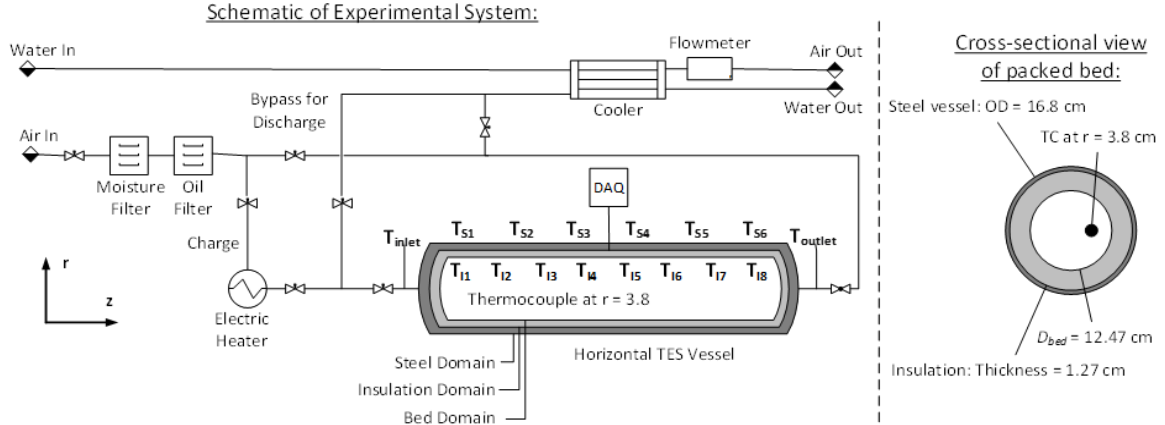


Figure 9. Left: Air flow schematic of TES apparatus utilizing two filters to purify air supply, electric heating apparatus to heat the HTF, horizontal TES vessel, DAQ collecting temperature data, and a cooler. There is a thermocouple (TC) with eight internal sensing points (TI) at an internal radius of  $r=3.8$ cm, six surface thermocouples (TS), and inlet and outlet thermocouples. A bypass valve routes flow for discharging in the opposite direction of charging. Right: Cross-sectional view of the packed bed highlighting key dimensions and the radial position of the internal thermocouple.

The storage vessel was fabricated and hydro-tested by the vendor, Power Service, Inc. The storage vessel is a horizontal cylinder made of carbon steel. Historically, vertical storage vessels have been investigated for exploring thermal energy storage. A vertical orientation provides advantages for thermal stratification; however, it reaches limitations in mechanical stability and accessibility. A horizontal apparatus can provide the mechanical stability and may be a more reasonable option for storage and accessibility in industry [45]. The outer and inner diameters are 16.8cm and 15.4cm respectively (6" NPS schedule 40 with 0.280" wall thickness).

The connections at the inlet and outlet of the vessel are flat flanges (ANSI 150# RF w/Blind). The length of the cylindrical vessel is 120cm. The storage packed bed length is 100cm. To obtain uniform flow through the vessel, distributors were used at a distance 10cm from the inlet and outlet of the storage tank. The distributor also prevents

the storage materials from falling in the inlet and outlet pipes. Internal microtherm insulation (Promat Inc., custom design) is used with 1.27cm thickness (15cm OD and 12.47cm ID). The insulation was constructed as two rigid cylinders with 60cm length each to avoid breaking due to the length to diameter ratio. The two cylinders were sealed to each other and inserted as one piece in the steel vessel. The insulation was covered with glass cloth for protection, and the final assembly led to 0.1cm clearance to help insert the insulation into the vessel. The insulation was sealed to the steel vessel with Loctite Superflex Red High-Temperature Silicone (McMaster Carr 7644A11) to avoid bypass flow. Ultimately, the storage packed bed is 12.47cm diameter and 100cm length. The inlet and outlet of the vessel is 2.54 cm FNPT (Female National Pipe Thread). A nipple pipe with 2.54 cm diameter and 10.2cm length is used at each flange. This part is insulated internally so that the supplied HTF passes to the storage materials in the bed without touching the flange body. At one side of the vessel one hole was drilled of 0.635cm FNPT to insert a K-type thermocouple in the axial direction to read the temperature variation inside the storage vessel. The radial location of this thermocouple is  $r=3.8\text{cm}$ . The internal thermocouple (Omega Custom Design) has eight K-type sensing points. The internal sensing points are evenly spaced at 14.22cm (TI1 – TI7) along the length of the vessel except for the last sensing point, which is spaced at 14.68cm (TI7 – TI8). In addition, several thermocouples are used to record the temperature at the inlet, outlet, and surface of the vessel (Omega, KMQSS-125G-6andSA1K) as shown in Figure 9. The error associated with the thermocouples is  $\pm 2.2^\circ\text{C}$  as specified by Omega. All thermocouples are connected to a data acquisition controller (National Instrument, NI

9213) that is further connected to a computer running LabView software to read and record the temperature data every second.

### 2.2.2 Experimental Conditions

A complete cycle can be defined via two processes, charging and discharging. To operate a cycle, the time during charge and discharge was calculated using Eqn. 2.1 as discussed in [29]:

$$t = L/v \quad (2.1)$$

where  $t$  is charge or discharge period,  $L$  is the length of the packed bed and  $v$  is the propagation velocity of the heat-exchange zone in the packed bed. The propagation velocity of the heat-exchange zone was calculated using Eqn. 2.

$$v = \frac{Cp_{f,h}\rho_{f,h}u_0}{\varepsilon Cp_{f,h}\rho_{f,h} + (1-\varepsilon)Cp_{s,h}\rho_{s,h}} \quad (2.2)$$

In Eqn. 2  $\varepsilon$  is porosity,  $Cp$  is specific heat,  $\rho$  is density and  $u_0$  is mean velocity at the inlet of the packed bed. The subscripts f, h and s are fluid, hot, and solid, respectively.

The stored/recovered energy is influenced by flow rate, and four flow rates from 0.0020 to 0.0061 m<sup>3</sup>/s were considered to see their impact on the exergetic efficiency and thermal behavior in the packed bed.  $\alpha$ -alumina beads were used as storage material with a diameter of 6mm. The alumina spheres were poured randomly in the bed, and the porosity is taken as approximately 0.375, which is in the range of 0.36–0.43 [46, 47].

Table 3 shows the time required for charging/discharging for the four flow rates based on Eqns. 2.1 and 2.2.

Table 3. Time for charging and discharging processes at four flowrates.

Conditions	Volumetric flow rate (m <sup>3</sup> /s)	Mass flow rate (kg/s)	Charge Time (s)	Discharge Time (s)
3 SCFM	0.0020	0.0017	16899 (4 hr and 41 min)	24254 (6 hr and 44 min)
5 SCFM	0.0034	0.0028	10138 (2 hr and 49 min)	14557 (4 hr and 2.5 min)
7 SCFM	0.0048	0.0040	7241 (2 hr and 0.5 min)	10400 (2 hr and 53 min)
9 SCFM	0.0061	0.0051	5632 (1 hr and 34 min)	8087 (2 hr and 14.5 min)

To study partial charge-discharge cycles, the bed was initially fully charged for each flow rate based on the charging time calculated from Eqn. 2.2. The partial charge and discharge times were then based on half of the full charge time. Five and six cycles were completed at 0.0020 and 0.0034m<sup>3</sup>/s, respectively, and eight cycles were completed at 0.0048 and 0.0061m<sup>3</sup>/s. Table 4 shows the partial charge-discharge times.

Table 4. Timing scheme for partial charging-discharging cycles at four flowrates.

Volumetric flow rate (m <sup>3</sup> /s)	Partial charging/discharging times (hr.)
0.0020	4 hr. & 40 min. full charging, 2 hr. & 20 min. partial charging/discharging
0.0034	2 hr. & 48 min. full charging, 1 hr. & 24 min. partial charging/discharging
0.0048	2 hr. full charging and 1 hr. partial charging/discharging
0.0061	1 hr. & 30 min. full charging, 45 min. partial charging/discharging

Further, the results at 0.0048m<sup>3</sup>/s with no hold were compared to holds of 30min (short) and 120min (long) between full cycles. Ultimately, the exergy efficiency was calculated to quantify the performance of the packed bed system based on experimental data.

### 2.2.3 Modeling Approach

The general governing equation is the energy equation for a single phase model, where the fluid and solid are assumed in local thermal equilibrium ( $T_f = T_s = T$ )[48]. This approach has been shown to be appropriate for the air-alumina system [20, 21]. The one-phase equation assumes a homogenous medium in the packed bed [49]. Due to the symmetry of the cylindrical packed bed, 2-D axisymmetric modeling was used. The resultant equation is a one-phase equation with equivalent properties denoted by subscript eq, which is used to solve for the transient temperature profile in the radial and axial (r- and z-) direction of the packed bed domain.

$$(\rho C_p)_{eq} \frac{\partial T}{\partial t} + (\rho C_p)_f V \cdot \nabla T = \nabla \cdot (k_{eq} \nabla T) + Q_{loss} \quad (2.3)$$

where:

$$(\rho C_p)_{eq} = \varepsilon \rho_f C_{p,f} + (1 - \varepsilon) \rho_s C_{p,s} \quad (2.4)$$

$$k_{eq} = \varepsilon k_f + (1 - \varepsilon) k_s \quad (2.5)$$

$Q_{loss}$  represents heat losses via conduction through the solid domains and natural convection from the vessel walls. The equation for the solid domains is:

$$(\rho C_p)_i \frac{\partial T}{\partial t} = \nabla \cdot (k_i \nabla T) \quad (2.6)$$

where the subscript  $i$  denotes either the insulation or the steel vessel.

Initial conditions and boundary conditions for the charging period  $T_{t=0} = T_{ambient}$ ,  $\dot{m}_{t=0} = 0$ , and  $\dot{m}_{x=0} = \dot{m}_{in}$ . To have accurate thermal boundary conditions for the model, the experimental results were used to find a time-dependent temperature boundary condition,  $T_{charging}$ , at the inlet of the model. This approach avoids having to

model the peripheral piping and flange system [21]. The time-dependent function is found using curve fitting for the best fit and is used in the solver. The wall heat transfer coefficient is  $3.71 \text{ W/m}^2 \text{ K}$  based on typical wall temperatures and heat transfer correlations [50]. Also, while there is the potential for buoyancy driven flow in the packed bed domain, the horizontal orientation would suggest minimal influence on the temperature profile. Additionally, the radial temperature profile in the bed (results not shown) is nearly isothermal, so buoyancy effects were not considered in the analysis.

Star-CCM+ is a commercial computational fluid dynamics (CFD) software that is used to solve the governing equations. An implicit unsteady model solver is used with the segregated flow and segregated fluid energy formulations. Three regions are defined in the model: porous, insulation and steel. The generalized Navier-Stokes flow solutions for velocity and pressure drop are coupled to the energy equation throughout the porous region. The porous viscous and inertial losses are included in the model to solve for velocities and pressure drop in the bed domain. The porous and inertial coefficients are determined by the Ergun equation [48]. The time step used in the model was 1.0s. The mesh size used in the model was 0.005m. The temperature-dependent thermophysical properties used in the CFD-model are shown in Eqns. 2.7–2.11. The density for the fluid was determined from the ideal gas law. Temperature dependent properties are fit from data in [51] for air and from [52, 53] for alumina.

$$c_{p,f} = 1.8144 \times 10^{-7} T_f^3 + 2.209 \times 10^{-4} T_f^2 - 1.433 \times 10^{-1} T_f + 1.0246 \times 10^3 \left[ \frac{J}{kg-K} \right] \quad (2.7)$$

$$k_f = -3.4782 \times 10^{-8} T_f^2 + 9.846 \times 10^{-5} T_f - 1.664 \times 10^{-4} \left[ \frac{W}{m-K} \right] \quad (2.8)$$

$$\rho_s = -9.83 \times 10^{-2} T_s^2 + 4020 \left[ \frac{kg}{m^3} \right] \quad (2.9)$$

$$C_{p,s} = -2.1796 \times 10^{-5} T_s^3 + 1.8895 \times 10^{-2} T_s^2 - 3.5216 T_s + 7.20986 \times 10^2 \left[ \frac{J}{kg \cdot K} \right] \quad (2.10)$$

$$k_s = -2.469 \times 10^{-8} T_s^3 + 9.509 \times 10^{-5} T_s^2 - 0.124 T_s + 61.76 \left[ \frac{W}{m \cdot K} \right] \quad (2.11)$$

The thermophysical properties, bed dimensions, and flow parameters used in the experiments and model are listed in Table 5. The Biot number characterizing the ratio of internal conduction to convection at the surface was checked and it was less than 0.1 in all cases.

Table 5. The thermophysical properties and conditions utilized in the modeling efforts.

Parameter	Value	Unit
Flow rate	0.0020, 0.0034, 0.0048, 0.0061	m <sup>3</sup> /s
Inlet Temperature	150	°C
Recovery inlet temperature	21.5	°C
Initial bed temperature	21.5	°C
Bead size	6	mm
Porosity	0.375	-
Packed bed length	1	m
Packed bed Diameter	12.47 (4.909)	cm (inch)
Insulation thermal conductivity	0.025	W/m K
Insulation specific heat	1050.0	J/kg.K
Insulation density	300.0	kg/m <sup>3</sup>
Steel thermal conductivity	20.0	W/m K
Steel spesific heat	485.0	J/kg.K
Steel density	7850.0	kg/m <sup>3</sup>

#### 2.2.4 Exergy Analysis

Exergy, or the work potential of energy, is the maximum work that can be extracted from a system and its surrounding at a different temperature before they reach



thermal equilibrium [54]. Maximum exergy is achieved when the process is completely reversible. In packed bed TES analysis, higher thermal exergy efficiency can be collected when the system has a sharp temperature profile, or two stratified layers without mixing between them [19]. The governing equations to calculate the exergy are adopted from [20]:

$$\Xi = \int_{t_p} \left[ \left\{ \dot{m} \int_{T_0}^{T_{hot}} C_p(T) dT \right\} - \left\{ \dot{m} T_0 \int_{T_0}^{T_{hot}} \frac{C_p(T)}{T} dT \right\} \right] dt \quad (2.12)$$

where  $\dot{m}$  is the mass flowrate,  $C_p$  is the specific heat capacity of the system,  $T_{hot}$  is the system temperature, and  $T_0$  is the ambient temperature. The thermal exergy efficiency is the ratio of net useful work in the recovery process to the net useful work in the storage process. The resulting fractional exergy efficiency for a charge-discharge cycle is:

$$\eta = \frac{\Xi_{recovery}}{\Xi_{storage}} = \frac{\int_{t_p} \left[ \left\{ \dot{m} C_p (T_r - T_0) \right\} - \left\{ \dot{m} T_0 C_p \ln \left( \frac{T_r}{T_0} \right) \right\} \right] dt}{\int_{t_p} \left[ \left\{ \dot{m} C_p (T_{hot} - T_0) \right\} - \left\{ \dot{m} T_0 C_p \ln \left( \frac{T_{hot}}{T_0} \right) \right\} \right] dt} \quad (2.13)$$

The change of specific heat capacity is negligible in the temperature range of this system. Also, the mass flow rate of the supplied heat transfer fluid remains constant during the storage and recovery times, which simplifies this expression to:

$$\eta = \frac{\Xi_{recovery}}{\Xi_{storage}} = \frac{\int_{t_p} \left[ \left\{ (T_r - T_0) \right\} - \left\{ T_0 \ln \left( \frac{T_r}{T_0} \right) \right\} \right] dt}{\left[ \left\{ (T_{hot} - T_0) \right\} - \left\{ T_0 \ln \left( \frac{T_{hot}}{T_0} \right) \right\} \right] t_p} \quad (2.14)$$

where  $T_r$  is the recovery temperature at the outlet, which is changing with time during the recovery period. There is no need to integrate for the storage period since the storage temperature ( $T_{hot}$ ) remains constant throughout the storage period. As mentioned, heat

losses have a significant impact on the exergetic efficiency. To address this effect for multiple cycles, the wall Stanton number was calculated for the four flow rates using Eqn. 2.15, where  $U_{loss}$  is the overall volumetric heat transfer coefficient for losses from the bed to the environment [20].

$$St_w = \frac{U_{loss}H}{\rho_s c_{p,s} u_0} \quad (2.15)$$

### 2.3 Experimental Results and Discussion

The experimental results focus on full charge/discharge processes for different flow rates, partial discharge cycles, and hold duration. In each case, the thermal exergy is presented.

#### 2.3.1 Model Results and Experimental Repeatability

Figure 10 shows the model and experimental results for 0.0048m<sup>3</sup>/s averaged from three separate trials during the charging portion. For each experimental trial,  $T_{hot}$  is set to 150°C. Each trial results in a unique temperature ramp at  $x = 0$ , which is used as an inlet boundary condition in the CFD model [21]. Shown here are the averages from these three model results and the three experimental trials. The experimental test results agree reasonably well with the model. The error bars confirm excellent repeatability of the experimental data. The modeling results help confirm the commissioned experimental vessel performs as designed, specifically that no issues such as internal bypass of flow occur (such as around or through the insulation and not into the packed bed [20]). In addition, the model results are used to show trends in how the axial thermal dispersion grows with the number of partial cycles.

The model results for the axial temperature are presented at one radial position in the packed bed at the centerline. However, other packed beds in the literature show temperature gradients in the radial direction during charging and discharging processes [34-36, 43]. For instance, their results show that approximately 30–40% of the radial distance can be affected, leading to a temperature gradient that drops from the centerline to a lower temperature near the wall [35, 36, 43]. Thus, the energy stored and recovered is reduced. In those systems, the insulation was located external of the containment vessel. Similar results are also noted in modeling work focusing on a packed bed of alumina with supercritical CO<sub>2</sub> as the working fluid, where using the centerline temperature alone would overestimate the exergetic efficiency and thus a radially-averaged temperature was needed in exergy calculations[55]. Cascetta et al. [34] note that using internal insulation between the bed and the wall may reduce the wall effect and improve the thermal efficiency of the packed bed. In the present study, internal insulation between the bed and the steel wall is used to minimize radial temperature distributions. Further, modeling results of the current system show a negligible temperature gradient in the radial direction, thus the axial temperature at one radial position is considered acceptable in this work.

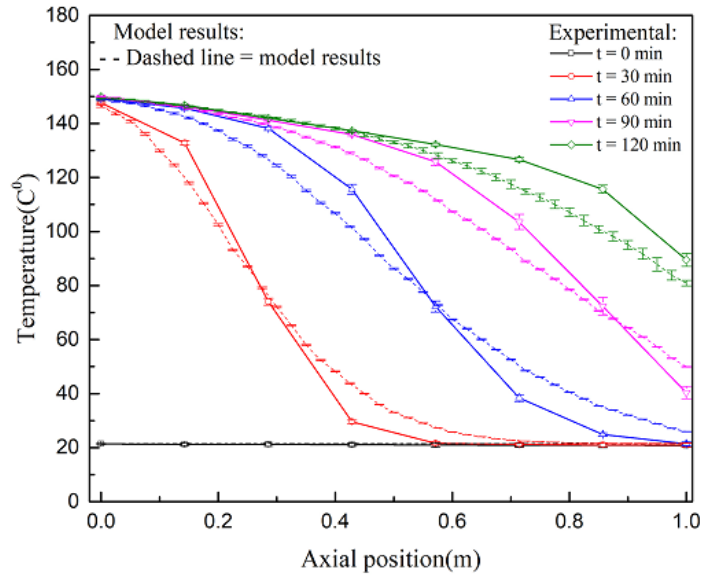


Figure 10. Experimental temperature profiles during charging for one full charge cycle (solid line) compared to Star-CCM+ model results (dashed line) at  $0.0048 \text{ m}^3/\text{s}$ .

### 2.3.2 Full Charge and Discharge

Full charge and discharge processes were considered at  $0.0020$ ,  $0.0034$ ,  $0.0048$ ,  $0.0061 \text{ m}^3/\text{s}$ . The time for charging and discharging cycles was calculated based on the propagation velocity of the heat exchange zone and the height of the bed[29]. The charging and discharging processes were performed in opposite directions of the packed bed. Figure 11 shows the experimental temperature profiles during charge along the axial (flow) direction at each flow rate.

Initially, the bed was at ambient temperature as seen in the first time interval of the charging process ( $t = 0 \text{ min}$ ). The energy stored in the bed then increases with time as the heated air flows through the packed bed and charging progresses. The temperature gradient along the length of the packed bed can be seen clearly in all four graphs. The temperature front spreads through the bed due to thermal dispersion effects and the heat

losses to the environment. The heat losses increase with time, and at the end of charging the inlet of the vessel has more stored energy (higher temperature) than the exit of the vessel due to these losses. The amount of energy stored in the bed increases with flow rate, which is an indication that the heat losses to the environment are less compared to the amount of energy stored in the packed bed as the flow rate increases. As will be shown, this leads to an increase in the exergetic efficiency with flow rate.

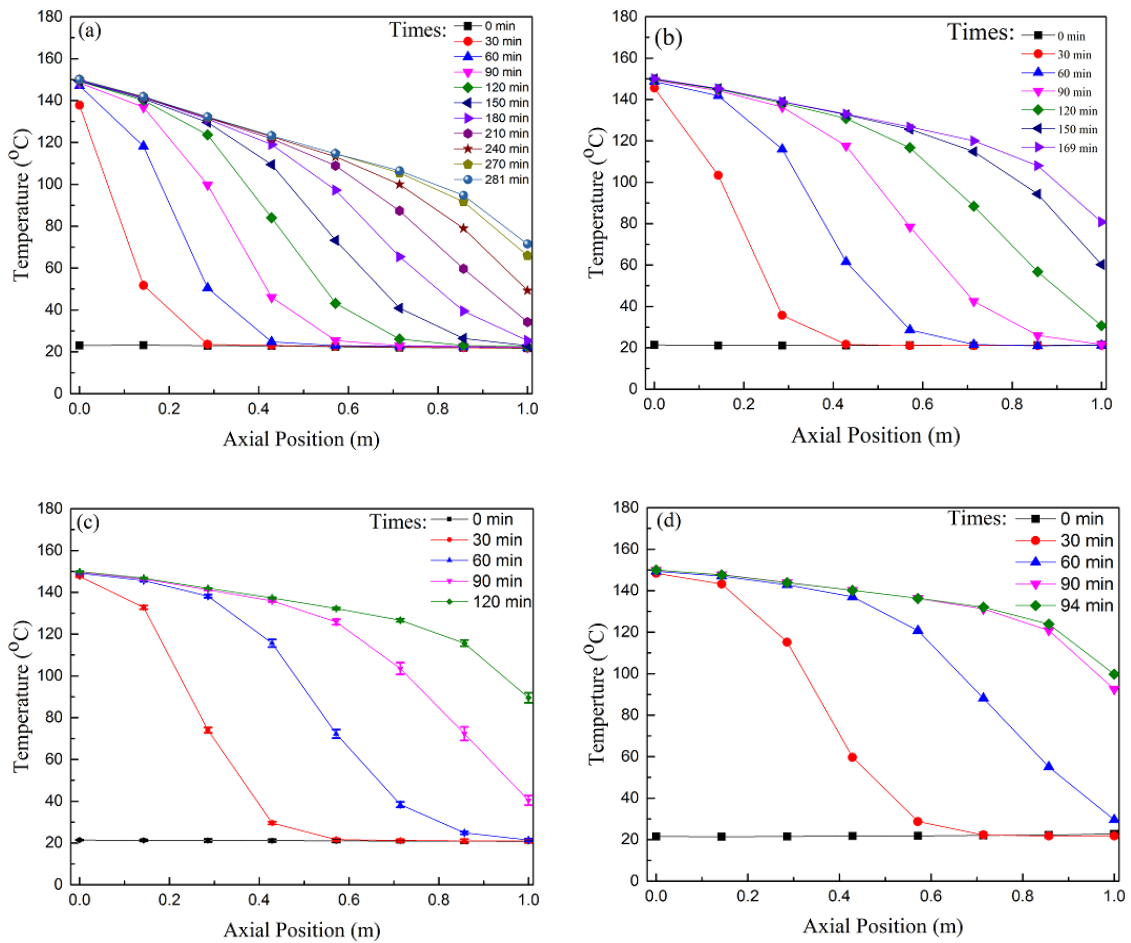


Figure 11. Temperature profiles for full charge with, (a)  $0.0020 \text{ m}^3/\text{s}$ , (b)  $0.0034 \text{ m}^3/\text{s}$ , (c)  $0.0048 \text{ m}^3/\text{s}$  and (d)  $0.0061 \text{ m}^3/\text{s}$ . The error bars at  $0.0048 \text{ m}^3/\text{s}$  are based on averaging the data from three trials.

Figure 12(a–d) show the temperature profiles during the discharge half cycle. During charging, all the presented time intervals are 30 min except the last time interval since the total time of charging is determined by Eqn. 2.2 (and may not be evenly divisible by 30 min). To compare the amount of energy in the bed at equivalent charge or discharge times, the time intervals for the discharge graphs were chosen to match the equivalent time intervals of the charge graphs. For example, the 11 min time interval in Figure 12a matches the 270 min time interval in Figure 12a. Then, the presented results return to 30min time intervals. The 0 min intervals in the discharge plots match the last time intervals in the charge plots.

For each cycle, the time required to reverse the flow for discharge is approximately two minutes and some heat is lost. However, the bed is at the high temperature as can be seen in the initial discharge time for each flow rate. The exit temperature during the recovery process, at the  $x = 0$  location, starts decreasing directly. As the steeper thermocline part of the thermal front reaches the exit, the temperature profile at this position drops more rapidly. The discharge time for each flowrate was different; however, in each case the bed was nearly depleted of thermal energy before reaching the full discharge time.

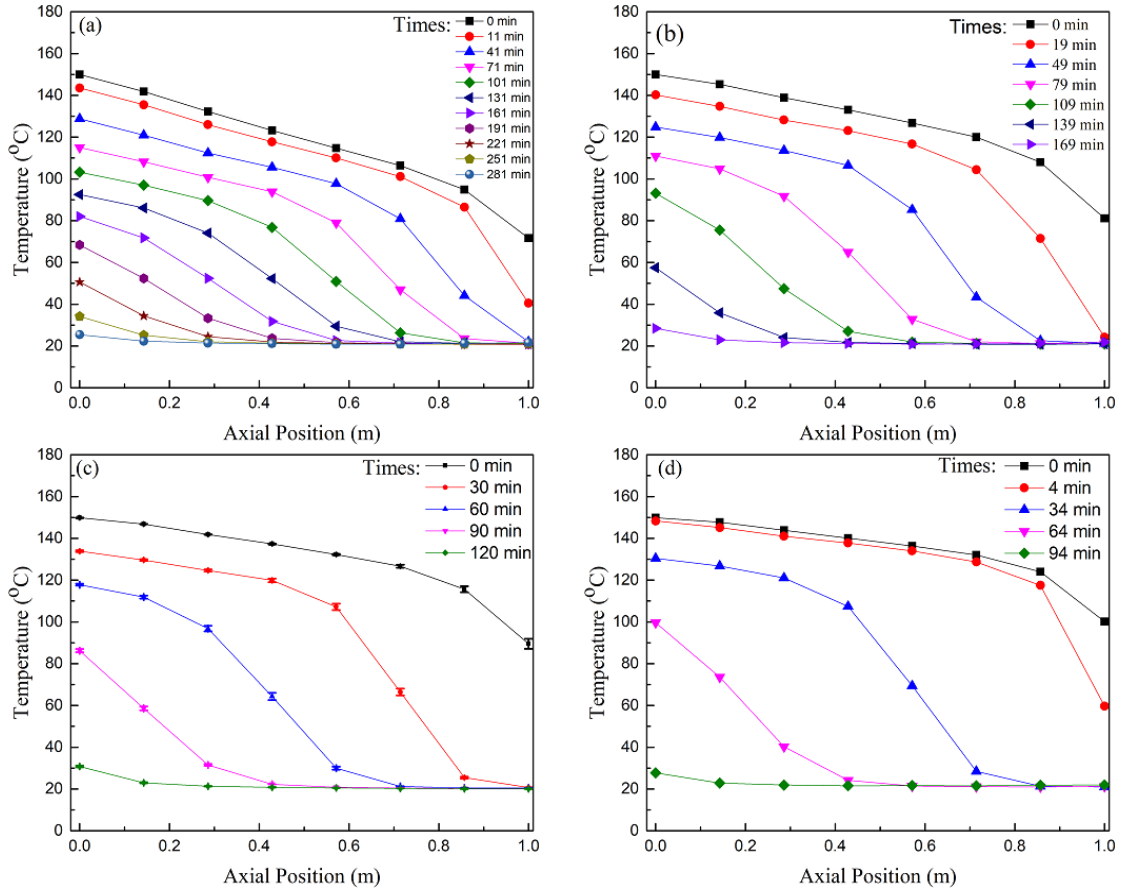


Figure 12. Temperature profiles for full discharge with (a)  $0.0020 \text{ m}^3/\text{s}$ , (b)  $0.0034 \text{ m}^3/\text{s}$ , (c)  $0.0048 \text{ m}^3/\text{s}$  and (d)  $0.0061 \text{ m}^3/\text{s}$ . The error bars at  $0.0048 \text{ m}^3/\text{s}$  are based on averaging the data from three trials.

Based on these experiments, Table 6 shows the thermal exergy efficiency for full charge and discharge processes for each flow rate. The exergy efficiency is calculated three times for  $0.0048 \text{ m}^3/\text{s}$  and the value in the table is the average value with standard deviation. Along with that, the accuracy of the thermocouple is  $\pm 2.2^\circ\text{C}$  as specified by the manufacturer, which results in a possible difference in exergy efficiency of  $\pm 4.2\%$  for three trials at  $0.0048 \text{ m}^3/\text{s}$ . For the full charge-discharge cycle, the exergy efficiency increases with flow rate, from  $35.7\%$  at  $0.0020 \text{ m}^3/\text{s}$  to  $55.4\%$  at  $0.0061 \text{ m}^3/\text{s}$ . These results are consistent with the temperature profiles in Figure 11, where higher heat losses

were noted at lower flow rates. With less available energy to recover due to those losses, the exergetic efficiency is lower at the lower flow rates.

Table 6. Percentage exergy with inlet temperature ( $T_f = 150\text{ }^\circ\text{C}$ ) and reference temperature ( $T_o = 21.5\text{ }^\circ\text{C}$ ).

Volumetric flow rate ( $\text{m}^3/\text{s}$ )	Percentage Exergy
0.0020	35.7
0.0034	46.8
0.0048	$53.2 \pm 0.4$
0.0061	55.4

### 2.3.3 Partial Charge-Discharge Cycles

Partial charge-discharge cycles were completed based on the times and four flow rates presented in Table 2. For  $0.0048\text{ m}^3/\text{s}$ , Figure 13a–c shows the axial temperature profiles for Cycles 2–4, respectively, while Figure 13d shows the axial temperature profiles of Cycles 5–8 together. The bed is fully charged during the first cycle. Then, a partial discharge for one hour left the bed at approximately  $115^\circ\text{C}$  at  $x = 0$  as shown in Figure 13a at the 0 min time interval. When starting a new cycle, the heater takes around 150 s to heat the air back up to the inlet temperature of  $150^\circ\text{C}$ . This results in the temperature of supplied air being less than the actual initial temperature in the bed ( $115^\circ\text{C}$ ) over that initial time interval. This leads to the temperature dropping at the inlet of the bed from  $115$  to  $101^\circ\text{C}$ . Then, it starts to increase to the inlet temperature as the heater and peripheral piping reheats and time progresses. This is the reason for the temperature behavior in the early times of charging for the second cycle. This behavior occurs in the rest of the cycles with less effect because as the cycles progress, the initial temperature at  $x = 0$  in the bed is decreasing, which can be seen in the rest of charging



plots (Figure 13, the 0min time intervals). Thus, in later cycles the temperature drop at the inlet of the bed is lower since the temperature of the supplied air approaches the initial bed temperature.

The stored energy decreases as the number of cycles increases until it reaches the steady state, after Cycle 5 under these conditions. Moreover, the thermal front profiles decrease in temperature as the number of cycles increases because of decreased length of bed heated to high temperature. This can be seen in the storage plots of each cycle. For example, in Cycle 2 at time interval 45min and  $x = 0.4$ , the temperature was  $\sim 113^{\circ}\text{C}$ , which dropped to  $\sim 103, 98$ , and  $95^{\circ}\text{C}$  in Cycles 3–5, respectively, and then to  $93^{\circ}\text{C}$  in Cycles 6–8. This can be seen for the rest of time intervals too. Therefore, the area under the storage temperature profile decreases with the number of cycles until the steady state case is reached. This indicates that the energy available for recovery during discharging is decreasing, leading to a reduction in thermal exergy recovered as will be shown.

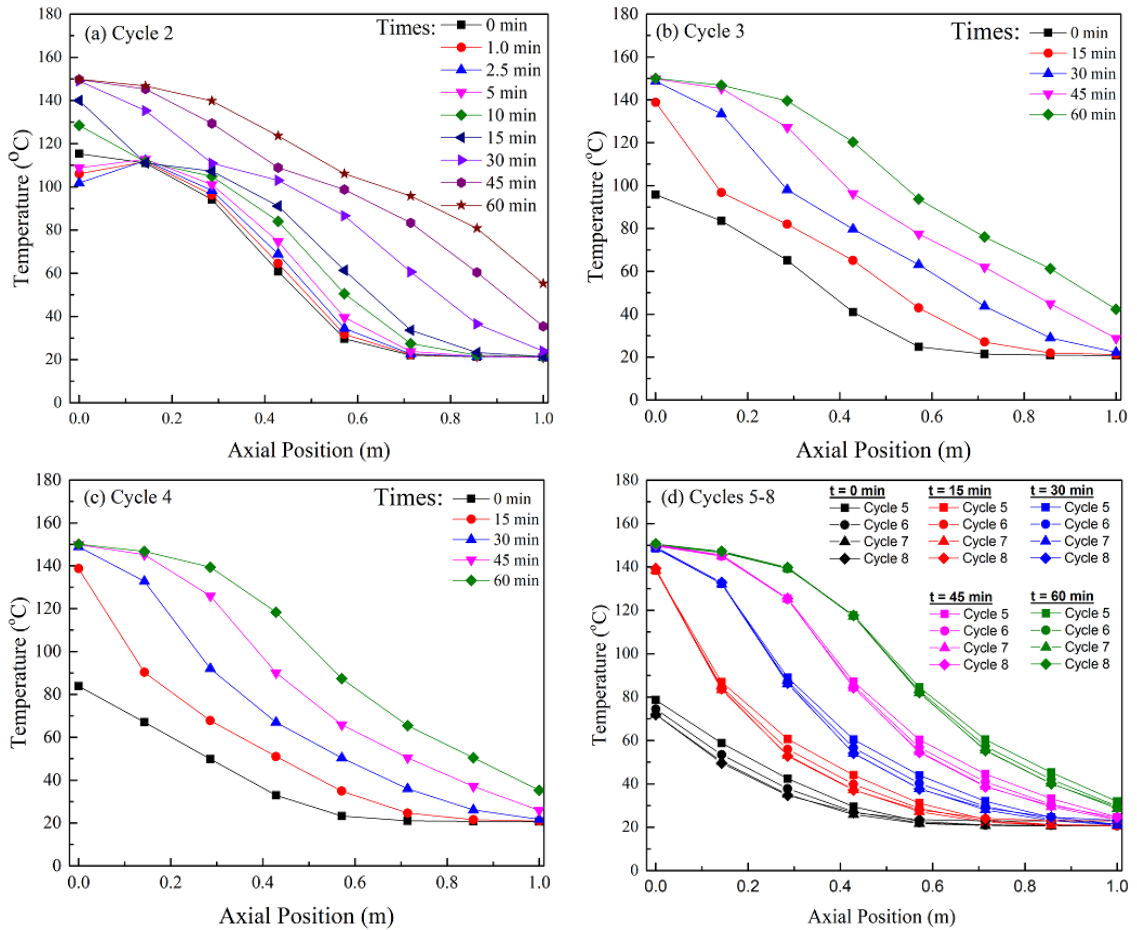


Figure 13. Axial temperature profiles for Cycles 2-8 during charging process with one hour charge and one hour discharge at  $0.0048 \text{ m}^3/\text{s}$ .

Figure 14 shows the temperature profiles versus the axial position for Cycles 2–8 during discharging for one hour at  $0.0048 \text{ m}^3/\text{s}$ . The total amount of remaining energy stored in the bed at the end of discharge also decreases as the number of cycles increases until it reaches steady state, as can be seen in each time interval.

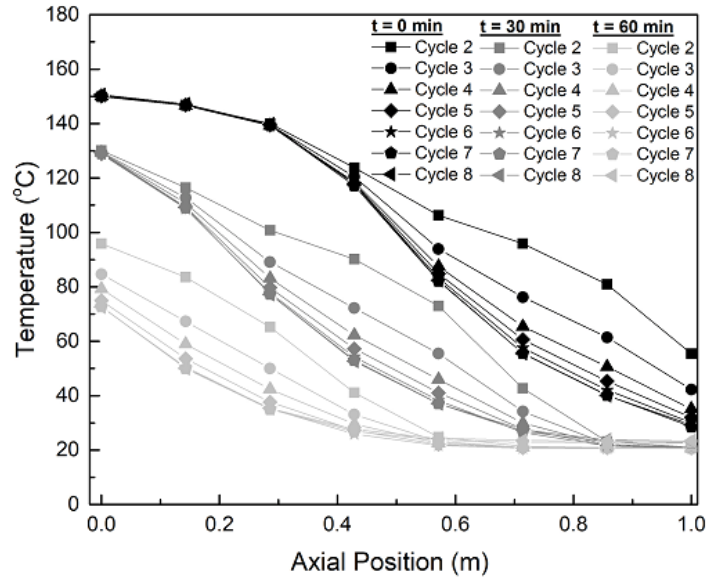


Figure 14. Axial temperature profiles for discharging cycles 2-8 at 0, 30 and 60 minutes at  $0.0048 \text{ m}^3/\text{s}$ .

The recovery temperature,  $T_r$ , decreases with time and number of cycles, which is shown in Figure 15 for multiple repeated cycles at  $x = 0$  for all flow rates. The exergetic efficiency decreases with the number of cycles until the system reaches steady state. The system reached steady state after Cycle 5 for  $0.0048$  and  $0.0061 \text{ m}^3/\text{s}$ , after Cycle 4 for  $0.0034 \text{ m}^3/\text{s}$  and after Cycle 3 for  $0.0020 \text{ m}^3/\text{s}$ .

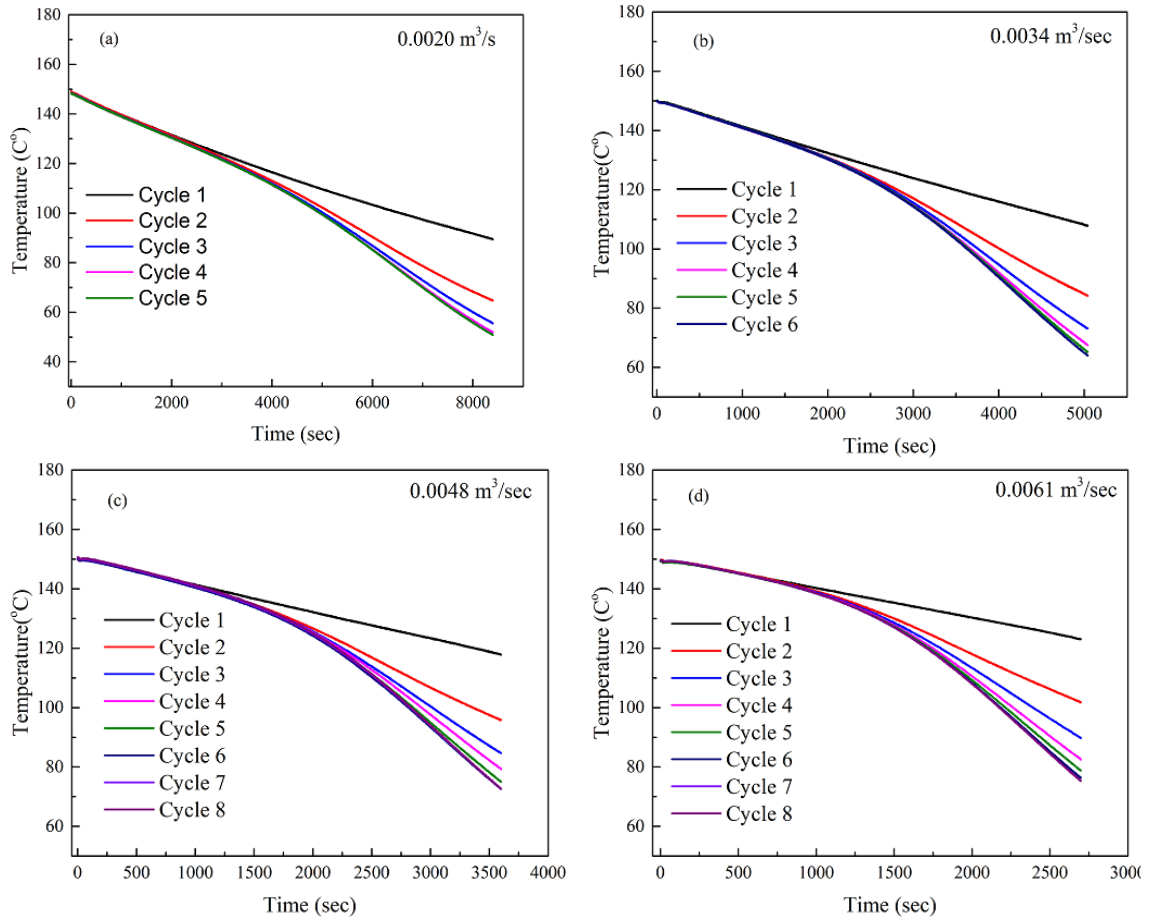


Figure 15. The recovered temperature,  $T_r$ , at the discharge outlet for multiple repeated cycles at four flow rates (a-d).

Figure 16a shows the exergy efficiency for several repeated cycles at four flow rates and the corresponding Stanton wall number. As can be seen, the exergetic efficiency decreases with the number of cycles until the system reaches steady state. The recovery and storage temperatures,  $T_r$  and  $T_{hot}$ , were used to determine the exergy efficiency of the bed, as shown in Eq. 2.14. The denominator in Eq. 2.14 depends on the storage temperature, which is constant ( $T_{hot} = 150^\circ\text{C}$ ). The numerator is the integration of the area under the recovery temperature lines in Figure 15a–d, which decreases with cycles and time. Therefore, the recoverable energy decreases, which is the reason for the decreasing exergy efficiencies with cycling at each flow rate. For 0.0048 m<sup>3</sup>/s, the exergy

efficiency decays from an initial value of approximately 79% to a steady state value of approximately 66%. As explained earlier, the heat losses to the environment are higher for lower flow rates, leading to the lowest exergy efficiency at 0.0020 m<sup>3</sup>/s. To capture this effect, the wall Stanton number ( $S_{tw}$ ) is included for each condition in Figure 16.  $S_{tw}$  is a dimensionless number that captures the effect of the heat loss and was calculated for the four flow rates with the maximum inlet temperature,  $T_{hot} = 150^{\circ}\text{C}$ , using the dimensions and properties of the experimental TES system. As shown here, a higher  $S_{tw}$ , which increases with decreasing flow rate, leads to a lower exergy efficiency.

The combined effects of axial thermal dispersion and heat losses from the system cause the exergetic reduction. As the exergetic efficiency varies between cycles, the effects from the heat losses and thermal dispersion can change, and this behavior should be considered by practitioners. To estimate the relative contributions of both effects, the model was run under the same cycling criteria as the experiments but in both adiabatic and non-adiabatic (baseline model) configurations. As agreement with the model shown above is reasonable, these efforts provide a qualitative explanation for the changing contributions of each loss mechanism. In running the adiabatic case, only exergetic losses from thermal dispersion are present. As expected based on  $S_{tw}$ , lower flow rates have higher exergy losses due to heat losses to the ambient. In all cases, the heat losses were a larger effect on the exergetic reduction than the dispersion. However, the magnitude of these heat losses at a given flow rate does not vary greatly with cycles. This result means the decrease in exergetic efficiency during cycles is caused by an increase in losses from thermal dispersion. Figure 16b shows how this effect varies with cycles at each flow rate.

A ratio is used to highlight how the dispersive contribution in each cycle grows relative to the contribution in the first cycle. The increase in thermal dispersion effect is greater for higher flow rates. Further, the percentage contribution of the dispersion to the overall reduction in exergetic efficiency increases with flow rate.

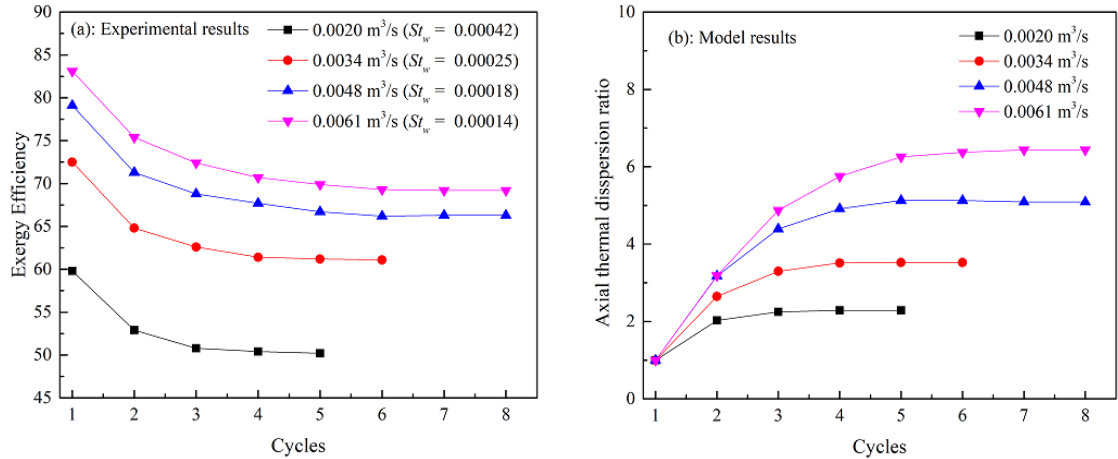


Figure 16. a) The exergy efficiency for multiple cycles at four flow rates. The Stanton wall number changes with flow rate and increases with decreasing flow rate. b) Increasing effect of thermal dispersion over all cycles, presented as a ratio of the dispersive effect at each cycle to the dispersive effect in Cycle 1.

### 2.3.4 Hold Time Between Charge-Discharge Cycles

The analysis of thermal exergy as a function of heat losses is an important step to make the storage process effective and to get the benefit of the supplied heat energy.

Three hold durations were considered to see the effect of heat losses on the temperature profiles and thermal exergy efficiency (0 min, 30 min and 120 min). These holds were considered between a full charge-discharge processes at 0.0048 m<sup>3</sup>/s. Figure 17a–c shows the axial temperature profiles during recovery (discharge) for each condition. The bed starts to lose energy with time due to heat losses to the environment. Figure 17d shows the recovery temperature,  $T_r$ , at  $x = 0$  m for the three holds. The recovery

temperature decreases with time and duration of holds. There is a linear increase in the recovery temperature in the first  $\sim 7$  and 14 min during the 30 and 120 min holds respectively. This is due to the position of the first sensing point in the bed at  $x = 0$  where the stainless-steel distributor plate is placed. During holding for 30 and 120 min, the bed loses heat through the insulation by radial conduction, conduction through the steel screen and flange insulation, and by convection through the stagnant air on the other side of the distributor. Therefore, the temperature drops from 150 to 121°C for the 30 min hold and from 150 to 87.5°C for the 120 min hold. When the discharge process starts, the temperature at the inlet (first sensing point) starts increasing linearly due to the recovered heat. Then, it starts decreasing in a steeper linear way as the sharper thermocline front reaches the exit of the bed. The recovery temperature decreases in a linear fashion only for the first  $\sim 75$  min. Table 7 shows the exergy efficiency for the three holds. All the temperature profiles drop due to the radial heat losses discussed. This causes the exergy efficiency decay from 53.2% to 31.0%. Heat losses to the environment can be mitigated by decreasing the surface to volume ratio, which would occur in the large-diameter vessels used in application. However, the capital cost of designing larger diameter vessels is high, particularly in cases of a pressurized vessel, and this consideration must be balanced against the thermal performance. While this paper addresses exergetic efficiencies for a laboratory sized apparatus, the trend in exergy change via cycles and hold time are useful design considerations in larger systems.

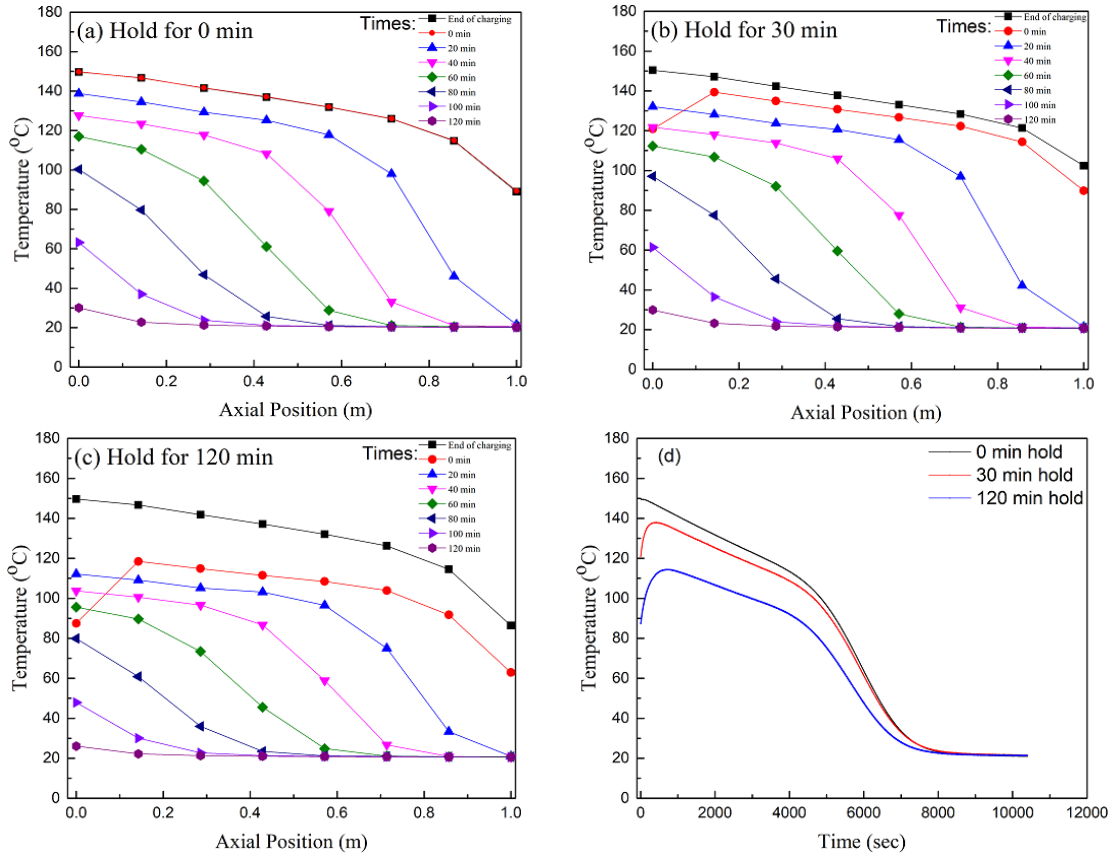


Figure 17. Temperature profiles during discharge times after holding. (a) Hold for 0 min, (b) hold for 30 min and (c) Hold for 120 min d) recovery temperature for three holds. Note: The 0 min time interval in each plot is the starting of discharge process after hold.

Table 7. Exergy calculation for hold times of 0, 30 and 120 minutes. All flows at were  $0.0048 \text{ m}^3/\text{s}$ .

Hold Time (min)	% Exergy
0	53.2
30	47.1
120	31.0

## 2.4 Conclusions

The thermal behavior of a packed bed thermal energy storage system was studied experimentally with a focus on full charge-discharge behavior, partial charge-discharge cycles, and length of storage time. Air was used as the HTF at an inlet temperature of



150°C and 6mm $\alpha$ -alumina beads were used as the packing material. A previously validated CFD model and multiple trials showed good accuracy and repeatability of the experimental results. The exergetic efficiency was calculated from experimental data for full charge-discharge times, several partial charging-discharging cycles, and holding at three different time intervals (no hold, short hold and long hold). Four flow rates were tested (0.0020, 0.0034, 0.0048 and 0.0061 m<sup>3</sup>/s), and the charging/discharging periods were considered based on the propagation velocity in the heat transfer zone. The results show an increase in the exergy with flow rate, from 35.7% to 55.4%. With partial charge/discharge times based on half of the charging time at four flow rates, the exergy decreased for multiple repeated cycles until the system reaches a steady state case. During these multiple cycles, the exergetic efficiency of the packed bed reached steady state after three, four, and five cycles for 0.0020, 0.0034, 0.0048 and 0.0061 m<sup>3</sup>/s. The model was used to estimate the relative contributions of heat losses and thermal dispersion to the reduction in exergetic efficiency. Heat losses remain similar during these partial cycles, but the thermal dispersion increases until the steady state is reached. The dispersive component was higher for higher flow rates, while the heat losses were larger for lower flow rates. With flows at 0.0048 m<sup>3</sup>/s, holds of 30 and 120 min reduced the exergetic efficiency from 53.2% to 47.1% and 31.0%, respectively. Heat losses and axial thermal dispersion have a significant effect on exergy efficiency and the thermal front profile of the packed bed. To get higher exergetic efficiency, thermal dispersion and heat losses to the ambient must be reduced in both full and partial charge-discharge cycles.

### Acknowledgments

This research did not receive any specific grant from funding agencies in the public, commercial, or not-for-profit sectors. The authors thank Montana State University for financial support. Mr. Al-Azawii thanks the Higher Committee for Educational Development in Iraq (HCED) for supporting his scholarship through the Iraqi government funding.

### References

1. Cumpston, J. and A. Mitsos, *Concentrating Solar Thermal Overview*. Chemical Engineering Progress, 2017. **113**(7): p. 21-28,42.
2. Öhman, H. and P. Lundqvist, *Comparison and analysis of performance using Low Temperature Power Cycles*. Applied Thermal Engineering, 2013. **52**(1): p. 160-169.
3. Jenkins, S., *Low-cost solar collectors provide renewable process heat*. Chemical Engineering: Essentials for the CPI Professional, 2017, June: p. 8-9.
4. Li, P., *Energy storage is the core of renewable technologies*. IEEE Nanotechnology Magazine, 2008. **2**(4): p. 13-18.
5. Hasnain, S.M., *Review on sustainable thermal energy storage technologies, Part I: heat storage materials and techniques*. Energy Conversion and Management, 1998. **39**(11): p. 1127-1138.

6. Fernandez, A.I., et al., *Selection of materials with potential in sensible thermal energy storage*. Solar Energy Materials and Solar Cells, 2010. **94**(10): p. 1723-1729.
7. Khare, S., et al., *Selection of materials for high temperature latent heat energy storage*. Solar Energy Materials and Solar Cells, 2012. **107**(C): p. 20-27.
8. Sharma, A., et al., *Review on thermal energy storage with phase change materials and applications*. Renewable and Sustainable Energy Reviews, 2009. **13**(2): p. 318-345.
9. Farid, M.M., et al., *A review on phase change energy storage: materials and applications*. Energy Conversion and Management, 2004. **45**(9): p. 1597-1615.
10. Alva, G., et al., *Thermal energy storage materials and systems for solar energy applications*. Renewable and Sustainable Energy Reviews, 2017. **68**: p. 693-706.
11. Okello, D., et al., *An experimental investigation on the combined use of phase change material and rock particles for high temperature ( $\sim 350$  °C) heat storage*. Energy Conversion and Management, 2014. **79**: p. 1-8.
12. Zanganeh, G., et al., *Stabilization of the outflow temperature of a packed-bed thermal energy storage by combining rocks with phase change materials*. Applied Thermal Engineering, 2014. **70**(1): p. 316-320.
13. Zanganeh, G., et al., *Experimental and numerical investigation of combined sensible–latent heat for thermal energy storage at 575 °C and above*. Solar Energy, 2015. **114**: p. 77-90.

14. Bruch, A., et al., *Experimental and Numerical Investigation of Stability of Packed Bed Thermal Energy Storage for CSP Power Plant*. 2014. p. 743-751.
15. Meier, A., C. Winkler, and D. Willemin, *Experiment for modeling high-temperature rock bed storage*. *Solar Energy Materials*, 1991. **24**(1-4): p. 255-264.
16. Mawire, A., et al., *Simulated performance of storage materials for pebble bed thermal energy storage (TES) systems*. *Applied Energy*, 2009. **86**(7): p. 1246-1252.
17. Bruch, A., J.F. Fourmigue, and R. Couturier, *Experimental and numerical investigation of a pilot-scale thermal oil packed bed thermal storage system for CSP power plant*. *Solar Energy*, 2014. **105**: p. 116-125.
18. Peng, H., H. Dong, and X. Ling, *Thermal investigation of PCM-based high temperature thermal energy storage in packed bed*. *Energy Conversion and Management*, 2014. **81**: p. 420-427.
19. Bindra, H., et al., *Thermal analysis and exergy evaluation of packed bed thermal storage systems*. *Applied Thermal Engineering*, 2013. **52**(2): p. 255-263.
20. Anderson, R., et al., *Experimental results and modeling of energy storage and recovery in a packed bed of alumina particles*. *Applied Energy*, 2014. **119**: p. 521-529.
21. Anderson, R., et al., *Packed bed thermal energy storage: A simplified experimentally validated model*. *Journal of Energy Storage*, 2015. **4**: p. 14-23.
22. Oró, E., et al., *Stratification analysis in packed bed thermal energy storage systems*. *Applied Energy*, 2013. **109**(SI): p. 476-487.

23. Liu, C., Cheng, M. S., Zhao, B. C., & Dai, Z. M., *Thermal performance analysis of a thermocline thermal energy storage system with FLiNaK molten salt*, in *Earth and Environmental Science* 2017 January IOP Publishing. p. 012039.
24. Warkhade, G.S., et al., *Experimental investigation of sensible thermal energy storage in small sized, different shaped concrete material packed bed*. World Journal of Engineering, 2016. **13**(5): p. 386-393.
25. Yin, H., et al., *Thermocline characteristics of molten-salt thermal energy storage in porous packed-bed tank*. Applied Thermal Engineering, 2017. **110**: p. 855-863.
26. Hoffmann, J.F., et al., *Experimental and numerical investigation of a thermocline thermal energy storage tank*. Applied Thermal Engineering, 2017. **114**: p. 896-904.
27. Ortega-Fernández, I., et al. *Parametric analysis of a packed bed thermal energy storage system*. in *AIP Conference Proceedings*. 2017. AIP Publishing.
28. Ismail, K.A.R. and R. Stuginsky Jr, *A parametric study on possible fixed bed models for pcm and sensible heat storage*. Applied Thermal Engineering, 1999. **19**(7): p. 757-788.
29. Yang, Z. and S.V. Garimella, *Cyclic operation of molten-salt thermal energy storage in thermoclines for solar power plants*. Applied Energy, 2013. **103**: p. 256-265.
30. Aly, S. and A. El-Sharkawy, *Effect of storage medium on thermal properties of packed beds*. Heat Recovery Systems & CHP, 1990. **10 no.5/6**(1990): p. 509-517.

31. Erregueragui, Z., et al., *Packed-bed thermal energy storage analysis: quartzite and palm-oil performance*. Energy Procedia, 2016. **99**: p. 370-379.
32. Cascetta, M., et al., *Numerical investigation of a packed bed thermal energy storage system with different heat transfer fluids*. Energy Procedia, 2014. **45**: p. 598-607.
33. Singh, H., R.P. Saini, and J.S. Saini, *Performance of a packed bed solar energy storage system having large sized elements with low void fraction*. Solar Energy, 2013. **87**(1): p. 22-34.
34. Cascetta, M., et al., *A comparison between CFD simulation and experimental investigation of a packed-bed thermal energy storage system*. Applied Thermal Engineering, 2016. **98**: p. 1263-1272.
35. Cascetta, M., et al., *Experimental and Numerical Research Activity on a Packed Bed TES System*. Energies, 2016. **9**(9): p. 758.
36. Cascetta, M., et al., *A Study of a Packed-bed Thermal Energy Storage Device: Test Rig, Experimental and Numerical Results*. Energy Procedia, 2015. **81**: p. 987-994.
37. Singh, H., R.P. Saini, and J.S. Saini, *A review on packed bed solar energy storage systems*. Renewable and Sustainable Energy Reviews, 2010. **14**(3): p. 1059-1069.
38. Yang, Z. and S.V. Garimella, *Molten-salt thermal energy storage in thermoclines under different environmental boundary conditions*. Applied Energy, 2010. **87**(11): p. 3322-3329.

39. Yang, Z. and S.V. Garimella, *Thermal analysis of solar thermal energy storage in a molten-salt thermocline*. Solar Energy, 2010. **84**(6): p. 974-985.
40. Hänchen, M., S. Brückner, and A. Steinfeld, *High-temperature thermal storage using a packed bed of rocks – Heat transfer analysis and experimental validation*. Applied Thermal Engineering, 2011. **31**(10): p. 1798-1806.
41. Bruch, A., et al., *Experimental investigation of cycling behaviour of pilot-scale thermal oil packed-bed thermal storage system*. Renewable Energy, 2017. **103**: p. 277-285.
42. Zavattoni, S., et al., *High temperature rock-bed TES system suitable for industrial-scale CSP plant–CFD analysis under charge/discharge cyclic conditions*. Energy Procedia, 2014. **46**: p. 124-133.
43. Cascetta, M., et al. *Experimental investigation of a packed bed thermal energy storage system*. in *Journal of Physics: Conference Series*. 2015. IOP Publishing.
44. Heller, P., et al., *Test and evaluation of a solar powered gas turbine system*. Solar Energy, 2006. **80**(10): p. 1225-1230.
45. Prenzel, M., et al., *Thermo-fluid dynamic model for horizontal packed bed thermal energy storages*. Energy Procedia, 2017. **135**: p. 51-61.
46. Scheidegger, A.E., *The physics of flow through porous media*. 1957, Toronto: Toronto University of Toronto Press.
47. Zhang, W., et al., *Relationship between packing structure and porosity in fixed beds of equilateral cylindrical particles*. Chemical Engineering Science, 2006. **61**(24): p. 8060-8074.

48. Nield, D.A. and A. Bejan, *Convection in porous media*. Vol. 3. 2013: New York: Springer.
49. Vortmeyer, D. and R.J. Schaefer, *Equivalence of one- and two-phase models for heat transfer processes in packed beds: one dimensional theory*. Chemical Engineering Science, 1974. **29**(2): p. 485-491.
50. Bejan, A. and A.D. Kraus, *Heat transfer handbook*. 2003, Hoboken, N.J.: Hoboken, N.J. : John Wiley & Sons, INC.
51. Hilsenrath, J., *Tables of thermal properties of gases: comprising tables of thermodynamic and transport properties of air, argon, carbon dioxide, carbon monoxide, hydrogen, nitrogen, oxygen, and steam*. 1955, Washington, D.C.: US Dept. of Commerce, National Bureau of Standards.
52. Morrell, R., *Handbook of properties of technical and engineering ceramics*. 1987: Part 2. Hmso.
53. Munro, M., *Evaluated Material Properties for a Sintered alpha-Alumina*. Journal of the American Ceramic Society, 1997. **80**(8): p. 1919-1928.
54. Bejan, A., *Thermal design and optimization*, ed. M.J. Moran and G. Tsatsaronis. 1996, New York: New York : John Wiley & Sons.
55. Johnson, E., et al., *Thermal energy storage with supercritical carbon dioxide in a packed bed: Modeling charge-discharge cycles*. The Journal of Supercritical Fluids, 2018. **137**: p. 57-65.



CHAPTER THREE

EXPERIMENTAL STUDY OF LAYERED THERMAL ENERGY STORAGE IN AN  
AIR-ALUMINA PACKED BED USING AXIAL PIPE INJECTIONS

Contribution of Authors and Co-Authors

Manuscript in Chapter 3

Author: Mohammad M. S. Al-Azawii

Contributions: Designed and installed the injected pipes, conceived and designed the experiments, collected the experimental data, performed the numerical model, performed the analyses, explained results, generated figures, and wrote the manuscript in preparation for editing and submission.

Co-Author: Carter Theade

Contributions: Collected preliminary data and edited the final manuscript for submission.

Co-Author: Pablo Bueno

Contributions: Conceived the study and edited the final manuscript for submission.

Co-Author: Ryan Anderson

Contributions: Conceived the study, designed experiments, assisted in the preparation of the manuscript, provided important insight and details of the entire study and manuscript, discussed results and implications, and edited the earlier manuscript and final versions of the manuscript for submission.

Manuscript Information page

Mohammad M.S. Al-Azawii, Carter Theade, Pablo Bueno, Ryan Anderson

Applied Energy

Status of Manuscript:

Prepared for submission to a peer-reviewed journal

Officially submitted to a peer-reviewed journal

Accepted by a peer-reviewed journal

Published in a peer-reviewed journal

Elsevier

Vol 249, pages 409-422, September 2019

<https://doi.org/10.1016/j.apenergy.2019.04.111>

EXPERIMENTAL STUDY OF LAYERED THERMAL ENERGY STORAGE IN AN  
AIR-ALUMINA PACKED BED USING AXIAL PIPE INJECTIONS

Abstract

This paper presents the experimental results of thermal behavior in an air-alumina packed bed storage system using a new technique for charging/discharging processes. A normal packed bed system, 100 cm in length, is divided into layers via pipes inserted internally along the axial length of the bed. Alumina beads were used as solid storage material and air was used as the heat transfer fluid (HTF) with an inlet temperature of 150 °C. This study analyzes the thermal behavior for full charge/discharge processes by dividing the bed domain into layers, focusing on the thermal exergetic efficiency for different charging/discharging schemes. One, two, and three layer configurations are considered along with various schemes including duration and magnitude of mass flow to each layer. In the most efficient configuration, the thermal exergetic efficiency increases with the number of layers from 53.2% to 69.6% for 0.0048 m<sup>3</sup>/s and 55.4% to 73.4% for 0.0061 m<sup>3</sup>/s, from one layer to two layers. At these same flow rates, thermal exergetic efficiencies increase to 76.8% and 80.3% for three layers. To determine the contributions of axial thermal dispersion and heat losses, a numerical model was run for a full charge/discharge cycle in adiabatic and non-adiabatic cases. The model results show that the dispersive effect is reduced by 23.2% in the best two-layer case and 25.6% in the best three-layer case for 0.0048 m<sup>3</sup>/s and by 22.8% in the best two-layer case and 26.5% in the best three-layer case for 0.0061 m<sup>3</sup>/s, resulting in these gains in exergetic efficiency.

Nomenclature

$t$	time (s)
$\varepsilon$	porosity (-)
$C_p$	specific heat capacity ( $\text{J kg}^{-1} \text{K}^{-1}$ )
$\rho$	density ( $\text{kg m}^{-3}$ )
$T$	temperature (K)
$V$	velocity ( $\text{m s}^{-1}$ )
$k$	thermal conductivity ( $\text{W/m K}$ )
$Q_{loss}$	energy losses to surrounding (J)
$\dot{m}$	mass flow rate ( $\text{kg s}^{-1}$ )
$\Xi$	exergy (W)
$\eta$	exergetic efficiency

Subscripts

$f$	fluid
$s$	solid
$h$	hot
$eq$	equivalent
$i$	solid domains (steel and insulation)
$0$	initial
$r$	recovery
$D$	dispersion
$H$	Heat
$T$	total
$ef - \textit{adiabatic}$	efficiency for adiabatic case
$ef - \textit{non}$ $- \textit{adiabatic}$	efficiency for non-adiabatic case

3.1 Introduction

Energy storage technologies integrate with renewable energy sources such as solar energy to offset variability and increase overall efficiency. Thermal energy storage (TES) systems are a promising solution to improve the continuity of processes that utilize solar energy such as electricity generation in concentrated solar power plants (CSP), domestic hot water and space heating, and process heat in industrial applications [1].

Further, TES technologies integrate with renewable energy sources such as solar energy to offset variability and increase overall efficiency. TES systems store and recover energy to match demand as needed, such as at peak times. In CSP power plants, TES systems are an important component in increasing the effectiveness of the whole power cycle.

Conventional concentrated solar power plants use two-tank storage systems. In these systems, one tank is used for hot fluid and the second tank is used for cold fluid [2-4], where the fluid is typically a molten salt. Two-tank storage systems are expensive, and a single-tank storage system could reduce the cost [5, 6]. For instance, using a single molten salt thermocline tank in a parabolic trough plant is about 66% of the cost of a two-tank molten salt system [6]. The present work shows an advance in single-tank performance, where an internal piping system segments the storage tank into shorter layers, resulting in substantial increases in exergetic efficiency during a charge/discharge cycle.

Amongst different structures considered for single-tank TES (e.g. channel-embedded structure, parallel-plate structure, rod-bundle structure and packed-bed structure), packed beds have shown higher performance [7]. A packed bed with two separated hot and cold zones is called a thermocline [8]. The thermocline's performance is based on several variables in the packed bed system, including the heat transfer fluid, flow rate, storage material type and size, and if the storage type is based on sensible heat media [9], latent heat [10], or a combination of latent and sensible media within the same bed [11, 12]. Heat transfer fluids have been studied experimentally and numerically. Molten salt has been considered in packed bed arrangements [13], where a numerical

investigation was carried out to study the effect of different charge/discharge cut-off temperatures on the packed bed thermal performance with three packed bed configurations for a 100 MWe CSP tower plant. In addition to molten salts, other liquid, supercritical, and gaseous fluids have been studied including: oil/pebble-bed [14], palm oil below 300 °C [15], thermal oil in a dual media thermocline [16], supercritical carbon dioxide [17], air [18, 19], and argon [20]. There are advantages and disadvantages related to each heat transfer fluid such as cost, high temperature limitation, freezing temperature, availability, toxicity, corrosiveness, flammability, volumetric heat capacity, and thermal conductivity. Air is considered as a suitable candidate and has been studied in several packed bed systems such as [21, 22] focusing on modeling efforts, heat losses, dispersion losses, thermal behavior for multiple cycles, and exergetic efficiency. High temperature air/rock thermal storage showed an increase in the first-law efficiency with multiple repeated cycles [23]. The flow rate determines how fast the bed can be charged/discharged and influences the heat transfer between the fluid and solid, the amount of energy stored/recovered in the bed, thermal dispersion (to be discussed), and heat losses to the environment. Four flow rates studied experimentally showed that exergetic efficiency increased with flow rate due to an increase in stored energy and a decrease in heat losses to the ambient [22]. Hoffmann et al. [24] studied the effects of five flow rates and two particle sizes on the size of the thermocline and the efficiency during storage/recovery processes. The study concluded that at low flow rate, heat losses are important and at high flow rate, thermal flux due to forced convection is important. An optimal mass flow rate with maximum discharge efficiency was found based on the

particle size numerically, showing that bigger particles lead to lower optimal mass flow rate. The influence of storage materials on the thermal performance of TES systems has been studied for several materials. The particles described in this work store energy via increases in the media temperature, sensible heat storage. Mawire et al. [25] studied fused silica glass, alumina, and stainless steel, where alumina showed the best exergy to energy ratio during the storage process. A summary of sensible and latent heat storage materials and thermal energy storage systems has been reported [26]. Particles should have high volumetric heat capacity to reduce the storage container size, which in return will reduce capital costs. Particles also influence porosity, where recovery effectiveness decreases consistently with increasing porosity [8]. Particles must also be chemically, mechanically, and thermally stable. For high efficiency, the particle size should be reduced to avoid intraparticle temperature gradients while not leading to a high pressure drop. Though more expensive than rock [27, 28],  $\alpha$ -alumina is stable over a wide range of temperatures and could thus be broadly applicable to a range of processes.

These factors (HTF, particle size and type, operating temperature, flow rate) influence thermal dispersion effects in the packed bed. For instance, axial thermal dispersion increases at large particle size [21]. In the ideal system, the temperature front propagating through the bed would proceed in the shape of a square wave, with the temperature only at  $T_{hot}$  or  $T_{cold}$ . However, dispersive effects induce temperature gradients along the flow direction of the bed, and this thermocline reduces TES efficiency. This effect has been considered during a full charge/discharge cycle [18] and for multiple repeated cycles [19, 29]. In [19], the impact of operating conditions (mass flow rate,

temperature and physical properties) on the thermal hysteresis was investigated experimentally. In [29], a numerical investigation on the thermal behavior of a storage vessel using air, oil and molten salt as HTF was presented, focusing on the thermal hysteresis phenomenon. These studies found that thermal dispersion reduces the energy stored/recovered and causes degradation in the packed-bed thermozone. Thermal dispersion effects can accumulate over multiple charge-discharge cycles, reducing the thermal exergetic efficiency with increasing cycles [22]. In our previous work [22], estimates for the relative contributions of heat loss and thermal dispersion to the reduction in exergetic efficiency with multiple partial cycles were reported. The results showed that the dispersion losses increased with flow rate and the number of cycles until the system reached the steady state case, resulting in a reduction of exergetic efficiency.

To improve the performance of the packed bed systems and achieve higher exergetic efficiency, the system losses, such as thermal dispersion losses, heat losses and pressure losses, must be reduced. As such, research has been done to study effective charging and discharging schemes within the packed beds. Esen et al. [30] studied the performance of the energy storage tank theoretically, focusing on two modes of contacting the storage media in the bed. In the first mode, the HTF flowed parallel to the phase change material (PCM), and in the second mode, pipes containing the HTF were embedded in a packed bed of PCMs internally. In that study, the performance of the second mode is better than the first mode in order to store more solar energy in a given time. Another approach to effective single-tank storage proposed numerically is layered thermal energy storage within a single-tank, which can improve the thermal performance



and efficiency. In 1995, Sanderson and Cunningham studied experimentally a vertical flow packed bed sensible storage system [31], where a storage tank of rectangular cross-section (412.75 mm square by 1219.2 mm tall) was used with five different packing arrangements. The study showed that a thermally short packing leads to better use of stored energy. The same study suggested further research must be done on longer storage packing. In addition, recent numerical studies introduced new methods to prevent or reduce the thermocline degradation, which is called thermocline control (TCC) methods [32, 33]. In two of these methods, the HTF is either extracted or injected through a port at the mid-length of the bed, which is considered as a segmented (i.e. layered) storage system. Segmentation of a packed bed was proposed and studied numerically as a solution to preserve the stratification in an air-rock packed bed [34]. The numerical results for charging processes showed that the stratification is maintained using three bed layers. Furthermore, McTigue and White [35] introduced a new segmented packed bed design in pumped thermal energy storage. The study focused on the thermodynamic behavior of the packed bed reservoir during the charging process in a pebble packed bed of magnetite ( $\text{Fe}_3\text{O}_4$ ) and argon gas by segmenting the thermal reservoir to several horizontal layers. The heat transfer fluid passes through the first active layer and, after full charge or discharge, the gas was diverted to the next layer. All layers were controlled with internal valves, and these numerical results showed that the segmentation could reduce conductive losses during the charging process and increase the energy storage and exergy content. White et al. [36] analyzed the behavior of packed bed thermal reservoirs with different segments using a numerical approach with simplified models of entropy

generation rates. The results showed that segmentation reduced the exergetic losses (heat losses, pressure and thermal dispersion) and thus increased the efficiency. A recent study by McTigue and White analyzed the thermal energy storage in a radial-flow packed bed compared to axial-flow packed bed [37]. It was found segmented packed beds have better performance due to the reduction in pressure losses, and it could be cheaper than radial-flow packed bed. For the segmented packed bed, the same configuration as in study [35] was used. In addition, the concept of dividing the packed bed into several layers is under development by Howes et al. [38, 39]. In [38], the vertical storage vessel was divided into several separately spaced layers along the bed length. An internal cylinder at the center of the vessel with a moving internal baffle system (valve) was used to pass and control the flow within the bed layers. In [39], a cylindrical pressure vessel with different layering schemes such as horizontal, hexagonal and partly tapered valved layers was proposed. All the layers were valved in order to control the flow entering and leaving each layer during charging and discharging periods. In both patents, the storage/recovery process assumes charging/ discharging the first specified layer, and then moving to the next layers after reaching the specified temperature.

Although layering techniques discussed here have been considered numerically [34-37], experimental lab scale results have not been investigated yet. This paper presents the first experiments that consider layers in the thermal energy storage field. Multiple layers in the axial direction show a significant increase in the exergetic efficiency due to reducing the length of one long bed layer into multiple small layers. In the present paper,  $\alpha$ -alumina is used as storage material and air as HTF. The approach divides the bed into

two and three distinct zones via an internal piping system. These results are compared to the traditional one zone approach. The two and three zones are in contact with each other (no space or insulation between layers or ports on the tank wall as used in [32-39] above). The layers are heated axially (with the flow direction) by inserting pipes along the length of the packed bed. To the best of the author's knowledge, no TES systems using this pipe injection technique have been considered in the literature. Several schemes are considered that vary the duration and magnitude of flow rate into each layer during charge and discharge processes. The experimental thermal exergetic efficiency was calculated for full charge/discharge at two flow rates (0.0048 and 0.0061 m<sup>3</sup>/s) for several charging/discharging schemes as will be explained in the next sections. The heat losses and thermal dispersion losses are coupled effects and it is impossible to separate them experimentally. Therefore, a previously validated CFD model is utilized to separate their effects via running the model for two cases (adiabatic and non-adiabatic), allowing for a quantitative estimate for the relative losses.

### 3.2 Experimental Methods, and Thermal Exergy Analysis

This section details the properties of the experimental storage vessel, flow loop setup, and experimental conditions. The model is also introduced in brief. Finally, the thermal exergy equations are presented for the charge-discharge cycles with a focus on the effects of layers.

3.2.1 Storage Vessel, Axial Pipe Injection, and Temperature Measurements

Figure 18 shows a schematic of the experimental setup with equipment specifications detailed in [22]. The dimensions of the horizontal bed are given in Table 8. Compressed air from the building is cleaned and dried with filters. In charging, the air flows into the heater and then into the packed bed to deposit heat into the storage materials at 150 °C. Air exiting the bed is cooled with a heat exchanger before being vented to the room. During discharge, gas at 21.5–22 °C enters the packed bed in the opposite direction of charging to recover the heat from the storage media. After the gas exits the storage vessel, it is cooled via the water cooled heat exchanger and vented to the room.

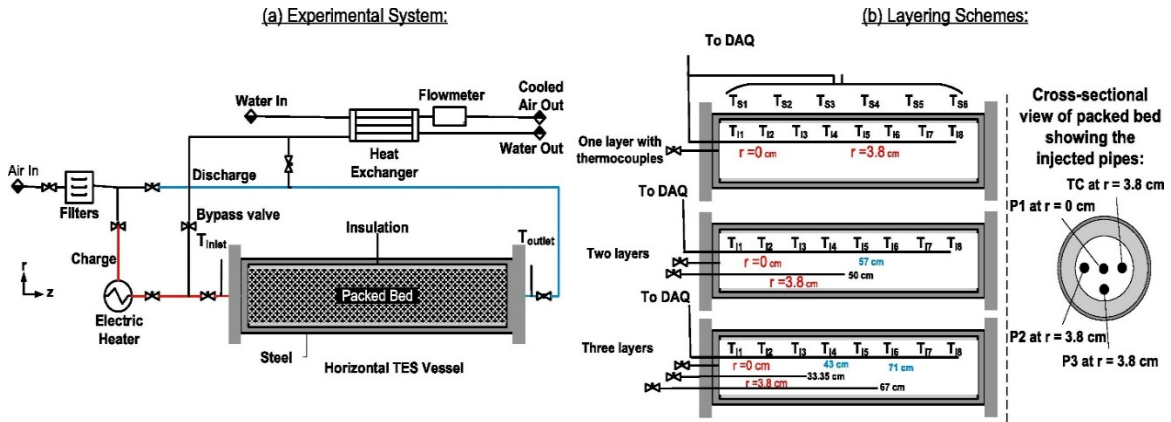


Figure 18. (a) Schematic of TES apparatus utilizing filters to purify air supply, electric heater to heat the HTF, TES vessel, DAQ collecting temperature data, and a cooler. The red line indicates the inlet of the charge process and the blue line indicates the inlet of the discharge process, and multiple valves are used to manipulate the flow during each process. (b) *Left*: The packed bed with one, two, and three layers highlighting the axial length and radial location of pipes and thermocouples (Black color highlights the axial length of the pipes, red color highlights the radial location of pipes/thermocouple, and blue color highlights the axial length of thermocouple measurements for each pipe. *Right*: Cross-sectional view of the packed bed highlighting the radial positions of the injected pipes (P1, P2 and P3) and internal thermocouple (TC). There are eight internal thermocouples (T<sub>I</sub>), six surface thermocouples (T<sub>S</sub>) and inlet and outlet thermocouples.

Table 8. Dimensions of the thermal energy storage unit including steel vessel, insulation and packed bed.

Parameter	$D_{\text{steel\_outer}}$	$D_{\text{steel\_inner}}$	Thickness <sub>Steel</sub>	Thickness <sub>Insulation</sub>	$D_{\text{Packed bed}}$	$L_{\text{vessel}}$	$L_{\text{Packed bed}}$
Value	16.8 cm	15.4 cm	0.7 cm	1.27 cm	12.47 cm	120 cm	100 cm

The packed bed system consists of an external carbon steel vessel,  $\alpha$  alumina packing material, and internal insulation between the particles and steel container. The vessel is a 6" NPS schedule 40 pipe with flat flanges (ANSI 150# RF w/Blind). Internal microtherm insulation was constructed as two rigid cylinders with 60 cm length each and then sealed to each other for insertion into the vessel. The insulation was covered with glass cloth and sealed to the steel vessel to avoid bypass flow. Custom flanges were utilized to insert a K-type thermocouple with eight sensing points down the axial length of the bed and to insert additional pipes for gas flow to divide the bed into layers. The center of the internal thermocouple is at  $r = 3.8$  cm and the sensing points are spaced at approximately 14.2 cm intervals. For the two layer experiments, the first sensing points for each layer are at  $x = 0$  cm (first layer) and at  $x = 57$  cm (second layer). For the three layer experiments, the first sensing points are  $x = 0$  cm,  $x = 43$  cm (second layer) and at  $x = 71$  cm (third layer). The commercially available thermocouple probe was chosen to maximize the spatial resolution of the temperature measurement, providing eight measurements per meter. The probe measures temperature at  $x = 0$  and  $x = 100$  cm with six additional points between. However, segmenting the bed for flow into two and three equally sized layers meant that a

thermocouple measurement was not identically co-located with the axial injection location. Experimental estimates show the injection temperature could be between 150 and 154 °C. However, this has a minimal effect on the exergy, as will be discussed. For the second and third pipes in the two and three layers, the inlet temperature is considered as 150 °C. The length of the entire packed bed is 100 cm. First, the bed is divided to two and three equal axial distances, i.e. the inlets of the axial injected pipes are at  $x = 0$ , and  $x = 50$  cm respectively. Then, for the three layers, the inlets of the three injected pipes are at  $x = 0$ ,  $x = 33.35$  and  $67$  cm respectively. These are shown schematically in Figure 18b. Several valves control the mass flow rate entering each layer, which is modified to ensure the inlet temperature to each layer is constant at 150 °C. Additional thermocouples measured temperature at the inlet, outlet, and surface of the vessel. The error associated with the thermocouples is  $\pm 2.2^\circ\text{C}$  as specified by Omega. Data was recorded with a National Instrument data acquisition controller (NI9213), and LabView software collected temperature data every second.

### 3.2.2 Experimental Conditions and Design

For this study, 17 schemes were tested based on time, which layers received flow during the charging and discharging processes, number of layers (two vs. three), and flow rates ( $0.0048 \text{ m}^3/\text{s}$  and  $0.0061 \text{ m}^3/\text{s}$ ). The accuracy of the flow reading are based on a percentage of the full scale reading, which correspond to  $\pm 0.28$  SLPM at 9 SCFM and  $\pm 0.16$  SLPM for 7 SCFM as specified by the manufacturer of the flow meters.

Appendix 3.A shows the charge and discharge schemes for two and three bed layers in detail. A complete cycle in this work is defined as full charging and discharging

processes. The times during charging and discharging processes are adopted from [40], which is shown in Table 9.

Table 9. Time for charging and discharging processes at two flowrates from the method in [40]

Conditions	Std. Vol. flow rate (m <sup>3</sup> /s)	Mass flow rate (kg/s)	Charge Time (s)	Discharge Time (s)
7 SCFM	0.0048	0.0040	7241 (2 hr and 0.5 min)	10,400 (2 hr and 53 min)
9 SCFM	0.0061	0.0051	5632 (1 hr and 34 min)	8087 (2 hr and 14.5 min)

This approach determines the charge and discharge period by using the density and heat capacity of the fluid at the inlet temperature of charging and discharging, the length of the packed bed, and the propagation velocity of the heat-exchange zone. The propagation velocity is determined by the heat capacity of the materials, porosity, and the fluid velocity evaluated at the inlet temperature during charge (150 °C) or discharge (21.5 °C). The calculated times define the time required to charge or discharge the bed with one, two, and three layers. This allows for a comparison of the thermal behavior of a packed bed with one, two and three layers. For example, the full charging time for 0.0048 m<sup>3</sup>/s is 120 min, which is divided by 2 to charge two layers (60 min for each layer) and by 3 to charge the bed with three layers (40 min for each layer). At the same flow rate based on the cooler inlet temperature, the expected time for full discharge is 173 min. In all cases, when various layers are opened, differing amount of flow or a different inlet temperature to each zone could occur. In all cases here, the external valve positions were set so the inlet temperature was at 150 °C as it is paramount to maintain  $T_{hot}$  at the highest temperature, as is shown in the exergy analysis. As will be shown in the definition of the

exergetic efficiency, the calculation is not affected by the individual mass flow rate to each zone and only the total mass flow rate is needed. Further, as will be detailed, small variations in the inlet temperature at each zone, utilized to ensure a fixed inlet temperature to each zone, do not affect the calculated exergy or numerical model results substantially. Thus, the ability to control a consistent temperature at the inlet of each zone was preferred to even flow distribution. Charging and discharging processes were performed in opposite directions of the packed bed. Therefore, in charging and discharging the layer number increases with the direction of flow.

### 3.2.3 Modeling Approach to Determine Thermal Dispersion Losses: Adiabatic vs. Non-Adiabatic

To determine how layers affect the exergetic efficiency in terms of heat losses vs. thermal dispersion, a previously validated CFD approach [22] was used to compare results for an adiabatic vs. non-adiabatic case. The model assumes local thermal equilibrium ( $T_f = T_s = T$ ) [41] and a homogenous porous medium [42]. The model solves for the transient temperature profile in the r-and z-direction of the packed bed, insulation, and steel domains. Equivalent properties are utilized that average the solid and fluid properties based on the porosity. Heat losses to the environment are included in Eqn. 3.1, and the temperature profiles in the insulation and steel are determined from Eqn. 3.4.

$$(\rho C_p)_{eq} \frac{\partial T}{\partial t} + (\rho C_p)_f V \cdot \nabla T = \nabla \cdot (k_{eq} \nabla T) + Q_{loss} \quad (3.1)$$

where:

$$(\rho C_p)_{eq} = \epsilon \rho_f C_{p,f} + (1 - \epsilon) \rho_s C_{p,s} \quad (3.2)$$

$$k_{eq} = \epsilon k_f + (1 - \epsilon) k_s \quad (3.3)$$



$Q_{loss}$  are the heat losses via conduction through the insulation and steel domains and natural convection from the surface to the ambient.

$$(\rho C_p)_i \frac{\partial T}{\partial t} = \nabla \cdot (k_i \nabla T) \quad (3.4)$$

The flow is laminar and 2-D axisymmetric modeling was used. The wall heat transfer coefficient is  $3.71 \text{ W/m}^2 \text{ K}$  based on typical wall temperatures and heat transfer correlations [43]. The temperature-dependent thermophysical properties used in the CFD-model are shown in our previous work [22]. The density for the fluid was determined from the ideal gas law. Temperature dependent properties are fit from data in [44] for air and from [45, 46] for alumina. The thermophysical properties used in the experiments and model are listed in Table 10. The bed porosity is set at 0.375. The charging and discharging inlet temperatures are the same as the experiments,  $150 \text{ }^\circ\text{C}$  and  $21.5 \text{ }^\circ\text{C}$ , respectively.

Table 10. The thermophysical properties of the TES apparatus utilized in the modeling efforts.

Material	Thermal conductivity (W/m K)	Specific Heat (J/kg K)	Density ( $\text{kg/m}^3$ )
Insulation	0.025	1050.0	300.0
Steel	20.0	485.0	7850.0
Alumina at $150 \text{ }^\circ\text{C}$	24.5	962	3978
Alumina at $25 \text{ }^\circ\text{C}$	32.6	772.9	3990
Air at $150 \text{ }^\circ\text{C}$	0.0353	1017	0.8345
Air at $25 \text{ }^\circ\text{C}$	0.0261	1006	1.1856

COMSOL Multiphysics is a commercial computational fluid dynamics (CFD) software that is used to solve the governing equations. Three regions are defined in the

model: porous, insulation and steel. The energy equation throughout the porous region is solved. For one layer a superficial velocity is used to solve the energy equation. This velocity is used to solve the energy equation in two and three bed layers via multiplying it by the percentage of flow expected in each layer. The mesh size used in the model was extremely fine (free Triangular) with maximum and minimum element sizes equal 0.01 and 2E-5 m. The temperature boundary conditions at the inlet of a layer are based on the time-dependent temperature responses noted in the experiments, as done in our previous work [22].

As discussed in the previous section, the flow was divided between layers to ensure that the inlet temperature was constant in each domain. Estimates were made experimentally, and multiple values of the flow splits were considered in the model to ensure minimal influence of this effect on the exergy calculations. Table 11 shows the flow splits between layers considered in the model at both flow rates for charging and discharging.

Table 11. The percentage of flow split used in the model.

Volumetric flow rate (m <sup>3</sup> /s)	Two layers, charging		Two layers, discharging		Three layers charging			Three layers discharging		
	L1	L2	L1	L2	L1	L2	L3	L1	L2	L3
0.0048			50	50						
	40	60	60	40	25	30	45	25	30	45
			40	60						
	25	75	–	–	–	–	–	–	–	–
	60	40	–	–	–	–	–	–	–	–
0.0061	40	60	50	50	25	30	45	25	30	45

### 3.2.4 Exergy Analysis

Exergy is defined as the maximum work that the system can deliver [47]. It represents a useful unit to quantify the effect of any governing parameter on the thermal performance in the packed bed system. The governing equations to determine the thermal exergy are adopted from [21], which is used to calculate the thermal exergy for a packed bed of one layer:

$$\Xi = \int_{t_p} [\dot{m} \int_{T_0}^{T_{hot}} C_p(T) dT - \dot{m} T_0 \int_{T_0}^{T_{hot}} \frac{C_p(T)}{T} dT] dt \quad (3.5)$$

where  $\dot{m}$  is the mass flowrate,  $C_p$  is the specific heat capacity of the fluid, which is considered constant in the temperature range used in the experiments,  $T_{hot}$  is the maximum system temperature, and  $T_0$  is the ambient temperature. The thermal exergetic efficiency is the ratio of exergy in the recovery process to the storage process:

$$\eta = \frac{\Xi_{recovery}}{\Xi_{storage}} = \frac{\int_{t_p} [\dot{m} C_p (T_r - T_0) - \dot{m} T_0 C_p \ln(\frac{T_r}{T_0})] dt}{\int_{t_p} [\dot{m} C_p (T_{hot} - T_0) - \dot{m} T_0 C_p \ln(\frac{T_{hot}}{T_0})] dt} \quad (3.6)$$

For two layers during the storage process, the total mass flow rate is divided between the two layers to  $\dot{m}_1$  and  $\dot{m}_2$ . The inlet temperature for each layer is 150°C, which represents the storage temperature ( $T_{hot}$ ) that remains constant during the charging process. For the recovery process, the mass flow rate is divided to  $\dot{m}_1$  and  $\dot{m}_2$  in some schemes. The mass flow rate during the recovery process used in Eqn. 3.6 remains constant (total mass flow rate) because the total energy recovered from the bed is collected at the outlet of the storage vessel, where the flow from the two layers is mixed again to determine the recovery temperature. The recovery temperature ( $T_r$ ) is measured at the outlet of the bed

during discharge ( $x = 0$ ) as an approximation of the temperature at the outlet of the storage vessel. The recovery temperature changes with time during the discharging time and an integration is achieved for the entire recovery period. There is no need to integrate for the charging period, as the inlet temperature is constant. Therefore, the resulting equation for two layers (case A1 and a1 as an example) will be:

$$\eta = \frac{\Xi_{recovery}}{\Xi_{storage}} = \frac{\dot{m} \int_{t_p} [(T_r - T_0) - T_0 \ln\left(\frac{T_r}{T_0}\right)] dt}{\dot{m} [(T_{hot} - T_0) - T_0 \ln\left(\frac{T_{hot}}{T_0}\right)] t_{p1} + \dot{m}_1 [(T_{hot} - T_0) - T_0 \ln\left(\frac{T_{hot}}{T_0}\right)] t_{p2} + \dot{m}_2 [(T_{hot} - T_0) - T_0 \ln\left(\frac{T_{hot}}{T_0}\right)] t_{p2}} \quad (3.7)$$

where:  $t_{p1} = t_{p2} = 3600$  s for flow rate equals  $0.0048$  m<sup>3</sup>/s.  $t_{p1}$  represents the charging time for layer 1 and  $t_{p2}$  represents the charging time for layer 2. In the numerator, the recovery temperature is the only variable that affects the recoverable exergy because the mass flow rate remains constant during the discharge period. Knowing that the storage temperature is  $T_{hot} = 150$  °C for the entire charging process, the above equation simplifies to:

$$\eta = \frac{\Xi_{recovery}}{\Xi_{storage}} = \frac{\dot{m} \int_{t_p} [(T_r - T_0) - T_0 \ln\left(\frac{T_r}{T_0}\right)] dt}{[(T_{hot} - T_0) - T_0 \ln\left(\frac{T_{hot}}{T_0}\right)] t_{p1} [\dot{m} + \dot{m}_1 + \dot{m}_2]} \quad (3.8)$$

Since  $\dot{m}_1 + \dot{m}_2 = \dot{m}$ ,  $\dot{m} + \dot{m}_1 + \dot{m}_2 = 2\dot{m}$ , which simplifies Eqn. 3.8 to:

$$\eta = \frac{\Xi_{recovery}}{\Xi_{storage}} = \frac{\dot{m} \int_{t_p} [(T_r - T_0) - T_0 \ln\left(\frac{T_r}{T_0}\right)] dt}{\dot{m} [(T_{hot} - T_0) - T_0 \ln\left(\frac{T_{hot}}{T_0}\right)] t_p} \quad (3.9)$$

where:  $t_p$  (*denominator*) =  $2t_{p1} = 7200$  for  $0.0048$  m<sup>3</sup>/s. Since the mass flow rate is the same in the charging and discharging processes, the final equation used to calculate the thermal exergy efficiency is:

$$\eta = \frac{\int_{t_p} [(T_r - T_0) - T_0 \ln(\frac{T_r}{T_0})] dt}{[(T_{hot} - T_0) - T_0 \ln(\frac{T_{hot}}{T_0})] t_p} \quad (3.10)$$

This approach applies to all charging and discharging schemes that have been tested with two and three bed layers. In addition, as mentioned earlier, the exergetic efficiency is calculated assuming the inlet temperature at the second pipe with two layers is in the range of 150–154 °C. This results in exergy values from 67.9 to 69.2%, which is higher than the normal one bed layer (53%). Therefore, the approximation of the inlet temperature as 150 °C is considered sufficient.

### 3.3 Results and Discussion

The experimental results focus on full charge/discharge processes for two flow rates with two and three bed layers. Several timing schemes are used to do the charging/discharging processes. In each scheme, the thermal exergetic efficiency is presented and compared to a base case (one bed layer). Example model results are included for a few charge and discharge cases to provide experimental validation for subsequent analysis of adiabatic vs. non-adiabatic cases. As noted, 17 schemes were considered in total. The exergetic efficiency results for all cases are noted in Appendix 3.A. However, in the detailed analysis provided in this section, only the most and least efficient cases for charging/discharging that effect the thermal behavior and thermal exergetic efficiency are considered. The remaining cases exhibit behavior bounded by this data. For the charging process, the least and most efficient charging schemes that have been proposed and tested are **Case A1** and **Case A3**, respectively. In **Case A3**, the first layer is charged for 1 hr and then the second valve (2<sup>nd</sup> pipe) is opened to charge the

2<sup>nd</sup> layer with the first valve remaining partially open to ensure the inlet temperature remained at 150 °C. This approach divides the total flow between the two layers but ensures the inlet temperature in both layers is 150 °C. An approximate calibration showed that pipe 1 has 40% of the flow and pipe 2 has 60% of the flow at 0.0048 m<sup>3</sup>/s. As will be detailed, this case is the most efficient when charging multiple layers because it reduces the heat losses in the first layer when charging the second or third layers, and reduces the thermal axial dispersion and pressure drop as the flow divides between the two layers. For discharging processes, the least efficient and most efficient discharging schemes that have been tested are **Case a1** and **Case a8**, respectively. In **Case a8**, the 1<sup>st</sup> and 2<sup>nd</sup> layer are discharged together for the entire discharging time. In this scheme, the two valves are fully opened, and an approximate calibration showed that the flow is evenly distributed in each pipe. Table 12 shows the scheme details and exergy results for the cases that the next section focuses on. For comparison, the full charge-discharge cycle exergetic efficiencies for one layer are 53.2% and 55.4% for 0.0048 m<sup>3</sup>/s and 0.0061 m<sup>3</sup>/s, respectively. The proposed three-layer experiments exhibit maximum exergetic efficiencies of 76.8% and 80.3% at those flow rates, a substantial improvement in exergetic efficiency. As mentioned, the error associated with the thermocouples is  $\pm 2.2$  °C, which can lead to a difference in the exergetic efficiency. Thus, the value of the exergy for 0.0061 m<sup>3</sup>/s at three layers is the average value from four trials with standard deviation. The following sections highlight the charge-discharge temperature profiles, recovery exit temperature, and consider adiabatic vs. non-adiabatic model results to explain the results shown in Table 12.

Table 12. Percentage exergy for the most efficient and least efficient cases with inlet temperature ( $T_f = 150^\circ\text{C}$ ) and ambient temperature ( $T_o = 21.5$ ).

Volumetric flow rate ( $\text{m}^3/\text{s}$ )	Layers	Charging cases	Discharging cases	Percentage exergy
0.0048	Two	A1: Two layers, charging L1 for 60 min and then L2 for 60 min after closing the 1st valve	a1: Two layers, discharging L1 for 60 min and then L2 for 153 min after closing the 1st valve	42.3
		A3: Two layers, charging L1 for 60 min and then L1 and 2 for 60 min	a8: Two layers, discharging L1 and 2 together for 173 min	69.6
	Three	B3: Three layers, charging L1 for 40 min and then L 1 and 2 for 40 min, then L 1, 2 and 3 for 40 min	b3: Three layers, discharging L1, 2 and 3 together for 173 min	76.8
0.0061	Two	C1: Two layers, charging L1 for 46.5 min and then L1 and 2 for 46.5 min	c5: Two layers, discharging L1 and 2 together for 134.5 min	73.4
	Three	D1: Three layers, charging L1 for 31.3 min and then L 1 and 2 for 31.3 min, then L 1, 2 and 3 for 31.3 min	d1: Three layers, discharging L1, 2 and 3 together for 134.5 min	$80.3 \pm 0.6$

### 3.3.1 Full Charge and Discharge: Effects of Flow Rate and Number of Layers

Two flow rates, 0.0048 and 0.0061  $\text{m}^3/\text{s}$ , were considered to investigate the effect of fluid flow conditions on the temperature front progression during full charging/discharging processes. The charging and discharging processes are performed in several timing schemes as shown in Appendix 3.A. Figure 19a shows the charging results

from previous work at the same flow rate where the entire bed is heated from the inlet (one layer). This result serves as a comparison for the two and three layer results. Figure 19b and c show the least efficient and most efficient cases of the experimental temperature profiles for two layers during the full charging process at flow rate  $0.0048 \text{ m}^3/\text{s}$ . Figure 19b shows the thermal behavior of the least efficient charging scheme, Case A1. This case is important as it highlights results related to energy losses to the environment. In Case A1, each layer is charged separately; the first layer is charged for one hour, then the 1<sup>st</sup> valve is closed and the 2<sup>nd</sup> valve is opened to start charging the second layer. In this case, the first layer starts to lose heat to the environment during the second layer charging time (60–120 mins). The bed temperature and stored energy of the first layer drops with time due to these heat losses, which can be seen in the last time intervals, 90 and 120 min. In this case, the first layer can be considered as in hold (no flow) from 60 to 120 minutes. This hold, particularly from the inlet to 0.5 m, causes the temperature to drop relatively evenly in that domain over time. The effect of the hold was explained in our previous study [22]. Therefore, the thermal exergetic efficiency decays because of these heat losses to the environment. The temperature increases at the mid-length of the bed as the second pipe is opened to charge the second layer with  $150 \text{ }^\circ\text{C}$  as inlet temperature, which can be seen in the time intervals 90 and 120 min.



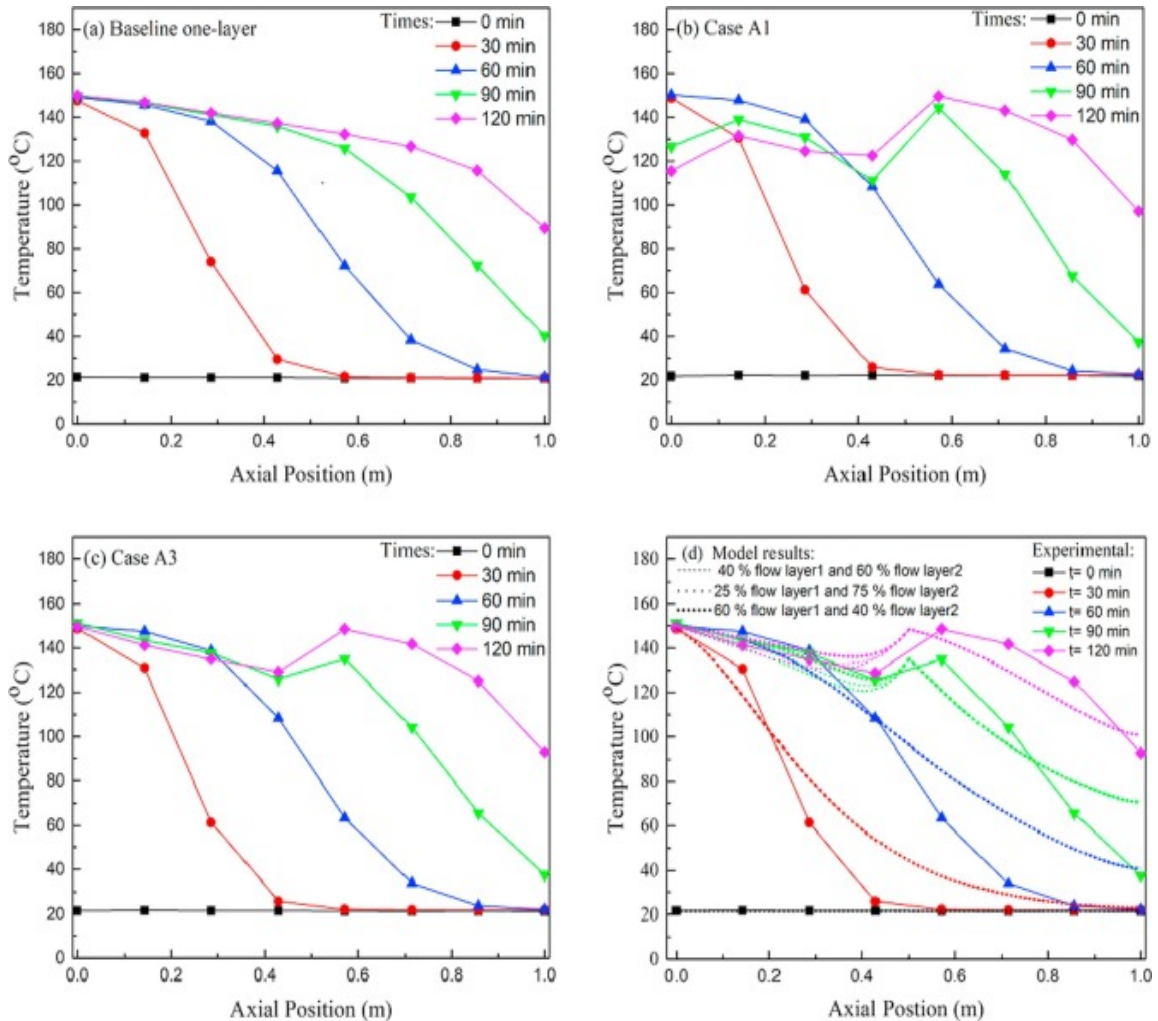


Figure 19. Temperature profiles for full charge with  $0.0048 \text{ m}^3/\text{s}$  and an inlet temperature of  $150 \text{ }^\circ\text{C}$ . (a) Charging for one layer [22], (b) Charging for two layers with least efficient case charging scheme Case A1, (c) Charging for two layers with most efficient case charging scheme Case A3, (d) Model and experimental charging results for the most efficient two layer case (Case A3), highlighting the effect of potential flow maldistribution with 40/60% (dashed lines), 25/75% (dotted lines) and 60/40% (short dotted lines) flow splits between the first and second layers.

Figure 19c shows the temperature profile during charging for the most efficient charging scheme, Case A3. The thermal front improved, which can be seen in the temperature lines at 90 and 120 min, where more of the bed is at a higher temperature compared to Figure 19a and b. When discharged, this results in a thermal exergy increase

from 53.2% to 69.6% for one layer in comparison to two layers. For the most efficient charging scheme with two layers, the effect of heat losses on thermal behavior is similar in the first layer to the same length in the one-layer case. The decrease in temperature along the axial length of the bed is due to heat losses to the ambient through the walls via conduction, which increases with time, bed length, and reduction in mass flow rate. In addition, the impact of thermal dispersion loss is still present and the temperature front spreads within the length of each layer although it has been reduced as will be discussed next. Therefore, there are two reasons contributing to the temperature profiles in the second half of the charging process (90 min and 120 min): The inlet temperature for each layer and the combined effect of heat losses to the environment and thermal dispersion losses within each layer due to the variable temperature along the axial length and different mass flow rate in each zone. The reduction in mass flow rate occurs due to opening the second valve to charge the second layer. In this case, the flow rate is divided between the two pipes and pipe 1 (feeding to Layer 1) had approximately 40% of the mass flow as an approximate calibration showed. The reduction in the mass flow rate leads to an increase in the heat loss to the environment [22]. However, the axial thermal dispersion decreases, which will be further explained later, and the amount of energy stored in the entire bed is increased. These are the reasons for the increase in the exergetic efficiency. Figure 19d explores this flow split numerically, and the experimental data validates the model for the two-layer case during charging. Shown are three flow splits used in the model. The flow split is 40% to layer 1 and 60% in layer 2 during the second half of the charge, which is considered the best estimate of the flow

split during the charging process. This flow split estimate is chosen based on charging temperature profile, discharging temperature profile, recovery temperature, and thermal exergy efficiency. These results show that the estimate for the flow split between layers is reasonable.

The recovery process depends on the temperature profile that results from the storage process. Figure 20a–d show the experimental temperature profiles during the discharge (recovery) process for one and two layers at  $0.0048 \text{ m}^3/\text{s}$ . This figure considers the most efficient and least efficient schemes from the charging results in Figure 19. The 0-minute time interval represents the end of the charging process from Figure 19 and thus the beginning of the discharging process. Figure 20a shows the baseline results for one layer from our previous work [22]. Figure 20b shows the temperature profiles for the least efficient recovery scheme, Case a1. The energy recovered in this scheme is less than the energy recovered from the one bed layer. In Case a1, the poor charging results and continued heat losses to the environment when the recovery is done via individual layers cause the thermal performance to decrease in recovery.

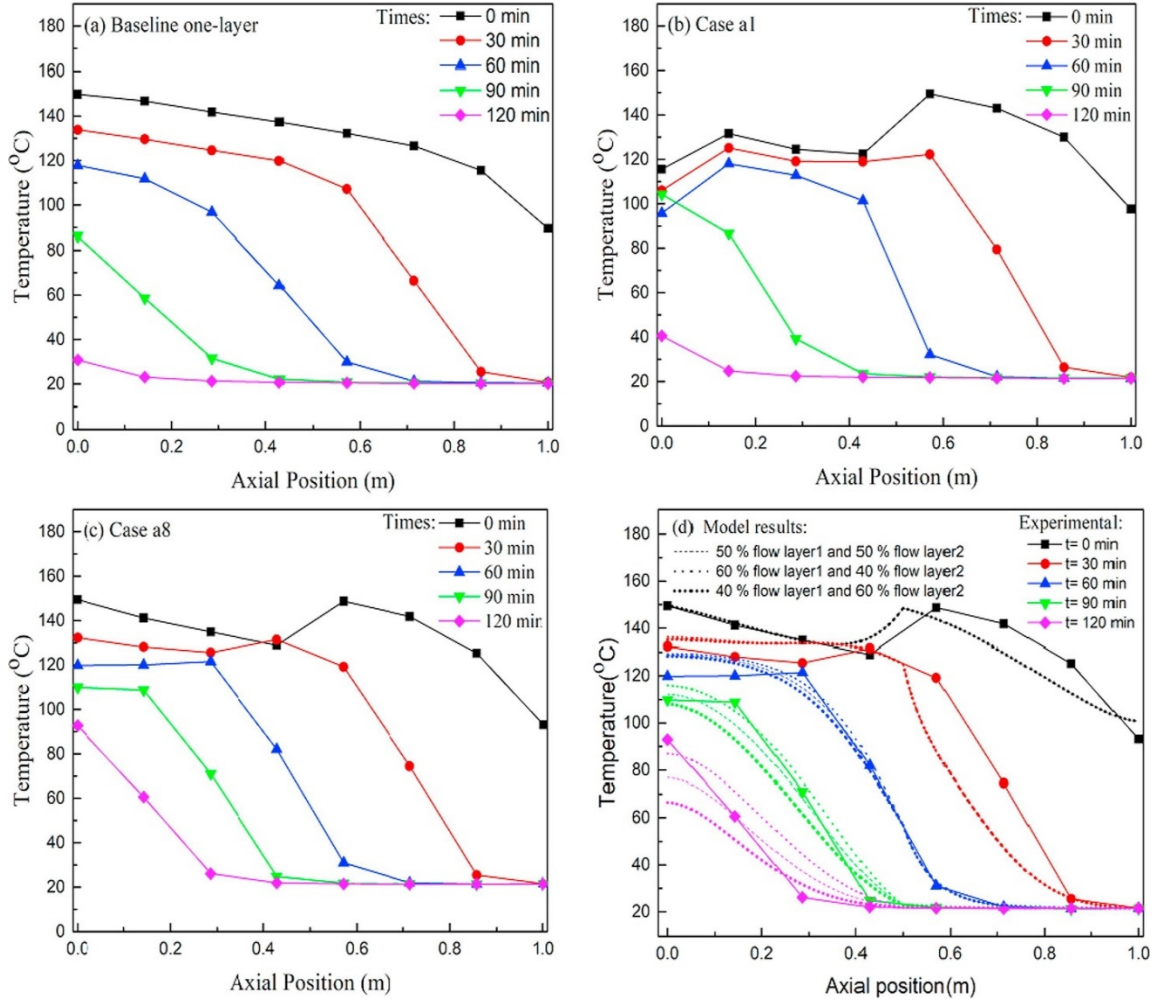


Figure 20. Temperature profiles for full discharge with  $0.0048 \text{ m}^3/\text{s}$  for one and two layers, (a) Discharging for one layer (baseline results) [22], (b) Discharging for two layers with least efficient discharging scheme Case a1, (c) Discharging for two layers with most efficient discharging scheme Case a8 where recovery is done in both layers simultaneously, and (d) Model and experimental discharging for the most efficient two layer Case a8, highlighting the effect of potential flow maldistribution with 50/50% (dashed lines), 60/40% (dotted lines) and 40/60% (short dotted lines) flow splits between the layers.

Figure 20c shows the recovery temperature for the most efficient discharging scheme, Case a8. The sharper temperature profiles are clear in each time interval. This is especially noted in 30, 60 and 90 min time intervals, where almost 20–50% of the bed length is at the same high temperature. This indicates that the dispersion effect is reduced by discharging in two layers simultaneously (Case a8) instead of one layer (baseline).

After 120 min of recovery, there is still more energy to recover from the bed in Case a8 and the bed's recovery outlet temperature is still at higher temperature (93 °C in Case a8 vs. 30 °C in the baseline). Therefore, the thermal performance is improved and the exergetic efficiency increases. Figure 20d shows the model result during the discharge process considering high, low, and even flow to recover the energy. The flow split 50% to the first recovery layer and 50% to the second recovery layer is the best flow configuration during this discharging process.

Figure 21a–d shows the temperature profiles for one and two layers with the most efficient charging/discharging schemes during full charging/discharging processes with  $0.0061 \text{ m}^3/\text{s}$ . As can be seen, the thermal front improves after the time interval 60 min, with the bed temperatures higher in Case C1 (Figure 21b) than in the baseline. However, heat and thermal dispersion losses still exist and lead to a temperature drop in the first layer as can be seen in the first 45% of the bed length in Figure 21b. Figure 21c and d show the experimental temperature profiles for one and two layers at  $0.0061 \text{ m}^3/\text{s}$  during discharging after the charge cycle in Figure 21a and b. These results only include the most efficient discharging case, which again is flow into both layers for the entire discharging period. The temperature profile improves with layers seen via the sharper thermal front, and the amount of energy recovered is increased compared to one bed layer. Thus, the thermal exergy efficiency increased from 55.4% to 73.4%. In addition, the amount of energy stored and recovered increases with flow rate, and thus the thermal exergy efficiency is increased (73.4% at  $0.0061 \text{ m}^3/\text{s}$  vs. 69.6% at  $0.0048 \text{ m}^3/\text{s}$  with two

layers). In addition, Figure 21b and d show the model results, which again show reasonable agreement with the experimental data.

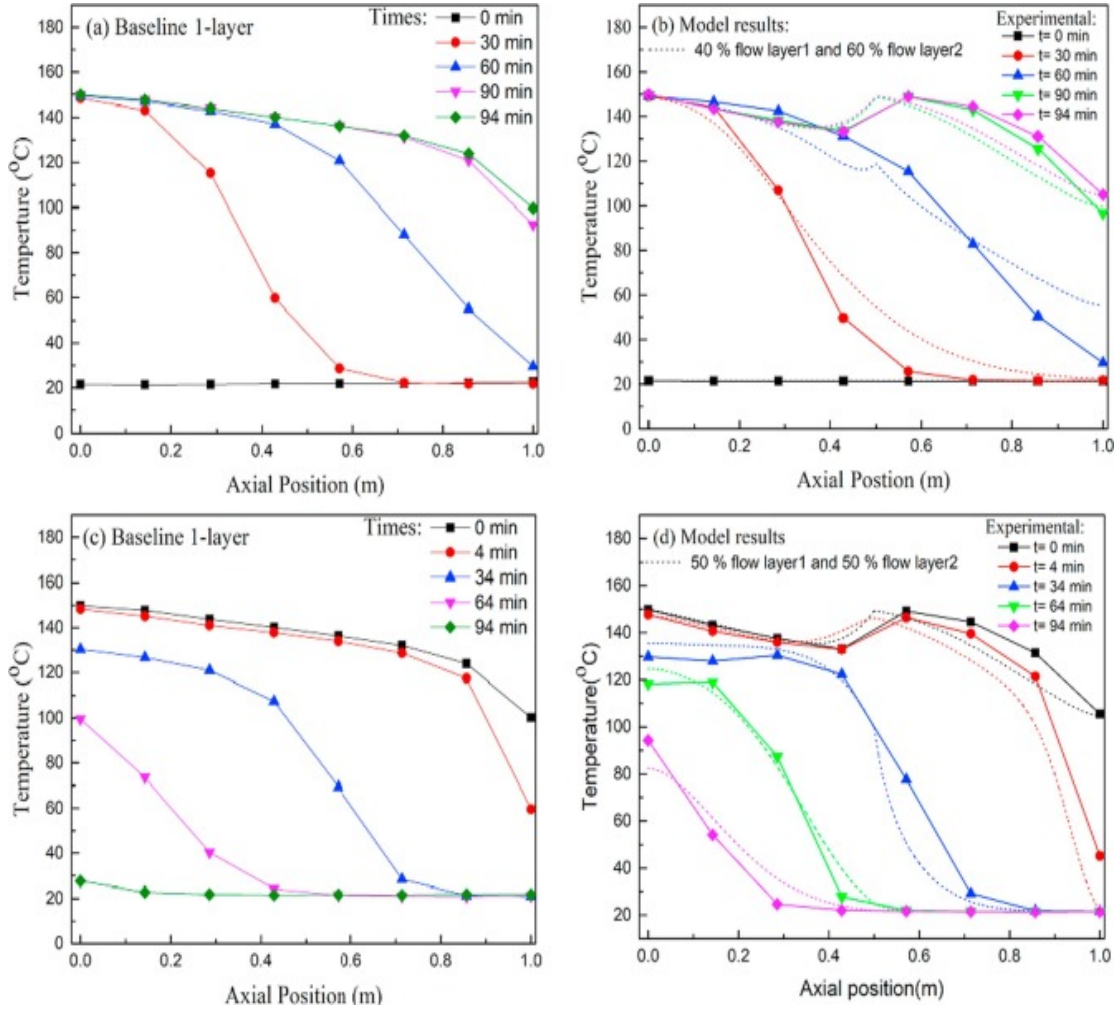


Figure 21. Temperature profiles for full charge/discharge with  $0.0061 \text{ m}^3/\text{s}$  for one and two layers with the most efficient charging/discharging scheme. (a) Charging for one layer [22], (b) Charging for two layers (Case C1), (c) Discharging for one layer [22] and (d) Discharging for two layers (Case c5) with model results.

Figure 22 shows the charging and discharging process at the highest flow rate with three layers, where the experiment is repeated four times to ensure the repeatability of the experimental data. As can be seen, the small error bars confirm that the

experimental data are reproducible. As discussed in the following section, these thermal profiles in the bed lead to higher recovery temperatures in the three layer cases compared to one and two layers, which in turns leads to higher exergetic efficiencies. However, the thermocline behaves as a wave profile in the last time intervals during the charging process and in early time intervals during the discharging process. The thermocline associated with each layer is affected via heat losses and thermal dispersion within the layer. The wave appears because of the segmentation in the bed. A thermocline must form in each zone, but a new injection pipe raises that temperature to  $T_{hot} = 150^{\circ}\text{C}$  at the location of injection. Hence, the ‘wave’ temperature profile occurs with peaks at the locations of heated gas injection. At early times during the discharging process, the waves appear because the bed is still at high temperature, and this effect disappears with the progress of recovery.

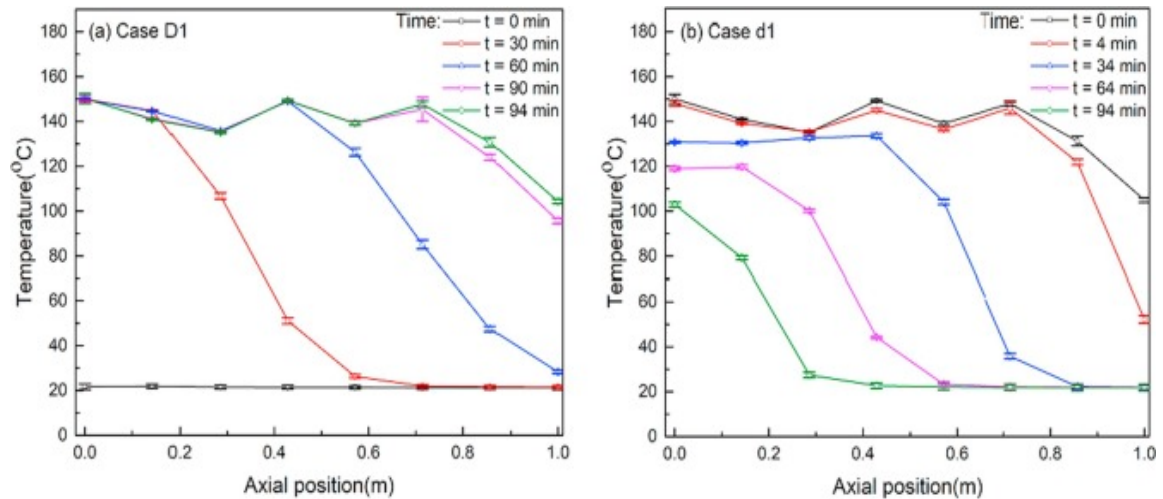


Figure 22. Temperature profiles for full charge/discharge with  $0.0061 \text{ m}^3/\text{s}$  for three layers with, (a) Charging (Case D1) and (b) discharging (Case d1). The error bars are average data from four trials.

As explained earlier, the single thermocline tank is considered a promising solution and its performance is affected by several parameters, which have been studied in literature. In the present study, the thermocline is affected by dividing the bed into two and three layers. However, the thermocline's formation is still impacted by the combined effects of heat and thermal dispersion losses. During the storage process, at the initial time, the entire bed is at low temperature as can be seen in Figures 2-5. After 30 min, the thermocline is forming with high constant temperature at the inlet and low temperature at the outlet of the storage tank. The thermocline spreads with time, and its formation depends on the number of layers and timing of the injection scheme. The high temperature at the outlet during the recovery period is not constant and varies with time and bed length as the thermocline reaches the outlet of the bed due to the heat and thermal dispersion losses. The thermocline continues to move through the length of the bed with the progression of the discharging process. This process is impacted by the layers' length (i.e. number of layer segments) and, similar to charging, how the discharge is enacted in terms of flow rate and flow duration to each layer. These effects are quantitatively estimated in a subsequent section.

### 3.3.2 Recovery Temperature for One, Two, and Three Layers

The recovery temperature represents an important component in thermal energy storage. It shows the effectiveness of the charging and discharging processes. If the storage/recovery cycle is achieved well, a high recovery temperature will be collected from the system, which will lead to higher recovery exergy values and thus exergetic efficiencies, as seen in Eqn. 3.10. The recovery temperature is usually collected at the



outlet of the bed. In this work for two and three layers, the recovery temperature is also collected at the outlet of the bed ( $x = 0$ ) for all layers because the mass flow rate from the injected pipes is mixed again at the outlet in one point as explained in the exergy analysis section. Figure 23a and b shows the recovery temperature profiles for two and three bed layers compared to one bed layer at two flow rates. These focus on the most efficient and least efficient cases only. Though the recovery temperature decreases with time, it increases with number of layers and mass flow rate. The area under the recovery temperature curves represents the recovered energy from the bed.

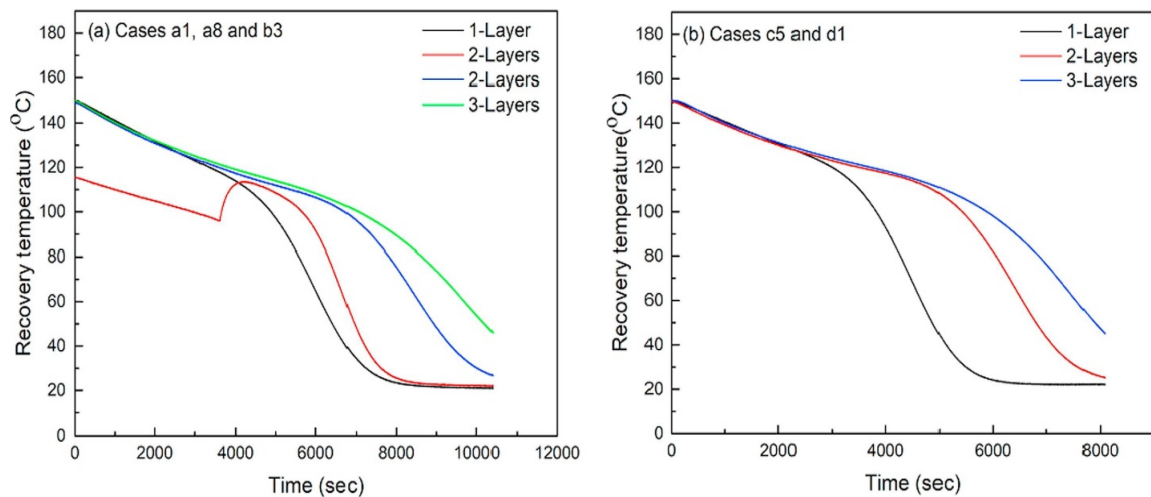


Figure 23. The experimental recovery temperature for two and three bed layers compared to one bed layer at two flow rates. (a) Most and least efficient cases at  $0.0048 \text{ m}^3/\text{s}$  and (b) Most efficient case at  $0.0061 \text{ m}^3/\text{s}$ .

The most efficient charge-discharge cases for two and three layers both exhibit higher exit recovery temperatures than the baseline, resulting in thermal exergetic efficiencies of 69.2% and 76.8%, respectively, compared to the baseline at 53.2% at  $0.0048 \text{ m}^3/\text{s}$ . These results are consistent with the higher amount of stored energy noted in the charge profiles (Figures 2c and 4b). Similarly, the exergetic efficiency increases to

73.4% and 80.3% at  $0.0061 \text{ m}^3/\text{s}$  for two and three layers, respectively. Thermal dispersion effects reduce with increased layers, and the recovery temperature profile for three layers is greater than for two layers. The least efficient two layer charge-discharge scheme exhibits performance lower than the baseline. This result is due to the large heat losses to the environment exacerbated by this particular charge-discharge scheme. By charging the bed in isolation, the first zone continually loses heat and the stored energy is low (Figure 19b). This then decreases the recovery temperature and results in poor thermal exergy efficiency (42.3%).

### 3.3.3 Quantification of Thermal Dispersion and Heat Losses to the Environment

As explained by Nield and Bejan [41], thermal dispersion occurs due to the spreading of heat because of hydrodynamic mixing of the fluid elements passing through the porous domain. This mixing can occur via multiple mechanisms. Mixing happens because of the obstructions, where fluid elements of the same velocity vary in distance from each other due to the tortuous nature of the domain. Mixing also occurs due to local pore accessibility, eddies in turbulent flow, and recirculation due to reduced pressure in local regions [41]. Dispersion losses increase with flow rate as has been reported [22]. In the present study, the velocity of the HTF is changing during the charging/discharging processes in each layer, which could lead to velocity variations in the pore scale and affect thermal dispersion. For example, consider case A3 at low flow rate, when the storage process of the first layer starts, the velocity is the total velocity. Then, when storage process of the second layer starts, the flow divides between the two layers (layer one has less flow, layer two has all the flow since it combines with the flow from layer

one). This affects the heat transfer and the thermal dispersion in each layer. Although thermal dispersion losses are reduced via increasing the number of bed layers, their effects are still present as explained below. In all cases, the efficiency results and recovery profiles are a function of heat loss to the ambient and thermal dispersion. While these effects are related, they cannot be isolated via experimental data. Thus, this section considers an adiabatic and non-adiabatic model to provide an estimate of each effect. In the adiabatic case, only thermal dispersion losses can occur to lower the exergetic efficiency. The model results, as shown, provide a reasonable estimate of the experimental results for the various layers during charging and discharging. In the adiabatic model, only the porous domain was considered, so no heat could conduct through the insulation or steel before being lost to the environment. In the non-adiabatic model, the heat losses via conduction through the solid domains are included. Figure 24a–c shows these results for one, two, and three layers at  $0.0048 \text{ m}^3/\text{s}$ , and Figure 24d–f shows the results for one, two, and three layers at  $0.0061 \text{ m}^3/\text{s}$ . These are based on the most efficient scenarios for the two and three layer cases (Cases A3, B3, C1 and D1 for charging; Cases a8, b3, c5 and d1 for discharging). As can be seen in these results, the agreement between the non-adiabatic model and experimental data is good. In addition, the exergy numbers are in good agreement as shown in Table 13. The effect of layers on the thermal behavior and efficiency of the packed bed is very clear as discussed in the previous sections. The results show a reduction in the dispersive effect by dividing the bed domain into two and three layers as shown in Table 13, which leads to an increase in the thermal exergy efficiency of the packed bed.

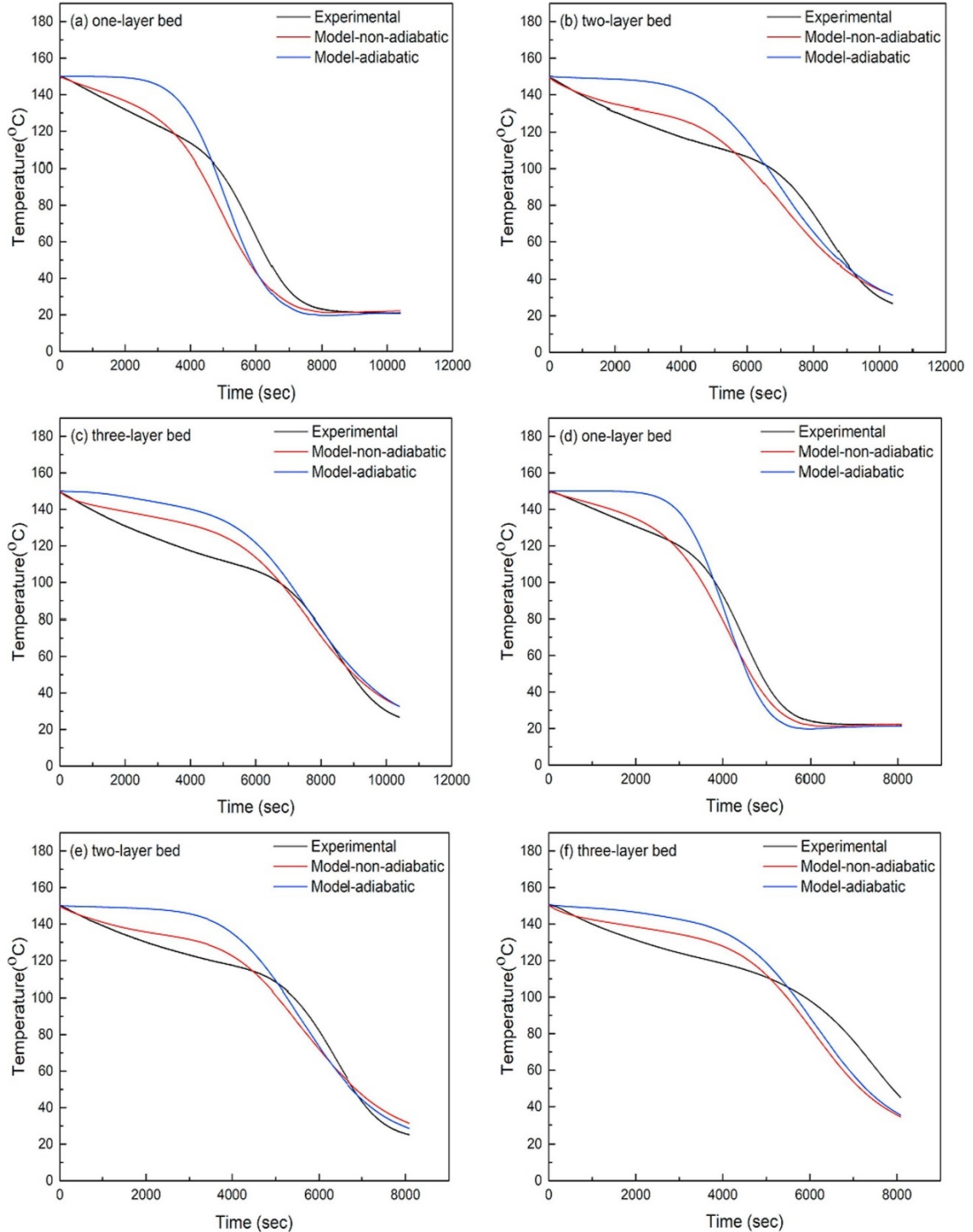


Figure 24. The experimental recovery temperature profiles at two flow rates compared to numerical model results. (a), (b) and (c) show results for one, two, and three layers, respectively for  $0.0048 \text{ m}^3/\text{s}$ . (d), (e) and (f) show results for one, two, and three layers for  $0.0061 \text{ m}^3/\text{s}$  with discharge cases a8, b3, c5, and d1.

Table 13. Percentage exergy and dispersive loss from the experimental and model (adiabatic and non-adiabatic) results. The experimental exergy numbers for one bed layer are from [22].

Volumetric flow rate (m <sup>3</sup> /s)	Layers	Percentage Exergy			% Total exergy loss ( $Loss_T$ )	% Exergy loss from heat losses ( $Loss_H$ )	% Exergy loss from thermal dispersion ( $Loss_D$ )
		Experimental	Non- adiabatic	Model Adiabatic			
0.0048	One	53.2	50.8	62.6	49.2	11.8	37.4
	Two	69.6	70.1	85.8	29.9	15.7	14.2
	Three	76.8	77.9	88.2	22.1	10.3	11.8
0.0061	One	55.4	54.3	64.9	45.7	10.6	35.1
	Two	73.4	74.9	89.8	25.1	14.9	12.3
	Three	80.3 ± 0.6	81.5	91.4	18.5	9.9	8.6

The loss in exergetic efficiency from thermal dispersion was calculated from Eqn. 3.11, where the effect of heat losses are set to zero with the adiabatic model case. The total losses (heat and thermal dispersion) are calculated from Eqn. 3.12, where both effects are considered via the non-adiabatic model results.

$$Loss_D = 100 - \eta_{ef-adiabatic} \quad (3.11)$$

$$Loss_T = 100 - \eta_{ef-non-adiabatic} \quad (3.12)$$

With the total loss in exergetic efficiency and the loss associated with thermal dispersion calculated, heat losses are calculated from Eqn. 3.13.

$$Loss_H = Loss_T - Loss_D \quad (3.13)$$

The dispersive loss is calculated for each layering configuration at both flow rates, and the results are presented in Table 6. Importantly, the loss in exergetic efficiency

decrease as the number of layers increases. For instance, the exergetic efficiency reduction due to thermal dispersion at  $0.0048 \text{ m}^3/\text{s}$  is estimated at 37.4, 14.2, and 11.8% for one, two, and three layers, respectively. The same trend can be seen for the higher flow rate too. Heat losses also have a significant impact on the thermal behavior of the packed bed, especially for the present vessel due to the high surface to volume ratio. However, the reduction in dispersive losses is substantial, which leads to the higher exergetic efficiency. For instance, the non-adiabatic exergetic efficiency result for two layers at  $0.0048 \text{ m}^3/\text{s}$  is 70.1%. This result shows 29.9% of the exergetic loss is from the combined effects of heat losses and thermal dispersion. When run in the adiabatic case, the result is an exergetic efficiency of 85.8%. Thus, as an estimate, 14.2% of the 29.9% is thermal dispersion losses and 15.7% of the 29.9% is heat losses to the environment. These results show the large, positive effect layers can have by reducing thermal dispersion. However, the approach to charging and discharging the bed layers is important and should be considered to design a packed bed with layers in order to achieve higher performance. This is why the focus in the previous sections was on the least efficient and most efficient cases that affect the thermal behavior during charging and discharging processes. The cases shown in Appendix Table A1 provide several additional charge-discharge scenarios, and the optimum may depend on what criteria are chosen for a charge-discharge cycle or if partial charges are being pursued.

The pipe injection technique in this work is a new method where the segmented layers are in contact with each other. Other segmentation strategies were used in literature as explained earlier. White et al. [36] used a segmented packed bed to control the thermal

front in large storage reservoirs (hot/cold thermal stores for pumped thermal energy storage and a large thermal store for adiabatic compressed air energy storage), where two segmented reservoirs schemes were introduced. In the first segmented reservoir, a central baffle moved to allow charging/discharging of the active layers. In the second segmented reservoir, independent valves controlled each layer. All layers were horizontal with space between the layers, allowing the HTF to pass through the active layers. Temperature profiles with eight segments showed a “sawtooth” variation in the thermal front due to their segmented control strategy, which decayed with time. In addition, the study concluded that segmentation reduced the exergetic losses (heat losses, pressure, and thermal dispersion) between 25% and 50%. In the present study similar behavior is noted, where the thermal front behaves as a wave profile during the charging/discharging processes. This thermocline behavior appears due to the segmentation in the bed and the combined effects of heat and thermal dispersion losses. This behavior reduces by increasing the number of layers. In addition, the present study showed a significant increase in the exergetic efficiency and decrease in the dispersive losses as shown in Table 6. However, practitioners should be aware of the way of doing charging/discharging processes using pipe injection with several layers in contact. Dividing the bed domain could be worse than the normal one bed layer as shown in Appendix 3.A, where some of the storage/recovery schemes show thermal exergy efficiency less than the normal one-bed layer.

Real applications can incorporate these results by using internal piping to segment application-scale beds into several layers. Designers should consider radial effects if the

bed diameter is large, such as using multiple injection pipes along the radial direction at a fixed axial location. The internal segments can be facilitated via piping inside the bed or through the bed walls as in [48]. Designers should also consider the charging and discharging schemes here, where large beds may be able to have less flow to an already heated zone due to less heat losses to the environment from advantageous surface to volume ratios. Large systems are also likely to benefit from a reduction in the packed bed pressure drop. Zones experiencing less flow rate contribute less to the overall pressure drop, and the zones with the full combined flow are for a shorter bed length, which also reduces the pressure drop. While the specifics of the design will need to be determined by those building the system, the concept presented here can lead to substantial exergetic efficiency increases.

### 3.4 Conclusions

The thermal performance of a layered packed bed using axial pipe injection was studied experimentally. The full charge/discharge cycle for two standard flow rates at 0.0048 and 0.0061 m<sup>3</sup>/s was tested with two and three bed layers. Air was used as the heat transfer fluid at an inlet temperature of 150 °C and 6 mm  $\alpha$ -alumina beads were used as sensible heat storage material. The study focused on determining the relative contributions of heat losses and axial thermal dispersion on the thermal behavior of the packed bed with two and three layers. These effects varied based on how the bed is charged and discharged when multiple layers are considered. Seventeen cases were presented focusing on the relative amount of flow to each segment during the



charge/discharge cycle while maintaining the same inlet temperature to each zone. It was necessary to keep some flow in all layers during charging to offset heat losses to the environment. In discharge, higher recovery performance was noted when recovery occurred in all domains simultaneously. In the most efficient schemes, the results show an increase in the exergy efficiency from 53.2% to 69.6% with two layers and to 76.8% with three layers at 0.0048 m<sup>3</sup>/s. For the higher flow rate, the exergy increased from 55.4% to 73.4% with two layers and to 80.3% with three layers. The axial thermal dispersion's contribution to the overall exergy loss is reduced via dividing the bed domain into two and three bed layers.

#### Acknowledgements

This research did not receive any specific grant from funding agencies in the public, commercial, or not-for-profit sectors. The authors thank Montana State University for financial support. Mr. Al-Azawii thanks the Higher Committee for Educational Development in Iraq (HCED) for supporting his scholarship through the Iraqi government funding.

#### Appendix 3. A

The total time used to charge/discharge a one-layer bed [22] is used in this work to charge/discharge the two and three bed layers. Table A.1 shows all the schemes that have been tested in this study. For instance, after the A3 charge cycle, five schemes were considered for the discharge (a4-a8).

**Table A1.** Charging and discharging processes using axial pipe injection for different injecting timing schemes with inlet temperature of approximately 150 °C. Two layers with 0.0048 m<sup>3</sup>/s are labeled with A1-A3 for charging and a1-a8 for discharging. Three layers with 0.0048 m<sup>3</sup>/s are labeled with B1-B3 for charging and b1-b3 for discharging. Two layers with 0.0061 m<sup>3</sup>/s are labeled with C1 for charging and c1-c5 for discharging. Three layers with 0.0061 m<sup>3</sup>/s are labeled with D1 for charging and d1 for discharging.

Flow rate m <sup>3</sup> /s	Charge-layers	Discharge -layers	% Exergy
0.0048	A1: Two layers, charging L1 for 60 min and then L2 for 60 min after closing the 1st valve	a1: Two layers, discharging L1 for 60 min and then L2 for 153 min after closing the 1st valve	42.3
	A2: Two layers, charging both layers together for 120 min	a2: Normal discharging (one layer)	52.5
		a3: Normal discharging (one layer)	46.9
		a4: Two layers, discharging L2 for 60 min and then L1 for 153 min after closing the 1st valve	56.4
		a5: Normal discharging (one layer)	57.7
	A3: Two layers, charging L1 for 60 min and then L1 and 2 for 60 min	a6: Two layers, discharging L1 and 2 together for 173 min (2nd valve is 75% opened and 1st valve is fully opened)	64.6
		a7: Two layers, discharging L1 for 60 min and then L1 and 2 for 153 min	68.2
		a8: Two layers, discharging L1 and 2 together for 173 min (two valves are fully opened)	69.6
0.0061	B1: Three layers, charging L1 for 45 min and then L 1and 2 for 45 min, then L 1, 2 and 3 for 30 min	b1 (a5 above)	59.5
	B2: Three layers, charging L1 for 40 min and then L 1and 2 for 35 min, then L 1, 2 and 3 for 45 min	b2 (a5 above)	60.5
	B3: Three layers, charging L1 for 40 min and then L 1and 2 for 40 min, then L 1, 2 and 3 for 40 min	b3 (same as a8, but for three layers)	74.6
	C1: Two layers, charging L1 for 46.5 min and then L1 and 2 for 46.5 min	c1: Two layers, discharging L1 for 45 min and then L2 for 89.5 min after closing the 2nd valve	59.2
		c2: Normal discharging (one layer)	60.2
		c3: Two layers, discharging L1 for 60 min and then L1 and 2 together for 89.5 min	66.4
		c4: Two layers, discharging L1 and 2 together for 134.5 min (2nd valve is 75% opened and 1st valve is fully opened)	68.6
		c5: Two layers, discharging L1 and 2 together for 134.5 min (two valves are fully opened)	73.4
D1: Three layers, charging L1 for 31.3 min and then L 1and 2 for 31.3 min, then L 1, 2 and 3 for 31.3 min	d1: three layers, discharging L1, 2 and 3 together for 134.5 min (three valves are fully opened)	80.3 ± 0.6	

References

1. IRENA, *Thermal Energy Storage: Technology Brief E17*. January 2013, International Renewable Energy Agency: Abu Dhabi.
2. Herrmann, U., B. Kelly, and H. Price, *Two-tank molten salt storage for parabolic trough solar power plants*. *Energy*, 2004. **29**(5): p. 883-893.
3. Medrano, M., et al., *State of the art on high-temperature thermal energy storage for power generation. Part 2—Case studies*. *Renewable and Sustainable Energy Reviews*, 2010. **14**(1): p. 56-72.
4. IRENA, *Concentrating solar power-renewable energy technologies: Cost analysis series, vol. 1: Power sector*. 2012, International Renewable Energy Agency: Abu Dhabi. p. 1-48.
5. *Concentrating solar power thermal storage system basics*. 2013 [cited 2018 July 31]; Available from: <https://energy.gov/eere/energybasics/articles/concentrating-solar-power-thermal-storage-system-basics>.
6. Pacheco, J.E., S.K. Showalter, and W.J. Kolb, *Development of a molten-salt thermocline thermal storage system for parabolic trough plants*. *Journal of solar energy engineering*, 2002. **124**(2): p. 153-159.
7. Wu, M., et al., *The impact of concrete structure on the thermal performance of the dual-media thermocline thermal storage tank using concrete as the solid medium*. *Applied Energy*, 2014. **113**: p. 1363-1371.
8. Reddy, K.S., et al., *Performance investigation of single-tank thermocline storage systems for CSP plants*. *Solar Energy*, 2017. **144**: p. 740-749.

9. Yang, Z. and S.V. Garimella, *Thermal analysis of solar thermal energy storage in a molten-salt thermocline*. Solar Energy, 2010. **84**(6): p. 974-985.
10. Nithyanandam, K., R. Pitchumani, and A. Mathur, *Analysis of a latent thermocline storage system with encapsulated phase change materials for concentrating solar power*. Applied Energy, 2014. **113**: p. 1446.
11. Zhao, B.-C., et al., *Thermal performance and cost analysis of a multi-layered solid-PCM thermocline thermal energy storage for CSP tower plants*. Applied Energy, 2016. **178**: p. 784-799.
12. Galione, P., et al., *Multi-layered solid-PCM thermocline thermal storage concept for CSP plants. Numerical analysis and perspectives*. Applied energy, 2015. **142**: p. 337-351.
13. Zhao, B.-C., et al., *System-level performance optimization of molten-salt packed-bed thermal energy storage for concentrating solar power*. Applied Energy, 2018. **226**: p. 225-239.
14. Mawire, A. and S.H. Taole, *A comparison of experimental thermal stratification parameters for an oil/pebble-bed thermal energy storage (TES) system during charging*. Applied Energy, 2011. **88**(12): p. 4766-4778.
15. Erregueragui, Z., et al., *Packed-bed thermal energy storage analysis: quartzite and palm-oil performance*. Energy Procedia, 2016. **99**: p. 370-379.
16. Bruch, A., et al., *Experimental investigation of cycling behaviour of pilot-scale thermal oil packed-bed thermal storage system*. Renewable Energy, 2017. **103**: p. 277-285.

17. Johnson, E., et al., *Thermal energy storage with supercritical carbon dioxide in a packed bed: Modeling charge-discharge cycles*. The Journal of Supercritical Fluids, 2018. **137**: p. 57-65.
18. Cascetta, M., et al. *Experimental investigation of a packed bed thermal energy storage system*. in *Journal of Physics: Conference Series*. 2015. IOP Publishing.
19. Cascetta, M., et al., *A comparison between CFD simulation and experimental investigation of a packed-bed thermal energy storage system*. Applied Thermal Engineering, 2016. **98**: p. 1263-1272.
20. White, A., J. McTigue, and C. Markides, *Wave propagation and thermodynamic losses in packed-bed thermal reservoirs for energy storage*. Applied Energy, 2014. **130**: p. 648.
21. Anderson, R., et al., *Experimental results and modeling of energy storage and recovery in a packed bed of alumina particles*. Applied Energy, 2014. **119**: p. 521-529.
22. Al-Azawii, M.M.S., et al., *Experimental study on the cyclic behavior of thermal energy storage in an air-alumina packed bed*. Journal of Energy Storage, 2018. **18C**: p. 239-249.
23. Zavattoni, S., et al., *High temperature rock-bed TES system suitable for industrial-scale CSP plant—CFD analysis under charge/discharge cyclic conditions*. Energy Procedia, 2014. **46**: p. 124-133.

24. Hoffmann, J.F., et al., *Experimental and numerical investigation of a thermocline thermal energy storage tank*. Applied Thermal Engineering, 2017. **114**: p. 896-904.
25. Mawire, A., et al., *Simulated performance of storage materials for pebble bed thermal energy storage (TES) systems*. Applied Energy, 2009. **86**(7): p. 1246-1252.
26. Alva, G., et al., *Thermal energy storage materials and systems for solar energy applications*. Renewable and Sustainable Energy Reviews, 2017. **68**: p. 693-706.
27. Zanganeh, G., et al., *Design of packed bed thermal energy storage systems for high-temperature industrial process heat*. Applied Energy, 2015. **137**: p. 812-822.
28. Zanganeh, G., et al., *Packed-bed thermal storage for concentrated solar power – Pilot-scale demonstration and industrial-scale design*. Solar Energy, 2012. **86**(10): p. 3084-3098.
29. Cascetta, M., et al., *Numerical investigation of a packed bed thermal energy storage system with different heat transfer fluids*. Energy Procedia, 2014. **45**: p. 598-607.
30. Esen, M., A. Durmuş, and A. Durmuş, *Geometric design of solar-aided latent heat store depending on various parameters and phase change materials*. Solar Energy, 1998. **62**(1): p. 19-28.
31. Sanderson, T.M. and G.T. Cunningham, *Packed bed thermal storage systems*. Applied Energy, 1995. **51**(1): p. 51-67.

32. Geissbühler, L., et al., *An assessment of thermocline-control methods for packed-bed thermal-energy storage in CSP plants, Part 1: Method descriptions*. Solar Energy, 2019. **178**: p. 341-350.
33. Geissbühler, L., et al., *An assessment of thermocline-control methods for packed-bed thermal-energy storage in CSP plants, Part 2: Assessment strategy and results*. Solar Energy, 2019. **178**: p. 351-364.
34. Crandall, D. and E. Thacher, *Segmented thermal storage*. Solar Energy, 2004. **77**(4): p. 435-440.
35. McTigue, J.D. and A. White, *Segmented packed beds for improved thermal energy storage performance*. IET Renew. Power Gener., 2016. **10**(10): p. 1498-1505.
36. White, A., J. McTigue, and C. Markides, *Analysis and optimisation of packed-bed thermal reservoirs for electricity storage applications*. Proceedings of the Institution of Mechanical Engineers, Part A: Journal of Power and Energy, 2016. **230**(7): p. 739-754.
37. McTigue, J.D. and A.J. White, *A comparison of radial-flow and axial-flow packed beds for thermal energy storage*. Applied Energy, 2018. **227**(C): p. 533-541.
38. Howes JS, M.J., Hunt RG, *Layered thermal store with selectivity alterable gas flow path*. 2017: US. Patent number US009658004B2.
39. Howes JS, M.J., Hunt RG, Bennet GR, Wilson BA, *Thermal energy storage apparatus*. 2018: US. Patent number US009970715B.

40. Yang, Z. and S.V. Garimella, *Cyclic operation of molten-salt thermal energy storage in thermoclines for solar power plants*. Applied Energy, 2013. **103**: p. 256-265.
41. Nield, D.A. and A. Bejan, *Convection in porous media*. Vol. 3. 2013: New York: Springer.
42. Vortmeyer, D. and R. Schaefer, *Equivalence of one-and two-phase models for heat transfer processes in packed beds: one dimensional theory*. Chemical Engineering Science, 1974. **29**(2): p. 485-491.
43. Bejan, A. and A.D. Kraus, *Heat transfer handbook*. 2003, Hoboken, N.J.: Hoboken, N.J. : John Wiley & Sons, INC.
44. Hilsenrath, J., *Tables of thermal properties of gases: comprising tables of thermodynamic and transport properties of air, argon, carbon dioxide, carbon monoxide, hydrogen, nitrogen, oxygen, and steam*. 1955, Washington, D.C.: US Dept. of Commerce, National Bureau of Standards.
45. Morrell, R., *Handbook of properties of technical and engineering ceramics*. 1987: Part 2. Hmsco.
46. Munro, M., *Evaluated Material Properties for a Sintered alpha-Alumina*. Journal of the American Ceramic Society, 1997. **80**(8): p. 1919-1928.
47. Bejan, A., *Thermal design and optimization*, ed. M.J. Moran and G. Tsatsaronis. 1996, New York: New York : John Wiley & Sons.



48. Bindra, H., P. Bueno, and J.F. Morris, *Sliding flow method for exergetically efficient packed bed thermal storage*. Applied Thermal Engineering, 2014. **64**(1-2): p. 201-208.

CHAPTER FOUR

EXPERIMENTAL STUDY OF THERMAL BEHAVIOR DURING CHARGING IN  
THERMAL ENERGY STORAGE PACKED BED USING RADIAL PIPE

Contribution of Authors and Co-Authors

Manuscript in Chapter 4

Author: Mohammad M. S. Al-Azawii

Contributions: Designed and installed different perforated tubes, conceived and designed the experiments, collected the experimental data, conceived the solid plate technique to improve the performance, performed the analyses, explained results, generated figures, and wrote the manuscript in preparation for editing and submission.

Co-Author: Duncan Jacobsen

Contributions: Designed and installed different perforated tubes used to charge the bed radially and edited the manuscript

Co-Author: Pablo Bueno

Contributions: Conceived the study, provided important insights about the study, and edited the manuscript.

Co-Author: Ryan Anderson

Contributions: Conceived the study, assisted in the preparation of the manuscript, provided important insights and details of the entire study and manuscript, discussed results and implications, and edited the earlier manuscript and final versions of the manuscript for submission.

Manuscript Information page

Mohammad M.S. Al-Azawii, Duncan Jacobsen, Pablo Bueno, Ryan Anderson

Applied Thermal Engineering

Status of Manuscript:

- Prepared for submission to a peer-reviewed journal
- Officially submitted to a peer-reviewed journal
- Accepted (pending revisions) by a peer-reviewed journal
- Published in a peer-reviewed journal

EXPERIMENTAL STUDY OF THERMAL BEHAVIOR DURING CHARGING IN  
THERMAL ENERGY STORAGE PACKED BED USING RADIAL PIPE

Abstract

The thermal behavior of an air-alumina packed bed storage system is studied experimentally via heating the bed domain radially. A perforated tube is inserted at the center along the axial length of the bed domain to charge the bed radially. Air was used as heat transfer fluid (HTF) with inlet temperature of 75 °C and 6 mm alumina beads were used as solid storage materials. This paper analyzes the storage efficiency of several radial designs compared to the traditional axial method. First, the storage process is analyzed by charging the bed radially using several different radial tube designs (six designs based on hole sizes). These hole patterns are analyzed to obtain the best even flow and thermal distribution in the radial direction, focusing on storage energy and temperature profiles. A gradient in hole sizes is needed, with smaller holes toward the outlet. To ensure HTF flowed radially from the center to the packed bed walls, additional plates were inserted into the bed to force gas to the wall. These plates were solid except for four holes around the edge of the plate at  $r = R$ . The charging efficiency is analyzed based on the first law of thermodynamics. The results show that during charging the radial configuration stores more energy compared to the axial flow configuration. The charging efficiency increases from 75.3 % (axial flow) to  $80.3 \pm 2.8$  % (radial flow with two plates).

#### 4.1 Introduction

Fossil fuel sources such as coal, oil and natural gas have provided energy for decades. However, fossil energy produces carbon dioxide emissions, the first driver of global warming (climate change). Climate change is leading to several environmental issues such as temperature rise, wildfires, drought, rise in sea level, floods, severe storms and hurricanes, and thus affecting power systems [1]. According to the U.S. Department of Energy (DOE), U.S. energy infrastructure is impacted by climate change effects, which threaten growth, national security, energy security and quality of life. Therefore, the DOE supports research to develop more reliable energy systems [2]. Renewable energy sources could be the alternative solution to reduce the harmful effects of fossil energy. The deployment of renewable energy sources has increased in recent years. For instance, the net production of electricity from solar energy increased from 8,161 GWh in 2007 to 253,593 GWh in 2015 [3]. However, renewable energy sources such as solar energy and wind power are of intermittent nature and low density, which leads to an inability to provide continuous energy generation for customers [4]. To utilize such sources, energy storage systems are required, where energy can be stored in different methods such as chemical, mechanical, biological, magnetic, and heat or thermal energy storage for a later usage [5].

Thermal energy storage (TES) systems store energy in the form of heat in two main ways, sensible and latent heat storage [6]. In sensible heat, energy is stored via raising the temperature of a material (liquid or solid) to a higher temperature. In latent heat, energy is stored when the storage material changes its phase (e.g. solid-liquid or solid-solid), and the materials used to store the energy are referred to as phase change materials (PCMs) [7].

In concentrated solar power plants, TES systems play a significant role to increase efficiency, where the storage tank(s) store excess solar energy by inserting them between the receiver and the generator [8]. Currently, two-tank are being used in CSP, one for hot fluid and one for cold fluid, in active (direct or indirect) storage systems [8, 9]. In the last few years, researchers focused on single-tank storage systems, where these systems are considered as a cheaper alternative compared to two-tank storage. Single-tank storage systems are also known as thermoclines [10]. Thermocline in a single tank means having two layers (hot and cold layers) with a temperature gradient between them, where a sharp temperature front leads to higher exergy efficiency [11]. Amongst single-tank options, packed bed devices to store the thermal energy are considered as the best storage structure [12]. Typically, the storage packed bed is a cylindrical container in a vertical layout, where the storage vessel is hot at the top and cold at the bottom, forming a thermocline [13]. Other vessel shapes are studied too. Zanganeh et al. [14] investigated the thermocline in a conical storage vessel and compared the performance to a cylindrical storage tank of the same volume. It was found that energy stored in a conical storage is higher and the wall heat losses are low due to the larger volume to surface ratio. However, the heat losses from the conical storage's cover is high due to the large diameter at the top. Horizontal packed beds have been studied as well [15], which can be built easily with high mechanical stability. Soprani et al. [16] studied a high temperature rock bed TES with air flow in a horizontal orientation, which was promising in terms of cost and structure design. However, it was concluded that the buoyancy force affects the temperature distribution and reduces efficiency. In addition to the vessel geometry, the system can also consider a range of heat

transfer fluids (HTFs) and storage media. Studied HTFs include air, carbon dioxide, oils, steam, or molten salts, reviewed in [17, 18]. Example storage materials include rocks, concrete, alumina, sand, and brick, which can be found in [19-21]. Various strengths and weaknesses are noted for both HTF and storage media, so optimization for thermal performance and cost depends on the system under consideration.

In all cases of packed bed TES, heated fluid enters from one side during storage and flows axially toward the outlet. This leads to thermal dispersion effects, causing a spreading of the thermal front in the bed and reducing thermal exergy efficiency [11]. Also, the cumulative effect of thermal dispersion increases with the number of cycles and flow rate, thus increasing thermocline degradation [22, 23]. This degradation leads to decreased stored/recovered energy and decreased exergetic efficiency for multiple partial charge-discharge cycles [24]. Limiting energetic and exergetic losses due to thermal dispersion is an emerging area of research. A new effective method used to charge/discharge the single-packed bed (horizontal or vertical layout) is via internal segmentation, where individual zones are created in the bed to receive flow. Segmentation (layering) the packed bed has shown a high thermal performance [25, 26]. In [25], Crandall and Thacher studied numerically the segmentation of a vertical storage tank and found that segmentation helps to preserve the thermocline. In [26], Al-Azawii et al. studied experimentally the thermal performance of a horizontal packed bed via dividing the bed domain into two and three layers. The results showed an increase in the exergy efficiency and a decrease in the dispersion losses with an increase in the number of layers and mass flow rate. In addition,

segmentation has been considered numerically in large reservoirs [27, 28], and via injecting or extracting the HTF through the wall a of storage tank [29, 30].

The flow of HTF in these segmented packed bed storage systems remains axial along the storage tank. However, radial flow has been investigated in literature and is used in the present study to provide a fundamentally different flow in the packed bed. In 1942, Bradley [31] introduced his invention (regenerative stove) as a first concept of radial flow TES to be used in a blast furnace to melt iron. It is considered as an annular bed of pebbles, where the solid materials can be placed between the walls of two concentric perforated cylinders. In 1996, Fassbinder [32] introduced a regenerator having an annular heat-storage medium, trying to solve the technical issues related to Bradley's invention. Furthermore, a pebble bed regenerator and storage system for high temperature with radial flow was studied experimentally by Daschner et al. [33]. The results showed high thermal efficiency and low pressure drop because of the radial flow in the pebble bed. Recently, McTigue and White [34] numerically studied the radial-flow behavior in packed bed TES and compared the results to axial-flow behavior, where a cylindrical storage tank was used. The HTF entered an inner plenum at the center and flowed radially through the bed domain. After depositing the energy, the cold HTF flowed through an outer plenum to the outlet. The storage materials are placed between the inner and outer plenums surrounded by a grid, allowing the HTF to pass through. For that design, it was found that radial flow reduces the pressure drop but increases the conductive and thermal losses compared to axial flow. In addition, it was concluded that radial flow is more expensive because of the extra volume



required to achieve the bypass flows and more studies are needed to clarify the costs required for such systems.

In the radial flow designs mentioned above, even flow in the bed is needed. However, it was not the focus of those studies. Uniform radial flow distribution was studied in 1994 by Heggs et al. [35]. In that study, the fluid-flow distribution in an annular carbon packed bed (central manifold, bed and outer manifold) was analyzed numerically, and the model has been applied on a commercial filter. Four flow arrangements were considered, focusing on the radial flow distribution: Z-type (gas flowing radially from central manifold to outer manifold and leaving from the other end), U- type (gas flowing radially from central manifold to outer manifold and leaving from the same end), reverse Z-type (gas flowing radially from outer manifold to central manifold and leaving from the other end), and reverse U-type (gas flowing radially from outer manifold to central manifold and leaving from the same end). The results show that the flow distribution improved via reversing the flow direction, and flow from outer manifold to central manifold reverse flow had the most uniform flow distribution. In addition, the predicted radial flow distribution for the four flow arrangements deviated by about 5% from uniform flow. Deviation from uniform flow in the present study is small too as will be shown in the results section.

In the present study, the radial flow concept is introduced experimentally using a new method (pipe injection method), where a perforated tube is inserted at the center of the bed domain to provide a radial flow distribution through the bed. This is shown schematically in Figure 25. Furthermore, in the new method there is no need for the extra volume required for bypass flow during charging/discharging processes. The same packed

bed dimensions are used as previous studies with axial flow [24, 26], which simplifies the new system and could be less expensive. A sensible heat storage system with  $\alpha$ -alumina as storage material and air as HTF is used. Three key contributions are presented to increase flow uniformity in the bed: 1) A plate is inserted into the packed bed with four circular holes at  $r = R$  at four angular positions ( $\theta = 0, 90, 180, 270^\circ$ ), forcing flow from the perforated pipe to flow outward toward  $r = R$ ; 2) The HTF passes axially through the injected tube and radially through the bed domain; 3) The radial pipe is divided into layers, where each layer has a different hole size. This narrowing hole size distribution from inlet toward outlet avoids high flow resistance through the packing nearer the bed inlet (e.g. larger hole sizes at the first half and smaller hole sizes at the second half). Six radial tubes were designed and tested via varying the number of layers and hole sizes to obtain the best even flow. The thermal performance is compared to a traditional axial flow configuration (normal configuration, where the bed is treated as one domain and heated axially. One flow rate ( $0.0048 \text{ m}^3/\text{s}$ ) is considered in the study. The experimental charging energy and efficiency are calculated and analyzed for radial and axial flow configurations. In addition, the thermocline in the bed domain is analyzed during the storage period.

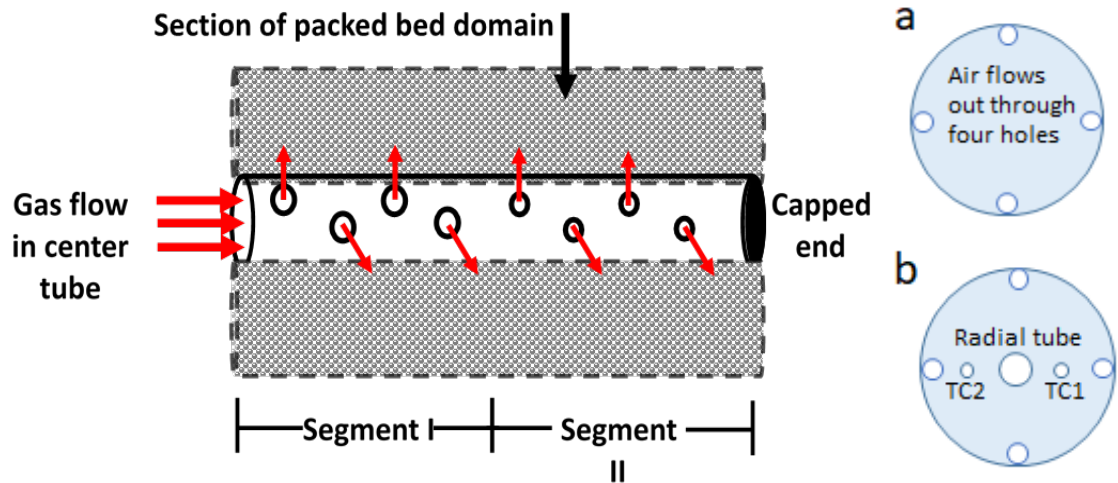


Figure 25: Left: Packed bed domain showing the radial inserted tube and two segments with different hole sizes (not to scale) and solid plates used in the experiments. Four holes are made at each axial location starting at  $x = 0$ , with one centimeter between each set of holes. Only one hole at each axial position is shown in the schematic for clarity. Each set of holes is rotated approximately  $45^\circ$ . The design of each tube is seen in Table 14. Right: Solid plate (a) used at the outlet only, and solid plate (b) can be used at different axial locations (in the present study it has been used at  $x = 80 \text{ cm}$ ).

#### 4.2 Experimental Setup, Energy and Charging Efficiency Analysis

This section details the properties of the experimental storage packed bed with radial configuration, flow loop setup, and experimental conditions. In addition, the thermal energy equations are presented for the storage/recovery cycles.

##### 4.2.1 Storage Packed Bed with Radial Pipe Injection

Figure 26 shows a schematic of the experimental setup of the packed bed with radial flow configuration, similar to the setup in [24]. Compressed air from the building is used as heat transfer fluid. Air passes through two filters to clean it of oil, water, and particulates before flowing through the heater and packed bed during storage processes. In charging, hot air from the heater flows into the storage packed bed at  $75^\circ\text{C}$ . Then, the air leaves the

packed bed after depositing heat into the storage materials. The exiting air passes through two water-cooled heat exchangers to cool it down to room temperature before venting to the room.

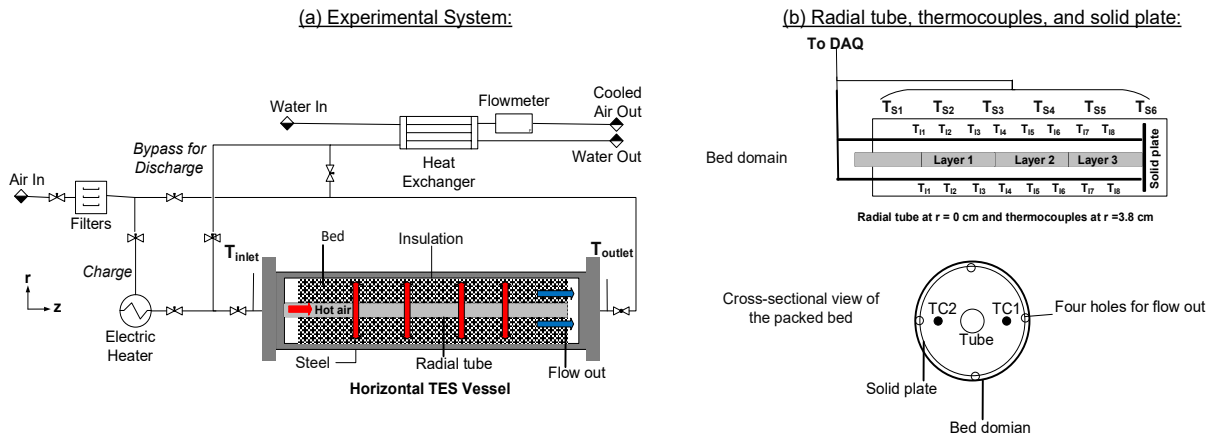


Figure 26. Left: Air flow schematic of packed bed TES utilizing filters to purify air supply, electric heater to heat the HTF, TES tank, DAQ collecting temperature data, and heat exchanger. Right: The packed bed with two thermocouples (TC1 and TC2), radial tube layers and solid plate. There are four holes drilled at the edge of the solid plate at  $0^\circ$ ,  $90^\circ$ ,  $180^\circ$ , and  $270^\circ$ , which allows air to flow out of the bed. There are eight internal sensing points ( $T_1$ ) for each internal thermocouple, six surface thermometers ( $T_s$ ), and inlet and outlet thermocouples.

The storage container consists of three domains (steel, insulation and storage bed). The first domain is a carbon steel tank, which is used as storage vessel (outer diameter = 16.8 cm, inner diameter = 15.4 cm and steel thickness = 0.7 cm). The length of the cylindrical storage tank is 120 cm. The vessel is a 6'' NPS schedule 40 pipe with flat flanges (ANSI 150# RF w/Blind). The second domain is Microtherm insulation, which is used as internal insulation with 1.27 cm thickness. The length of the cylindrical internal insulation is 120 cm and the outer and inner diameters are 15 and 12.47 cm, respectively. The internal insulation is constructed as two rigid cylinders with 60 cm length each to avoid breaking, and silicone is used to seal the two insulation cylinders to each other. The internal insulation is also sealed to the storage vessel to avoid bypass flow. The third domain is the

packed bed domain, where  $\alpha$ -alumina is used as packing material. The length of the packed bed domain is 100 cm. Perforated screens at 10 cm from the inlet and outlet helped to get uniform flow [24] and prevent the storage materials from falling into the inlet and outlet pipes during the axial cases. These remain in the bed for the radial charging case for consistency of vessel design.

To accomplish the radial injection of HTF during charging, at the inlet flange a  $\frac{1}{2}$  inch (1.27 cm) tube (McMaster Carr 1487T3) is inserted along the axial length of the bed. This tube is perforated with a drill to provide radial flow into the packed bed. The wall of the tube acts as a screen to provide radial flow and to prevent the storage materials from falling in the tube. There are four holes every one centimeter at  $0^\circ$ ,  $90^\circ$ ,  $180^\circ$ , and  $270^\circ$ . The hole sizes are in the range of 1.58 – 3.18 mm, which is small compared to the storage materials size (6 mm). A solid circular plate with 12.2 cm diameter was inserted at the end of the bed domain to prevent axial bypass flow and support the radial flow toward the wall of the bed. An additional plate in the packing domain are also considered. Detailed specifications of the radial tube and the solid plate are explained in the next section.

At the charging inlet side of the storage vessel, two holes were drilled in the flange of 0.635 cm FNPT (Female National Pipe Thread) to insert two K-type thermocouples down the axial length of the bed. Each K-type thermocouple has eight sensing points with four points at the same axial positions to check for radial temperature variation. The internal thermocouples are at 3.8 cm from the center of the bed and the sensing points are spaced at approximately 14.2 cm intervals for the 1<sup>st</sup> thermocouple [24, 26] and the 2<sup>nd</sup> thermocouple except two points with 7.2 cm in the second thermocouple. Data in Figures

26, 30 and A1 highlight the relative locations of sensing positions in the two thermocouples. The error associated with the thermocouples is  $\pm 2.2^{\circ}\text{C}$  as specified by Omega. The surface temperature of the wall was measured using six K-type thermocouples, and additional thermocouples measured temperature at the inlet and outlet of the vessel. A National Instrument data acquisition controller (NI 9213) was used to record data, and LabView software collected temperature data every second.

#### 4.2.2 Experimental Conditions and Design

For the present study, six different radial tubes were evaluated to obtain even flow in the bed domain and then to investigate the thermal behavior based on the radial flow distribution. The variables in each design are the dimensions of the radial hole perforation in the center tube and the number of layers within a tube that had a different perforation diameter. The dimensions of these designs are shown in Table 14. Two factors are considered to contribute to uneven flow. First, gas by bypass the packed bed by flowing through the internal tube and exiting only in holes closer to  $x = L$ . This bypass is caused by the high flow resistance through the packed bed domain. CFD analysis with COMSOL Multiphysics (results not shown) was used preliminarily to assess and inform the hole designs tested experimentally. The Ergun equation was used to determine the pressure drop in the packing and the resulting flow distribution. Numerical results indicated most flow bypassed nearly 75% of the packed bed when constant diameter holes sizes were used, qualitatively consistent with the experimental work. In addition, the mass flow rate for axial and radial configurations is the same and constant for the entire charging period,  $0.0048 \text{ m}^3/\text{s}$ . However, the velocity profiles in the packed bed are different. In the axial

flow, the hot gas flows axially from the inlet to the outlet with constant mass flow at each axial position. In the radial flow configuration, the flow exits the radial tube through the radial holes toward the bed wall with constant velocity. Then, the flow changes direction and heads axially toward the packed bed outlet. In this case, there is lower total mass flow rate at  $x = 0$  and a maximum flow rate at  $x = 1$  because the flow from the first set of radial holes combines with the flow from the next set radial holes and so on. Thus, the length of the injected tube was divided into one, two, three and four layers. Each layer has different hole sizes, which helps to increase the resistance of the flow through the radial tube toward the exit of the bed and provide approximately even flow along the axial length of the bed. The tubes are labeled as Design A-F. Second, air exiting the tube's perforations may then flow axially toward the packed bed exit without sufficient flow from  $r = 0$  to  $r = R$  (gas does not flow evenly to the bed wall). Therefore, a solid plate is inserted at  $x = 100 \text{ cm}$ , exactly at the end of the bed domain to provide a resistance to the air flowing axially and force it toward the wall. Four holes are drilled in the solid plate at the edges, which provide outlets of HTF as shown in Figure 25 a and b above. An additional internal solid plate with four holes at  $r = R$  is examined in a subsequent section.

Table 14: Dimensions of the internal radial tube holes, number of layers, and length of lengths

Design	No. of layers	Length of layers (cm)		Hole diameter (in) mm	Number of holes
A	1	L	100	(3/32) 2.38	Four holes at each axial location are spaced one centimeter apart. Note: the first four holes are located at $x = 0$ , then the next four holes are rotated approximately $45^\circ$ and so on as shown in Figure 25.
B	2	L1	50	(1/8) 3.18	
		L2	50	(3/32) 2.38	
C	3	L1	50	(3/32) 2.38	
		L2	25	(5/64) 1.98	
		L3	25	(1/16) 1.58	
D	3	L1	50	(1/8) 3.18	
		L2	25	(5/64) 1.98	
		L3	25	(1/16) 1.58	
E	4	L1	25	(3/32) 2.38	
		L2	25	(1/8) 3.18	
		L3	25	(3/32) 2.38	
		L4	25	(1/16) 1.58	
F	4	L1	25	(3/32) 2.38	
		L2	25	(1/8) 3.18	
		L3	25	(7/64) 2.78	
		L4	25	(1/16)1.58	

One flow rate was used,  $0.0048 \text{ m}^3/\text{s}$  (7 SCFM). The accuracy of the flow reading is based on a percentage of the full-scale reading, which correspond to  $\pm 0.16$  SLPM for 7 SCFM ( $0.0048 \text{ m}^3/\text{s}$ ) as specified by the manufacturer of the flowmeters. In this work, charging processes are compared for the various radial configurations and compared to the traditional axial configuration. The time required to charge the bed is adopted from [36]. This approach was used in our previous work [24, 26] and allows for a comparison between the thermal behavior of the radial flow to that of axial flow. This approach depends on density and heat capacity of the fluid at the inlet temperature of the storage process, the



length of the bed domain, and the propagation velocity of the heat-exchange zone. The propagation velocity depends on the heat capacity of storage material, porosity, and the fluid velocity at the inlet temperature during storage at 75°C. For the conditions in this work, the charging time in all cases is 6562 s (1 hr 49 min).

#### 4.2.3 Energy Analysis

In order to compare the thermal behavior of the radial and axial flow charging process, the energy stored in the packed bed is calculated from the first law of thermodynamics (steady-flow thermal energy equation) in Eqn. 4.1 [37]:

$$Q_{bed} = \int_{T_o}^{T_{bed}} mCp_{alumina}(T)dT \quad (4.1)$$

where  $Q_{bed}$  is the net amount of energy (heat) gained via heating the storage material in the packed bed,  $T_o$  and  $T_{bed}$  are the initial and local bed temperature,  $m$  is the mass of the alumina beads, and  $Cp_{alumina}$  is the heat capacity of the alumina beads. The heat capacity of the alumina beads as a function of temperature are used from [24]. The energy supplied to the bed,  $Q_{supplied}$  is defined in Eqn. 4.2:

$$Q_{supplied} = \dot{m}Cp_{air} \int_0^{t_s} (T_{hot} - T_o)dt \quad (4.2)$$

where  $\dot{m}$  is the mass flow rate, which is constant during the charging process, and  $Cp_{air}$  is the specific heat capacity of the fluid and its variation is considered constant in the range of temperature used,  $T_{hot}$  is the set inlet temperature ( $T_{hot} = 75^\circ\text{C}$ ),  $T_o$  is the ambient temperature, and  $t_s$  is the storage time.

The charging efficiency is calculated and analyzed based on the first law analysis as shown in Eqn. 4.3 based on the energy supplied to the bed and energy stored in the bed during the charging process. The temperature supplied from the heater is constant during

the charging period. Therefore, no integration is needed for the supplied energy, which simplifies to:

$$\zeta_{charging} = \frac{Q_{bed}}{Q_{supplied}} = \frac{m \int_{T_o}^{T_{bed}} c_{p_{alumina}}(T) dT}{\dot{m} c_{p_{air}} (T_{hot} - T_o) t_s} \quad (4.3)$$

The energy stored into the alumina beads during the charging time was calculated at several time intervals. The total mass of the alumina beads used in the bed was 26.5 kg for 6 mm beads size. The thermophysical properties of air and alumina beads are listed in Table 15. The size and thermal conductivity of storage materials have a significant impact on the thermal performance of the bed. It is important the Biot number ( $Bi = \frac{h*d}{k_{solid}}$ ) be less than 0.1 to avoid intra-particle temperature gradients. Larger solid particles with low thermal conductivity will lead to higher Biot numbers and thus temperature gradients within the particles, which lowers system efficiency. In the present study, the size of alumina beads is 6 mm and the maximum temperature used is 75°C, where the thermal conductivity is 26.8 W/m.K. Based on our previous study [24], the Biot number was checked here and it was less than 0.1. Another key consideration is the pressure drop in the bed. As the bead size affects the pressure drop in the packed bed, the hole sizes in the radial pipe may need to be reconsidered to ensure even flow distribution. Smaller beads for instance would increase flow resistance in the packed bed [38], meaning even narrower holes toward the end of the radial pipe and larger holes near the radial pipe inlet may be necessary.

Table 15: The thermophysical properties of air and alumina beads at low and high temperatures.

Material	Thermal conductivity (W/m. K)	Specific heat (J/kg. K)
Alumina at 75 °C	26.8	920.9
Alumina at 21.5 °C	32.8	766.2
Air at 75 °C	0.033	1009
Air at 21.5 °C	0.0258	1006.2

### 4.3 Results and Discussion

This section focuses on the experimental results, where two areas are covered. First, the results show the thermal behavior during the charging process focusing on even flow distribution to obtain uniform temperature profiles. As noted in Table 14, six radial tubes were considered and tested in total. However, only the most and least efficient radial tubes were considered in the detailed discussion in this section. The temperature profiles from the other four tubes are shown in Appendix 4.A, where thermal performance exhibits behavior bounded by the best and least efficient cases. Then, the impact of using solid plate on the thermal performance and even flow distribution is explained. Second, the energy and charging efficiency based on the most efficient configuration is calculated for three different charging schemes, and compared to axial flow configuration. One flow rate,  $0.0048 \text{ m}^3/\text{s}$ , was considered. However, for different flow rates, the same trends are expected in terms of even flow distribution, temperature profiles, and energy stored in the bed. Initial results (not shown here) at a higher flow rate ( $0.0061 \text{ m}^3/\text{s}$ ), which will be studied in future research, show uneven flow with Design A and improved thermal performance with Design E. The inlet temperature was  $75^\circ\text{C}$  in all cases. A relatively low

storage temperature was chosen so several radial tube designs could be fabricated with inexpensive materials. However, the flow distribution, thermal performance, and solid plate's impact due to using radial flow charging should be considered by practitioners, where the same trends would be expected at high temperature. Even flow distribution is observed based on the temperature distribution in the packed bed during the charging process. In the present study, there is no measurement for the velocity or flow distribution in the packed bed because there is no possible way to determine the velocity profiles experimentally from the inserted radial tube. However, the temperature distribution is used as an analog for uniform flow in the packed bed. As discussed for this particular packed bed TES application, two modifications to the system were needed for flow uniformity, variation in hole diameter along the axial length of the radial injection tube and a plate with four holes at  $r = R$  for flow to exit the bed.

#### 4.3.1 Effect of Variable Hole Size in the Radial Pipe; Hole Diameter and Numbered of Zones with Fixed Diameter

Figure 27 a-b shows the experimental temperature profiles for designs A and E in Table 14. Shown here are the temperature distribution from sixteen sensing points (solid lines for the 1<sup>st</sup> thermocouple, TC1 and dash lines for the 2<sup>nd</sup> thermocouple, TC2) in the bed domain. Sensing points 3, 4, 5, and 6 are at the same axial length to see the temperature variations in the radial direction of the bed domain. Each design (A-F) is divided into 1 to 4 layers, and each layer has different hole diameters. In the proposed configurations in Figure 27, the temperature increases in the entire bed over the charging interval. Same trend can be seen for the other configurations B, C, D, and F in Appendix 4.A. However, there is a variation in the temperature distribution depending on the design due to deviation

from uniform flow. For example, Figure 27a shows the temperature profiles for design A, where the inserted tube is designed as one layer with one size (2.38 mm diameter) for all holes. The flow through the radial tube is high at the last 15 cm of the tube length, where high temperature can be seen, especially at the early times before reaching steady state. This result is due to the low resistance to the flow at the outlet. In this case, there is no uniform flow in the radial direction, and a large amount of hot air bypassed the bed instead of heating the storage material. Therefore, this design is considered bad in terms of even flow distribution.

In addition, the temperature variation in the radial direction is considered reasonable which can be seen from sensing points 3, 4, 5 and 6 for each thermocouple. There are three reasons for this variation: the non-uniform flow along the length of the radial tube (which provides the largest contribution to this variation), the difference in temperature readings from each thermocouple due to measurement error (which is small but can affect the results in general), and the flexible nature of the inserted plastic tube (the tube might move when the alumina beads are poured in the storage bed, which leads to some temperature variations too). Also, there is the potential for buoyancy driven flow in the packed bed domain due to the packed bed's horizontal orientation. However, due to the small diameter of the bed domain and small temperature variation in the radial direction, the buoyancy effects on the temperature distribution are considered minimal and not included in the analysis [24].

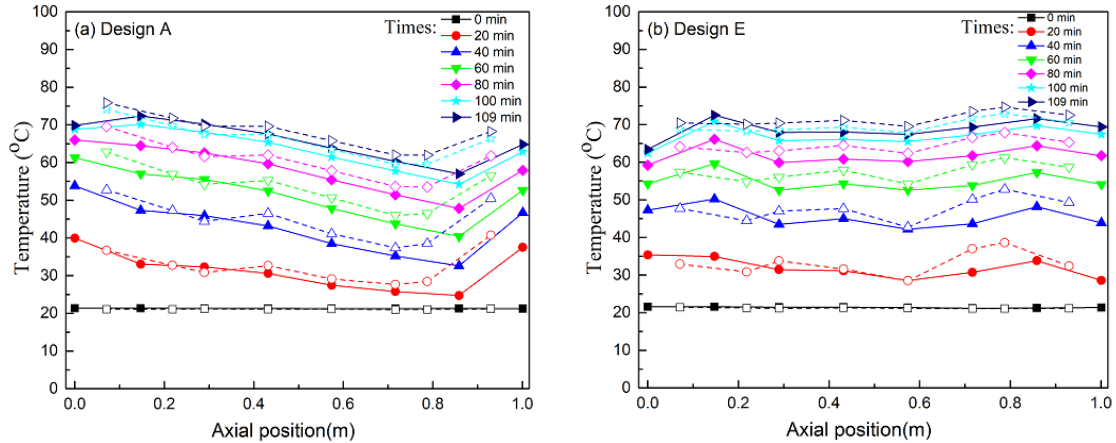


Figure 27. Temperature profiles in the packed bed (1 m length) from sixteen sensing points (solid lines for TC1 and dash lines for TC2). (a) and (b) here correspond to the designs A and E presented in Table 14. The results show relative levels of even flow distribution based on the uniformity of the temperature response from  $x = 0 - 1$ .

In order to quantify the performance of each design in terms of flow uniformity, the experimental temperature results were used to determine the percentage deviation from even flow. Figure 28 shows the average temperature from sixteen sensing points at each time interval and error bars based on the standard deviation. Small error bars indicate uniform temperature in the bed and thus a small deviation from uniform flow, while larger error bars indicate a larger deviation from even flow distribution. The larger error bars can be seen for designs A, B, C, and F. Designs E and then D has the smallest error bars. This indicates that design E has the most even flow compared to other designs. Design A has the largest error bars, where high flow can be seen in the last 15 cm of the bed length due to the bypass effect discussed. Dividing the length of the radial tube into several shorter layers helped in reducing this effect. These layers with engineered hole sizes improve even flow distribution and thus the thermal performance.

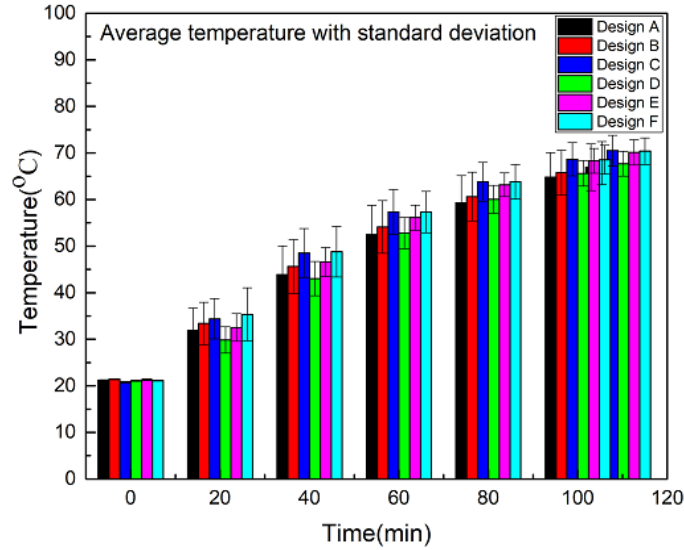


Figure 28. The average temperature from two thermocouples (TC1 and TC2) at 0.0048 m<sup>3</sup>/s with standard deviation, showing the deviation from even flow distribution and temperature variation in the radial direction.

The percentage deviation was calculated based on the absolute temperature of each single sensing point and mean temperature of eight sensing points of each thermocouple, which is shown in Eqn. 4.5.

$$Percentage_{dev} = \left( \frac{T_{abs} - T_{mean}}{T_{mean}} \right) * 100 \quad (4.5)$$

where  $T_{abs}$  is the absolute temperature at each sensing point for TC1 or TC2 and  $T_{mean}$  is the mean temperature from eight sensing points for TC1 or TC2. These results highlight the uniformity of the axial temperature profile, where the maximum deviation is approximately 4%. The most efficient designs are designs C, E and F. However, design E is considered the most efficient based on charging efficiency and flow distribution.

#### 4.3.2 Effect of Plates on Temperature Uniformity in the Bed

Typically, the heat transfer fluid will flow radially and then axially toward the outlet of the bed domain. This might result in a smaller amount of hot HTF toward the bed wall

depending on the bed resistance in the axial and radial directions. Therefore, a solid plate was inserted at the outlet of the bed ( $x = L = 100 \text{ cm}$ ) in all cases above to force the hot air to flow radially toward the wall in order to leave the bed. This method improved the radial flow, reduced the outlet temperature, and thus improved energy stored in the bed. To enhance performance further a second plate was inserted in the bed. The specification of the solid plates are shown in Table 16.

Table 16: The specifications of the solid plate used to force flow from the center of the bed to the wall.

Diameter of solid plate (cm)	Number of holes	Diameter of holes (mm)	Distance (cm)
12.2	4	6.35	One plate case: $x = 100$ Two plates case: 1 <sup>st</sup> at $x = 100$ and 2 <sup>nd</sup> at $x = 80$

Figure 29 a and b show the experimental temperature profiles with zero plate and with one plate for Designs A and E (the most and least efficient cases from the design of the radial hole profiles) from TC1 with zero plate and one plate as can be seen in a and b. In Figure 29 a and b, the temperature profiles are based on the data results from TC1 with zero plate and with one plate. The plate reduced the outlet temperature and increased the temperature in the bed compared to no plate, especially at the last 15 cm of the bed domain. This can be seen clearly in Figure 29 a and b, where the experimental data from TC1 is plotted with one plate (dash lines) and with zero plate (solid lines). In Figure 29 a, the impact of the solid plate is small; the poor design of the holes in the tube is not offset by the solid plate. In Figure 29 b, the thermal behavior improved in the entire bed, but the effect is small in the first 75 % of the bed length. This result means that multiple solid



plates are needed to improve the thermal performance in the entire bed domain. For example, for design E, a solid plate can be used at the end of each of the four layers. However, a balance between the diameter of the tube holes and the position of the plates should be determined to avoid the by-pass flow to the last layer due to the flow resistance created via each solid plate.

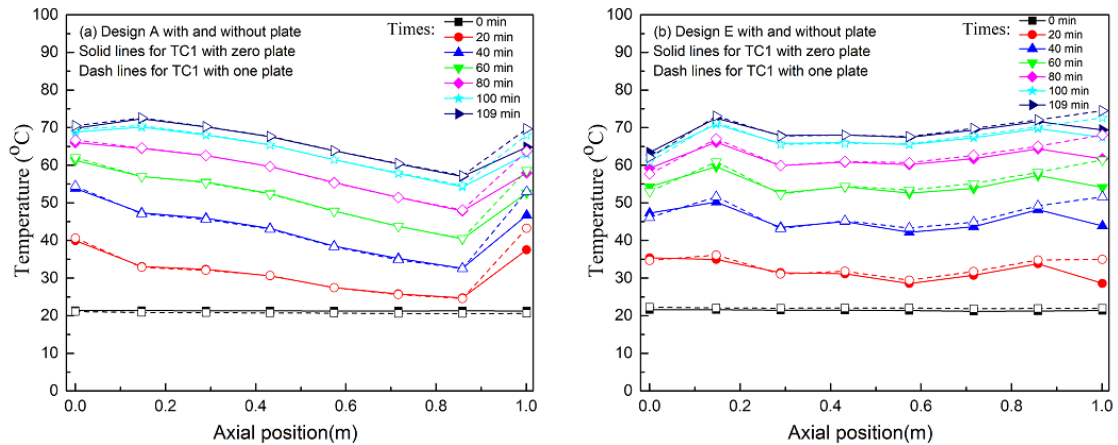


Figure 29. Temperature profiles in the packed bed (1 m length) at  $0.0048 \text{ m}^3/\text{s}$  for full charge. a) and b) Temperature data directly comparing with zero plate and with one plate from TC1 for Design A and Design E, respectively (solid lines for zero plate and dash lines for one plate).

In the present study, it is difficult to insert more than two solid plates due to the small diameter and the horizontal orientation of the packed bed storage. Therefore, one and two plates are only used in the present study. Figure 30 shows the impact of inserting two solid plates on the temperature profiles at three time intervals based on the hole profiles in Design E. The impact of inserting one plate is very small compared to two plates. As can be seen, the amount of energy stored in the bed with two plates increased. However, the heat losses from the wall is increased as will be explained next.

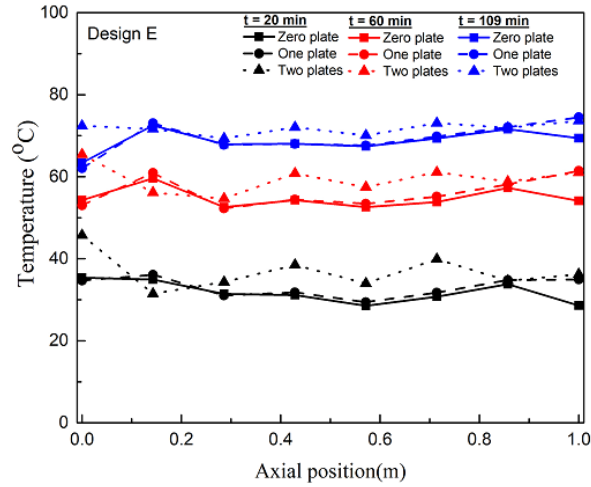


Figure 30. Temperature profiles in the packed bed (1 m length) during full charge at 0.0048 m<sup>3</sup>/s. The temperature lines are solid lines for zero plate, dash lines for one plate and dot lines for two plates.

Figure 31 shows the temperature results with two plates averaged from four separate trials during the charging period to confirm the repeatability of the experimental data. The overall small error bars confirm excellent repeatability of the results. However, larger error bars can be seen especially at the outlet of the bed.

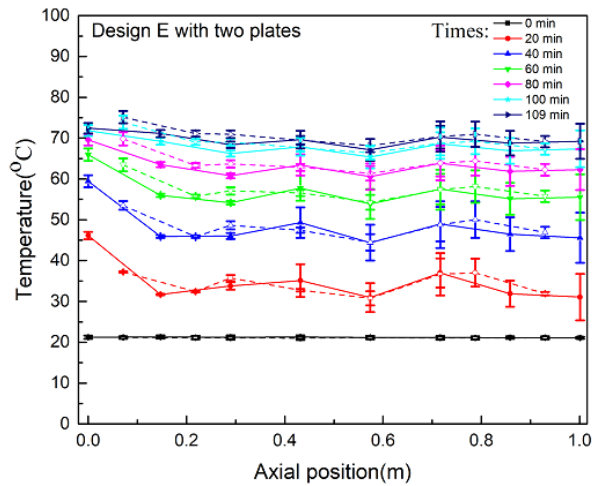


Figure 31. Experimental temperature profiles during radial charging flow in the packed bed for full charge from sixteen sensing points (solid lines for TC1 and dash lines for TC2). These results were collected from four trials, with the average and standard deviation for temperature presented at each spatial location over time.

### 4.3.3 Comparison of Axial and Radial Flow Charging: Outlet Temperature, Wall Losses, Energy stored and Charging Efficiency

In axial flow configuration, a thermocline forms during the charging process, leading to high temperature at the inlet of the bed and low temperature at the outlet of the bed. The thermocline (thermal front) moves along the length of the bed domain with time, which is affected by heat losses to the environment and axial thermal dispersion [26]. Therefore, the outlet temperature for axial flow configurations is low and starts to increase with time after approximately one hour of the charging period as can be seen in Figure 32a for axial flow. In radial flow configuration, the temperature increases in the entire bed ( $x = 0 - 1$ ), leading to approximately the same temperature along the length of the bed based on how even the flow is from the radial tube. Therefore, the outlet temperature during the radial flow configuration starts to increase rapidly as can be seen in Figure 32a for six designs (A-F). The outlet temperature was measured after the outlet flange (14.5 cm from the outlet flange) as shown in Figure 26. Design A and B had the highest temperature, especially at the early times (0 to 3500 sec). This result is due to a large amount of heat energy bypassing the packed bed, where most flow only enters the bed near the exit. This again highlights the need for a gradient in holes in the radial tube design to ensure heated gas reaches all of the packing in the bed. Design E shows the lowest outlet temperature at the early times compared to the other designs, consistent with that flow going into the packing material. Heat losses through the wall by conduction and to the ambient by convection have a significant impact on the energy stored in the bed domain. Figure 32b also includes the surface wall temperature for the axial flow configuration during charging at the same flow rate and inlet temperature. As can be seen, the wall temperature increases

especially in the last 40 minutes of the charging time (1 hr and 49 min), and the surface wall temperature with one and two plates is higher than that with zero plate. This indicates that the flow in the radial direction increased by adding plates, which means heated gas accesses more of the packing material. However, more heat losses occur by conduction through the packed bed wall. In addition, the surface wall temperature for axial flow is higher than that for radial flow, which means heat losses to the ambient for axial flow is higher than that for axial flow.

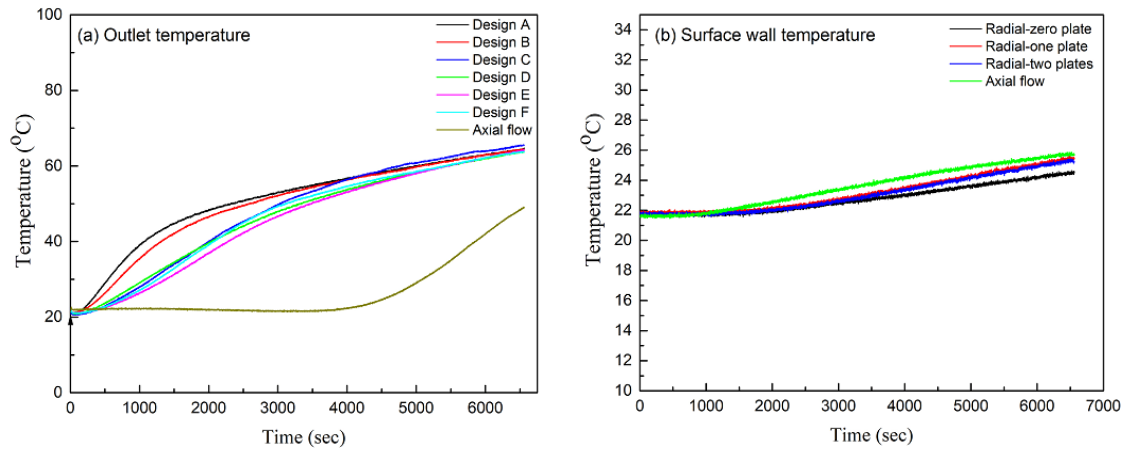


Figure 32. a) The outlet temperature profiles at  $0.0048 \text{ m}^3/\text{s}$  for designs A-F during charging process compared to each other and to the outlet temperature for axial flow configuration. b) The average surface wall temperature profiles with zero plate, one plate, and two plates of Design E compared to the traditional axial flow charging configuration at  $0.0048 \text{ m}^3/\text{s}$ .

As discussed in the introduction, axial flow is the most typical way used in literature to charge/discharge the storage packed bed. However, axial flow suffers from the axial thermal dispersion losses, which lead to the spread of the temperature front along the length of the bed domain and thus reduce the bed performance. Figure 33a shows the experimental temperature profiles in the bed domain with axial and radial flows for different time intervals at the same flow rate,  $0.0048 \text{ m}^3/\text{s}$ . The radial flow case is from Design E with

two plates based on the results in this work. During the axial flow method, a thermocline forms with bed positions towards the inlet at high temperature. A thermal front is noted from  $T_{hot}$  toward the inlet to room temperature toward the exit of the bed at the early time intervals (20 and 40 min). The thermocline degrades with time and axial position as can be seen in later time intervals (60, 80, 100 and 109 min) due to axial thermal dispersion and heat losses to the environment. During the radial flow, the temperature increases uniformly in the entire bed domain (dashed lines). Compared to axial flow, the radial flow scheme provides a full charge for approximately 95-100 % of the bed as can be seen at the steady state, where the entire bed at a high temperature. Therefore, the energy stored in the bed for radial charging is higher than that of axial flow charging.

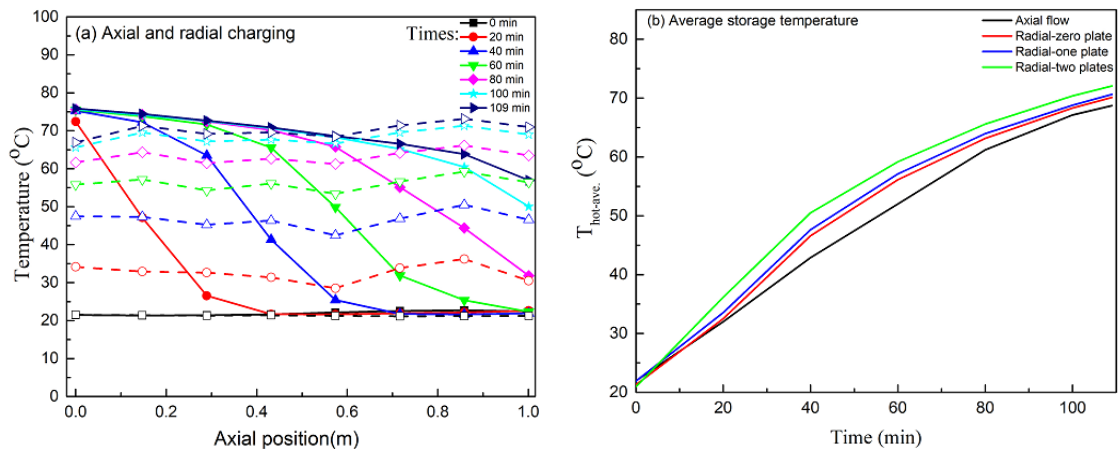


Figure 33. (a) Temperature profiles in the packed bed with axial and radial flow during charging process. Solid lines are for the axial flow and dash lines are for the radial flow based on Design E. Note: The temperature lines for axial and radial flow are plotted with the axial length of the bed ( $x = 0 - 1$ ) and averaged from TC1 and TC2. (b) The average storage temperature, averaged from all local temperatures at each time interval for four configurations, radial flow with zero plate, radial flow with one plate, and radial flow with two plates compared to axial flow.

Energy and efficiency analyses are important units to quantify the thermal performance of the storage system. As explained, the energy stored in the storage packed

bed is analyzed based on the first law of thermodynamics. The energy stored was calculated based on the local temperature in the bed from Eqn. 4.1. Charging the bed radially increases the energy stored as explained and shown in Figure 33a, where the bed is approximately fully charged. In addition, the average bed temperature during the entire charging processes for radial flow is higher than that of axial flow as can be seen in Figure 33b, where average bed temperature with two plates configuration is the best one. The total amount of energy stored at the end of the charging period using radial flow and axial flow is shown in Table 17. In addition, Table 17 shows the percentage charging efficiency based on the first law analysis at the end of the charge cycle. The value for energy stored in the bed and percentage charging efficiency with two plates is averaged from four separate trails with standard deviation. The charging efficiency was calculated using Eqn. 4.3, where the denominator represent the amount of energy supplied during the entire charging process, and the numerator represents the amount of energy stored into the storage bed.

Table 17: Energy and percentage charging efficiency for traditional axial flow and Design E with zero, one, and two plates.

Flow	Energy ( $10^3$ kJ)	Charging efficiency
Axial	1076.1	75.3
Radial with zero plate	1109.9	77.8
Radial with one plate	1124.9	78.6
Radial with two plates	$1148.3 \pm 4.05$	$80.3 \pm 2.8$

As can be seen, the charging efficiency for radial flow is higher than that of axial flow. At full charge, these efficiencies are 75.3, 77.8, 78.6 and  $80.3 \pm 2.8\%$  for axial, radial with zero plate radial with one plate, and radial with two plates flow configurations

respectively. This is because the amount of energy stored in the bed using the radial flow configuration is higher than in the axial flow configuration. This can be observed in temperature profiles too, where the whole bed ( $x = 0 - 1$ ) is at high temperature at the end of charging process. The charging efficiency was improved by using the solid plate. The efficiency gain noted via radial flow with two plates is approximately 5%. While not large, it is noted that this improvement is only during the charge cycle. As thermal dispersion effects will still occur in traditional axial flow systems during discharge, a higher overall gain in a full charge-discharge cycle with radial flow is expected and the focus of future work.

To get higher charging efficiency of the storage bed, the bed needs to be at higher temperature, which means more of the energy supplied will be stored in the bed. However, some of the supplied energy will be lost during the charging process. There are two forms of heat losses during the radial charging period: Heat losses to the ambient through the insulation and steel of the bed by conduction and convection, which reduces the energy stored in the bed. The second form of heat losses is the heat lost through the outlet of the bed during charging period, which can be seen in Figure 32a, where hot air leaves the bed instead of depositing the energy in the storage materials. However, the radial charging method mitigates axial thermal dispersion losses, leading to higher charging efficiency than the traditional axial charging.

Radial pipe injection is a new, novel method which could be considered in the design of TES systems. Large scale storage systems can be designed by injecting several internal radial tubes or pipes. One significant advantage of radial flow is the reduction in

the flow's length scale, which reduces dispersion. Sanderson and Cunningham [39] studied experimentally a vertical flow packed bed with sensible TES. A rectangular cross-section storage vessel (412.75 mm square by 1219.2 mm tall) was used with five different packing arrangements. The study showed that a thermally short packed bed reduced the radial temperature dispersion and led to better use of stored energy. Therefore, multiple radial pipes can be inserted along the storage bed domain to provide radial flow in shorter packing length scales. Solid plates with holes can be used in wide storage geometry to ensure flow evenly distributes in the storage packed bed. Each injected pipe will be divided into several layers with different hole diameters to assist in even flow based on coupling the hole design with the local resistance in the packing.

#### 4.4 Conclusions

The thermal behavior of an air-alumina packed bed was studied experimentally using a new radial pipe technique to heat the bed radially, focusing on the charging process. One flow rate at  $0.0048 \text{ m}^3/\text{s}$  was used. The heat transfer fluid was air with inlet temperature of  $75 \text{ }^\circ\text{C}$ , and the storage material used in the experiments was  $\alpha$ -alumina beads of diameter 6 mm. The thermal behavior during the charging process was analyzed for six different designs of the inserted radial tube. First, the study focused on even flow distribution along the length of the storage bed. Even flow was achieved by dividing the length of the radial tube into several layers with different hole sizes. Design E is considered as the best design based on even flow analysis, where the deviation from even flow is small compared to the rest of designs. This design utilized four layers, each 25 cm, where the hole size for radial injection decreased along the length of the tube. A solid plate was inserted at the outlet to



improve the thermal performance and reduce the outlet temperature. This plate has four holes at  $r = R$ , forcing flow from the radial tube toward the packed bed wells, improving the amount of energy stored in the bed. To further improve performance, a second internal plate was considered with the same hole pattern. In terms of thermal efficiency compared to traditional axial flow performance, the energy stored in the bed using radial charging with two plates is higher than that of axial flow. The charging efficiency increased from 75.3 % to  $80.3 \pm 2.8\%$ .

### Acknowledgements

This research did not receive any specific grant from funding agencies in the public, commercial, or not-for-profit sectors. The authors thank Montana State University for financial support. Mr. Al-Azawii thanks the Higher Committee for Educational Development in Iraq (HCED) for supporting his scholarship through the Iraqi government funding.

### Nomenclature

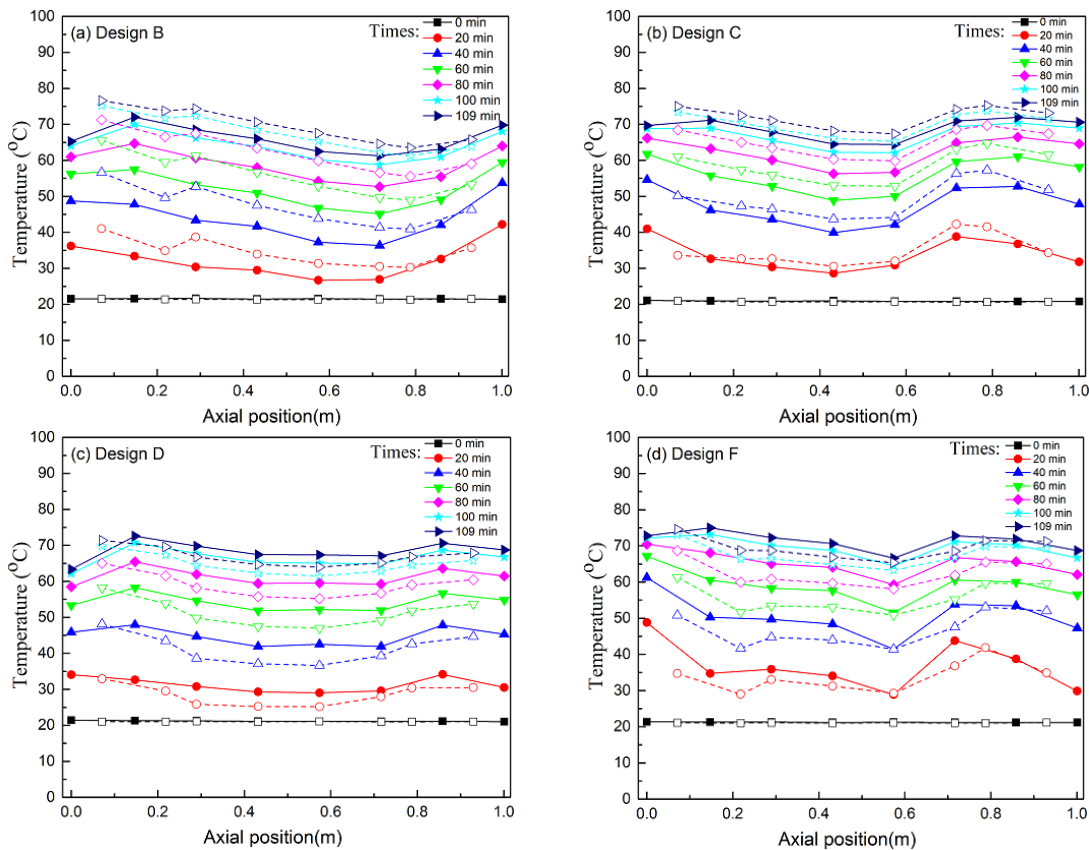
$t$	time (s)
$L$	length of packed bed (m)
$C_p$	specific heat capacity ( $\text{J kg}^{-1} \text{K}^{-1}$ )
$T$	temperature (K)
$Q_{bed}$	energy stored in the packed bed (kJ)
$Q_{supplied}$	energy supplied to the packed bed (kJ)
$\dot{m}$	mass flow rate ( $\text{kg s}^{-1}$ )
$\zeta_{charging}$	charging efficiency (-)

### Subscripts

$s$	storage
$hot$	storage temperature
$0$	initial
$abs$	absolute
$dev$	deviation

Appendix 4.A

Figure A1 shows the temperature profiles for designs B, C, D and F, where different hole sizes are used as explained in the experimental conditions and design section, Table 14.



**Figure A1:** Temperature profiles in the packed bed (1 m length) from sixteen sensing points (solid lines for TC1 and dash lines for TC2) for four designs, B, C, D, and F as presented in Table 14. The results show relative levels of even flow distribution based on the uniformity of the temperature response from  $x = 0 - 1$ .

Table A2 shows the percentage charging efficiency for radial and axial flow configurations. In radial flow, six designs were considered and analyzed. As can be seen, design A has the lowest charging efficiency and design E has the highest charging

efficiency. The charging efficiency for designs C and F are high too. However, the flow distribution and temperature profiles for design E were considered the most even.

**Table A2:** Percentage charging efficiency for Radial flow with six designs and traditional axial flow.

Flow	Charging efficiency (%)
Radial-design A	71.5
Radial-design B	73.5
Radial-design C	77.9
Radial-design D	73.2
Radial-design E-zero plate	77.8
Radial-design E-one plate	78.6
Radial-design E-two plates	80.2 ± 2.85
Radial-design F	77.4
Axial flow	75.3

### References

1. Panteli, M. and P. Mancarella, *Influence of extreme weather and climate change on the resilience of power systems: Impacts and possible mitigation strategies*. Electric Power Systems Research, 2015. **127**: p. 259-270.
2. *United States: MAP: How Climate Change Threatens America's Energy Infrastructure in Every Region*. 2015 [cited 2019 July 8]; Available from: <https://www.energy.gov/articles/map-how-climate-change-threatens-america-s-energy-infrastructure-every-region>.
3. IRENA, *Renewable Energy Statistics 2017*. 2017, International Renewable Energy Agency: Abu Dhabi.

4. Li, P., *Energy storage is the core of renewable technologies*. IEEE Nanotechnology Magazine, 2008. **2**(4): p. 13-18.
5. Dinçer, I.b., *Thermal energy storage : systems and applications*. 2nd ed.. ed, ed. M. Rosen. 2011: Chichester, England : Wiley.
6. Luo, X., et al., *Overview of current development in electrical energy storage technologies and the application potential in power system operation*. Applied Energy, 2015. **137**(C): p. 511-536.
7. Sharma, A., et al., *Review on thermal energy storage with phase change materials and applications*. Renewable and Sustainable Energy Reviews, 2009. **13**(2): p. 318-345.
8. Gil, A., et al., *State of the art on high temperature thermal energy storage for power generation. Part 1—Concepts, materials and modellization*. Renewable and Sustainable Energy Reviews, 2010. **14**(1): p. 31-55.
9. Medrano, M., et al., *State of the art on high-temperature thermal energy storage for power generation. Part 2—Case studies*. Renewable and Sustainable Energy Reviews, 2010. **14**(1): p. 56-72.
10. Pacheco, J.E., S.K. Showalter, and W.J. Kolb, *Development of a molten-salt thermocline thermal storage system for parabolic trough plants*. Journal of solar energy engineering, 2002. **124**(2): p. 153-159.
11. Bindra, H., et al., *Thermal analysis and exergy evaluation of packed bed thermal storage systems*. Applied Thermal Engineering, 2013. **52**(2): p. 255-263.

12. Wu, M., et al., *The impact of concrete structure on the thermal performance of the dual-media thermocline thermal storage tank using concrete as the solid medium*. Applied Energy, 2014. **113**: p. 1363-1371.
13. Reddy, K.S., et al., *Performance investigation of single-tank thermocline storage systems for CSP plants*. Solar Energy, 2017. **144**: p. 740-749.
14. Zanganeh, G., et al., *Packed-bed thermal storage for concentrated solar power – Pilot-scale demonstration and industrial-scale design*. Solar Energy, 2012. **86**(10): p. 3084-3098.
15. Prenzel, M., et al., *Thermo-fluid dynamic model for horizontal packed bed thermal energy storages*, in *Energy Procedia*. 2017. p. 51-61.
16. Soprani, S., et al., *Design and testing of a horizontal rock bed for high temperature thermal energy storage*. Applied Energy, 2019. **251**: p. 113345.
17. Vignarooban, K., et al., *Heat transfer fluids for concentrating solar power systems—a review*. Applied Energy, 2015. **146**: p. 383-396.
18. Benoit, H., et al., *Review of heat transfer fluids in tube-receivers used in concentrating solar thermal systems: Properties and heat transfer coefficients*. Renewable and Sustainable Energy Reviews, 2016. **55**: p. 298-315.
19. Alva, G., et al., *Thermal energy storage materials and systems for solar energy applications*. Renewable and Sustainable Energy Reviews, 2017. **68**: p. 693-706.
20. Tian, Y. and C.-Y. Zhao, *A review of solar collectors and thermal energy storage in solar thermal applications*. Applied energy, 2013. **104**: p. 538-553.

21. Hasnain, S.M., *Review on sustainable thermal energy storage technologies, Part I: heat storage materials and techniques*. Energy Conversion and Management, 1998. **39**(11): p. 1127-1138.
22. Cascetta, M., et al., *Numerical Investigation of a Packed Bed Thermal Energy Storage System with Different Heat Transfer Fluids*. 2014. p. 598-607.
23. Cascetta, M., et al., *A comparison between CFD simulation and experimental investigation of a packed-bed thermal energy storage system*. Applied Thermal Engineering, 2016. **98**: p. 1263-1272.
24. Al-Azawii, M.M.S., et al., *Experimental study on the cyclic behavior of thermal energy storage in an air-alumina packed bed*. Journal of Energy Storage, 2018. **18C**: p. 239-249.
25. Crandall, D.M. and E.F. Thacher, *Segmented thermal storage*. Solar Energy, 2004. **77**(4): p. 435-440.
26. Al-Azawii, M.M.S., et al., *Experimental study of layered thermal energy storage in an air-alumina packed bed using axial pipe injections*. Applied Energy, 2019. **249**: p. 409-422.
27. McTigue, J.D. and A. White, *Segmented packed beds for improved thermal energy storage performance*. IET Renew. Power Gener., 2016. **10**(10): p. 1498-1505.
28. White, A., J. McTigue, and C. Markides, *Analysis and optimisation of packed-bed thermal reservoirs for electricity storage applications*. Proceedings of the

- Institution of Mechanical Engineers, Part A: Journal of Power and Energy, 2016. **230**(7): p. 739-754.
29. Geissbühler, L., et al., *An assessment of thermocline-control methods for packed-bed thermal-energy storage in CSP plants, Part 1: Method descriptions*. Solar Energy, 2019. **178**: p. 341-350.
  30. Geissbühler, L., et al., *An assessment of thermocline-control methods for packed-bed thermal-energy storage in CSP plants, Part 2: Assessment strategy and results*. Solar Energy, 2019. **178**: p. 351-364.
  31. Bradley, L., *Regenerative Stove*. 1942: US patent 2,272,108.
  32. Fassbinder, H.-G., *Regenerator*. 1996: US patent 5,577,553.
  33. Daschner, R., S. Binder, and M. Mocker, *Pebble bed regenerator and storage system for high temperature use*. Applied Energy, 2013. **109**: p. 394-401.
  34. McTigue, J.D. and A.J. White, *A comparison of radial-flow and axial-flow packed beds for thermal energy storage*. Applied Energy, 2018. **227**(C): p. 533-541.
  35. Heggs, P.J., D.I. Ellis, and M.S. Ismail, *The modelling of fluid-flow distributions in annular packed beds*. Gas Separation and Purification, 1994. **8**(4): p. 257-264.
  36. Yang, Z. and S.V. Garimella, *Cyclic operation of molten-salt thermal energy storage in thermoclines for solar power plants*. Applied Energy, 2013. **103**: p. 256-265.
  37. Incropera, F.P., *Fundamentals of heat and mass transfer*. 6th ed. / Frank P. Incropera ... [et al.]. ed. 2007, Hoboken, NJ: Hoboken, NJ : John Wiley.

38. Gautam, A. and R. Saini, *A review on technical, applications and economic aspect of packed bed solar thermal energy storage system*. Journal of Energy Storage, 2020. **27**: p. 101046.
39. Sanderson, T.M. and G.T. Cunningham, *Packed bed thermal storage systems*. Applied Energy, 1995. **51**(1): p. 51-67.



## CHAPTER FIVE

## CONCLUSIONS AND RECOMMENDATIONS

5.1 Conclusions

The present thesis investigated the thermal performance of an air-alumina thermal packed bed energy storage system. The thermal performance was analyzed based on the temperature distribution and thermal efficiencies of the system. Three objectives related to gas flow into/from the packed bed were considered, studied and analyzed: traditional axial flow, layered axial flow, and radial flow. The study focused on experimental data with complementary modeling results.

For the entire thesis, air and  $\alpha$ -alumina ( $\text{Al}_2\text{O}_3$ ) beads were used as HTF and storage material, respectively. Air represents the energy carrier during storage/recovery processes at an inlet temperature of  $150^\circ\text{C}$  (chapters 2 and 3) and  $75^\circ\text{C}$  (chapter 4). Alumina represents the storage medium to absorb and release the energy, and 6 mm  $\alpha$ -alumina beads were poured randomly into the packed bed forming a porous storage domain. The length of the bed domain is 100 cm. The bed was designed, installed, and commissioned at Montana State University, including storage container flanges, custom installation, and custom thermocouples. To confirm that the experimental storage packed bed performed as designed, a computational fluid dynamics (CFD) model was built, and the model results agreed with the experimental results for four flow rates during charging. When starting a test, there were fluctuations in the inlet temperature during the first 15-20 minutes because of heat losses in the pipes (between heater and inlet of the bed) and the

entrance of the packed bed (flange, 10 cm free space and stainless steel perforated plate). After that, the temperature is constant. This temperature transient was considered in models and in experimental exergy calculations. The bed's design was intentionally modular, so various piping schemes could be considered. As demonstrated in the literature review, thermal exergetic efficiency is a function of heat losses to the environment and thermal dispersion within the bed. The analysis on multiple charging cycles of a typical bed and the new axial and radial pipe injection schemes were conceived to address these losses and increase the thermal efficiency of the bed. These three topics were presented in Chapters 2-4, respectively.

The work in chapter two quantified the thermal performance during traditional gas injection/recovery considering three variables: full charge/discharge cycle, multiple repeated partial charge/discharge cycles, and duration of storage time (no-flow hold after full charging). Each variable was considered at four flow rates. The results further served as a baseline for comparison to results in Chapters three and four. The quantification of thermal performance was performed based on the second law of thermodynamics, via analyzing the temperature distribution in the storage bed and the resulting recovery temperature of the gas, thus calculating the thermal exergy efficiency. The temperature profiles demonstrate the degree of thermocline in the bed domain during charging/discharging processes. At early times, the thermocline starts to form with high temperature in the first section of the bed length and low temperature in the rest of the bed. The outlet temperature is at room temperature in early times and starts to increase with time as the thermocline moves toward the exit of the bed. The spreading of the

temperature gradient along the length of the bed domain is due to axial thermal dispersion and heat losses. A less-sharp thermal front reduces the thermal exergy efficiency. The results show that energy stored in the bed increases with flow rate due to the faster contact between the hot gas and the storage materials. As a result, the thermal exergetic efficiency increases from 35.7 % at 0.002 m<sup>3</sup>/s (3 SCFM) to 55.4 % at 0.0061 m<sup>3</sup>/s (9SCFM). Partial cycles were defined as half of the full charge-discharge times. The energy stored per cycle decreases with the number of cycles for all flow rates that have been tested until the system reaches the steady state case, where the energy stored and recovered is constant. For instance, at 0.0048 m<sup>3</sup>/s (7 SCFM), the system reached a steady state after 8 cycles, and the exergy decreased from 79.1 % at cycle one to 66.3% at cycle 8. The thermal exergy efficiency for several repeated partial charge/discharge cycles with four flow rates can be seen in Figure 16a in chapter two. In addition, it was found that the energy stored in the bed decreases during the no-flow hold, which leads to a reduction in the exergetic efficiency. Thermal exergetic efficiency decreased from 53.2 % to 47.1 % after holding on for 30 minutes and to 31.0 % after holding on for 120 minutes between full cycles at 7 SCFM. This is because of the heat losses by radial conduction through the insulation and storage tank walls, which is high due to the high surface to volume ratio of the present laboratory scale storage packed bed. Thermal losses to the ambient can be reduced by decreasing the surface to volume ratio, which would occur in the large-diameter vessels used in application. However, the capital cost of designing larger diameter vessels is high, particularly in cases of a pressurized vessel, and this consideration must be balanced against the thermal performance. The reduction in

thermal performance and exergy efficiency is due to the combined impact of dispersive and heat losses. The relative contributions of dispersion and heat losses to the reduction in thermal exergy efficiency were estimated using model results by studying adiabatic and non-adiabatic models. Dispersive effects accumulate over multiple cycles, leading to a reduction in energy stored/recovered and thermal exergy efficiency. This reduction eventually reaches a minimum exergetic efficiency at each flow rate during partial charge-discharge cycles, which is an important consideration in industrial applications.

As noted, the dispersion phenomenon leads to the spreading of the temperature front along the bed length. This effect is reduced by a novel method to charge/discharge the bed domain, experimentally tested for the first time in this work. This method divides the bed domain (100 cm) into two (50 cm each) or three (33.33 cm each) layers. The layers are achieved by inserting pipes internally along the length of the bed domain length, where the outlet of each pipe represents the inlet to a layer. The experiments considered 17 configurations for testing. In the best cases, the spreading of the temperature front is reduced by reducing the length of the bed domain, mitigating the dispersive impacts. The thermocline is improved, particularly for three bed layers compared to one layer (i.e. the traditional case), and the thermal exergetic efficiency is increased. For instance, the thermal exergetic efficiency increases with the number of layers from 53.2% to 69.6% for 0.0048 m<sup>3</sup>/s and 55.4% to 73.4% for 0.0061 m<sup>3</sup>/s, from one layer to two layers. For three layers, thermal exergetic efficiencies increase to 76.8% and 80.3% at 0.0048 and 0.0061 m<sup>3</sup>/s respectively. However, the impact of heat and dispersion losses still exist. Heat losses and thermal dispersion are combined effects, and their contributions cannot be separated

experimentally. Therefore, the model was used again to separate the heat losses via removing the insulation and steel and assuming no heat flux at the boundary. Axial thermal dispersion was estimated by running the model for these adiabatic and non-adiabatic cases at two flow rates, which helped to separate the dispersion effects from the heat loss effects. It was found that the dispersion losses were reduced by 23.2% in the best two-layer case and 25.6% in the best three-layer case for  $0.0048 \text{ m}^3/\text{s}$  and by 22.8% in the best two-layer case and 26.5% in the best three-layer case for  $0.0061 \text{ m}^3/\text{s}$ . Reducing dispersion via this new gas flow technique leads to a substantial increase in the exergy efficiency.

In chapter 4, the idea of pipe injection is extended, but the charging process is changed to charge the bed radially instead of charging it axially. These experiments are the first time the radial flow concept has been applied to packed bed thermal energy storage, and results indicate increase in thermal energetic efficiency. The study first designed a radial tube that provides even flow within the bed. In order to avoid the large and small resistance of flow along the length of the bed, the length of the radial tube was designed into two, three, and four segments. Each segment had a different hole size, with larger diameters at the first half of the tube and smaller holes at the second half of the tube length. Six different tubes were designed and tested, with one considered as reasonable for even flow distribution. However, even flow was selected based on the resulting temperature distribution because it is difficult to measure the velocity distribution through the holes of the radial tube inside the storage tank. To further improve the thermal performance, increase the flow uniformity in the bed, and force the flow from the radial tube to flow outward toward  $r = R$  (the bed wall), a solid plate was inserted into the bed with four

circular holes at  $r = R$  at four angular positions ( $\Theta = 0, 90, 180, 270^\circ$ ). With this configuration, the thermal behavior during the charging process and charging efficiency based on the first law of thermodynamics was analyzed. The flow rate was  $0.0048 \text{ m}^3/\text{s}$  (7 SCFM) at an inlet temperature of  $75^\circ\text{C}$ . The results show the energy stored in the bed using the radial charging process is higher than the axial normal charging. In addition, the charging efficiency increases from 75.3 % (axial flow) to  $80.3 \pm 2.8$  % (radial flow with two plates). Complementary analysis of the pressure drop shows the pressure drop from the radial configuration may be lower than the traditional axial injection. These results provide a novel pathway for packed bed TES designers to improve system efficiency.

## 5.2 Recommendations

The present study gives reliable data on the thermal behavior of an air-alumina thermal energy storage packed bed system by providing lab-scale results, focusing on thermal temperature front profiles, heat losses, axial thermal dispersion losses and thermal efficiencies (based on first and second law of thermodynamics). The provided data are important in the TES field. Experimental and CFD issues, paths to improve the study, areas that need more investigation, and future work are explained below.

The quantified results in chapter two of full charge/discharge cycle and multiple repeated partial cycles show how the thermal performance can be affected via losses (heat and dispersion), flow rate and number of repeated cycles. The study could be extended by changing the operating conditions such as beads size (3 mm) and temperature focusing on exergetic efficiency for multiple repeated cycles. The maximum

temperature the current heater can provide is 430°C (800°F). However, the maximum temperature the storage packed bed can go is 343.4 °C (650°F).

In chapter three, the pipe injection technique results show good thermal performance, where thermocline and exergy efficiency are improved and dispersion losses are reduced by using two and three bed layers. The new method confirms/proves that increasing the bed layers can lead to improved thermal performance. Although the study was accomplished successfully, some related issues exist, which include:

1. To control the inlet temperature and keep it constant at 150°C during the charging process of the second and third layers, the heater temperature is changed. For example, consider the bed with two layers at 0.0048 m<sup>3</sup>/s (7 SCFM). When the charging process of layer one starts, the heater temperature is 173°C. Then, when the charging process of layer two starts, the heater temperature is 197°C. This is because the mass flow rate is divided between layer one and two (40% for layer one and 60% for layer 2 based on an approximate calibration and CFD model results), which leads to a reduction in inlet temperature due to mass flow reduction and thermal losses from the peripheral piping system. Therefore, the set temperature of the heater is changed to control the inlet temperature and have it at 150°C for both pipes. Calibration had been achieved to set up the heater temperature for each layer based on the percentage of air flowing in each pipe, controlled by valves. The most significant disadvantage of this procedure is concern that more energy is provided into the bed domain (more than 150°C ) as the mass flow rate in each pipe is not 100% controlled/known, and

there is no thermocouple to measure the temperature at the inlet of each layer into the bed.

2. The commercially available thermocouple probe was chosen to maximize the spatial resolution of the temperature measurement, providing eight measurements per meter. The probe measures temperature at  $x = 0$  and  $x = 100$  cm with six additional points between. However, segmenting the bed for flow into two and three equally sized layers meant that a thermocouple measurement was not identically co-located with the axial injection location (for two layers, the 2<sup>nd</sup> layer starts at  $x = 50$  cm and the closest sensing point is at  $x = 57$  cm). For three layers, the 2<sup>nd</sup> and 3<sup>rd</sup> layers start at  $x = 33.33$  and  $66.8$  cm and the closest sensing points are at  $x = 43$  and  $71$  cm.
3. The diameter of the packed bed is 12.47 cm. Therefore, it is difficult to divide the bed into more than three layers and inject more pipes. In addition, it is difficult to control the flow and temperature for four layers or more.

To perform the same experiments in an efficient way, and solve the flow and inlet temperature issues, two procedures are recommended:

- 1- Use a high temperature flowmeter at the inlet of each pipe/layer to measure the air flowing through the pipe. While this resolves the issue with knowing the amount of flow introduced to each layer, the heater temperature should still be increased when the charging process starts for the second layer. High temperature flowmeters are expensive, so the second procedure is recommended.
- 2- Use a second heater and split the flow before the heaters along with low temperature flowmeters to measure the mass flow rate flowing in each pipe/layer, and then



calibrate for the inlet temperature. It could be expensive for another heater, but not as expensive as the first procedure.

In addition, design a new internal thermocouple with temperature measurements identically co-located with the axial injection location of the pipes, or divide the bed into unequal size (length of layers is not identical). This will help to measure the inlet temperature for each layer accurately. Then, the study can be extended more accurately to study the effect of governing parameters on thermal behavior with multiple bed layers focusing on thermocline, dispersion and heat losses. Future work on pipe injection with multiple layers should focus on specifying the number of layers needed based on the bed dimensions (length and diameter). This can be achieved for the present packed bed via dividing the bed into four or six layers and analyzing the temperature front distribution and energy efficiency numerically and experimentally (the current equipment can be used to do only four layers experimentally, but a second heater is needed to control the inlet temperature). To test more than four layers (for example six layers) using the current equipment experimentally, a new custom flange should be utilized to insert six pipes of  $\frac{1}{4}$  inch diameter to charge the layers and two thermocouples to measure the temperature in the bed domain, Another study should focus on cyclic behavior for multiple bed layers (for two layers or more, a second heater would be needed to control the temperature for multiple cycles). In addition, the injected pipes are from one side (the charging side), which have been used to study 17 schemes for charging/discharging processes. Different charging/discharging schemes can be studied by injecting pipes from the discharging side as well, which could provide more details about multiple bed layers' performance. Another

study can be achieved by insulating the bed layers using insulations between the bed layers and comparing the results to the results from chapter 3, focusing on the thermal dispersion losses. The product, McMaster Carr, 9353K31 (rigid calcium silicate insulation, which was used to insulate the cover flange from inside (shown in the appendix) can be used to insulate the bed layers and will represent a barrier to separate the mass flow rate of each layer and prevent velocity variations. A new custom flange will be needed at the outlet side with several outlets (2-4) to insert pipes and use them as an outlet for each layer. The spreading of heat occurs because of hydrodynamic mixing of the fluid elements passing through the porous domain, which leads to thermal dispersion [1]. As explained in chapter 3, one of the reasons for this mixing is velocity variations, which impact the thermal dispersion phenomenon. Dispersion losses increase with flow rate as was explained in chapter 2. In the present study (chapter 3), the velocity of the heat transfer fluid is changing during the charging/discharging processes in each layer, which could lead to velocity variations in the pore scale and then affect thermal dispersion; for example, at  $0.0048 \text{ m}^3/\text{s}$  with two layers (case A3 in chapter 3), when the charging process of the 1<sup>st</sup> layer starts, the mass flow rate is the total flow. Then, when charging process of the 2<sup>nd</sup> layer starts, the flow divides between the two layers (layer one has less flow, layer two has all the flow since it combines with the flow from layer one). This behavior influences the heat transfer and the thermal dispersion in each layer. This behavior could be reduced by separating the bed layers using the proposed insulation technique. In addition, insulating the bed layers will help to separate the temperature thermal front profile for each layer, which might help reduce the temperature wave profile effect.

In chapter four, a new pipe injection technique was used, radial flow charging. Two paths should be considered to develop/extend the study. First, build a CFD model, which should focus on even flow distribution. It should be noted that some CFD modeling efforts have been achieved using COMSOL Multiphysics software to solve the even flow issue. However, the model needs to be extended to consider turbulent flow in the radial tube. The second path is considering the discharging process radially and analyzing the thermocline, dispersion and heat losses, and thermal exergy efficiency.

Related issues that have been recognized are:

- 1- The first sensing point in some designs were low ( $69^{\circ}\text{C}$  or less in some cases) due to two reasons: the high resistance at the first 5-10 cm of the bed and the flow behavior (flow starts radial and then axial). The first sensing point is at  $x = 0$  and  $r = 3.8$  cm, and not enough flow is provided to this first small layer of beads.
- 2- There was some temperature variation in the radial direction. One of the reasons for this variation is the flexible nature of the injected plastic tube. The tube might move to the right or left when the alumina beads are poured in the storage bed, which leads to some temperature variations.
- 3- The maximum temperature used was  $75^{\circ}\text{C}$  due to the temperature limit of the injected plastic tube (McMaster Carr 1487T3).
- 4- The radial holes were drilled by hand using a drill, which is not accurate 100% regarding size and spatial location.
- 5- The maximum flow rate used was  $0.0048\text{ m}^3/\text{s}$  (7 SCFM). The tube failed three times when a higher flow rate,  $0.0061\text{ m}^3/\text{s}$  (9 SCFM), was used. The tube failed at one

- location (the connection between the metal and plastic tube) as shown in Figure 34. Metal pipes connected the heater to the inlet (plastic tube) of the storage tank, which leads to the plastic tube bending at the connection point due to an unbalance in weight and the flexible nature of plastic tube. This led to a weak point under tension due to high flow with higher temperature. In addition, the failure of the tube could be due to increasing pressure drop. However, no information is available regarding pressure drop using radial flow, and it should be studied.
- 6- Solid plates were used to improve the thermal behavior and uniform flow distribution. It was impossible to use more than two solid plates at this time due to the small diameter of the bed, the internal insulation, and the horizontal layout of the storage tank.
  - 7- There was some leak of air flow from a small space between the solid plate and the bed wall, especially for the second inserted solid plate. The outer diameter of the solid plate is smaller than the inner diameter of the internal insulation. This space is left to easily insert the solid plate into the bed.
  - 8- The present experiment cannot do radial discharge using the same injected tube.

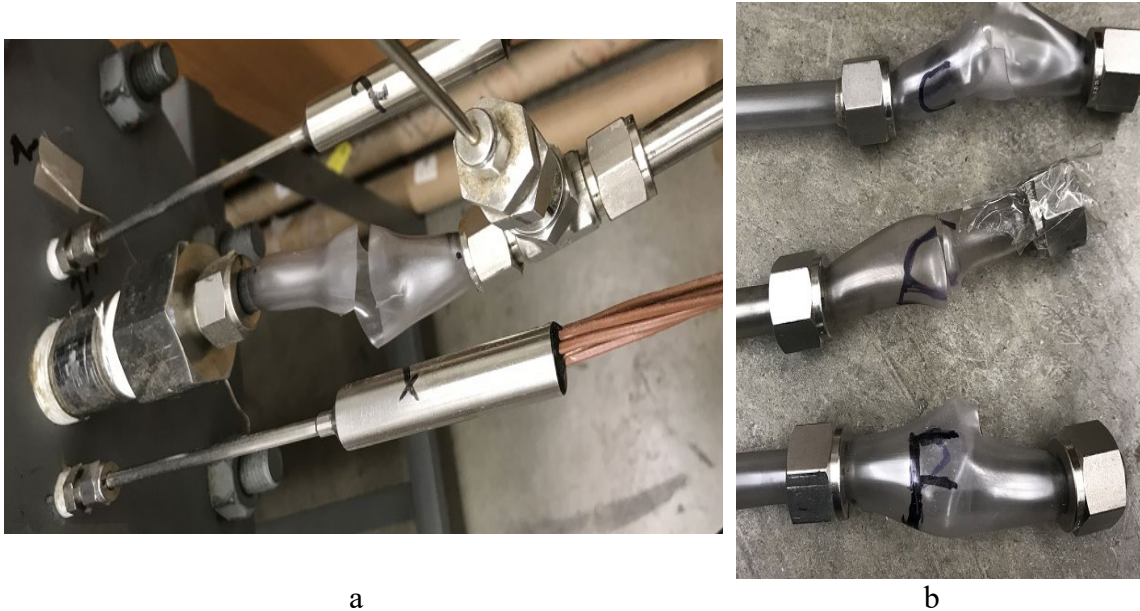


Figure 34: a) The radial tube fails at the connection point between the tube and the metal pipe, which are connected by a tee. b) Design C, E and F, which failed at the same axial location of the radial tube length.

To avoid or mitigate these issues, the following suggestions are recommended:

- 1- Perform an accurate CFD study to solve the even flow issue.
- 2- Add one or two sets of holes (four at each axial location) before the perforate plate (in the free space). This will help provide enough flow for the first layer of beads (the first 5 cm). This technique was used in the study and improved the temperature for the first sensing point.
- 3- Use a metal pipe instead of plastic tube. This will help to design the radial holes accurately, avoid any movement of the radial pipe inside the bed domain, and increase the temperature and flow rate ranges. However, it will be more expensive.
- 4- Inject another tube to do discharging processes. However, it is difficult to perform that in the present storage tank due to the vessel's small diameter.

- 5- Use a vertical storage tank to make the insertion of multiple solid plates easier. However, a balance between the radial holes' diameters based on the layers and number of solid plates should be investigated and analyzed (an extensive CFD study is recommended).
- 6- Seal the space between the solid plate and bed wall to stop flow leaking. Currently, this can be achieved only for the solid plate at the outlet. It was difficult to seal the 2<sup>nd</sup> inserted solid plate due to the small diameter of the packed bed.
- 7- Use four radial pipes at the wall to do the discharging process. The diameters of the pipe and radial holes should be investigated and designed.

Future work on pipe injection with radial flow should focus on even flow distribution and thermal behavior in the bed domain based on charging/discharging processes. The suggested studies that could be performed are:

- 1- Analyze the charging processes using two internal thermocouples via changing the angular positions of the thermocouples to measure the radial variation at different angular positions in the bed domain based on the radial locations of the both thermocouples. This can be achieved by rotating the flange at the inlet side clockwise or counterclockwise, where the first thermocouple will be at angular positions ( $\theta = 0, 45, 90, 135^\circ$ ) and the second thermocouple will be at angular positions ( $\theta = 180, 225, 270, 315^\circ$ ) providing eight different angular positions for temperature variation measurements. In addition, to get more information about the temperature variation in the r-direction, two holes

could be drilled in the cover flange at approximately  $r = 6.2 \text{ cm}$  (internal diameter of the insulation). Same experiment can be repeated two times with varying the radial locations of thermocouples to collect data at different radial directions.

- 2- Study the full charge/discharge processes and analyze the thermal performance and thermal exergy efficiency. Normal and radial flow with four pipes at the wall are suggested methods to perform the discharging process.
- 3- Study the full charge/discharge processes by dividing the bed domain into multiple layers and charge/discharge them radially.
- 4- Study partial discharging cycles with radial flow by charging the bed radially and discharging the bed axially. Note: In partial charging, the bed might not get back to the desired storage temperature.
- 5- In the suggested studies above, the analysis can be extended by studying/investigating different operating conditions such as flow rate (5, 9 and 11 SCFM), beads size (3 mm), and inlet temperature (150 and 300 °C). The maximum temperature that can be used is 343.4°C (650°F), which is the maximum temperature that the storage packed bed can go. Note: Designs B, D, E, and F cannot be used with 3 mm beads because each of these designs has one layer with 1/8 ( 3.18) inch (mm) of hole diameter. This hole size will allow some beads to fall inside the tube and block the flow. Therefore, new designs should be studied to see the effects of beads size on the even flow distribution and temperature profile, and the results should be compared to the results of 6

mm beads sizes. In addition, a screen mesh can be rolled around the radial tube (the 1/8 inch layer) to prevent the falling of the beads, which will help to compare the results of 6 mm beads size to 3 mm for the same tube design. An extensive CFD study on radial tube design should be considered.

- 6- Study the pressure drop via deriving the Ergun equation for radial flow distribution and compare that to the normal Ergun equation results. The pressure drop effect due to using solid plates should be studied too.
- 7- Study the pressure drop for all cases mentioned above with radial flow configuration and compare the results to axial flow configuration.

#### References

1. Nield, D.A. and A. Bejan, *Convection in porous media*. Vol. 3. 2013: New York: Springer.



CUMULATIVE REFERENCES CITED

1. Panteli, M. and P. Mancarella, *Influence of extreme weather and climate change on the resilience of power systems: Impacts and possible mitigation strategies*. Electric Power Systems Research, 2015. **127**: p. 259-270.
2. *United States: MAP: How Climate Change Threatens America's Energy Infrastructure in Every Region*. 2015 [cited 2019 July 8]; Available from: <https://www.energy.gov/articles/map-how-climate-change-threatens-america-s-energy-infrastructure-every-region>.
3. Li, P., *Energy storage is the core of renewable technologies*. IEEE Nanotechnology Magazine, 2008. **2**(4): p. 13-18.
4. Dinçer, I.b., *Thermal energy storage : systems and applications*. 2nd ed.. ed, ed. M. Rosen. 2011: Chichester, England : Wiley.
5. *The battery energy storage system market is expected to grow from USD 1.98 billion in 2018 to reach USD 8.54 billion by 2023, at a CAGR of 33.9% between 2018 and 2023*. 2018 [cited 2019 30 May]; Available from: [http://link.galegroup.com/apps/doc/A533445555/AONE?u=mtlib\\_1\\_1123&sid=AONE&xid=e7923f07](http://link.galegroup.com/apps/doc/A533445555/AONE?u=mtlib_1_1123&sid=AONE&xid=e7923f07).
6. *Taking battery technology from the lab to the big city*. 2013 [cited 2019 12 June]; Available from: <https://www.energy.gov/articles/taking-battery-technology-lab-big-city>.
7. Sharma, A., et al., *Review on thermal energy storage with phase change materials and applications*. Renewable and Sustainable Energy Reviews, 2009. **13**(2): p. 318-345.
8. Huggins, R.A., *Energy Storage*. 2010, Boston, MA: Boston, MA: Springer US.
9. Gil, A., et al., *State of the art on high temperature thermal energy storage for power generation. Part 1—Concepts, materials and modellization*. Renewable and Sustainable Energy Reviews, 2010. **14**(1): p. 31-55.
10. IRENA, *Thermal Energy Storage: Technology Brief E17*. January 2013, International Renewable Energy Agency: Abu Dhabi.
11. Chen, H., et al., *Progress in electrical energy storage system: A critical review*. 2009. p. 291-312.
12. Muthusivagami, R.M., R. Velraj, and R. Sethumadhavan, *Solar cookers with and without thermal storage—A review*. Renewable and Sustainable Energy Reviews, 2010. **14**(2): p. 691-701.

13. Indora, S. and T.C. Kandpal, *Institutional cooking with solar energy: A review*. Renewable and Sustainable Energy Reviews, 2018. **84**: p. 131-154.
14. Medrano, M., et al., *State of the art on high-temperature thermal energy storage for power generation. Part 2—Case studies*. Renewable and Sustainable Energy Reviews, 2010. **14**(1): p. 56-72.
15. *Linear concentrator system basics for concentrating solar power*. 2013 [cited 2019 13 June]; Available from: <https://energy.gov/eere/energybasics/articles/linear-concentrator-system-basics-concentrating-solar-power>.
16. Perez, R. and M. Perez, *A fundamental look at energy reserves for the planet*. Vol. 50. 2009.
17. IRENA, *Renewable Energy Statistics 2017*. 2017, International Renewable Energy Agency: Abu Dhabi.
18. *Goals of the Solar Energy Technologies Office*. [cited 2020 March, 20]; Available from: <https://www.energy.gov/eere/solar/goals-solar-energy-technologies-office>.
19. Murphy, C., et al., *The Potential Role of Concentrating Solar Power within the Context of DOE's 2030 Solar Cost Targets*. 2019, National Renewable Energy Lab.(NREL), Golden, CO (United States).
20. Cengel, Y.A., J.M. Cimbala, and R.H. Turner, *Fundamentals of thermal-fluid sciences*. 2012.
21. Incropera, F.P., *Fundamentals of heat and mass transfer*. 6th ed. / Frank P. Incropera ... [et al.]. ed. 2007, Hoboken, NJ: Hoboken, NJ : John Wiley.
22. Lane, G.A. and N. Shamsundar, *Solar heat storage: Latent heat materials, Vol. I: Background and scientific principles*. 1983, American Society of Mechanical Engineers.
23. Hasnain, S.M., *Review on sustainable thermal energy storage technologies, Part I: heat storage materials and techniques*. Energy Conversion and Management, 1998. **39**(11): p. 1127-1138.
24. Alva, G., et al., *Thermal energy storage materials and systems for solar energy applications*. Renewable and Sustainable Energy Reviews, 2017. **68**: p. 693-706.

25. Singh, H., R.P. Saini, and J.S. Saini, *A review on packed bed solar energy storage systems*. Renewable and Sustainable Energy Reviews, 2010. **14**(3): p. 1059-1069.
26. Fernandez, A.I., et al., *Selection of materials with potential in sensible thermal energy storage*. Solar Energy Materials and Solar Cells, 2010. **94**(10): p. 1723-1729.
27. Khare, S., et al., *Selection of materials for high temperature sensible energy storage*. Solar Energy Materials and Solar Cells, 2013. **115**: p. 114-122.
28. Wyman, C., J. Castle, and F. Kreith, *A review of collector and energy storage technology for intermediate temperature applications*. Solar Energy, 1980. **24**(6): p. 517-540.
29. Galione, P., et al., *A new thermocline-PCM thermal storage concept for CSP plants. Numerical analysis and perspectives*. Energy Procedia, 2014. **49**: p. 790-799.
30. Nithyanandam, K., R. Pitchumani, and A. Mathur, *Analysis of a latent thermocline storage system with encapsulated phase change materials for concentrating solar power*. Applied Energy, 2014. **113**: p. 1446.
31. Ramana, A., et al., *Experimental investigation of the LHS system and comparison of the stratification performance with the SHS system using CFD simulation*. Solar energy, 2014. **103**: p. 378-389.
32. Zanganeh, G., et al., *Experimental and numerical investigation of combined sensible-latent heat for thermal energy storage at 575 °C and above*. Solar Energy, 2015. **114**: p. 77-90.
33. Zanganeh, G., et al., *Stabilization of the outflow temperature of a packed-bed thermal energy storage by combining rocks with phase change materials*. Applied Thermal Engineering, 2014. **70**(1): p. 316-320.
34. Okello, D., et al., *An experimental investigation on the combined use of phase change material and rock particles for high temperature (~350 °C) heat storage*. Energy Conversion and Management, 2014. **79**: p. 1-8.
35. Galione, P., et al., *Multi-layered solid-PCM thermocline thermal storage concept for CSP plants. Numerical analysis and perspectives*. Applied energy, 2015. **142**: p. 337-351.

36. Galione, P., et al., *Multi-layered solid-PCM thermocline thermal storage for CSP. Numerical evaluation of its application in a 50 MWe plant*. Solar Energy, 2015. **119**: p. 134-150.
37. Farid, M.M., et al., *A review on phase change energy storage: materials and applications*. Energy Conversion and Management, 2004. **45**(9): p. 1597-1615.
38. de Gracia, A. and L.F. Cabeza, *Numerical simulation of a PCM packed bed system: a review*. Renewable and Sustainable Energy Reviews, 2017. **69**: p. 1055-1063.
39. Lin, Y., G. Alva, and G. Fang, *Review on thermal performances and applications of thermal energy storage systems with inorganic phase change materials*. Energy, 2018. **165**: p. 685-708.
40. Wei, G., et al., *Selection principles and thermophysical properties of high temperature phase change materials for thermal energy storage: A review*. Renewable and Sustainable Energy Reviews, 2018. **81**: p. 1771-1786.
41. Elias, C.N. and V.N. Stathopoulos, *A comprehensive review of recent advances in materials aspects of phase change materials in thermal energy storage*. Energy Procedia, 2019. **161**: p. 385-394.
42. Herrmann, U., B. Kelly, and H. Price, *Two-tank molten salt storage for parabolic trough solar power plants*. Energy, 2004. **29**(5): p. 883-893.
43. Kelly, B., *Thermal storage commercial plant design study for a 2-tank indirect molten salt system final report, May 13, 2002 - December 31, 2004*, D. Kearney, et al., Editors. 2006, Golden, Colo. : National Renewable Energy Laboratory: Golden, Colo.
44. *Concentrating solar power thermal storage system basics*. 2013 [cited 2018 July 31]; Available from: <https://energy.gov/eere/energybasics/articles/concentrating-solar-power-thermal-storage-system-basics>.
45. Tamme, R., et al. *Innovative thermal energy storage technology for parabolic trough concentrating solar power plants*. in *Proceedings EuroSun*. 2002.
46. Pacheco, J.E., S.K. Showalter, and W.J. Kolb, *Development of a molten-salt thermocline thermal storage system for parabolic trough plants*. Journal of solar energy engineering, 2002. **124**(2): p. 153-159.
47. Bindra, H., et al., *Thermal analysis and exergy evaluation of packed bed thermal storage systems*. Applied Thermal Engineering, 2013. **52**(2): p. 255-263.

48. Wu, M., et al., *The impact of concrete structure on the thermal performance of the dual-media thermocline thermal storage tank using concrete as the solid medium*. Applied Energy, 2014. **113**: p. 1363-1371.
49. Johnson, E., et al., *Thermal energy storage with supercritical carbon dioxide in a packed bed: Modeling charge-discharge cycles*. The Journal of Supercritical Fluids, 2018. **137**: p. 57-65.
50. Prenzel, M., et al., *Thermo-fluid dynamic model for horizontal packed bed thermal energy storages*. Energy Procedia, 2017. **135**: p. 51-61.
51. Al-Azawii, M.M.S., et al., *Experimental study on the cyclic behavior of thermal energy storage in an air-alumina packed bed*. Journal of Energy Storage, 2018. **18C**: p. 239-249.
52. Al-Azawii, M.M.S., et al., *Experimental study of layered thermal energy storage in an air-alumina packed bed using axial pipe injections*. Applied Energy, 2019. **249**: p. 409-422.
53. Gautam, A. and R. Saini, *A review on technical, applications and economic aspect of packed bed solar thermal energy storage system*. Journal of Energy Storage, 2020. **27**: p. 101046.
54. Cárdenas, B., et al., *Effect of design parameters on the exergy efficiency of a utility-scale packed bed*. Journal of Energy Storage, 2018. **18**: p. 267-284.
55. Meier, A., C. Winkler, and D. Wuillemin, *Experiment for modeling high-temperature rock bed storage*. Solar Energy Materials, 1991. **24**(1-4): p. 255-264.
56. Wu, C. and G. Hwang, *Flow and heat transfer characteristics inside packed and fluidized beds*. Journal of heat transfer, 1998. **120**(3): p. 667-673.
57. Hänchen, M., S. Brückner, and A. Steinfeld, *High-temperature thermal storage using a packed bed of rocks – Heat transfer analysis and experimental validation*. Applied Thermal Engineering, 2011. **31**(10): p. 1798-1806.
58. Cascetta, M., et al., *Numerical investigation of a packed bed thermal energy storage system with different heat transfer fluids*. Energy Procedia, 2014. **45**: p. 598-607.
59. Anderson, R., et al., *Experimental results and modeling of energy storage and recovery in a packed bed of alumina particles*. Applied Energy, 2014. **119**: p. 521-529.

60. Coutier, J.P. and E. Farber, *Two applications of a numerical approach of heat transfer process within rock beds*. Solar Energy, 1982. **29**(6): p. 451-462.
61. Yang, Z. and S.V. Garimella, *Thermal analysis of solar thermal energy storage in a molten-salt thermocline*. Solar Energy, 2010. **84**(6): p. 974-985.
62. Bruch, A., J.F. Fourmigue, and R. Couturier, *Experimental and numerical investigation of a pilot-scale thermal oil packed bed thermal storage system for CSP power plant*. Solar Energy, 2014. **105**: p. 116-125.
63. Ismail, K.A.R. and R. Stuginsky Jr, *A parametric study on possible fixed bed models for pcm and sensible heat storage*. Applied Thermal Engineering, 1999. **19**(7): p. 757-788.
64. Bejan, A., *Convection heat transfer*. 4th ed.. ed. 2013: Hoboken, New Jersey : Wiley.
65. Hsu, C. and P. Cheng, *Closure schemes of the macroscopic energy equation for convective heat transfer in porous media*. International communications in heat and mass transfer, 1988. **15**(5): p. 689-703.
66. Nield, D.A. and A. Bejan, *Convection in porous media*. Vol. 3. 2013: New York: Springer.
67. Schumann, T.E., *Heat transfer: a liquid flowing through a porous prism*. Journal of the Franklin Institute, 1929. **208**(3): p. 405-416.
68. Amundson, N.R., *Solid-fluid interactions in fixed and moving beds fixed beds with small particles*. Industrial & Engineering Chemistry, 1956. **48**(1): p. 26-35.
69. Beasley, D.E. and J.A. Clark, *Transient response of a packed bed for thermal energy storage*. International Journal of Heat and Mass Transfer, 1984. **27**(9): p. 1659-1669.
70. Furnas, C., *Heat transfer from a gas stream to bed of broken solids*. Industrial & Engineering Chemistry, 1930. **22**(1): p. 26-31.
71. Löf, G. and R. Hawley, *Unsteady-state heat transfer between air and loose solids*. Industrial & Engineering Chemistry, 1948. **40**(6): p. 1061-1070.
72. Handley, D. and P. Heggs, *The effect of thermal conductivity of the packing material on transient heat transfer in a fixed bed*. International Journal of Heat and Mass Transfer, 1969. **12**(5): p. 549-570.

73. Sanderson, T. and G. Cunningham, *Performance and efficient design of packed bed thermal storage systems. Part I*. Applied energy, 1995. **50**(2): p. 119-132.
74. Regin, A.F., S. Solanki, and J. Saini, *An analysis of a packed bed latent heat thermal energy storage system using PCM capsules: Numerical investigation*. Renewable energy, 2009. **34**(7): p. 1765-1773.
75. Felix, R., S. Solanki, and J. Saini. *Thermal performance analysis of phase change material capsules*. in *ISES 2005 Solar world congress*. 2005.
76. Ismail, K. and J. Henriquez, *Numerical and experimental study of spherical capsules packed bed latent heat storage system*. Applied Thermal Engineering, 2002. **22**(15): p. 1705-1716.
77. Anderson, R., et al., *Packed bed thermal energy storage: A simplified experimentally validated model*. Journal of Energy Storage, 2015. **4**: p. 14-23.
78. Wakao, N. and S. Kagei, *Heat and mass transfer in packed beds*. Vol. 1. 1982: Taylor & Francis.
79. Vortmeyer, D. and R.J. Schaefer, *Equivalence of one- and two-phase models for heat transfer processes in packed beds: one dimensional theory*. Chemical Engineering Science, 1974. **29**(2): p. 485-491.
80. Dixon, A.G. and D.L. Cresswell, *Theoretical prediction of effective heat transfer parameters in packed beds*. AIChE Journal, 1979. **25**(4): p. 663-676.
81. Vortmeyer, D. and R. Schaefer, *Equivalence of one-and two-phase models for heat transfer processes in packed beds: one dimensional theory*. Chemical Engineering Science, 1974. **29**(2): p. 485-491.
82. Sanderson, T.M. and G.T. Cunningham, *Packed bed thermal storage systems*. Applied Energy, 1995. **51**(1): p. 51-67.
83. Zanganeh, G., et al., *Packed-bed thermal storage for concentrated solar power – Pilot-scale demonstration and industrial-scale design*. Solar Energy, 2012. **86**(10): p. 3084-3098.
84. Cascetta, M., et al., *A comparison between CFD simulation and experimental investigation of a packed-bed thermal energy storage system*. Applied Thermal Engineering, 2016. **98**: p. 1263-1272.
85. Prenzel, M., et al., *Thermo-fluid dynamic model for horizontal packed bed thermal energy storages*, in *Energy Procedia*. 2017. p. 51-61.



86. Öhman, H. and P. Lundqvist, *Comparison and analysis of performance using Low Temperature Power Cycles*. Applied Thermal Engineering, 2013. **52**(1): p. 160-169.
87. Hettiarachchi, H.M., et al., *Optimum design criteria for an organic Rankine cycle using low-temperature geothermal heat sources*. Energy, 2007. **32**(9): p. 1698-1706.
88. Heller, P., et al., *Test and evaluation of a solar powered gas turbine system*. Solar Energy, 2006. **80**(10): p. 1225-1230.
89. Tijani, M. and S. Spoelstra, *A hot air driven thermoacoustic-Stirling engine*. Applied thermal engineering, 2013. **61**(2): p. 866-870.
90. González-Roubaud, E., D. Pérez-Osorio, and C. Prieto, *Review of commercial thermal energy storage in concentrated solar power plants: Steam vs. molten salts*. Renewable and sustainable energy reviews, 2017. **80**: p. 133-148.
91. Laing, D., et al., *Thermal energy storage for direct steam generation*. Solar Energy, 2011. **85**(4): p. 627-633.
92. Esence, T., et al., *A review on experience feedback and numerical modeling of packed-bed thermal energy storage systems*. Solar Energy, 2017. **153**: p. 628-654.
93. Cascetta, M., et al. *Experimental investigation of a packed bed thermal energy storage system*. in *Journal of Physics: Conference Series*. 2015. IOP Publishing.
94. Erregueragui, Z., et al., *Packed-bed thermal energy storage analysis: quartzite and palm-oil performance*. Energy Procedia, 2016. **99**: p. 370-379.
95. Aly, S. and A. El-Sharkawy, *Effect of storage medium on thermal properties of packed beds*. Heat Recovery Systems & CHP, 1990. **10 no.5/6**(1990): p. 509-517.
96. Mawire, A., et al., *Simulated performance of storage materials for pebble bed thermal energy storage (TES) systems*. Applied Energy, 2009. **86**(7): p. 1246-1252.
97. Warkhade, G.S., et al., *Experimental investigation of sensible thermal energy storage in small sized, different shaped concrete material packed bed*. World Journal of Engineering, 2016. **13**(5): p. 386-393.
98. Singh, H., R.P. Saini, and J.S. Saini, *Performance of a packed bed solar energy storage system having large sized elements with low void fraction*. Solar Energy, 2013. **87**(1): p. 22-34.

99. Yeboah, S. and J. Darkwa, *A critical review of thermal enhancement of packed beds for water vapour adsorption*. Renewable and Sustainable Energy Reviews, 2016. **58**: p. 1500-1520.
100. Kadoli, R. and T.A. Babu, *Performance studies on the desiccant packed bed with varying particle size distribution along the bed*. International journal of refrigeration, 2012. **35**(3): p. 663-675.
101. Kuravi, S., et al., *Investigation of a high-temperature packed-bed sensible heat thermal energy storage system with large-sized elements*. Journal of solar energy engineering, 2013. **135**(4).
102. Okello, D., O.J. Nydal, and E.J. Banda, *Experimental investigation of thermal de-stratification in rock bed TES systems for high temperature applications*. Energy conversion and management, 2014. **86**: p. 125-131.
103. Cascetta, M., et al., *A Study of a Packed-bed Thermal Energy Storage Device: Test Rig, Experimental and Numerical Results*. Energy Procedia, 2015. **81**: p. 987-994.
104. Cascetta, M., et al., *Experimental and Numerical Research Activity on a Packed Bed TES System*. Energies, 2016. **9**(9): p. 758.
105. Nakayama, A., F. Kuwahara, and Y. Kodama, *An equation for thermal dispersion flux transport and its mathematical modelling for heat and fluid flow in a porous medium*. Journal of Fluid Mechanics, 2006. **563**: p. 81-96.
106. Gunn, D., *Theory of axial and radial dispersion in packed beds*. Trans. Inst. Chem. Eng, 1969. **47**(10): p. T351-T359.
107. Saez, A.E. and B. McCoy, *Dynamic response of a packed bed thermal storage system—a model for solar air heating*. Solar Energy, 1982. **29**(3): p. 201-206.
108. Çengel, Y.A. and M.A. Boles, *Thermodynamics: An Engineering Approach,-PDF*. 2008: McGraw-Hill.
109. Bejan, A., *Thermal design and optimization*, ed. M.J. Moran and G. Tsatsaronis. 1996, New York: New York : John Wiley & Sons.
110. Dincer, I. and M.A. Rosen, *Exergy: energy, environment and sustainable development*. 2012: Newnes.
111. Cumpston, J. and A. Mitsos, *Concentrating Solar Thermal Overview*. Chemical Engineering Progress, 2017. **113**(7): p. 21-28,42.

112. Jenkins, S., *Low-cost solar collectors provide renewable process heat*. Chemical Engineering: Essentials for the CPI Professional, 2017, June: p. 8-9.
113. Khare, S., et al., *Selection of materials for high temperature latent heat energy storage*. Solar Energy Materials and Solar Cells, 2012. **107**(C): p. 20-27.
114. Bruch, A., et al., *Experimental and Numerical Investigation of Stability of Packed Bed Thermal Energy Storage for CSP Power Plant*. 2014. p. 743-751.
115. Peng, H., H. Dong, and X. Ling, *Thermal investigation of PCM-based high temperature thermal energy storage in packed bed*. Energy Conversion and Management, 2014. **81**: p. 420-427.
116. Oró, E., et al., *Stratification analysis in packed bed thermal energy storage systems*. Applied Energy, 2013. **109**(SI): p. 476-487.
117. Liu, C., Cheng, M. S., Zhao, B. C., & Dai, Z. M., *Thermal performance analysis of a thermocline thermal energy storage system with FLiNaK molten salt*, in *Earth and Environmental Science* 2017 January IOP Publishing. p. 012039.
118. Yin, H., et al., *Thermocline characteristics of molten-salt thermal energy storage in porous packed-bed tank*. Applied Thermal Engineering, 2017. **110**: p. 855-863.
119. Hoffmann, J.F., et al., *Experimental and numerical investigation of a thermocline thermal energy storage tank*. Applied Thermal Engineering, 2017. **114**: p. 896-904.
120. Ortega-Fernández, I., et al. *Parametric analysis of a packed bed thermal energy storage system*. in *AIP Conference Proceedings*. 2017. AIP Publishing.
121. Yang, Z. and S.V. Garimella, *Cyclic operation of molten-salt thermal energy storage in thermoclines for solar power plants*. Applied Energy, 2013. **103**: p. 256-265.
122. Yang, Z. and S.V. Garimella, *Molten-salt thermal energy storage in thermoclines under different environmental boundary conditions*. Applied Energy, 2010. **87**(11): p. 3322-3329.
123. Bruch, A., et al., *Experimental investigation of cycling behaviour of pilot-scale thermal oil packed-bed thermal storage system*. Renewable Energy, 2017. **103**: p. 277-285.
124. Zavattoni, S., et al., *High temperature rock-bed TES system suitable for industrial-scale CSP plant—CFD analysis under charge/discharge cyclic conditions*. Energy Procedia, 2014. **46**: p. 124-133.

125. Scheidegger, A.E., *The physics of flow through porous media*. 1957, Toronto: Toronto University of Toronto Press.
126. Zhang, W., et al., *Relationship between packing structure and porosity in fixed beds of equilateral cylindrical particles*. *Chemical Engineering Science*, 2006. **61**(24): p. 8060-8074.
127. Bejan, A. and A.D. Kraus, *Heat transfer handbook*. 2003, Hoboken, N.J.: Hoboken, N.J. : John Wiley & Sons, INC.
128. Hilsenrath, J., *Tables of thermal properties of gases: comprising tables of thermodynamic and transport properties of air, argon, carbon dioxide, carbon monoxide, hydrogen, nitrogen, oxygen, and steam*. 1955, Washington, D.C.: US Dept. of Commerce, National Bureau of Standards.
129. Morrell, R., *Handbook of properties of technical and engineering ceramics*. 1987: Part 2. Hmsco.
130. Munro, M., *Evaluated Material Properties for a Sintered alpha-Alumina*. *Journal of the American Ceramic Society*, 1997. **80**(8): p. 1919-1928.
131. IRENA, *Concentrating solar power-renewable energy technologies: Cost analysis series, vol. 1: Power sector*. 2012, International Renewable Energy Agency: Abu Dhabi. p. 1-48.
132. Reddy, K.S., et al., *Performance investigation of single-tank thermocline storage systems for CSP plants*. *Solar Energy*, 2017. **144**: p. 740-749.
133. Zhao, B.-C., et al., *Thermal performance and cost analysis of a multi-layered solid-PCM thermocline thermal energy storage for CSP tower plants*. *Applied Energy*, 2016. **178**: p. 784-799.
134. Zhao, B.-C., et al., *System-level performance optimization of molten-salt packed-bed thermal energy storage for concentrating solar power*. *Applied Energy*, 2018. **226**: p. 225-239.
135. Mawire, A. and S.H. Taole, *A comparison of experimental thermal stratification parameters for an oil/pebble-bed thermal energy storage (TES) system during charging*. *Applied Energy*, 2011. **88**(12): p. 4766-4778.
136. White, A., J. McTigue, and C. Markides, *Wave propagation and thermodynamic losses in packed-bed thermal reservoirs for energy storage*. *Applied Energy*, 2014. **130**: p. 648.

137. Zanganeh, G., et al., *Design of packed bed thermal energy storage systems for high-temperature industrial process heat*. Applied Energy, 2015. **137**: p. 812-822.
138. Esen, M., A. Durmuş, and A. Durmuş, *Geometric design of solar-aided latent heat store depending on various parameters and phase change materials*. Solar Energy, 1998. **62**(1): p. 19-28.
139. Geissbühler, L., et al., *An assessment of thermocline-control methods for packed-bed thermal-energy storage in CSP plants, Part 1: Method descriptions*. Solar Energy, 2019. **178**: p. 341-350.
140. Geissbühler, L., et al., *An assessment of thermocline-control methods for packed-bed thermal-energy storage in CSP plants, Part 2: Assessment strategy and results*. Solar Energy, 2019. **178**: p. 351-364.
141. Crandall, D. and E. Thacher, *Segmented thermal storage*. Solar Energy, 2004. **77**(4): p. 435-440.
142. McTigue, J.D. and A. White, *Segmented packed beds for improved thermal energy storage performance*. IET Renew. Power Gener., 2016. **10**(10): p. 1498-1505.
143. White, A., J. McTigue, and C. Markides, *Analysis and optimisation of packed-bed thermal reservoirs for electricity storage applications*. Proceedings of the Institution of Mechanical Engineers, Part A: Journal of Power and Energy, 2016. **230**(7): p. 739-754.
144. McTigue, J.D. and A.J. White, *A comparison of radial-flow and axial-flow packed beds for thermal energy storage*. Applied Energy, 2018. **227**(C): p. 533-541.
145. Howes JS, M.J., Hunt RG, *Layered thermal store with selectivity alterable gas flow path*. 2017: US. Patent number US009658004B2.
146. Howes JS, M.J., Hunt RG, Bennet GR, Wilson BA, *Thermal energy storage apparatus*. 2018: US. Patent number US009970715B.
147. Bindra, H., P. Bueno, and J.F. Morris, *Sliding flow method for exergetically efficient packed bed thermal storage*. Applied Thermal Engineering, 2014. **64**(1-2): p. 201-208.
148. Luo, X., et al., *Overview of current development in electrical energy storage technologies and the application potential in power system operation*. Applied Energy, 2015. **137**(C): p. 511-536.

149. Soprani, S., et al., *Design and testing of a horizontal rock bed for high temperature thermal energy storage*. Applied Energy, 2019. **251**: p. 113345.
150. Vignarooban, K., et al., *Heat transfer fluids for concentrating solar power systems—a review*. Applied Energy, 2015. **146**: p. 383-396.
151. Benoit, H., et al., *Review of heat transfer fluids in tube-receivers used in concentrating solar thermal systems: Properties and heat transfer coefficients*. Renewable and Sustainable Energy Reviews, 2016. **55**: p. 298-315.
152. Tian, Y. and C.-Y. Zhao, *A review of solar collectors and thermal energy storage in solar thermal applications*. Applied energy, 2013. **104**: p. 538-553.
153. Cascetta, M., et al., *Numerical Investigation of a Packed Bed Thermal Energy Storage System with Different Heat Transfer Fluids*. 2014. p. 598-607.
154. Crandall, D.M. and E.F. Thacher, *Segmented thermal storage*. Solar Energy, 2004. **77**(4): p. 435-440.
155. Bradley, L., *Regenerative Stove*. 1942: US patent 2,272,108.
156. Fassbinder, H.-G., *Regenerator*. 1996: US patent 5,577,553.
157. Daschner, R., S. Binder, and M. Mocker, *Pebble bed regenerator and storage system for high temperature use*. Applied Energy, 2013. **109**: p. 394-401.
158. Heggs, P.J., D.I. Ellis, and M.S. Ismail, *The modelling of fluid-flow distributions in annular packed beds*. Gas Separation and Purification, 1994. **8**(4): p. 257-264.

APPENDICES


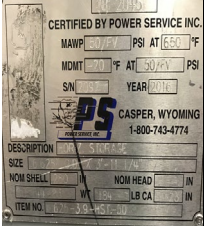




APPENDIX A

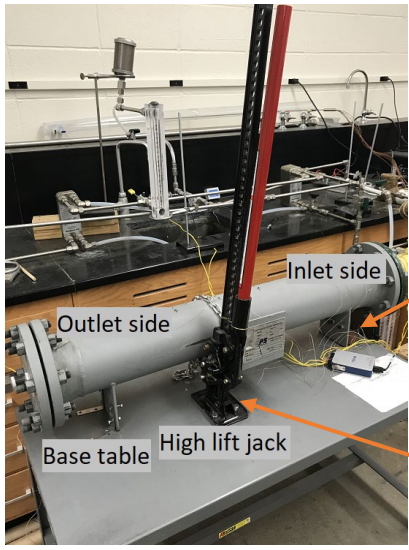

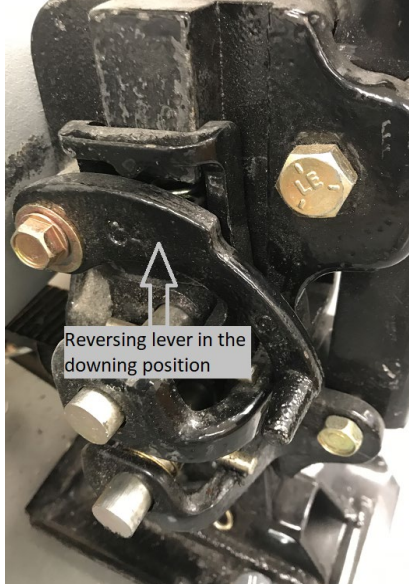
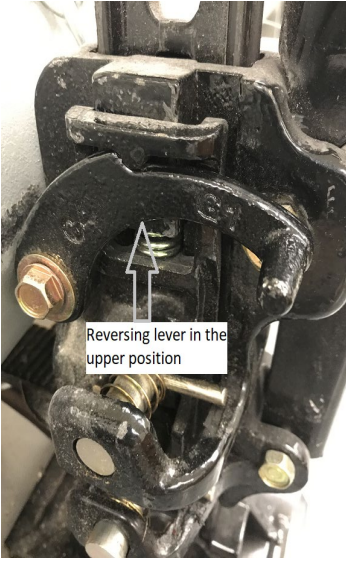
PIECES OF APPARATUS AND EQUIPMENT USED IN THE LAB; AND  
SCREENSHOTS OF LABVIEW CODE AND DATA ANALYSIS



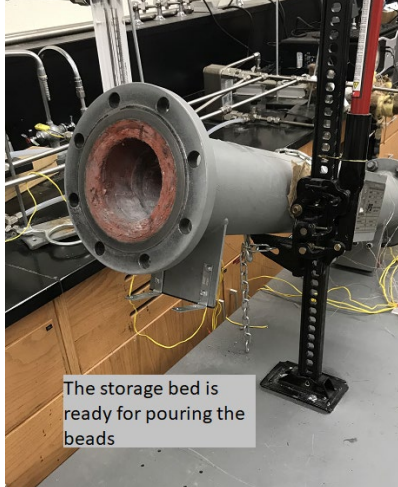
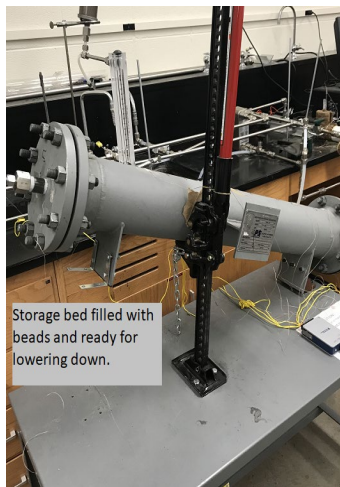


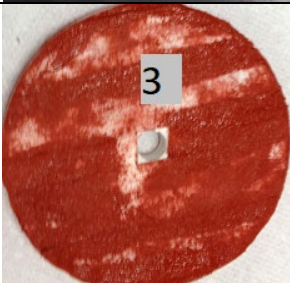



This appendix includes tables of the storage apparatus, all equipment used to run the experiments with images of pieces and their descriptions, and screenshots of LabView code and data analysis. Note: Appendix E shows equipment used with parts numbers and manufacturer.

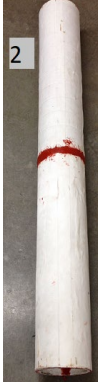

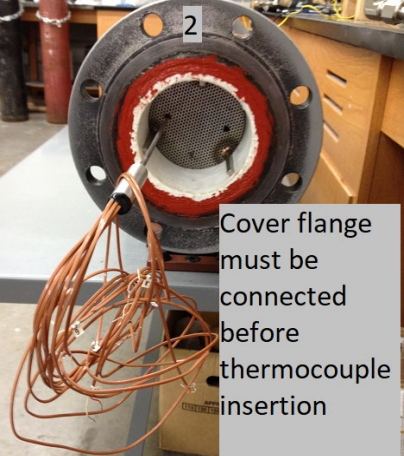
Table A.1 Storage Packed Bed Apparatus, Internal Insulation, and Internal Thermocouple

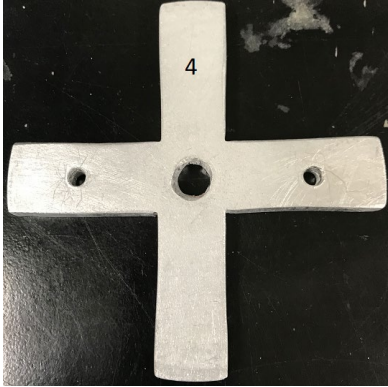
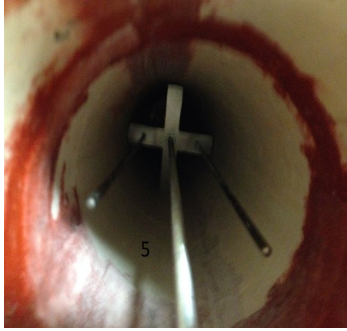
Name	Image		Description
<p>Packed bed apparatus</p>	 <p>Storage vessel before installation</p>		<p>Packed bed is rated to 650°F and 60 PSI</p> 
<p>Cover flange</p>	 <p>Inlet fitting, SS-810-7-16</p> <p>Internal thermocouples fittings, SS-300-1-4BT</p>	 <p>1" nipple</p>	<p>Left: Cover flange inlet side showing air flow inlet fitting and internal thermocouples fittings. Right: Cover flange outlet side (side view) showing the nipple connector, outlet fitting and bolts</p>
<p>Custom flange for injected pipes</p>			<p>Custom flange from inside showing five holes (four with 1/2 inch FNPT for injected pipes and one with 1/4 inch FNPT for internal thermocouple) and from outside showing pipe fitting (two layers),</p>

			<p>thermocouple fitting and 1/2 inch hole steel plug</p>
<p>Installed storage bed</p>			<p>The horizontal storage vessel installed on a table. A high lift jack is used to tilt the bed about 45-60°, which is connected to the table. The inlet is on the right side and the outlet is on the left side</p>
<p>Reversing lever position of high lift jack</p>			<p>The high lift jack showing the reversing lever. When you tilt the bed, the reversing lever must be in the upper position.</p>

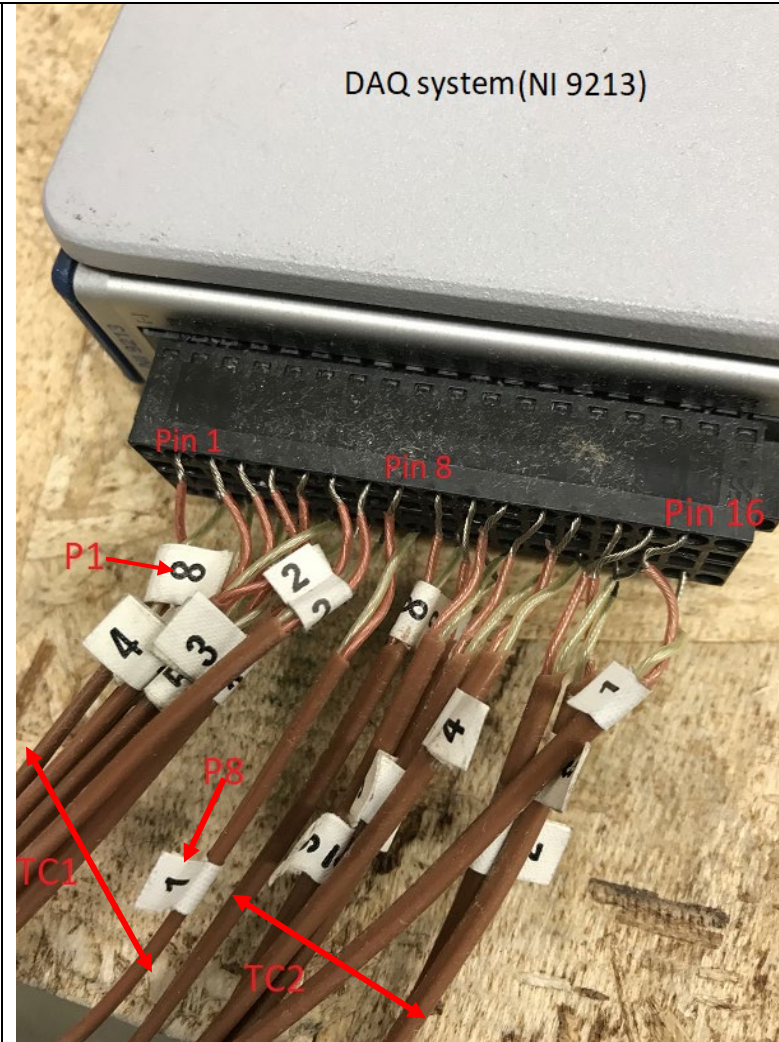
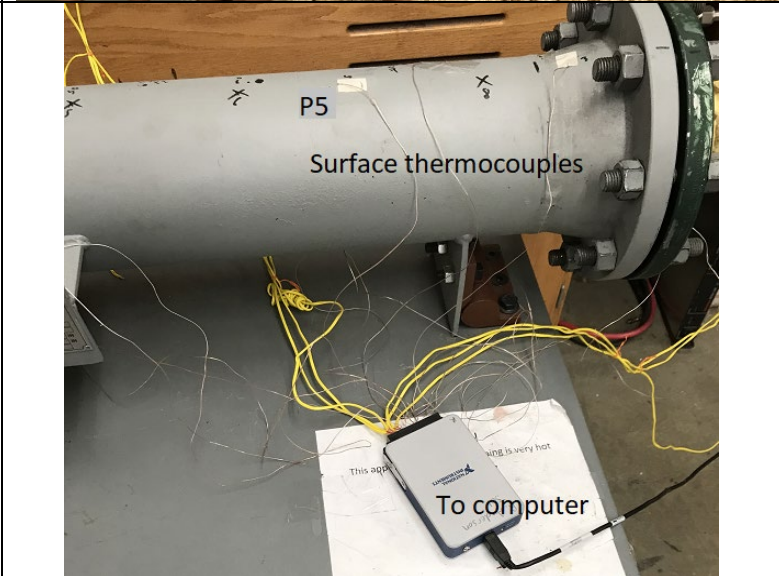


<p>Storage bed tilted about 30-45°</p>	 <p>The storage bed is ready for pouring the beads</p>	 <p>Storage bed filled with beads and ready for lowering down.</p>	<p>The bed is tilted approximately 30- 45° to pour the beads. You can tilt the bed more than 45° if needed.</p>
<p>Cover flange insulation</p>	 <p>1</p>	 <p>2</p>	<p>High temperature calcium silicate insulation (image 1) is used to insulate the cover flange from the inside, creating continuous internal insulation inside the storage packed bed. The diameter of the circular insulation is the inner diameter of the cylindrical internal insulation. The insulation is covered with High-Temperature Felt fabric and sealed with high temperature sealant (images 2, 3, 4, and 5) to prevent</p>
 <p>3</p>	 <p>4</p>		
 <p>5</p>	 <p>6</p>		

			<p>calcium silicate dust from spreading in the lab. Image 6 shows the cover flange insulation for injected pipes.</p>
<p>Internal insulation</p>			<p>Internal cylindrical insulation designed as two pieces each 60 cm in length (image 1). The two pieces are sealed together with high temperature silicon sealant (image 2). The internal insulation inserted and sealed to the storage bed (image 3).</p>
			
<p>Internal thermocouple</p>			<p>Custom internal thermocouple (image 1), showing the sensing points 1-8 (not to scale). Thermocouple inside the bed from inlet side (image 2). Thermocouples from outlet side, showing the tip point of each sensor</p>
			

			<p>while pouring alumina beads.</p> <p>Due to the bending of thermocouples inside the bed, a T-cross is used to hold the thermocouples from the outlet side while pouring the alumina beads (images 4 and 5). Note: make sure that the cover flange with two holes (<math>\frac{1}{4}</math> inch FNPT) is on the hinge side.</p>
--	---	--	---



<p>Internal Thermocouple wires connection</p>		<p>Each thermocouple (TC1 and TC2) has eight sensing points connected to the DAQ system. As can be seen, sensing point 8 is connected to Pin 1 and represents point 1 in the data analysis. Sensing point 1 is connected to pin 8. same connections are used for TC2.</p>
<p>Surface, heater outlet, vessel inlet/outlet, water and air thermocouples</p>		<p>The second DAQ system recorded the surface wall temperature (10 sensing points were connected). P5 is the fifth point on the surface. The yellow wires are heater outlet, vessel inlet/outlet, water and air thermocouples.</p>

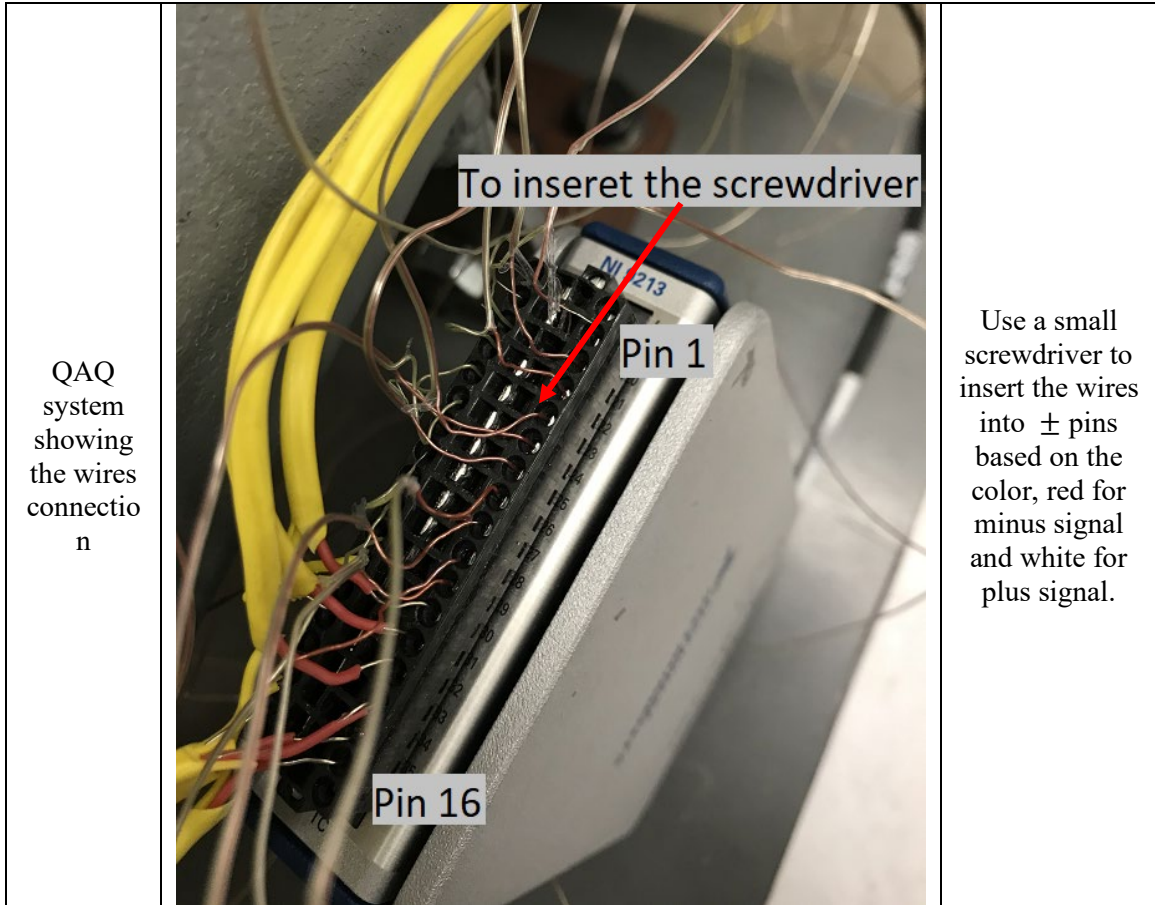

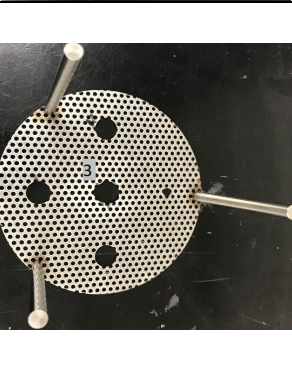

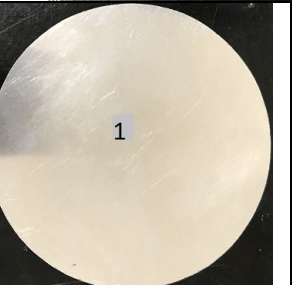
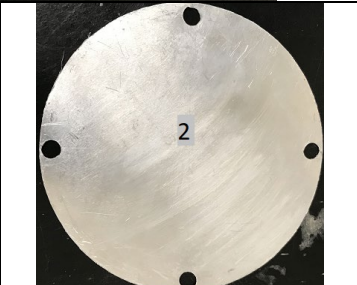
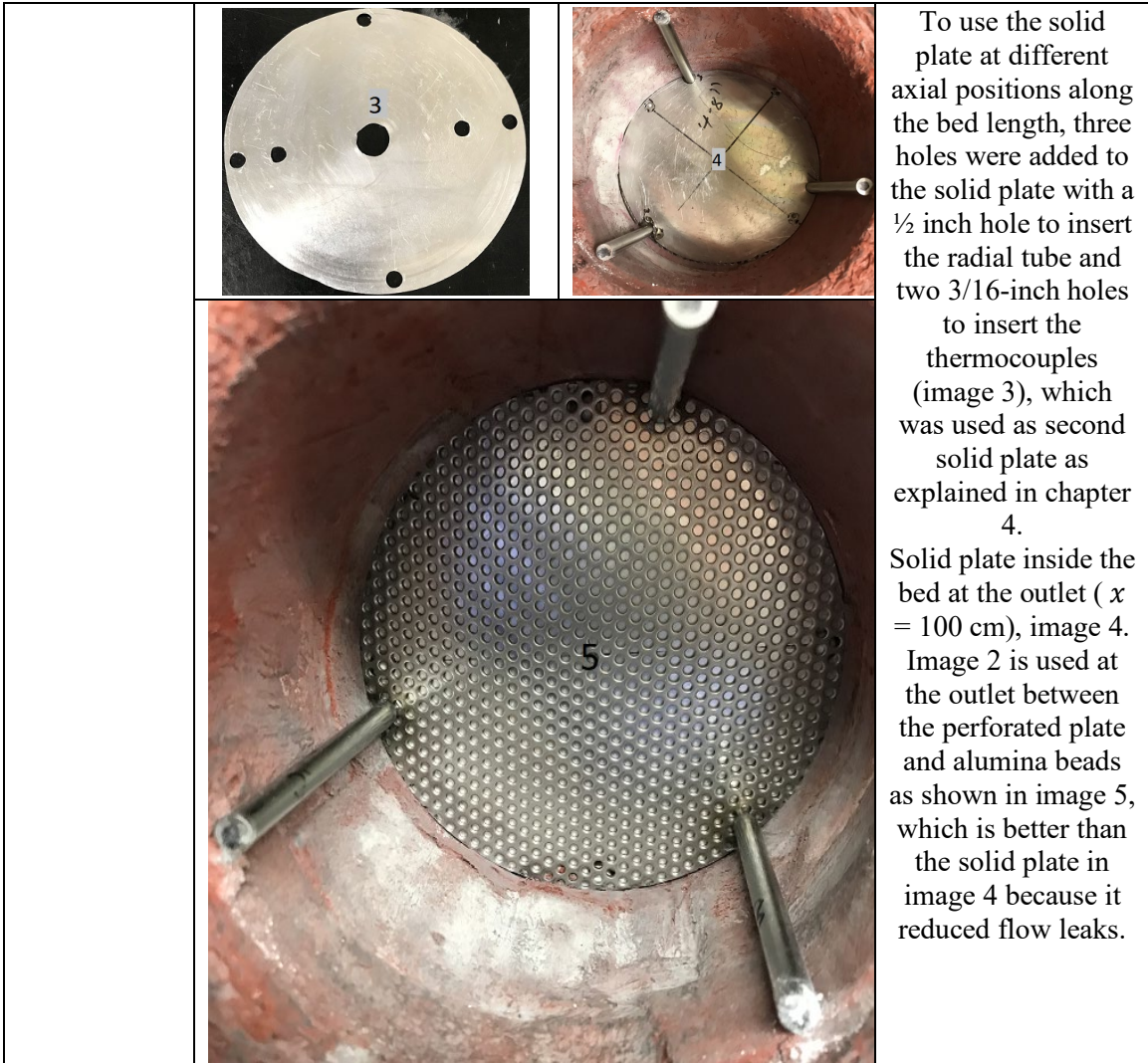




Table A.2 Packed Bed Associated Equipment

Name	Image	Description
Perforated plate (screen or flow distributor plate)		<p>Screen with two holes for insertion of internal thermocouples (image 1). Three legs (each 10 cm in length) welded to the edges of the screen to define the length of free space and bed domain (image 2). Screen with four holes of 1/2 inch diameter used with pipe injection experiments (image 3). Screen at the outlet side, no holes are needed (image 4). Screen with one 1/2 hole for radial flow technique (image 5)</p>
		
		
Solid plate (radial flow only)	 	<p>Plain solid plate (image 1). Solid plate with four holes at <math>r = R</math> (image 2), which can be used at the bed outlet only.</p>

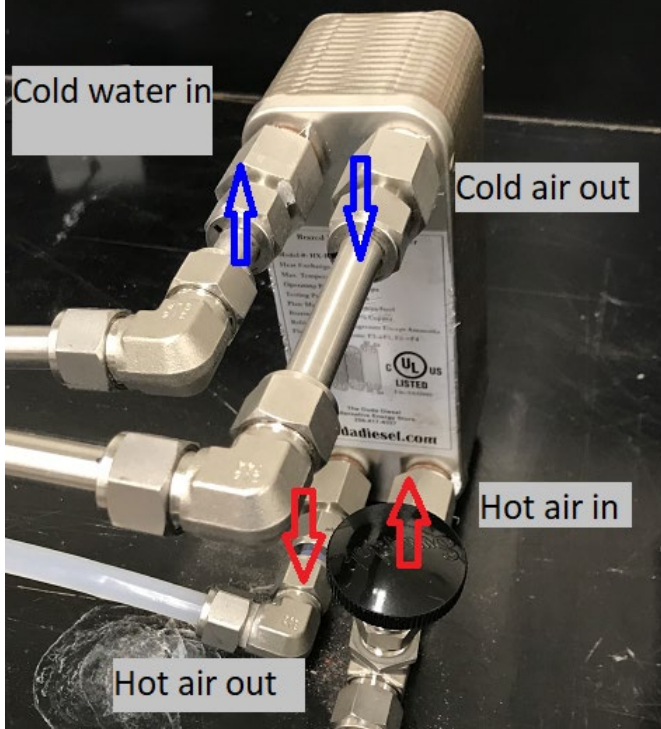




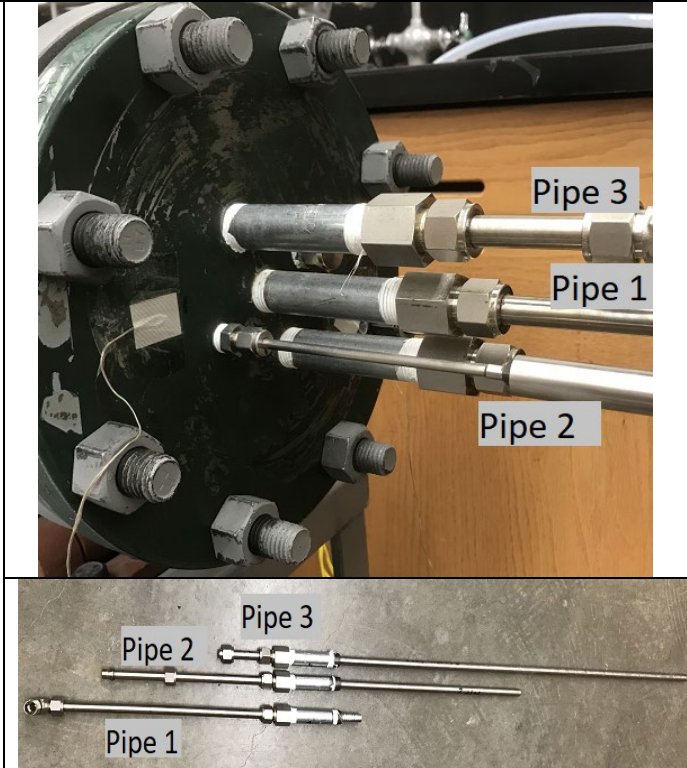


To use the solid plate at different axial positions along the bed length, three holes were added to the solid plate with a  $\frac{1}{2}$  inch hole to insert the radial tube and two  $\frac{3}{16}$ -inch holes to insert the thermocouples (image 3), which was used as second solid plate as explained in chapter 4.


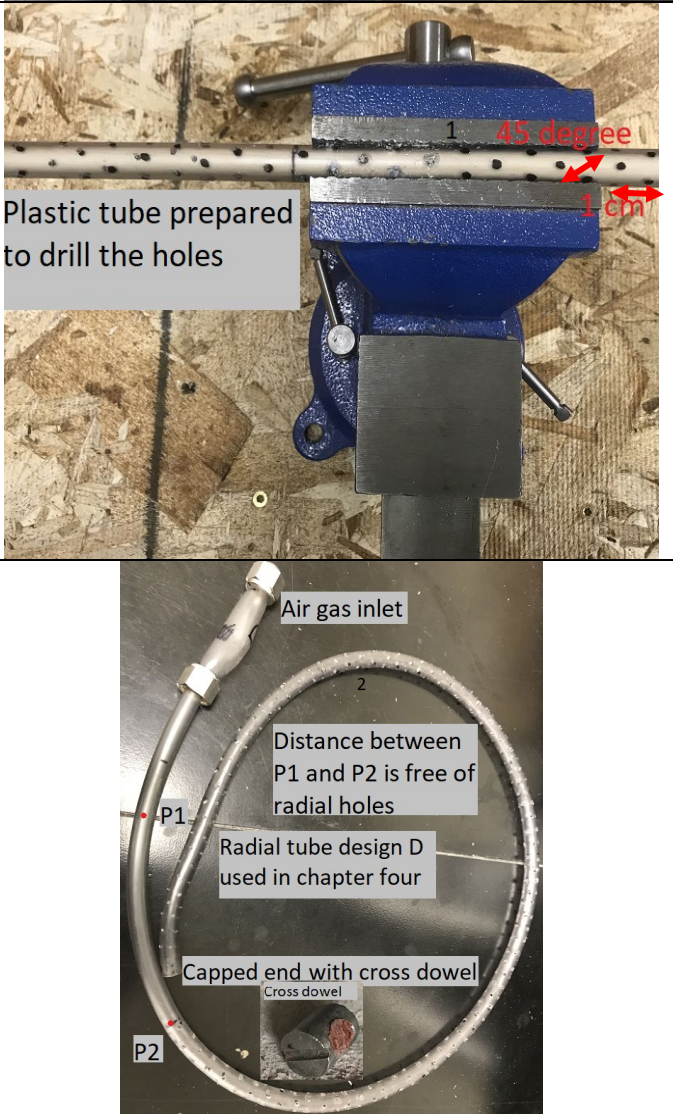
Solid plate inside the bed at the outlet ( $x = 100$  cm), image 4.

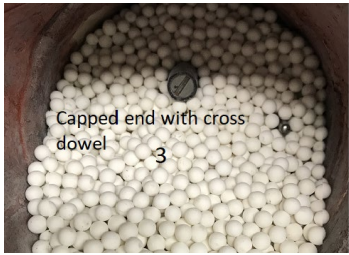
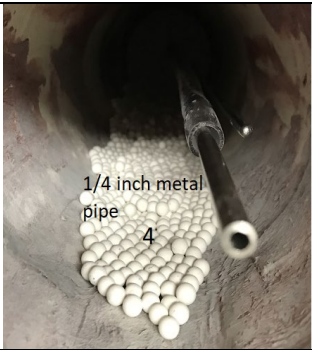

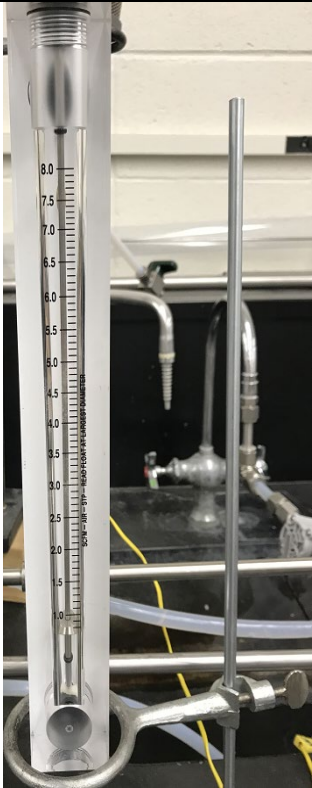
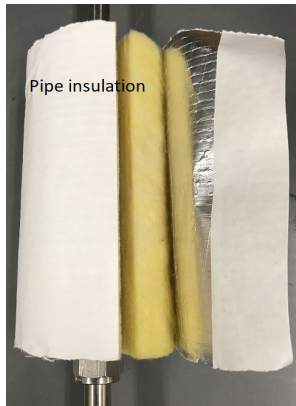

Image 2 is used at the outlet between the perforated plate and alumina beads as shown in image 5, which is better than the solid plate in image 4 because it reduced flow leaks.

Cooler	 <p>Cold water in</p> <p>Cold air out</p> <p>Hot air in</p> <p>Hot air out</p>	<p>Two coolers were used (DudaDiesel, Duda Energy LLC), one at the inlet side and one at the outlet side to cool down the hot air to room temperature.</p>
Digital water flowmeter	 <p>DigiFlow 8100T</p>	<p>Maximum water flow is 3 gal/min.</p>

<p>Filters and HTF direction</p>		<p>Filters to clean the air before entering the entire system. Note: The air used is not clean, it has oil with it. The metal tube between air source and oil filter is very oily. Most of the entire flow system is connected using metal tubing. However, the distance between the water filter and charge/discharge valves is connected using clear white plastic tube as shown to check that the air is clean after exit the filters.</p>
<p>Injected pipes (bed domain with layers)</p>		<p>Cover flange showing three injected pipes. Note: Four pipes are available in the lab for two, three and four layers, assuming equal sized layers. Nipples of 1/2 inch diameter are connected to the drilled FNPT inlets. Install the tube fitting SS-810-7-8BT on the pipe. Note: The item SS-810-7-8BT was bored through in the machine shop.</p>



<p>Screen mesh</p>		<p>Screen mesh is connected at the outlet of each injected pipe to prevent beads from falling inside the pipe. Worm-Drive Clamps connect the mesh to the pipe tightly.</p>
<p>Radial tube</p>		<p>Due to the flexible nature of the plastic tube used in the radial flow experiments, A wooden rod was used to help drilling the holes (image 1). Image 2 shows the radial tube before insertion into the bed. A steel cross dowel was used to block the flow at the outlet of the tube (images 2 and 3). Metal pipe of ¼ inch is inserted into the radial tube to hold it in place and prevent right/left movement (image 4). T-cross shown in (table A.1) was used as well to hold the thermocouple and the radial tube.</p>

	 <p>Capped end with cross-dowel 3</p>	 <p>1/4 inch metal pipe 4</p>	
<p>Flow meter</p>			<p>Two flow meters (Omega product) were use, one for low flow rate and one for high flow rate. Note: The maximum temperature that the flow meters can withstand is 37°C</p>
<p>Pipe insulation</p>	 <p>Pipe insulation</p>	 <p>Tee Elbow Pipe</p>	<p>Insulations used to insulate the distance between the heater outlet and bed inlet (pipes, elbow, valves and tees)</p>

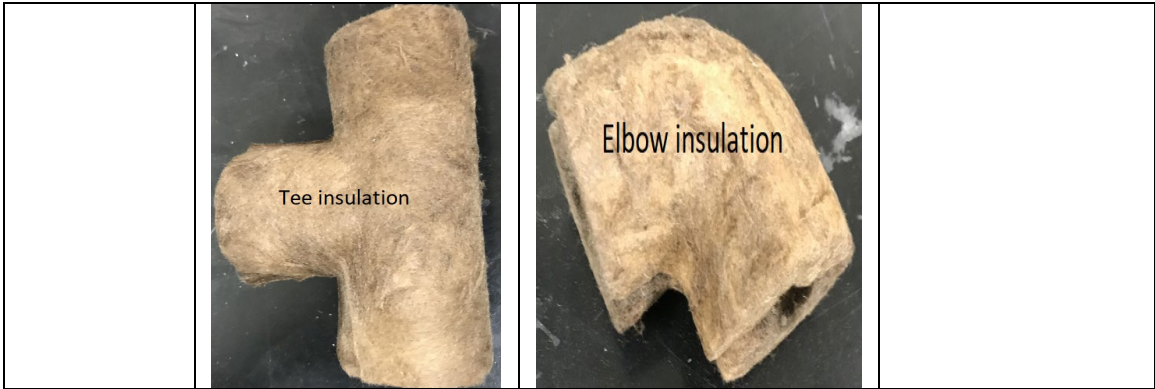
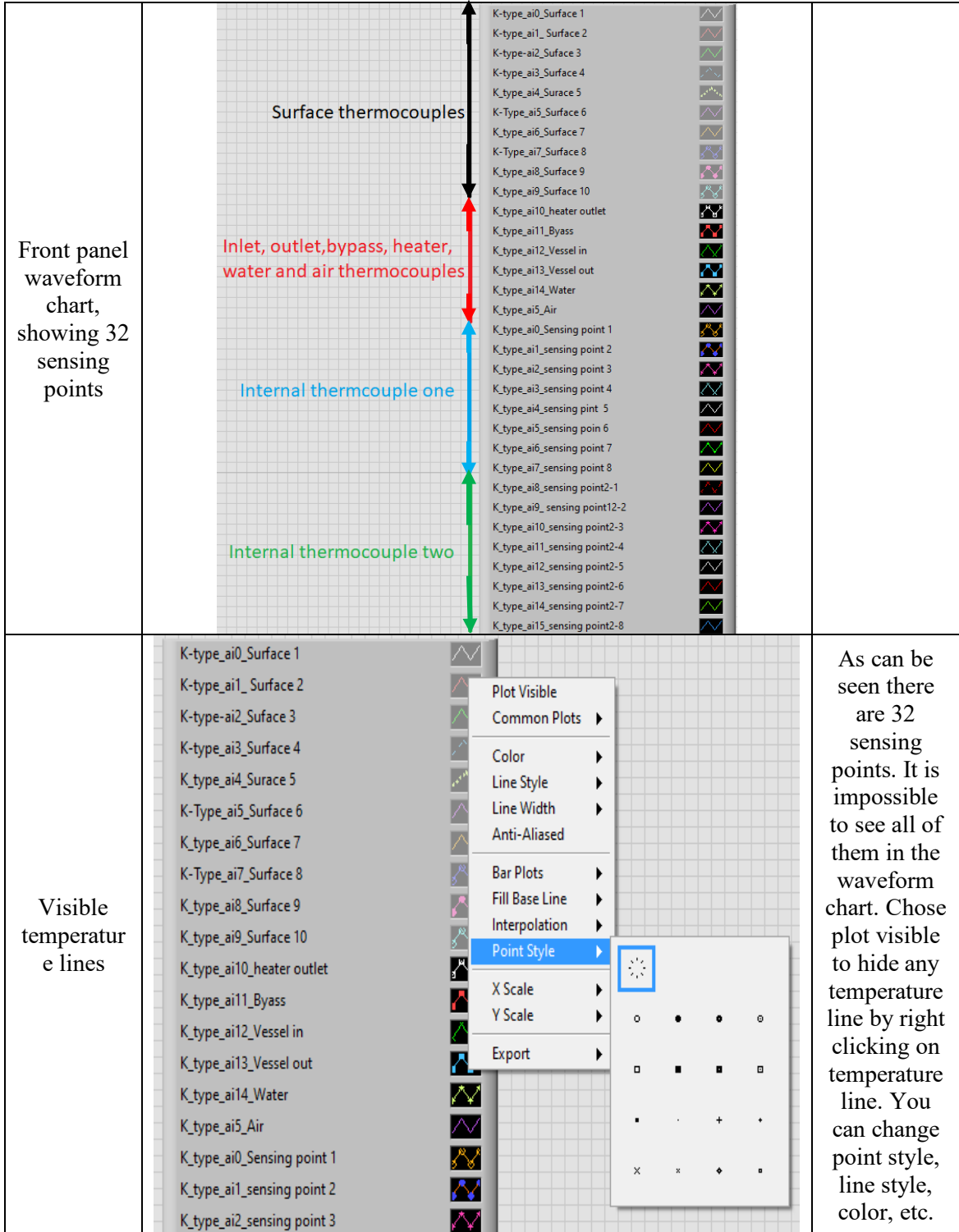


Table A.3 Screenshots of LabView Code and DAQ System Connection/Channels

Name	Screenshots of the LabView interface	Notes
<p>Block diagram</p>	<p>The block diagram illustrates a data acquisition process within a 'For Loop'. It starts with a 'Maximum Iteration' control and an 'Iteration Count' indicator. The loop contains two 'DAQ Assistant' data collectors connected to 'National Instruments 9213'. The outputs are merged into 'Merge signals' and then sent to a 'Waveform Chart' labeled 'To display the collected data'. The data is also processed by an 'Input signals collector, one for each DAQ system' and then sent to a 'Write to Measurement File' block. This block is configured with a 'Delay Time (s)' of 1 and a 'Filename Out' path. A 'Saving Data' indicator is also present.</p>	
<p>Front panel</p>	<p>The front panel provides user controls for the data acquisition. It includes 'Run' and 'Stop' buttons, a 'Maximum Iteration' slider set to 0, and a 'Delay Time (s)' slider set to 1 with the instruction 'Collect data every single second'. A 'Counting starts from zero' indicator is also present. The 'Waveform Chart' displays 'Temperature' data over 'Time'. The y-axis ranges from 0 to 250, and the x-axis shows the time from 7:49:34.316 AM on 4/24/2020 to 7:49:39.316 AM. A text overlay on the chart states 'All sesing points at room temperature'. A 'Saving Data' indicator shows a green dot, with a note: 'Green color indicates that charge/discharge process is completed and data are saved'.</p>	





<p>DAQ system interface, (express task)</p>		<p>In the block diagram double click on DAQ system. The DAQ assistant window will appear. You can run to see temperature readings, change the display type, change the thermocouple setup, check connection diagram and add or remove channels,</p>
<p>Device</p>	<p><b>Thermocouple Setup</b></p> <p>Settings Device Calibration</p> <p>Auto Zero Mode Every Sample</p> <p>ADC Timing Mode High Speed</p> <p>ADC Timing Mode applies to all channels on this device.</p>	<p>Device should be on High Speed</p>



<p>Run</p>	<table border="1"> <thead> <tr> <th>Channel</th> <th>Value</th> </tr> </thead> <tbody> <tr><td>Temperature_0</td><td>20.647834</td></tr> <tr><td>Temperature_1</td><td>20.644129</td></tr> <tr><td>Temperature_2</td><td>20.615185</td></tr> <tr><td>Temperature_3</td><td>20.572967</td></tr> <tr><td>Temperature_4</td><td>20.599902</td></tr> <tr><td>Temperature_5</td><td>20.470453</td></tr> <tr><td>Temperature_6</td><td>20.570493</td></tr> <tr><td>Temperature_7</td><td>20.41904</td></tr> <tr><td>Temperature_8</td><td>20.65177</td></tr> <tr><td>Temperature_9</td><td>21.994718</td></tr> <tr><td>Temperature_10</td><td>20.347012</td></tr> <tr><td>Temperature_11</td><td>20.341222</td></tr> <tr><td>Temperature_12</td><td>20.450537</td></tr> <tr><td>Temperature_13</td><td>20.424135</td></tr> <tr><td>Temperature_14</td><td>13.263721</td></tr> <tr><td>Temperature_15</td><td>20.359982</td></tr> </tbody> </table>	Channel	Value	Temperature_0	20.647834	Temperature_1	20.644129	Temperature_2	20.615185	Temperature_3	20.572967	Temperature_4	20.599902	Temperature_5	20.470453	Temperature_6	20.570493	Temperature_7	20.41904	Temperature_8	20.65177	Temperature_9	21.994718	Temperature_10	20.347012	Temperature_11	20.341222	Temperature_12	20.450537	Temperature_13	20.424135	Temperature_14	13.263721	Temperature_15	20.359982	<p>All sensing points should read room temperature except water (~ 12 – 16 °C)</p>
Channel	Value																																			
Temperature_0	20.647834																																			
Temperature_1	20.644129																																			
Temperature_2	20.615185																																			
Temperature_3	20.572967																																			
Temperature_4	20.599902																																			
Temperature_5	20.470453																																			
Temperature_6	20.570493																																			
Temperature_7	20.41904																																			
Temperature_8	20.65177																																			
Temperature_9	21.994718																																			
Temperature_10	20.347012																																			
Temperature_11	20.341222																																			
Temperature_12	20.450537																																			
Temperature_13	20.424135																																			
Temperature_14	13.263721																																			
Temperature_15	20.359982																																			
<p>Add channels</p>		<p>Click on add channels, then thermocouple, then choose the device (1 or 2), and finally select the channel(s) to add.</p>																																		
<p>Remove channels</p>		<p>Select the channels you want to remove and hit remove (X), confirm the cancellation.</p>																																		

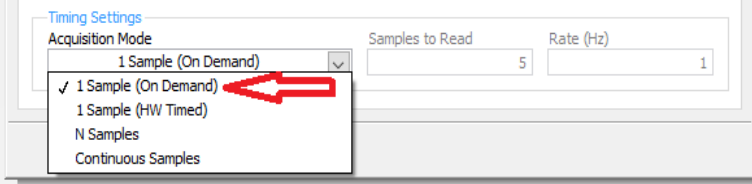
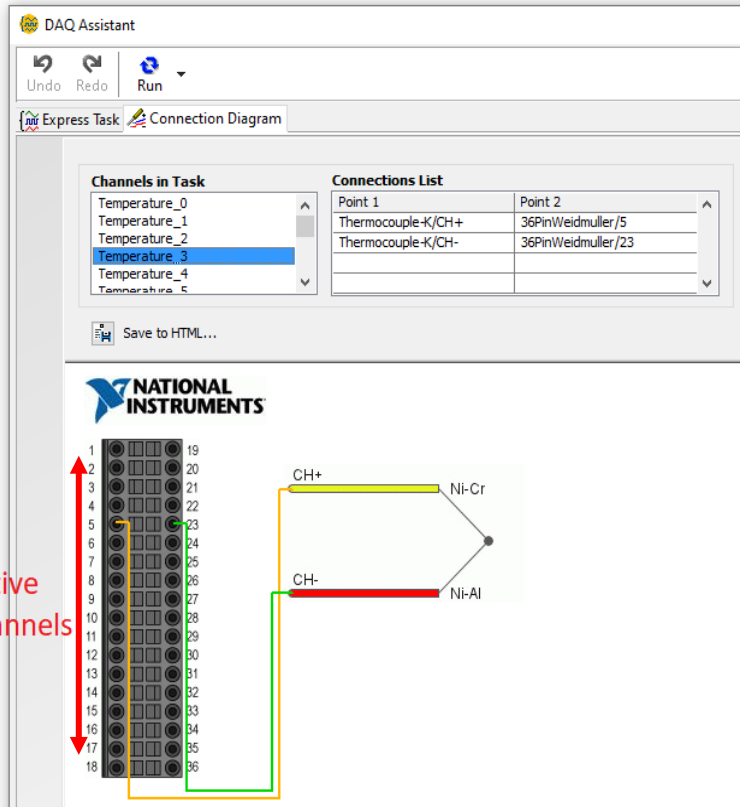
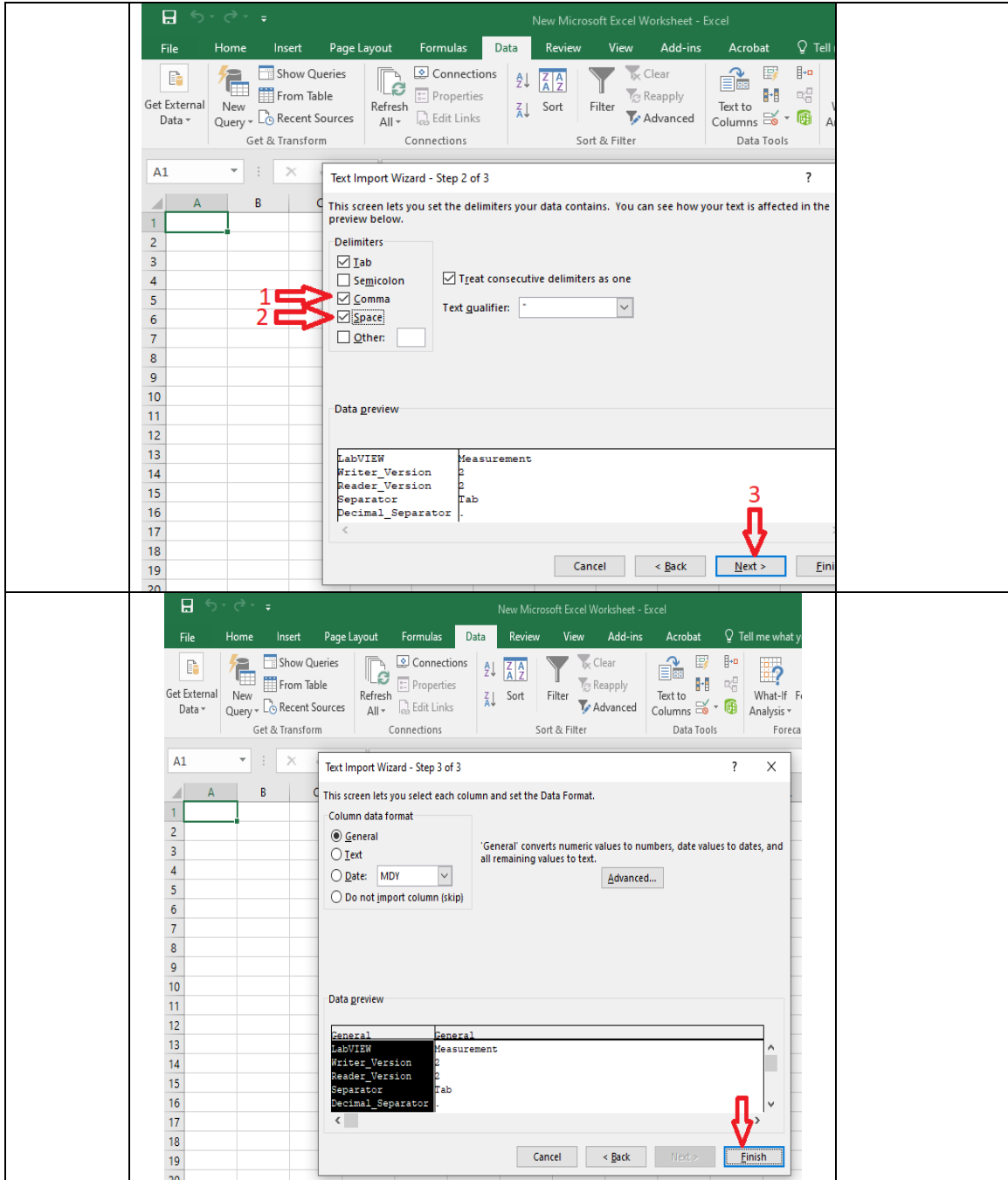
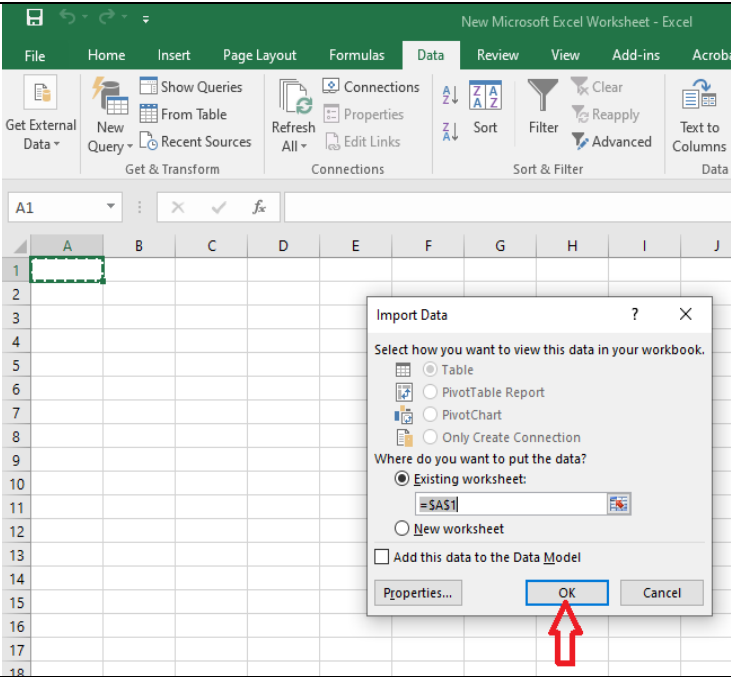
<p>Samples</p>		<p>In the timing setting, 1 sample (on demand) is selected</p>
<p>Connection diagram</p>		<p>If you disconnect the thermocouples wires with the DAQ system for any reason or remove/add channels and then connect them again, you can check the connection is right by going to the Connection Diagram window. It shows all the channels in task and the plus/minus signals. Note: Based on active channels, Temperature_0 is channel 2 and so on.</p>

Table A.4 Screenshots of Data Analysis

Name	Screenshot	Description
<p>Moving data points from the saved file to excel file</p>	<p>1</p> <p>2</p> <p>3</p> <p>4</p> <p>5</p> <p>Some of the saved files</p>	<p>Open excel file, select cell and follow the steps 1-5. Note: The files order is one for charging and the next for discharging (59 for charging and 60 for discharging).</p>
	<p>1</p> <p>2</p>	



Collecte  
d data



Collected temperature

Time

Time	20.669733	20.689183	20.724145	20.729934	20.617403	20.651673	20.625507	20.681774
1	20.849983	20.800901	20.681663	20.70528	20.685599	20.749503	20.5902	20.728897
2	20.839621	20.721081	20.737057	20.725017	20.797485	20.658796	20.702558	20.609707
3	20.857836	20.733046	20.681645	20.733972	20.717534	20.684655	20.687897	20.629083
4	20.785442	20.809751	20.637721	20.784053	20.730107	20.836376	20.734969	20.779422
5	20.612132	20.549378	20.6075	20.693174	20.666546	20.533631	20.546831	20.563967

Collected data labeled based on different sensing points

	A	B	C	D	E	F	G	H	I	
1	LabVIEW	Measurement								
2	Writer_Version	2								
3	Reader_Version	2								
4	Separator	Tab								
5	Decimal_Separator	.								
6	Multi_Headings	Yes								
7	X_Columns	One								
8	Time_Pref	Absolute								
9	Operator	TES								
10	Date	4/24/2020								
11	Time	05:16.8								
12	***End_of_Header***									
13										
14	Channels	37								
15	Samples	20	20	20	20	20	20	20	20	
16	Date	4/24/2020	4/24/2020	4/24/2020	4/24/2020	4/24/2020	4/24/2020	4/24/2020	4/24/2020	
17	Time	05:16.8	05:16.8	05:16.8	05:16.8	05:16.8	05:16.8	05:16.8	05:16.8	
18	X_Dimension	Time	Time	Time	Time	Time	Time	Time	Time	
19	X0	0.00E+00	0.00E+00	0.00E+00	0.00E+00	0.00E+00	0.00E+00	0.00E+00	0.00E+00	
20	Delta_X	1	1	1	1	1	1	1	1	
21	***End_of_Header***									
22	X_Value	point 1	point 2	point 3	point 4	point 5	point 6	point 7	point 8	
23		0	20.669733	20.689183	20.724145	20.729934	20.617403	20.651673	20.625507	20.681774
24		1	20.849983	20.800901	20.681663	20.70528	20.685599	20.749503	20.5902	20.728897
25		2	20.839621	20.721081	20.737057	20.725017	20.797485	20.658796	20.702558	20.609707
26		3	20.857836	20.733046	20.681645	20.733972	20.717534	20.684655	20.687897	20.629083

Point 1 in the excel file is point 8 on the thermocouple. Point 8 in the excel file is point 1 on the thermocouple.

APPENDIX B  
EXPERIMENTAL PROTOCOLS

### B.1 Normal Configuration Packed Bed Setup Protocol

Here, normal configuration refers to the traditional method of charge-discharge, with gas flowing axially into and from the ends of the packed bed. This protocol describes the steps to insert the internal thermocouples and pour the storage materials. Note: right and left sides are just arbitrary choice, you could choose any side to be inlet based on the installation of the entire storage bed system in the lab. However, the order of the sensing points inside the bed (sensing points from internal thermocouple) will change based on your choice; for example, sensing point 1 is the recovery point if the left side is the inlet side, while sensing point 8 will be the recovery point if the right side is the inlet side as was used in the present study. In the present study, right is the inlet side and left is the outlet side as shown in Table A.1 (installed storage bed).

1. The storage tank is assumed empty at this point. To start, remove the flanges from both sides by unscrewing the bolts/hex nuts. The cover flanges are heavy, so be careful when moving/carrying them.
2. Insert the perforated plate from the right side 10 cm from the edge of packed bed. The screen has three legs that should touch the cover flange from inside. It has two holes with 3/16 inch diameter to insert the internal thermocouples. Note: a rectangular 304 stainless steel perforated sheet (McMaster Carr, 9358T58) with staggered holes, 0.06 inch thick, 0.094 inch hole diameter was used. Circular pieces were cut off the rectangular sheet and prepared to be used as perforated plates. The edges were polished very well to avoid tearing the fabric cover of the internal insulation. Then, three legs (stainless steel rod column) are welded to the perforated plate to define the 10 cm free space and to hold the perforated plate in place.
3. Connect the cover flange to the storage bed on the right. It has eight bolts, one inlet for HTF (1 inch Female National Pipe Thread, FNPT) and two holes (1/4 inch FNPT) for thermocouple insertion as shown in Table A.1.
4. Insert the internal thermocouple through the cover flange and perforated plate along the bed length. Note: you need to center the screen with the cover flange (to easily insert the internal thermocouple), or insert the thermocouple into the flange and screen and insert all of them as one piece into the bed (push the screen from the other side using a wooden rod until its legs touch the cover flange).
5. Tilt the bed 45- 60° using a high lift jack that is connected to the base table of the packed bed as shown in Table A.1. Ensure the high lift jack is securely affixed to the table and the pipes on inlet and outlet sides are disconnected. The bed is fixed to the base table using a hinge (at the inlet side) to easily tilt the packed bed. Ensure this hinge is firmly connected to the table as well. The nose of the high lift jack is under the bed and connected to the bed by a steel chain. Ensure that the chain is firmly connected to the bed and the high lift jack. Note: The high lift jack is designed to lift cars, it is very useful and dangerous at the same time. There are many videos on YouTube channel that show how to use it safely (<https://www.youtube.com/watch?v=0KbEfqJJLWQ> ).
6. Use the T-cross (Table A.1) to hold the thermocouple(s) and avoid bending/moving of thermocouples to the left/right.



7. Wear gloves and face mask (available in the lab) to avoid the dust of the alumina beads.
8. Pour the beads from the left side. A wooden rod can be used to push the beads to the very end of the bed.
9. Insert the second perforated plate from the outlet side as shown in Table A.2. The perforated plate should touch the beads, the legs should touch the cover flange.
10. Connect the cover flange on the outlet side.
11. Lower the bed to the horizontal layout by downing the high lift jack. Lowering is done by flipping the reversing lever in the downing position as shown in Table A.1.
12. Connect the pipes on the inlet and outlet sides. Use a wrench to tighten the nuts (Swagelok Tube Fitting). Do not tighten the nut too much because it will fail and leak.
13. Insulate the pipes between the heater and bed entrance, see the images in Table A.2, which shows more details regarding specific sections of the pipe with specific insulation. You do not need to insulate the pipes at the outlet side. Note: the distance from the heater outlet to the vessel inlet is 100-110 cm. If you change the experiment setup and (or) the inlet/outlet directions, make sure to keep the same distance (~ 110 cm) between the heater and the inlet of the bed. Otherwise, you may need more pipe insulation or to change the heater setpoint temperature to achieve the correct inlet temperature. In addition, do not install the heater very close to the vessel inlet. The outlet temperature from the heater is a sinusoidal function as shown in Figure B1 at 7 SCFM (this is how the temperature controller works; for example, if the set temperature is 175°C, you will see the temperature from the temperature controller going up to about 180 °C and down to about 170 every 1-2 minutes, making the outlet temperature as a sine wave. However, this sine wave disappears due to heat losses from the pipes, leading to a constant temperature at the inlet. Therefore, installing the heater very close (10-30 cm) to the vessel inlet will lead to a sinusoidal inlet temperature as will be explained below, which should be avoided.
14. Connect the packed bed surface thermocouples and internal thermocouples to the DAQ system. Note: as shown above for internal thermocouple, each sensing point has two wires (white and red, where white for + signal and red for - signal). The DAQ system has two sides, one for the USB cable and the second for the thermocouple wire's connection. To connect the wires, there are 32 pins. Use a small screwdriver to connect the wires as shown in Table A.1. Numbering of sensing points is very important; for example, point 8 in the internal thermocouple is the first point if the inlet is on the right side as was in the present study. This means point 8 will be the first point to be connected to the DAQ system as can be seen in Table A.1. For surface thermocouples, you need to mark the numbers of the points on the vessel surface from 1 to 10, starting from the inlet side and then connect the points to the DAQ system based on the order of numbers you made ( note: you could connect to the DAQ system in any order you want, but make sure you name that correctly in the LabView, front panel waveform chart). The bed is ready now for testing.
15. It is worth noting that if you open the flanges and take out the beads for any reason, you need to check if there are any cracks in the internal insulation. Use high

temperature sealant (McMaster Carr, 7644A11) to seal/fix them. This sealant takes 24 hrs to set. Also, if the cracks are big, High-Temperature Felt (McMaster Carr, 8796K42) can be used to cover the crack and then seal it. It can be used as as insulation and cover with 1.3 mm thickness.

Figure B1 shows the temperature profiles from three thermocouples installed between the heater and the inlet of the vessel and from the first sensing of the internal thermocouple inside the bed at 0.0048 m<sup>3</sup>/s (7 SCFM). The temperature exits the heater as a sine wave. Then the sinusoidal effect starts to vanish with increasing distance between the heater outlet and vessel inlet due to the heat losses to the environment. At Vessel inlet 2, the sinusoidal effect becomes small until its effect completely disappears as can be seen from the inlet temperature profile. Table B1 shows the distances between each thermocouple and the vessel inlet, which can give an idea how to avoid the sinusoidal effect if the experimental setup will be changed for any reason. Note: Vessel inlet 1 and 2 are between the heater and vessel inlet; 1 very close to the heater outlet and 2 very close to the vessel inlet. The heater outlet and vessel inlet 1 starts from higher temperature because the results in Figure B1 were reordered after heating up the pipes for about five minutes by passing the hot air through the bypass valve to the cooler before the charging process started.

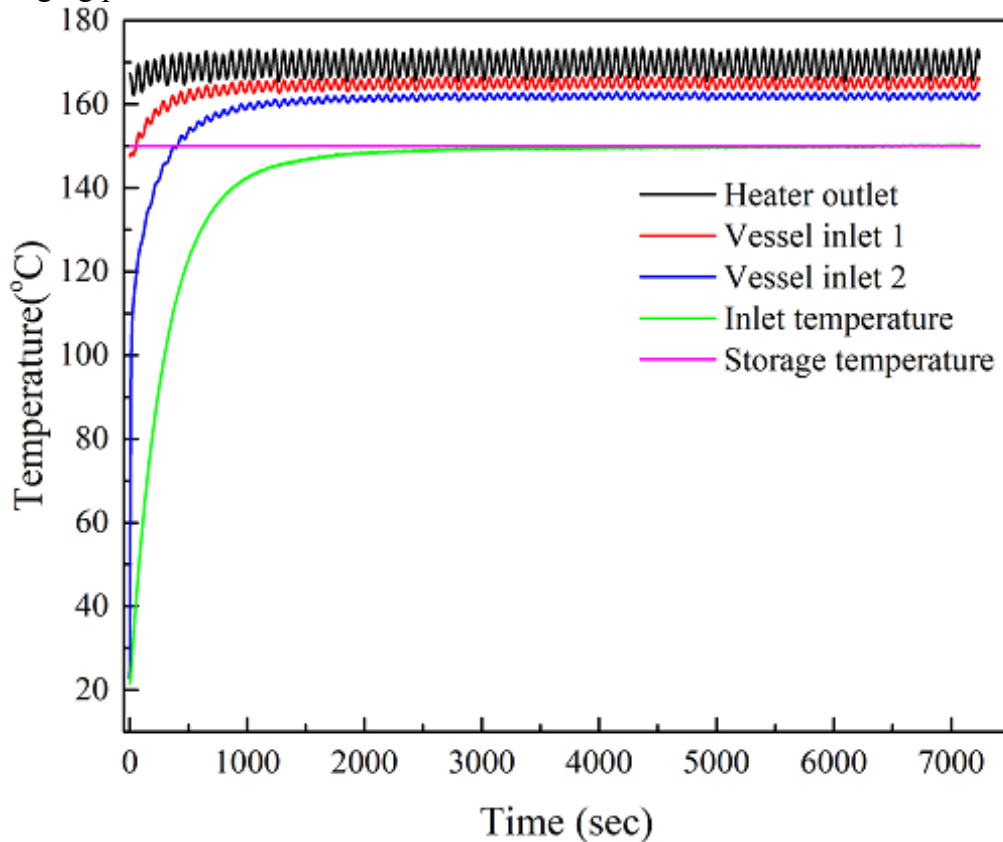


Figure B1: Temperature profiles between the heater outlet and vessel inlet, showing the effect of sinusoidal temperature function, and the final constant bed inlet temperature.

Table B1: The distances of thermocouples connected between the heater outlet and vessel inlet. Note: Vessel inlet is inlet to the vessel (cover flange), which is 11.5 cm (flange + free space) from the inlet of the bed domain.

Thermocouple	Distance from vessel inlet (cm)	Notes
Heater outlet	100-110	
Vessel inlet 1	50	
Vessel inlet 2	20	
Inlet temperature	11.5	First sensing point inside the bed

### B.1.1 Charging and Discharging Test Protocol

When the packed bed is ready for running the experiment, charging and discharging processes can be tested. Note: Some steps will be explained in detail in another protocol regarding LabView, data analysis, calibration of flow and temperature, and temperature controllers.

1. Start the computer. Start the LabView software. Go to the DAQ system and check that all thermocouple sensing points (internal, surface, inlet, outlet, water and air) are reading lab room temperature (20-22°C). Screenshots of the LabView code and DAQ system can be seen in Table A.3 for more detail.
2. Open/close the valves to direct the flow for charging or discharging processes. For the system in the lab, the valves are marked with “CH” for charging and “DIS” for discharging as can be seen in Table A.2.
3. Start the air source from the building, the yellow ball valve as shown in Table A.2.
4. Adjust the flow to the desired flow rate from the next valve (Bonnet needle valve, valve 1) after the yellow ball valve directly. You can see the flow through the flowmeters (FL-4611 for low flow (0- 8 SCFM) and FL-4612 for high flow (0- 14 SCFM)).
5. Start the cold water from the sink. A digital water flowmeter is connected with maximum flow of 3 gal/min. 1.98 gal/min is enough to cool down the hot air at 150 °C to room temperature using the connected heat exchangers.
6. Direct the flow toward the coolers through the bypass valve. This task will help to heat up the pipes between the heater and the bed entrance and to make sure everything is working as desired.
7. Set the temperature controller to the calibrated temperature (assuming that calibration is achieved, and this is the temperature that will give the desired inlet temperature). For instance, in previous calibrations the temperature controller needed to be set to 175°C at 7 SCFM to have an inlet temperature of 150°C. This calibration may need to be checked in future experiments. **DO NOT START THE HEATER AT THIS POINT.**
8. Type the charge time (in seconds) in the “maximum iteration box”, front panel of LabView software if you are using the code built in the computer as shown in Table A.3. Based on the number typed in the iteration box, the code will run until reaching

this number minus one, starting from zero (zero represents the first second of the charge time); for example, if charging time is 100 sec, the code will stop iteration count at 99.

9. Plug the heater cable in the outlet strip, which will be shown in appendix D.3, Figure D1. Make sure the power switch is off.
10. Make sure that everything is set as it should be. Then, start the heater by turning on the power switch from the outlet strip.
11. Hit “run” from the LabView, front panel.
12. Wait for 3-5 minutes to warm up the pipes.
13. Hit stop from the LabView, front panel.
14. Hit “run” on the LabView panel again, close the bypass valve and open the inlet valve to start the charging process.
15. Monitor the flow (air flowmeter) every 10-15 minutes because the air might fluctuate up and down as it comes from the building and some other labs might use it during the same time.
16. Wait until the charging process completes.
17. Shut down the heater (turn off the power switch from the outlet strip) when you see the “saving data circle” on the front panel of LabView turns to green, indicating that charging process is completed, and data are saved.
18. Unplug the heater cable from the outlet strip and the outlet strip from the electricity source on the wall.
19. The data will be saved automatically at the local desktop with file name “Packed Bed”, more details will be explained in appendix D.2 regarding the collected/saved data.
20. Type the discharge time (in seconds) in the “maximum iteration box”, front panel of LabView.
21. Hit “run” on the LabView panel again.
22. Change the valves for the discharging process as quick as you can.
23. Repeat steps 15-16, but for discharging process.
24. Shut down the air and water when you see the “saving data circle” turns to green, indicating that the discharging process is completed, and data are saved.
25. Unplug the cable for the temperature controller from the electricity source on the wall.

### B.2 Layers Configuration Packed Bed Setup Protocol

This protocol describes the steps to divide the bed into layers via internal piping, insert the internal thermocouple, and pour the storage materials.

1. A new cover flange was designed to insert the pipes and thermocouple as shown in Table A.1. It has four holes ( $\frac{1}{2}$  inch, FNPT) to insert four pipes (four bed layers) and one hole ( $\frac{1}{4}$  inch, FNPT) for one internal thermocouple. However, only three bed layers were tested and analyzed in the present study.

2. Cut the metal pipes based on the length of each layer in the bed, including the free space (10 cm), thickness of the cover flange and distance from flange to the valve that controls the flow for this layer. Note: Four pipes are available in the lab for two, three and four bed layers, assuming equal sized layers. Table A.2 shows the pipes with their lengths for two and three layers that were tested in the lab.
3. Install the required fitting on the pipes (Swagelok fittings were used). Note, Swagelok Tube Fitter's Manual, chapter three explains how to install the tube fittings in detail (available in the lab).
4. Connect the cover flange, insert the pipes (two or three layers) and connect them to the connectors valves between the heater outlet and vessel inlet to make sure that all lengths and fittings used are right.
16. At this point, the storage packed bed is empty. To start, remove the flanges from both sides by unscrewing the bolts/hex nuts.
5. The perforated plate, image 3 in Table A.2 can be used. The screen has three legs that should touch the cover flange. It has one hole with 3/16 inch diameter to insert the internal thermocouple and four holes with 1/2 inch to insert the injected pipes. Note: for two layers, two pipes will be injected. The perforated plate has four 1/2 inch holes and two of them should be blocked to avoid the falling of beads in the 10 cm free space. Block the holes using a screw with nut. For three layers, one hole must be blocked as shown in Figure B2, image 1.
6. Insert the internal thermocouple and the pipes through the cover flange and perforated plate as shown in Figure B2, image 1. Connect the screen mesh at the very end of each pipe. Then insert all of them as one piece into the bed and screw the bolts. Push the perforated plate from the other side using a wooden rod until its legs touch the cover flange
7. Repeat steps 5-14 in B.1 above except in step 12, where there will be two or three pipes to be connected based on the number of layers that will be tested. Several valves should be used to direct the flow as can be seen in Figure B2 images 2 and 3.



Figure B2. Custom flange for pipe injection showing the injected pipes with perforated plate as one piece. The flow in the injected pipes was controlled using several valves. Note: Image 1 shows inserting of a radial tube (primarily radial testing). However, for pipe injection, the same procedure was used.

### B.2.1 Charging and Discharging Test Protocol

The steps in B.1.1 can be followed exactly to charge/discharge the bed. However, since there are two or three layers, the charging/discharging procedure will depend on the scheme used to do the two processes. See Chapter 3, Appendix A that explains 17 charge/discharge schemes that have been used in the present study. Depending on the scheme you want to test, you can manage how to charge/discharge the bed. The best charge/discharge scheme with two layers at 7 SCFM is explained here in details. The

charging time for 7 SCFM is two hours, 120 minutes. The bed will be treated as two layers. The length for each layer is 50 cm. The best charging scheme assumes charging the first layer for 60 min and then start charging the second layer keeping the valve for the first layer open in order to avoid heat losses in the first layer due to holding on for 60 min as explained in the below steps:

- 1- At this point, we will assume that all pipes/valves are connected, and calibration is achieved. Calibration with pipe injection is explained in Appendix D.4.
- 2- Repeat steps 1-15 in B.1.1 exactly as the charging process for the first layer is the same as normal charging except step 8, where two options can be used to run the LabView code: 1) you can run the code for 60 min to charge the first layer and then run it again for another 60 min to charge the second layer after you open the 2<sup>nd</sup> valve and change the set temperature from the temperature controller. 2) Run the code for 120 min (0- 60 min for the 1<sup>st</sup> layer and 60-120 for the 2<sup>nd</sup> layer), where after 60 min you open the second valve. It is recommended to use the 2<sup>nd</sup> option because you will avoid any mistakes that might happen. For example, you need to change the set temperature from the controller and if you forget to run the code, you will lose your data points.
- 3- When you open the second valve, leave the 1<sup>st</sup> valve open and set the temperature from the temperature controller based on the achieved calibration. For two layers at 7 SCFM, the first layer set temperature was 175°C (normal configuration charging) and for the second layer the set temperature was 193°C. However, these calibrated temperatures should be checked for future tests especially if the experimental setup in the lab and/or the lengths of layers are changed.
- 4- The flow is divided between two pipes, which should be controlled by the valves. An approximate calibration showed that pipe one has about 40 % of mass flow rate and pipe two has about 60 % of flow. Approximately, the second valve should be almost fully opened and the second valve almost 50 % opened. This flow percentage kept the inlet temperature at 150°C for both layers for the entire charging period. This approach is an approximation and not accurate 100%. However, the model results agree very well with the experimental data.
- 5- Monitor the inlet temperature for layers 1 and 2 based on the sensing points inside the bed (sensing point 1 for the 1<sup>st</sup> layer and sensing point 5 for the 2<sup>nd</sup> layer). Based on that, adjust the valves in order to have a constant inlet temperature. You should know that from the calibration with labels as well; for example, when you do the calibration, label or draw a picture of the percentage of opening for each valve to get the desired inlet temperature.
- 6- Repeat steps 16-19 in B.1.1.
- 7- For discharging process, the best scheme was to have both valves opened for the entire discharging time. This means that steps 20-25 in B.1.1 can be followed exactly. However, if another discharging scheme will be tested, the steps will be different. Check chapter three, Appendix A for more information.
- 8- Repeat steps 20-25 in B.1.1

### B.3 Radial Configuration Packed Bed Setup Protocol

This protocol describes the steps to design the radial tube and have the packed bed ready for testing. The case described here is used to design six different radial tubes, one of them is considered the best design based on even flow distribution and thermal performance during a charging process.

1. The tube used in the experimental test to provide radial flow is McMaster Carr 1487T3. The length of the radial tube used in the bed is about 3.9-4.1 ft, 120-125 cm (100 cm for bed length and the additional 20-25 cm represents the free space before the screen, thickness of the flange and the connection outside the bed). Use the Tube Cutter to cut the tube accurately. Insert a metal pipe inside the tube to be able to cut using the Tube Cutter due to the flexible nature of the tube.
2. Using a marker, mark the first set of holes, four holes per axial location, which are distributed at angular degree ( $\theta = 0, 90, 180, 270^\circ$ ).
3. Move 1 cm, shift the angular position  $45^\circ$ , and mark the second set of holes. The holes will be at  $\theta = 45, 135, 225, \text{ and } 315^\circ$  as shown in Table A.2.
4. The third set will be at  $\theta = 0, 90, 180, 270^\circ$  and the fourth set at  $\theta = 45, 135, 225, \text{ and } 315^\circ$  and so on.
5. You can change the angular positions and the distance between each two sets of holes. However, we think that 4 holes at a distance of 1cm is enough to provide uniform flow in each direction. As was explained in chapter five, because of the plastic nature of the tube, it was difficult to design the holes accurately and it would be hard to add more than four holes per axial location.
6. Insert a wooden rod in the tube. The inner and outer diameter of the radial tube are  $3/8$  and  $1/2$  inch respectively. The wooden rod diameter is  $3/8$  inch. This will help to drill the holes easily as shown in Table A.2.
7. Use the “support system” to hold the tube as shown in Table A.3.
8. Use the drill to drill the holes based on the sizes proposed. The sizes of the drill bit used were  $1/16$  (1.58),  $5/64$  (1.98),  $3/32$  (2.38),  $7/64$  (2.78) and  $1/8$  (3.18) inch (mm). Note: the size of alumina beads used in the experiments is 6 mm, which is bigger than the radial tube holes, However, if 3 mm beads will be used (available in the lab), the radial tubes (designs B, D, E, and F) cannot be used because these designs have one layer of hole diameter of 3.18 mm. A solution for this issue is recommended in chapter five.
9. Add one or two sets of holes before the perforated plate to solve the issue of the first sensing point as was explained in chapter five. You could wait until you complete the first test and see the temperature distribution, and then decide how to improve it.
10. At this point, you need to install the Swagelok fittings on the plastic tube. Due to the flexible nature of the plastic tube, you need to do it while the tube is already inserted inside the bed. Connect the cover flange (inlet side) and insert the radial tube along the length the bed. Insert a  $1/4$  inch metal pipe inside the radial tube to help installing the fittings on the tube. Chapter three of Swagelok Tube Fitter’s Manual explains how to install the fittings on  $1/2$  inch tube/pipe.



11. Use a plug to block the outlet of the radial tube. A “cross dowel” is used as shown in Table A.2 with sealant (high temperature sealant (McMaster Carr, 7644A11) was used), which worked well to prevent any flow leaking.
12. Use the perforated plate with three holes, which is shown in Table A.2: two holes of 3/16 inch for internal thermocouples and one ½ inch hole at the center to insert the radial tube. Note: the purpose of the perforated plate in radial flow configuration is preventing the beads from falling in the free space and to define the length of the bed domain, three legs were welded to the perforated plate to define the 10 cm free space at the inlet and outlet of the bed.
13. Insert a metal pipe in the radial tube because the tube is flexible. This will help to hold the radial tube in place and prevent movement to the right/left while pouring the beads.
14. Insert the thermocouple(s) and the radial tube into the flange and screen and insert all of them as one piece into the bed as shown in Figure B2 image 1. Push the perforated plate from the other side using a wooded rod until its legs touch the cover flange.
15. Use the normal cover flange. It has one inlet for HTF (1 inch Female National Pipe Thread, FNPT) and two holes (¼ inch FNPT) for thermocouple insertion if the focus is on charging only as was used in chapter 4 in the present study. Note: This flange is used because two internal thermocouples can be inserted, which provides more sensing points to measure the temperature during the charging process as can be seen in Figure B3. If you want to study the discharging process and do normal discharging, you must use the second custom flange (the one used for axial pipe injections). It has four inlets for HTF (1/2 inch Female National Pipe Thread, FNPT) and one hole (¼ inch FNPT) for thermocouple insertion. Use the pipe plug (Swagelok, SS-8-P) to plug unneeded ½ inch pipe holes as was shown in Figure B2.
17. Repeat steps 5-14 in B.1 above exactly. However, if you use a solid plate (explained below), the steps 5 - 7 will differ, and will be explained after step 20 below.
16. To improve the flow and force the flow toward the bed wall, a solid plate is used as explained in chapter four. A thin aluminum rectangular plate was used (local commercial stores, no part number is available) as shown in Table A.2.
17. Measure the internal diameter and cut a circular piece out of the rectangular plate. Note: the internal diameter is not the internal diameter of the insulation because sealant is used at the inlet/outlet and inside the bed to prevent bypass flow and to fix cracks, which adds some very small thickness. Therefore, the diameter of the solid plate should include that to easily insert the solid plate. However, a leak should be expected between the solid plate and the wall as explained in chapter five.
18. Use a file to polish the circumference (make edges smooth) to avoid damaging the internal insulation.
19. Drill four holes at angular positions ( $\theta = 0, 90, 180, 270^\circ$ ), each with ¼ inch at the edge of the plate. This solid plate can be used at the outlet only.
20. To use a solid plate inside the bed, repeat step 18 and add another three holes (½ inch at the center of plate to insert the radial tube through it and 3/16 inch to insert the thermocouples, both at 1.5 inch from the center as shown in Table A.2.

21. In order to be able to insert the solid plate easily, the storage vessel needs to be in the vertical layout. This cannot be achieved with the current storage vessel, but you can improve it.
22. Try to tilt the bed more than  $60^\circ$  but less than  $75^\circ$  using the high lift jack, this will help you to insert the solid plate easier. However, be very careful and make sure that the high lift jack base and the hinge are both connected firmly to the storage vessel base table. Note: Stop tilting the bed if you see that high lift jack starts to bend right or left.
23. Use the T-cross (Table A1) to hold the thermocouple(s) and the radial tube and avoid bending/moving of them to the left or the right.
24. Wear gloves and face mask (available in the lab) to avoid the dust of the alumina beads.
25. Start pouring the beads from the left side. Push the beads to the very end of the bed using a wooden rod.
26. You need to decide how many plates you will use and based on that, measure the length after you push the beads to the end using a measurement tape; for example, if you use four plates every 25 cm, the first plate will be at 85 cm ( 75 cm bed + 10 cm free space) from the outlet and so on. Note: Because the bed is tilted about  $60\text{-}75^\circ$ , you cannot get an accurate length measurement, but it will be a reasonable approximation. The solid plate at 35 cm and at 10 cm from the outlet will be very accurate (in terms of length measurements) and easy to insert into the bed. In the present study only two plates were used because it is difficult to insert three or four plates due to the small diameter of the bed as explained in chapter 4.
27. Insert the plate and push it very slow to avoid damaging the insulation and the thermocouples. The solid plates shown in Table A.2 can be used. Use plate 2 at the outlet and plate 3 at any other axial location inside the bed. Solid plate, image 4 was used at the outlet. As can be seen, three extra holes were drilled to insert the plate through the legs of the perforated plate, but it leads to flow leaking. Therefore, solid plate in image 2 was used at the outlet behind the perforated plate (between the perforated plate and beads, which was better than solid plate, image 4.
28. Repeat step 25 after the insertion of each solid plate.
29. Repeat steps 9-14 in B.1.



Figure B3: Cover Flange (inlet side) which was used to study the charging process with radial flow configuration.

### B.3.1 Charging and Discharging Test Protocol

The steps 1-19 in B.1.1 can be followed exactly to charge the bed. Note: the present study focused on charging process only by inserting two internal thermocouples to analyze the temperature distribution. As mentioned in chapter five, the inserted radial tube cannot be used to do radial discharging; another tube(s) should be inserted to perform radial discharging. Normal discharging can be achieved, but the second flange with four  $\frac{1}{2}$  drilled holes should be used to perform the normal discharging as can be seen in Figure B4.

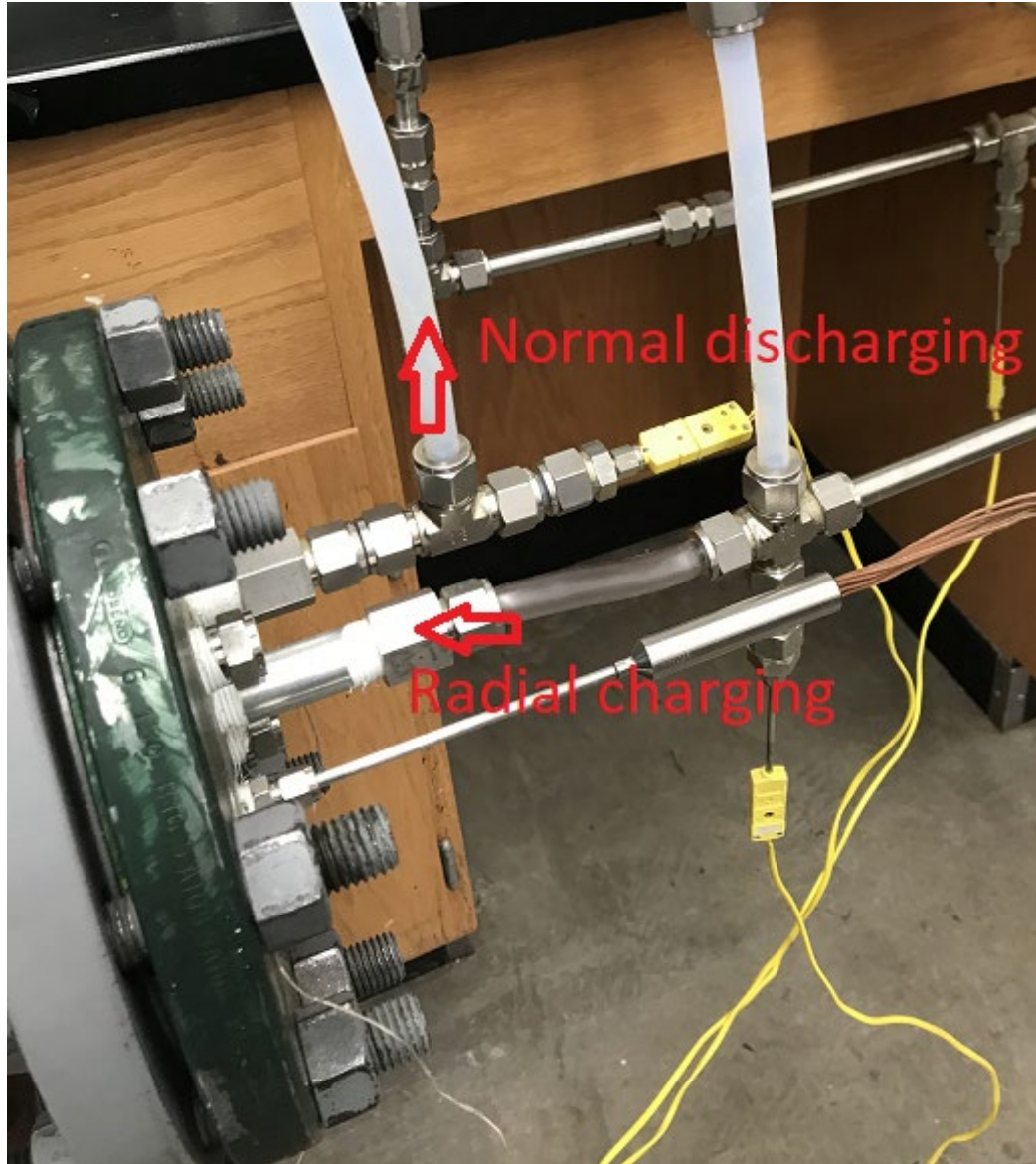


Figure B4: The custom cover flange (inlet side) showing the radial charging and normal discharging setup. Note: a thermocouple (Omega, KMQSS-125G-6) is inserted axially at the outlet of the normal discharging to be able to measure the recovery temperature. However, the probe length is very short (10 cm), a thermocouple with probe length 25 cm should be used.

#### B.4 Removing the Beads from the Storage Vessel for Normal, Layers and Radial Configurations Protocol

This protocol explains the steps needed to empty the packed bed from the beads in order to switch from one configuration to another; for example, from normal configuration to pipe injection configuration (layers or radial) or change the set up. To empty the packed bed from beads, follow the below steps.

- 1- Remove the insulation from the pipe(s), elbow(s) and tee(s) between the heater and the vessel inlet. You don't need to remove all the insulations, only insulations close to the vessel inlet to be able to disconnect the pipes.
- 2- Disconnect the pipes on the inlet and outlet sides.
- 3- Tilt the packed bed 45-60° using the high lift jack.
- 4- Open the flange on the outlet side only.
- 5- Take out the alumina beads, at least 40-50% of the beads by hand after wearing gloves and face mask.
- 6- Screw off the nut (Swagelok Tube Fitting, Bored-Through Male Connector) for the thermocouple.
- 7- Start to pull the thermocouple very slow until you pull it completely out of the bed. If you feel it does not move, try to take more beads out of the bed from the outlet side. Note: Do not try to pull the thermocouple out of the bed if the bed is completely filled with beads because you will either break or bend the probe of the thermocouple (long internal thermocouple inside the bed).
- 8- Lower the bed to the horizontal layout by downing the high lift jack.
- 9- Place a bucket under the bed inlet, close to the base table to collect the rest of the beads.
- 10- Open the flange of the inlet side and pull out the perforated plate.
- 11- Push the beads using a wooden rod from the outlet side or tilt the bed to collect the remaining beads inside the bed.
- 12- For pipe injection configuration, repeat steps 1-7.
- 13- Screw off the nut (Swagelok Tube Fitting, Bored-Through Male Connector) for the injected pipes. Pull the injected pipes very slow until you feel the end of the pipe reaches the perforated plate. Do not pull the pipes completely out of the bed. There is a screen mesh connected at the outlet of each pipe as can be seen in Table A.2, which will prevent the pipe from going through the perforated plate and thus can avoid damage to the internal insulation.
- 14- Repeat steps 8-9.
- 15- Screw off the flange bolts of the inlet side. You need to carry the flange with the pipes and pull them as one piece; the perforated plate will be pulled with the pipes and the flange too. Do it very slow to avoid damaging the internal insulation.
- 16- Repeat step 11.
- 17- For radial flow configuration, repeat steps 1-7.
- 18- Remove the cross dowel from the injected tube (outlet side).
- 19- Screw off the nut (Swagelok Tube Fitting, Bored-Through Male Connector) for the injected tube. Pull the injected tube very slow until you pull it completely out of the bed.
- 20- Repeat steps 8-11.

APPENDIX C

SPECIFIC HEAT CAPACITY VARIATION

The specific heat capacity of air is considered constant in the range of temperature used in the present study, from ambient to 150°C. However, the variation in specific heat is considered in this appendix to prove the variation is very small and can be neglected. Table C1 shows the calculations for thermal exergetic efficiency based on specific heat capacity variations. Eqn. C1 (Eqn. 2.7 in chapter two) is used to calculate the specific heat at each time step during charging and discharging processes. The calculated specific heat is used to calculate the exergy stored and the exergy recovered. Then, an integration is performed for the entire expression ( $\dot{m}C_p\Delta T$ ) over time using Matlab built-in function *trapz* command. Mass flow rate was constant during the charging and discharging processes and thus was dropped from the thermal exergetic efficiency, Eqn. C2. Note: The inlet temperature is integrated to include the change in temperature for the first 15-30 minutes (the ramp temperature effect) for all flow rates and will be explained next.

$$c_{p,f} = 1.8144 \times 10^{-7}T_f^3 + 2.209 \times 10^{-4}T_f^2 - 1.433 \times 10^{-1}T_f + 1.0246 \times 10^3 \left[ \frac{J}{kg-K} \right] \quad (C1)$$

$$\eta = \frac{\Xi_{recovery}}{\Xi_{storage}} = \frac{\int_{t_p} \left[ \{C_p(T)(T_r - T_o)\} - \{T_o C_p(T) \ln\left(\frac{T_r}{T_o}\right)\} \right] dt}{\int_{t_p} \left[ \{C_p(T)(T_{hot} - T_o)\} - \{T_o C_p(T) \ln\left(\frac{T_{hot}}{T_o}\right)\} \right] dt} \quad (C2)$$

Table C1. Percentage exergy with and without specific heat capacity variations with inlet temperature ( $T_f = 150$  °C) and reference temperature ( $T_o = 21.5$  °C ).

Flowrate, m <sup>3</sup> /s (SCFM)	Percentage exergy- C <sub>p</sub> constant	Percentage exergy- C <sub>p</sub> variation	Percentage exergy difference
0.002 (3)	38.2	37.5	1.83
0.0034 (5)	50.6	50	1.19
0.0048 (7)	57.1	56.5	1.05
0.0061 (9)	59.8	59.3	0.84

The storage inlet temperature is supposed to be constant during the charging period. However, during the first ~ 15-30 minutes as shown in Figure C1, the inlet storage temperature increase as a ramp function. This ramp temperature effect is because at time = 0 min, the temperature in the entire system is at room temperature. Then when the charging process starts, the temperature starts to increase gradually from zero to the maximum inlet temperature. The heat losses from the pipes, flanges, free space (between cover flange and perforated plate) and stainless-steel perforated plate lead to thermal losses by conduction and convection to the ambient environment. These thermal losses affect the inlet temperature and lead to the ramp temperature until reaching a constant inlet temperature. Higher losses occur at lower flow rate, e.g. 3 SCFM as can be seen in Figure C1. The area under the storage temperature curves represent the energy stored over the entire storage period. The thermal exergetic efficiency is calculated assuming constant and ramp inlet temperature,  $T_{hot} = 150^\circ\text{C}$  and  $T_{hot} = f(t)$ . The thermal exergy

efficiency equation, Eqn. C3 (Eqn. 2.13 in chapter two) is used. Integration is performed for the exergy recovery and exergy storage. Table C2 shows the thermal exergetic efficiency assuming storage temperature is constant and a function of time.

$$\eta = \frac{\varepsilon_{recovery}}{\varepsilon_{storage}} = \frac{\int_{t_p} [\{\dot{m}C_p(T_r - T_0)\} - \{\dot{m}T_0C_p \ln(\frac{T_r}{T_0})\}] dt}{\int_{t_p} [\{\dot{m}C_p(T_{hot} - T_0)\} - \{\dot{m}T_0C_p \ln(\frac{T_{hot}}{T_0})\}] dt} \quad (C3)$$

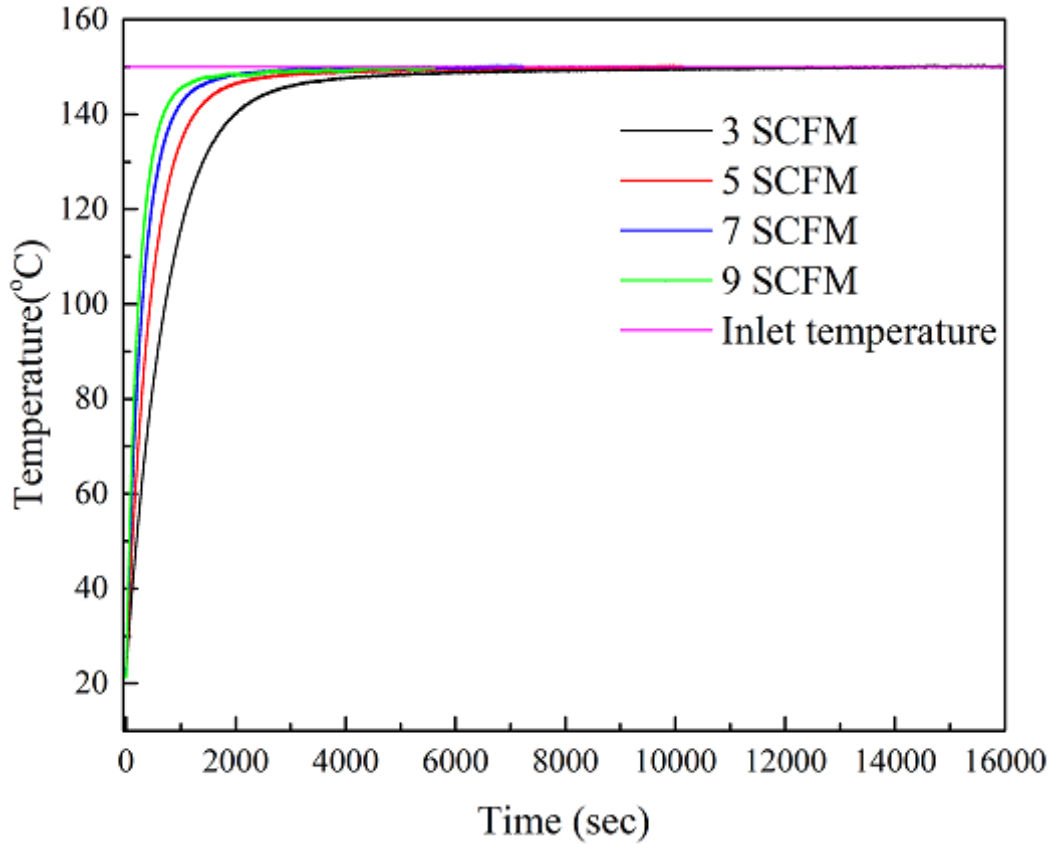


Figure C1: The storage temperature profiles during charging process with time at four flow rates.

Table C2: Percentage exergy with  $T_{hot} = 150^\circ\text{C}$  and  $T_{hot} = f(t)$  at four flow rates, constant specific heat capacity, and reference temperature ( $T_0 = 21.5^\circ\text{C}$ ).

Flow rate (SCFM)	Percentage exergy ( $T_{hot} = f(t)$ )	Percentage exergy ( $T_{hot} = 150^\circ\text{C}$ )
3	38.2	35.7
5	50.6	46.8
7	$57.3 \pm 0.4$	$53.2 \pm 0.4$
9	59.8	55.4



APPENDIX D

LABVIEW, DATA ANALYSIS, TEMPERATURE CONTROLLER, AND  
CALIBRATION OF FLOW AND TEMPERATURE

### D.1 LabView Code Protocol

LabView is the software used to control the tests by recording temperature measurements and display/save them for data analysis. Below are the steps to use the code called “Packed Bed” available on the computer (BZ-CHBE-CB30101.msu.montana.edu) in the lab. Note: if you need more information about LabView, go to <https://www.ni.com/en-us.html>. In addition, you could build a different code to collect the measured data. A screen shot of the code “Packed Bed” can be seen in Table A.3, showing the two windows of the LabView code, block diagram and front panel.

1. The code is “For Loop” to execute 1 Samples (On Demand). Inside the for loop, two data acquisition controller (DAQ) systems (National Instrument, NI 9213) are used to collect the experimental data. Both are connected to a waveform chart to display the data visually and to collectors to collect the input signals from each DAQ system. The collectors are set to 30,000 samples as maximum number (increase the number if you run the code to collect more samples; for example, if your charge/discharge time is more than 30,000 sec). These collectors are connected to “write to measurements file” to specify the file path, save the collected data and specify the time to collect the samples (samples are collected every one second in the code). The code is built in the block diagram window, which is connected to the front panel window. The front panel window has a waveform chart (where you can see the collected temperature data with time), maximum iteration box, iteration count box, delay time box, and filename with specified path as can be seen in Table A.3.
2. To start, search for LabView software. It is on the taskbar too.
3. Select file, open, “Packed Bed file”, which is saved on the local desktop.
4. The front panel will open directly, which represents the graphical user interface, and you can see the waveform chart. The front panel is connected directly to the block diagram, the second window of LabView.
5. Press Ctrl + E, and the block diagram window will open. This window represents the graphical source code of LabView. It includes terminals, subVIs, functions, constants, structures, and wires to transfer data collected.
6. Two data acquisition systems are connected (DAQ assistant and DAQ assistant2).
7. Sixteen sensing points are connected to DAQ assistant (surface, inlet, outlet, bypass, water and air thermocouples).
8. Sixteen sensing points are connected to DAQ assistant2 (two internal thermocouples, each with 8 sensing points).
9. Double clicking on either of them will open a new window (DAQ Assistant) as can be seen in Table A.3, where you could add and remove channels from the DAQ systems, see the connection diagram based on channels, and run the DAQ system to check if all points read room temperature or not. Note: if any of the sensing points reads k values, you need to check the connection of its wire with the DAQ system and fix it.
10. Under Thermocouple Setup, setting, you can check maximum and minimum amplitude (temperature in degree Celsius) and thermocouple type (K-type for all

thermocouples used in the study). Under device, ADC Timing Mode, check that the device is on “High Speed”.

11. Press OK.
12. Repeat steps 9-11 for the DAQ Assistant2.
13. Under the Connection Diagram, you can see the plus/minus signals and check the connections.
14. Go to the front panel window and enter the charging or discharging time (in seconds) in the box “maximum iteration” based on the process you are running.
15. Hit run on the left top side of the front panel when you are ready.
16. In the front panel, there is a box “iteration count” where you can see the count of time starting from zero.
17. When the “saving data circle” in the front panel turns green, this means the run is completed and the data is saved.
18. The data will be saved to a text file called “Packed Bed”. The code directly saves the first file on the desktop with name Packed Bed. If you run the LabView again without deleting or moving the file Packed Bed from the desktop, the code will automatically save the next file on the desktop with names Packed Bed\_1 and then Packed Bed\_2 and so on. Note: you can change the name of the file each time you run the experiment from the front panel, filename.
19. Important note: If you hit stop while the LabView is running, you will lose all the data collected and you need to start again.

## D.2 Data Analysis Protocol

The data from charging/discharging processes were saved to pdf files on the desktop. To analyze the data collected, move the data from the pdf files to Excel files as will be explained below. Note: Table A.4 shows screenshots of the data analysis steps.

1. Open Excel file
2. Select Data, Get External Data, From Text. Desktop, All Files.
3. A Text Import Wizard- Step 1-3 will appear. Select Delimited, Next, Comma and Space, Next, Finish, OK.
4. In the Excel file, “X-value” represents the time in seconds
5. In the Excel file, “Collected” represents the collected data from all thermocouples. Name them according to their sources (internal, surface, inlet, outlet, bypass, water and air thermocouples). Note: the sensing points from internal thermocouples are labeled 1,2....8, where 1 is the first sensing point at the tip of each thermocouple and 8 is the last point as shown in Table A.1. These points should be marked with 1 or 8 in the Excel file based on the typical axial charging/discharging direction. In the present study, sensing point with label 1 is point 8 in the Excel file and sensing point with label 8 is point 1 in the Excel file (charging from right to left) as shown in Table A1.

6. Use MATLAB or any other program to analyze/plot your data and calculate efficiency. MATLAB was used to analyze the data and Origin Graphing & Analysis 2016 was used to plot all the data in the thesis.
7. MATLAB was used to calculate the exergy efficiency. Numerical integration was used to integrate the recovery exergy (see exergy analysis in chapters two and three) which is a function of the recovery temperature with time using the built-in function, *trapz* command. This command uses the trapezoidal method of numerical integration.
8. For the thermal exergetic efficiency calculation, you need the storage time, the storage temperature, the recovery time and recovery temperature. The recovery temperature will be a function of the recovery time. Table D1 shows the code used to calculate the thermal exergetic efficiency.
9. In the MATLAB code enter the storage temperature, the room temperature, and charging time. The code will calculate the storage exergy based on that when you run the code.
10. Copy the data points of recovery temperature and time from the excel file.
11. Paste the data points of step 10 in the r-array in the MATLAB code shown in Table D1. The code will integrate for recovery exergy based on the recovery data using the MATLAB built-in function, *trapz* command.
12. Run the code. The ratio of the exergy recovery to the storage recovery is the thermal exergetic efficiency.

Table D1: MATLAB code used to calculate the thermal exergetic efficiency.

```

% Thermal exergetic efficiency calculator
% Calculation of exergy (useful work).
% Thermal exergetic efficiency = exergy recovery/exergy storage.
% No integration is needed for the exergy storage
% Integration is needed for exergy recovery
% Note: The numbers used here are just proposed numbers
clc;clear;close all;
% Storage
Ts= 150+273.15;% Storage temperature in degree K,
% assuming inlet temperature is 150 degree C
To= 21.5+273.15;% cold temperature in degree K (room temperature,
% which is in the range 21-22 degree C
ts= 10; % Charging time in sec
% Exergy storage equation as shown in chapter 2 and 3,
%Not: specific heat and mass flow rate are removed out
Ex_storage= ((Ts-To)-(To*log(Ts/To)))*ts; %
% Recovery
% Assume recovery time is 20 sec
% Create an array with two columns (first column is time ( 0- 20 sec)
% and second column is temperature measured form first sensing point
% at each single second) and 20 rows
r=[0 150
1 149.792505
2 149.907213
3 149.698173
4 149.739172
5 149.602294
6 149.656629
7 149.575928
8 149.516157
9 149.528932
10 149.483784
11 149.410766
12 149.639168
13 149.392273
14 149.298416
15 149.248075
16 149.393671
17 149.309765
18 149.347758
19 149.256959
20 149.216165];
tr=r(:,1); % represents the time column
Tr=r(:,2) +273.15; % The recovery temperature in degree K
% Exergy recovery equation as shown in chapter 2 and 3,
% Not: specific heat and mass flow rate are removed out
Q1=(Tr-To)-(To*log(Tr/To));
% Numerical intgration using Matlab built-in function "trapz" command
Ex_recovery=trapz(tr,Q1);
Exergy_eff= (Ex_recovery/Ex_storage)*100;

```

### D.3 Temperature Controller and Heater Protocol

To run the experiment and start the charging process, a heater is required to heat up the air to the desired temperature. The heater used (Omega, AHPF-121) can go to maximum temperature of 430°C (800°F). Therefore, a temperature controller is used to control the temperature outlet from the heater. Note: the maximum flow rate that can be used with the present heater is 15 cubic per feet minute (CFM). Therefore, make sure that you convert the mass flow rate from SCFM to CFM, which should be less than 15 CFM to avoid damaging the heater. Figure D1 shows the heater, which is connected to other equipment (explained below) to provide the hot heat transfer fluid.

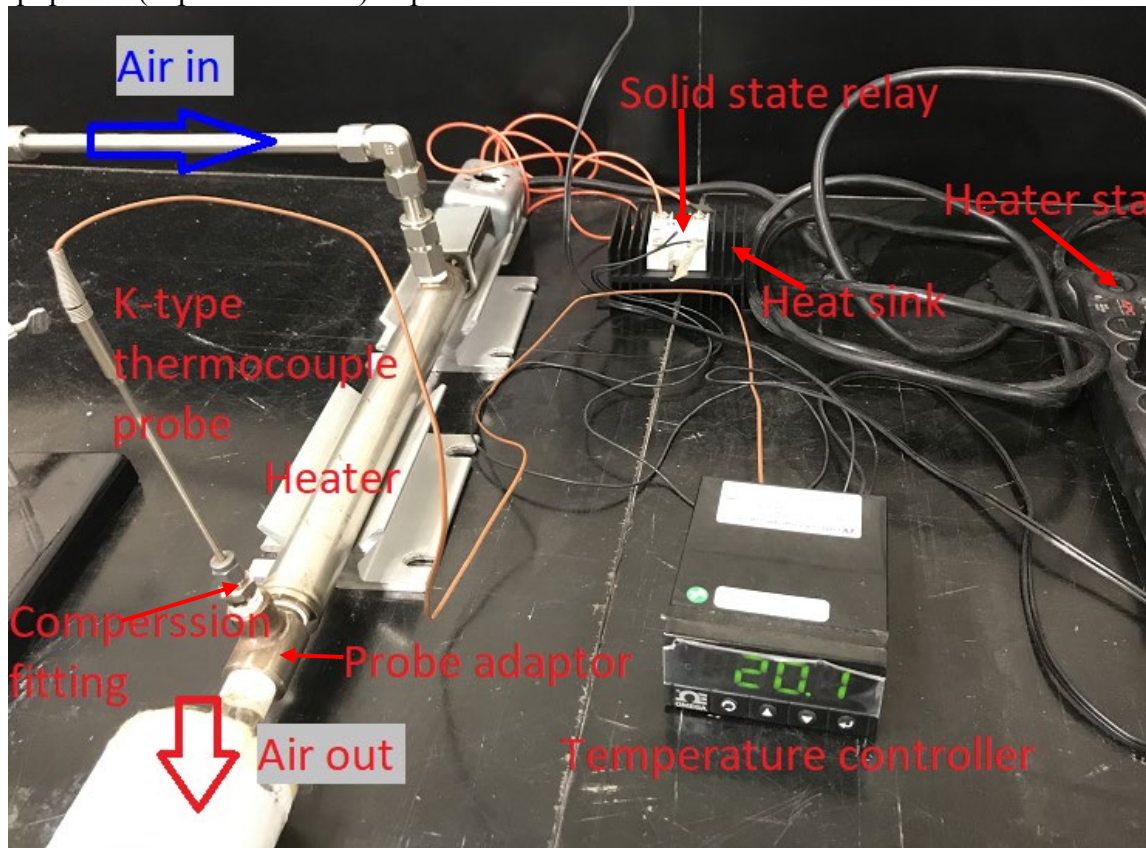


Figure D1: Heater and associated equipment, which was used to provide hot HTF.

The below steps explain the heater's connection with the associated equipment and how to run it:

1. The heater is connected to the temperature controller (Omega, CNi843) by a solid state relay (Omega, SSRL2400DC25). The solid state relay is placed on a heat sink (Omega, FHS-1) to cool it down. A K-type thermocouple probe (Omega, TJ36-CASS-18U-6) is inserted into the heater outlet through the probe adaptor (Omega, AHPF-NPT12) and

compression fitting (Omega, SSLK-18-14). The K-type thermocouple probe wires are connected to the temperature controller to display the outlet temperature from the heater.

2. The temperature controller has two set points, which can be used to control two heaters. However, one set point was used and programmed (set point one) to control the heater temperature.
3. Plug the temperature controller input cable into the electrical outlet from the wall.
4. Figure D shows the temperature controller before and after operating, reading the lab temperature.



Figure D2. The front window of the temperature controller.

5. Press the left button with the circular arrow one time to go to set point one (SP1).
6. Press the right button with 90-degree arrow one time to start changing the set temperature.
7. Use the up and down arrows to increase or decrease the set temperature. If you press the up or down arrows for more than 3 seconds, it will jump up or down very fast.
8. Press the right button with 90-degree arrow one time to save the updated set temperature. Two messages will appear: “StRd” means stored, then “SP2” to move to set point 2. Note: Press the same button if you need to change SP2, in case another heater is programmed/connected.
9. Press the left button with the circular arrow two times to return to the room temperature mode. Note: pressing the left button with the circular arrow one time will display “CNfO”, which means Configuration Menu, where you could change several features if needed.
10. You could change the set temperature while the device is running, a feature that you need when doing calibration and pipe injection experiments.
11. Now the temperature controller is ready, and the displayed temperature is in degree Celsius.
12. Note: Check the User’s Guide if you need to connect another heater or change any feature.
13. To run the heater, connect the heater cable to the outlet strip, which is shown in Figure D1. The outlet strip has on/off power switch to turn the heater on or off.

#### D.4 Calibration Protocol

In order to get a constant, desired inlet temperature at the bed inlet, the outlet temperature from the heater was calibrated as explained below:

#### D.4.1 Normal Configuration Calibration Protocol

1. Choose the flow rate that you want to test and the desired packed bed inlet temperature.
2. Set the temperature from the temperature controller (inlet temperature + 10 to 20 degrees); for example, if the desired packed bed inlet temperature is 150°C, set the temperature from the temperature controller to 160, 165, or 170 °C in order to get constant 150°C. Due to the heat losses from the pipes between the heater and the storage vessel inlet, the set temperature from the temperature controller must be higher than the desired inlet temperature. In addition, the distance between the heater outlet and vessel inlet affects the set temperature as was explained in appendix B.1.
3. Start the charging process by running the LabView code for 60 minutes (for 0.0048 m<sup>3</sup>/s, 7 SCFM, the charging time is 120 minutes). You could run the LabView code for more or less time. Record the inlet temperature (first sensing point inside the bed). Based on the recorded temperature, the set temperature from the temperature controller will be changed, up or down.
4. Repeat step 3 and record the inlet temperature. Based on the recorded temperature, the temperature from the controller can be increased or decreased again.
5. Repeat step 4. It is recommended after two or three steps to run the LabView for 15 minutes and record the inlet temperature to ensure a steady state inlet temperature.
6. Continue repeating step 5 until the recorded packed bed inlet temperature is constant. Usually, it takes 3-6 hours until you reach the right set temperature from the heater that gives constant inlet temperature based on the flow rate.
7. When you reach the constant temperature, run the code 2-3 times to check the repeatability of the inlet storage temperature
8. You need to do that for each flow rate.

#### D.4.2 Layers Configuration Calibration Protocol

1. If you run the same flow rate at the same inlet temperature in D.4.1 above, then you do not need to calibrate for the first layer. However, if the insulation between the heater outlet and vessel inlet and (or) the setup are changed, you should check/repeat the calibration for the 1<sup>st</sup> layer too.
2. Run the test for 60 minutes, charging the first layer, where the input temperature should be constant.
3. Open the second valve for the second layer, leaving the first valve open and increase the set temperature from the controller (10 – 15 degrees). Run the LabView for 60 minutes.
4. Monitor the temperature from the first layer. Adjust the 1<sup>st</sup> and 2<sup>nd</sup> valves and the set temperature to keep the inlet temperature constant for 1<sup>st</sup> layer.
5. Record the temperature and change the set temperature based on that.
6. Repeat steps 4 and 5 (you might do it several times) until you get a constant inlet temperature for the two layers. Note: the valves (Figure B2) used to control the flow through layers are Plug valves (Swagelok, SS-8P6T, a quarter turn instrument (zero flow at 0° and full flow at 90°), which is easy to control, but it is not the right valve



regarding the valve’s longevity. Therefore, when you adjust the valve, you need to measure the angle of the opening; this will help to approximate the amount of flow in this particular valve. An angle protractor is used to approximate the angle of opening of the valve. Note: this is just an approximation and not 100% accurate. However, the approximation used agreed with CFD modeling results very well.

7. Open the third valve to start calibrating for the third layer, keeping the 1<sup>st</sup> and 2<sup>nd</sup> valves opened. Increase the set temperature and run the LabView.
8. Repeat steps 4-6, monitoring the inlet temperature for the 1<sup>st</sup> and 2<sup>nd</sup> layers to keep them constant and adjusting the valves to get the desired inlet temperature for the 3<sup>rd</sup> layer.
9. The process could take several hours until you reach the constant inlet temperature for each layer. For 0.0048 m<sup>3</sup>/s (7 SCFM) with three layers, the calibration took eight hours, knowing that the first layer was already calibrated. Record the final set temperature that provides constant inlet temperature and a picture of the adjusted valves. Table D2 shows an example of calibration at 0.0048 m<sup>3</sup>/s (7 SCFM).

Table D2: The calibration results at one flow rate for three layers. Note: The mass flow rate in each pipe was approximated and discussed in chapter 3.

Flow rate (SCFM)	Layer	Set temperature from controller (°C )	Valves
7	1	174	1 <sup>st</sup> valve is fully opened, 2 <sup>nd</sup> and 3 <sup>rd</sup> valves are closed
	2	190	1 <sup>st</sup> valve is ~ 70% opened, 2 <sup>nd</sup> valve is fully opened, and the 3 <sup>rd</sup> valve is closed
	3	220	1 <sup>st</sup> valve is ~ 55% opened, 2 <sup>nd</sup> valve is ~ 60% opened, and the 3 <sup>rd</sup> valve is fully opened.

#### D.4.3 Radial Configuration Calibration Protocol

You can follow the same procedure in D.4.1. However, because the flow is radial, you will see that all sensing points will start increasing at the same time. Based on the flow distribution in the bed, some points will be at the same temperature and some will be up or down. Therefore, monitor all sensing points and make sure that most of them are reading approximately the same temperature at the desired inlet temperature when you do the calibration. The first sensing point reads a low temperature as was seen in chapter four and cannot be used as an inlet temperature sensing point. In order to measure the inlet temperature accurately, a thermocouple should be inserted in the radial tube (at  $x = -1$  cm, 1 cm before the first set of the radial holes), but it is expensive and difficult to install such thermocouple. An approximation based on temperature readings from all sensing points and even flow distribution was used in the present study.

### D.5 Flowmeter Calibration and Calculations of Flowrate Protocol

Two flowmeters (Omega, FL-4611 and FL-4612 for low and high flow respectively) were used to monitor the air flow. The readings of flow are in standard cubic feet per minute (SCFM). These flowmeters are calibrated at sea level. Therefore, calibration is achieved based on the equations provided by the manufacturer to correct the flow measured in the lab. Table D3 shows the corrected flows that have been used. As can be seen in the table to get real 3 SCFM, the rotameter should read 3.3 SCFM.

Table D3. Calibration of air flow for four flow rates.

Flowmeter reading (SCFM)	True flow (SCFM)
3.2368	3
5.3947	5
7.5526	7
9.7104	9

### D.6 Air Purity and Muffler

The air used in the experiments is from the building. The air is not clean and has oil and solid particulates. The air should be dry and clean to be used during charging/discharging processes. Two filters (McMaster Carr, 41745K21 and 8282K31) for water and oil vapor particulates were used to clean the air as can be seen in Table A.2. These filters should be cleaned every six months based on how heavily they are being used; for example, if you run the experiment every day, you need to clean the filters after six months. You may need to change the filter element only, which is very cheap compared to buying a new one. Filter elements are McMaster Carr, 98875K614 and 8282K52 for water and oil filters, respectively.

A high flow muffler, McMaster Carr, 4440K124 is connected to the air line before leaving the outlet pipes to the lab room to reduce the noise of flow, especially at high flow rate. Do not run the experiment without this muffler or if it is not functioning properly to avoid excessive pollution/danger to occupants in the room. The muffler is connected after the flowmeter as can be seen in Figure D3

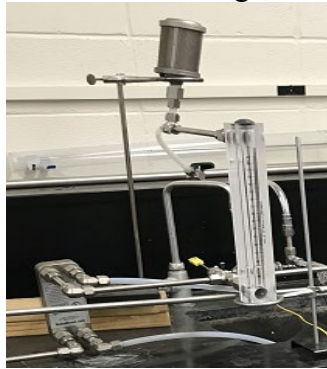


Figure D3: The muffler used to reduce noise in the lab.

APPENDIX E

PART NUMBERS AND MANUFACTURER FOR THE EQUIPMENT USED IN THE  
LAB

Table E1. Part numbers of the storage vessel and associated equipment used in the lab.

List	Equipment and fittings	Part number	Comments
1	Storage tank	-	Fabricated and tested by Power Service Inc.
2	Heater	AHPF-121	Omega
3	Temperature controller	CNi843	Omega
4	Solid state relay	SSRL2400DC25	Omega
5	Finned heat sink	FHS-1	Omega
6	1/8 X1/4 Compression fitting	AND SSLK-18-14	Omega
7	K-type thermocouple probe	TJ36-CASS-18U-6	Omega
8	Probe adaptor	AHPF-NPT12	Omega
9	Heater accessories	7248K21, 70355K84, 7059K452, And 7716k85	McMaster Carr, Light Duty Power Cord NEMA 1-15 Plug, 6 Feet Long, SPT-1, Power Cord Light Duty, NEMA 5-15 Plug, 9-1/2 Feet Long, 0.38" OD, SJT, Fast-Acting Midget Fuse Manufacturer Equivalent: BAF, BLF and OTM, 12A, AND Fuse Block for 1 Midget Fuse
10	Data acquisition system	NI 9213	National Instrument
11	Cooler	B3-12A-10ST	DudaDiesel, Duda Energy LLC
12	Water vapor Filter	41745K21	McMaster Carr, Compressed Air Filter for Water and Particles Heavy Duty, Aluminum Bowl, 1/4 NPT, 20 scfm @ 100 PSI
13	Oil vapor particulates filter	8282K31	McMaster Carr, Compressed Air Filter for Water, Oil and Particles Aluminum Bowl with Sight Glass, 1/4 NPT, 10 scfm @ 100 PSI
14	Filter connection fitting	50785K614	McMaster Carr, High-Pressure Brass Pipe Fitting Reducing Adapter, 1/2 NPT Female x 1/4 NPT Male
15	Filter element	98875K82 AND 8282K52	McMaster Carr, Filter Element for Heavy Duty 1/4 NPT Compressed Air Filter for Water and Particles AND Filter Element for 1/4 NPT Compressed Air Filter for Water, Oil and Particles
16	Pressure gauge	4003K61	McMaster Carr, Single Scale Pressure Gauge with 304Stainless Steel Case, 1/4 NPT Male Bottom Connection, 4" Dial
17	Flowmeter	FL-4612, FL-4611	Omega

18	Flowmeter	41945k59	McMaster Carr, Panel-Mount Flowmeter for Air PVC Fittings, 1/4 Female x 1/2 Male NPT, 5" Center-to-Center
19	Muffler	4440K124	McMaster Carr, High-Flow Muffler, 1/2 NPT Male
20	Internal K-type Thermocouples	OSK2K3918-1 and OSK2K4097-1	Omega Custom Design
21	Inlet/outlet and Surface thermocouples	KMQSS-125G-6, SA1-K	Omega
22	Internal thermocouples fittings (compression fittings)	SS-300-1-4BT	Stainless Steel Swagelok Tube Fitting, Bored-Through Male Connector, 3/16 in. Tube OD x 1/4 in. Male NPT
23	Inlet/outlet thermocouples fittings	SS-810-6-2BT	Stainless Steel Swagelok Tube Fitting, Bored-Through Reducing Union, 1/2 in. x 1/8 in. Tube OD
24	Plug Valve	SS-8P6T	Stainless Steel Quarter Turn Instrument Plug Valve, 1/2 in. Swagelok Tube Fitting, 4.4 Cv
25	Bonnet needle valve	SS-1RS8 And SS-1VS8	Stainless Steel Integral Bonnet Needle Valve, 0.73 Cv, 1/2 in. Swagelok Tube Fitting, Regulating Stem, and Stainless Steel Integral Bonnet Needle Valve, 0.73 Cv, 1/2 in. Swagelok Tube Fitting, Vee Stem
26	Elbows	SS-810-9	Stainless Steel Swagelok Tube Fitting, Union Elbow, 1/2 in. Tube OD
27	Tees	SS-810-3	Stainless Steel Swagelok Tube Fitting, Union Tee, 1/2 in. Tube OD
28	Union cross	SS-810-4	Stainless Steel Swagelok Tube Fitting, Union Cross, 1/2 in. Tube OD
29	Fittings	SS-810-6	Stainless Steel Swagelok Tube Fitting, Union, 1/2 in. Tube OD
30	Fitting, Heater inlet	SS-810-7-6	Stainless Steel Swagelok Tube Fitting, Female Connector, 1/2 in. Tube OD x 3/8 in. Female NPT
31	Fitting	SS-810-1-6	Stainless Steel Swagelok Tube Fitting, Male Connector, 1/2 in. Tube OD x 3/8 in. Male NPT
32	Fitting, Reducer	SS-810-7-8	Stainless Steel Swagelok Tube Fitting, Female Connector, 1/2 in. Tube OD x 1/2 in. Female NPT
33	Fitting, Reducer	SS-810-7-8BT	Stainless Steel Swagelok Tube Fitting, Female Connector, 1/2 in. Tube OD x 1/2

			in. Female NPT. Note: The item SS-810-7-8BT is not available in the market. The standard item, SS-810-7-8 has been bored through in the machine shop
34	Fitting, Reducer at the flange inlet/outlet	SS-810-7-16	Stainless Steel Swagelok Tube Fitting, Female Connector, 1/2 in. Tube OD x 1 in. Female NPT
35	Plug	SS-810-P	316 Stainless Steel Plug for 1/2 in. Swagelok Tube Fitting
36	Plug for flange drilled holes	SS-8-P	Stainless Steel Pipe Fitting, Pipe Plug, 1/2 in. Male NPT
37	Pipe insulation	45295K53	McMaster Carr, Tear-Resistant Silicone Foam Pipe Insulation, 1/2" Thick Wall, 1/2" ID, 6 Feet Long
38	Pipe insulation	44745K51	McMaster Carr, Flexible Rubber Foam Pipe Insulation Tube, Slit, 3/4" Thick Wall, 7/8" ID, 6 Feet Long
39	Pipe insulation	5556K31	McMaster Carr, Steam-Resistant High-Temperature Fiberglass Insulation Tube, 1" Thick Wall, 7/8" ID, 3 Feet Long
40	Tee-Insulation	93715K134	McMaster Carr, Flexible Rubber Foam Pipe Insulation, Tee, 3/4" Thick Wall, 7/8" ID
41	Tee-Insulation	5556K733	McMaster Carr, Steam-Resistant High-Temperature Fiberglass Insulation Tee, 1" Thick Wall, 7/8" ID
42	Elbow-insulation	93715K25	McMaster Carr, Flexible Rubber Foam Pipe Insulation, Elbow, 3/4" Thick Wall, 7/8" ID
43	Elbow-insulation	5556K714	McMaster Carr, Steam-Resistant High-Temperature Fiberglass Insulation Elbow, 1" Thick Wall, 7/8" ID
44	Cover flange insulation	9353K31	McMaster Carr, Extra-High Temperature Calcium Silicate Insulation 1/2" Thick, 12" x 12"
45	Cover to fix internal insulation cracks	8796K42	High-Temperature Felt, 1" Wide, 0.05" Thick
46	High temperature sealant for insulation	7644A11 And 7479A21	McMaster Carr, Self-Leveling Superflex Silicone Sealant Loctite® Model 596, 2.7 oz. Tube

47	Screen at inlet/outlet of the bed	9358T58	McMaster Carr, 304 Stainless Steel Perforated Sheet, Staggered Holes, 0.06" Thick, 0.0938" Hole Diameter, 35% open, 24" X 24".
48	Steel tube	89785K843	McMaster Carr, Smooth-Bore Seamless 316 Stainless Steel Tubing, 1/2" OD, 0.028" Wall Thickness
49	Tube for radial flow	1487T3	McMaster Carr, UV-Resistant Firm PVC Tubing for Air and Water, Clear, 3/8" ID, 1/2" OD
50	Support Stand and Rings	G7564706	ZORO, 18 in, 5/16 in, Stl
51	Table-storage tank base	46715T332	McMaster Carr, Steel Table, Low-Profile, Stationary, 24" High x 48" Wide x 24" Deep, Gray
52	Nut and Ferrule	SS-812-1, SS-813-1 and SS-814-1  OR SS-810-NFEST	316 Stainless Steel Nut for 1/2 in. Swagelok Tube Fitting, 316 Stainless Steel Front Ferrule for 1/2 in. Swagelok Tube Fitting, and 316 Stainless Steel Back Ferrule for 1/2 in. Swagelok Tube Fitting. OR 316 Stainless Steel Nut and Ferrule Set (1 Nut/1 Front Ferrule/1 Back Ferrule) for 1/2 in. Tube Fitting,